

---

---

# Development of a reliable and environmentally friendly synthesis for fluorescence carbon nanodots.

*Preparation and characterisation of excellent and well-defined carbon nanodots by a fast, simple and cost-efficient synthesis method; with special focus on future exploration and large scale applications.*

---

---

By

TILL THOMAS MEILING



Department of Chemistry  
UNIVERSITY OF POTSDAM

A dissertation submitted to the University of Potsdam in accordance with the requirements of the degree of DOCTOR RERUM NATURALIUM (DR. RER. NAT.) in the Faculty of Science.

SEPTEMBER 2017

Published online at the  
Institutional Repository of the University of Potsdam:  
URN urn:nbn:de:kobv:517-opus4-410160  
<http://nbn-resolving.de/urn:nbn:de:kobv:517-opus4-410160>

“YOU CAN’T WIN.”  
“YOU CAN’T BREAK EVEN.”  
“YOU CAN’T STOP PLAYING.”

THE LAWS  
OF THERMODYNAMICS





## LIST OF PUBLICATIONS

### Journal Publications

1. T. T. MEILING, R. SCHÜRMAN, S. VOGEL, K. EBEL, C. NICOLAS, A. MILOSAVLJECIC, AND I. BALD, *Photophysics and Chemistry of Nitrogen-Doped Carbon Nanodots with High Photoluminescence Quantum Yield*; The Journal of Physical Chemistry C, Manuscript accepted.
2. T. T. MEILING, P. J. CYWIŃSKI, AND H.-G. LÖHMANNSRÖBEN, *Two-Photon Excitation Fluorescence Spectroscopy of Quantum Dots: Photophysical Properties and Application in Bioassays*; The Journal of Physical Chemistry C, Manuscript accepted.
3. T. T. MEILING, P. J. CYWINSKI, AND I. BALD, *White carbon: Fluorescent carbon nanoparticles with tunable quantum yield in a reproducible green synthesis*, Scientific Reports, 6 (2016), p. 28557.
4. P. WESSIG, N. BEHREND, M. U. KUMKE, U. EISOLD, T. T. MEILING, AND C. HILLE, *Two-photon FRET pairs based on coumarin and DBD dyes*, RSC Advances, 6 (2016), p. 33510.
5. M. K. WECLAWSKI, T. T. MEILING, A. LENIAK, P. J. CYWINSKI, AND D. T. GRYKO, *Planar, Fluorescent Push-Pull System That Comprises Benzofuran and Iminocoumarin Moieties*, Organic Letters, 17 (2015), pp. 4252-4255.
6. R. NAZIR, T. T. MEILING, P. J. CYWINSKI, AND D. T. GRYKO, *Synthesis and Optical Properties of  $\alpha,\beta$ -Unsaturated Ketones Bearing a Benzofuran Moiety*, Asian Journal of Organic Chemistry, 4 (2015), pp. 929-935.
7. T. T. MEILING, H.-G. LÖHMANNSRÖBEN, K. KON, AND O. KARTHAUS, *Solvent Effect of the Adsorption of Titanium Dioxide Nanoparticles onto Microporous Polymer Films*, e-Journal of Surface Science and Nanotechnology, 8 (2010), pp. 309-312.

---

## Oral Presentations

1. T. T. MEILING, I. BALD, AND P. J. CYWINSKI, *White carbon: Fluorescent carbon nanoparticles with tunable quantum yield in a reproducible, green synthesis*, AsiaNANO 2016, Sapporo, Japan (2016).
2. T. T. MEILING, I. BALD, AND P. J. CYWINSKI, *White carbon: Fluorescent carbon nanoparticles with tunable quantum yield in a reproducible, green synthesis*, ChinaNANO 2015, Beijing, China (2015)
3. T. T. MEILING, I. BALD, P. J. CYWINSKI, AND H.-G. LÖHMANNSRÖBEN, *Photoluminescent carbon dots by a green microwave-assisted synthesis*, NaNaX 6, Bad Hofgastein, Austria (2014)

## Poster Presentations

1. T. T. MEILING, AND I. BALD, *Fluorescent carbon nanoparticles - Influence of carboxylic acids on the photoluminescence properties of nitrogen-doped carbon nanodots*, 17th Chitose International Forum on Photonics Science and Technology, Chitose, Japan (2016).
2. T. T. MEILING, I. BALD, P. J. CYWINSKI, AND H.-G. LÖHMANNSRÖBEN, *Photoluminescent carbon dots by a green microwave-assisted synthesis*, 113th General Assembly of the German Bunsen Society for Physical Chemistry, Hamburg, Germany (2014).
3. T. T. MEILING, D. HILL, S. STUFLER, AND H.-G. LÖHMANNSRÖBEN, *Quantum Dots as Donors in FRET and in Two-Photon Spectroscopy*, NaNaX 5, Fuengirola Spain (2012).
4. T. T. MEILING, D. HILL, S. STUFLER, AND H.-G. LÖHMANNSRÖBEN, *Quantum Dots as Donors in single pair FRET studies and 2-Photon Spectroscopy*, Laser Optics Berlin, Berlin, Germany (2012).

## Awards

1. Poster Award at 17th Chitose International Forum on Photonics Science and Technology, Chitose, Japan (2016).
2. Bachelor Award (3rd place) for “Outstanding Bachelor degree in Chemistry” from Gesellschaft Deutscher Chemiker (GDCh - German Chemical Society), Potsdam, Germany (2009)
3. Chitose Institute of Science and Technology - innoFSPEC Photonic Prize for “Extraordinary efforts for the collaboration between University of Potsdam and CIST in the areas of photonic research and education.” from Chitose Institute of Science and Technology, Chitose, Japan; and University of Potsdam, Potsdam, Germany (2009)

## ABSTRACT-ENGLISH

Carbon nanodots (CNDs) have generated considerable attention due to their promising properties, e.g. high water solubility, chemical inertness, resistance to photobleaching, high biocompatibility and ease of functionalization. These properties render them ideal for a wide range of functions, e.g. electrochemical applications, waste water treatment, (photo)catalysis, bio-imaging and bio-technology, as well as chemical sensing, and optoelectronic devices like LEDs. In particular, the ability to prepare CNDs from a wide range of accessible organic materials makes them a potential alternative for conventional organic dyes and semiconductor quantum dots (QDs) in various applications. However, current synthesis methods are typically expensive and depend on complex and time-consuming processes or severe synthesis conditions and toxic chemicals. One way to reduce overall preparation costs is the use of biological waste as starting material. Hence, natural carbon sources such as pomelo peel, egg white and egg yolk, orange juice, and even eggshells, to name a few; have been used for the preparation of CNDs. While the use of waste is desirable, especially to avoid competition with essential food production, most starting-materials lack the essential purity and structural homogeneity to obtain homogeneous carbon dots. Furthermore, most synthesis approaches reported to date require extensive purification steps and have resulted in carbon dots with heterogeneous photoluminescent properties and indefinite composition. For this reason, among others, the relationship between CND structure (e.g. size, edge shape, functional groups and overall composition) and photophysical properties is yet not fully understood. This is particularly true for carbon dots displaying selective luminescence (one of their most intriguing properties), i.e. their PL emission wavelength can be tuned by varying the excitation wavelength.

In this work, a new reliable, economic, and environmentally-friendly one-step synthesis is established to obtain CNDs with well-defined and reproducible photoluminescence (PL) properties via the microwave-assisted hydrothermal treatment of starch, carboxylic acids and Tris-EDTA (TE) buffer as carbon- and nitrogen source, respectively. The presented microwave-assisted hydrothermal precursor carbonization (MW-hPC) is characterized by its cost-efficiency, simplicity, short reaction times, low environmental footprint, and high yields of approx. 80 % (w/w). Furthermore, only a single synthesis step is necessary to obtain homogeneous water-soluble CNDs with no need for further purification.

Depending on starting materials and reaction conditions different types of CNDs have been prepared. The as-prepared CNDs exhibit reproducible, highly homogeneous and favourable PL properties with narrow emission bands (approx. 70 nm FWHM), are non-blinking, and are ready to use without need for further purification, modification or surface passivation agents. Furthermore, the CNDs are comparatively small (approx. 2.0 nm to 2.4 nm) with narrow size distributions; are stable over a long period of time (at least one year), either in solution or as a dried solid; and maintain their PL properties when re-dispersed in solution. Depending on CND type, the PL quantum yield (PLQY) can be adjusted from as low as 1 % to as high as 90 %; one of

---

the highest reported PLQY values (for CNDs) so far.

An essential part of this work was the utilization of a microwave synthesis reactor, allowing various batch sizes and precise control over reaction temperature and -time, pressure, and heating- and cooling rate, while also being safe to operate at elevated reaction conditions (e.g. 230 °C and 30 bar). The hereby-achieved high sample throughput allowed, for the first time, the thorough investigation of a wide range of synthesis parameters, providing valuable insight into the CND formation. The influence of carbon- and nitrogen source, precursor concentration and -combination, reaction time and -temperature, batch size, and post-synthesis purification steps were carefully investigated regarding their influence on the optical properties of as-synthesized CNDs. In addition, the change in photophysical properties resulting from the conversion of CND solution into solid and back into the solution was investigated. Remarkably, upon freeze-drying the initial brown CND-solution turns into a non-fluorescent white/slightly yellow to brown solid which recovers PL in aqueous solution. Selected CND samples were also subject to EDX, FTIR, NMR, PL lifetime (TCSPC), particle size (TEM), TGA and XRD analysis.

Besides structural characterization, the pH- and excitation dependent PL characteristics (i.e. selective luminescence) were examined; giving insight into the origin of photophysical properties and excitation dependent behaviour of CNDs. The obtained results support the notion that for CNDs the nature of the surface states determines the PL properties and that excitation dependent behaviour is caused by the “Giant Red-Edge Excitation Shift” (GREES).

## ABSTRACT-DEUTSCH

**K**ohlenstoff-Nanopunkte (CNDs, *engl. carbon nanodots*) haben im letzten Jahrzehnt insbesondere durch ihre vielversprechenden Eigenschaften immer mehr an Popularität gewonnen. CNDs zeichnen sich insbesondere durch ihre Wasserlöslichkeit, hohe chemische Stabilität, Biokompatibilität, hohe Resistenz gegen Photobleichen, und die Möglichkeit zur Oberflächenfunktionalisierung aus. Diese Eigenschaften machen sie somit ideal für eine breite Palette von Anwendungen: z.B. Abwasserbehandlung, (Foto-) Katalyse, Bioimaging und Biotechnologie, chemische Sensorik, sowie elektrochemische- und optoelektronische Anwendungen (z.B. LEDs). Insbesondere die Möglichkeit, CNDs aus einer Vielzahl organischer Materialien herzustellen, machen sie zu einer möglichen Alternative für herkömmliche organische Farbstoffe und Halbleiter-Quantenpunkte (QDs). Derzeitigen Synthesestrategien erweisen sich jedoch häufig als teuer, komplex und zeitaufwändig; bzw. benötigen toxischen Chemikalien und/oder drastische Reaktionsbedingungen. Eine Möglichkeit, die Herstellungskosten von CNDs zu reduzieren, ist die Verwendung von biologischem Abfall als Ausgangsmaterial. So wurden bereits eine Vielzahl an natürlichen Kohlenstoffquellen, z.B. Pomelo-Schale, Eiweiß und Eigelb, Orangensaft und sogar Eierschalen, für die Darstellung von CNDs verwendet. Während die Verwendung von biologischem Abfall wünschenswert ist, insbesondere um Wettbewerb mit der Nahrungsmittelproduktion zu vermeiden, fehlt den meisten Ausgangsmaterialien jedoch die notwendige Reinheit und strukturelle Homogenität um einheitliche CNDs zu erhalten. So führen bisherige Syntheseansätze oft zu CNDs mit heterogenen photophysikalischen Eigenschaften und unbestimmter Zusammensetzung. Für die Untersuchung des Zusammenhangs zwischen CND Struktur und photophysikalischen Eigenschaften werden aber möglichst homogene und vergleichbare Proben benötigt. In dieser Arbeit wird daher eine neue, zuverlässige, ökonomische und umweltfreundliche Einstufen-Synthese zur Darstellung von CNDs mit klar definierten und reproduzierbaren Photolumineszenz- (PL) -Eigenschaften vorgestellt. Die vorgestellte Methode basiert auf der mikrowellenunterstützten, hydrothermischen Behandlung (MW-hPC, *engl. microwave-assisted hydrothermal precursor carbonization*) wässriger Lösungen aus Stärke, Carbonsäuren (als Kohlenstoffquelle) und Tris-EDTA (TE) -Puffer (als Stickstoffquelle). Die MW-hPC zeichnet sich insbesondere durch die hohe Reproduzierbarkeit, einfache Handhabung, geringen Reaktionszeiten, geringe Umweltbelastung, Kosteneffizienz und die hohen Ausbeuten von ca. 80 % (w/w) aus. Darüber hinaus wird nur ein einziger Syntheseschritt (ohne weitere Aufreinigung) benötigt um homogene, wasserlösliche CNDs zu erhalten. In Abhängig der gewählten Ausgangsmaterialien und Reaktionsbedingungen können verschiedene Typen an CNDs gewonnen werden. Die so gewonnenen CNDs sind verhältnismäßig klein (ca. 2.0 nm - 2.4 nm); besitzen eine geringe Größenverteilung, hochgradig homogenen PL-Eigenschaften, und geringen Halbwertsbreiten (FWHM) von ca. 70 nm. Darüber hinaus erwiesen sie sich als nicht blinkend; sind langzeitstabil (min. ein Jahr) sowohl in Lösung als auch als Feststoff; und sind direkt gebrauchsfertig, d.h. benötigen keine weitere Aufreinigung oder Oberflächenpassivierung. In Abhängigkeit vom CND-Typ kann

---

die PL-Quantenausbeute zwischen 1 % bis 90 % betragen; einer der höchsten Werte der je (für CNDs) erreicht wurde.

Ein wesentlicher Bestandteil dieser Arbeit war die Verwendung eines Mikrowellensynthesereaktors (MiWR) und die damit einhergehende präzise Kontrolle über die Reaktionstemperatur und -zeit, den Druck, und die Heiz- und Abkühlgeschwindigkeit. Des Weiteren ermöglichte der MiWR unterschiedliche Ansatzgrößen und das sichere Arbeiten bei erhöhten Reaktionsbedingungen (z.B. 230 °C und 30 bar). Der hierdurch erreichte hohe Probendurchsatz ermöglichte somit erstmals die sorgfältige Untersuchung einer Vielzahl an Syntheseparametern hinsichtlich ihres Einflusses auf die photophysikalischen Eigenschaften der dargestellten CNDs. Die untersuchten Parameter reichen hierbei von der Reaktionstemperatur und -zeit über die Edukt-Konzentration und -Kombination (Kohlenstoff- und Stickstoffquelle) bis hin zur Ansatzgröße. Bemerkenswerterweise, und unabhängig vom CND-Typ, transformieren die ursprünglich braunen CND-Lösungen während der Trocknung zu einem nicht fluoreszierenden, weißen/leicht gelblich bis bräunlichen Feststoff; und regenerieren ihre photophysikalischen Eigenschaften verlustfrei in wässriger Lösung.

Im Rahmen dieser Arbeit wurden ausgewählte CND-Proben der EDX-, FTIR-, NMR-, TCSPC-, Partikelgrößen (TEM)-, TGA- und XRD-Analyse unterzogen. Die hierbei gewonnenen Erkenntnisse stützen die Theorie, dass die photophysikalischen Eigenschaften der CNDs durch ihre Oberflächenzustände bestimmt werden und dass die s.g. "Riesen-Rotkanten-Anregungsverschiebung" (GREES, engl. *Giant Red Edge Excitation Shift*) eine mögliche Ursache für die häufig beobachtete Anregungswellenlängenabhängigkeit der Emissionswellenlänge (bzw. selektive Lumineszenz) in CNDs ist.

## ACKNOWLEDGEMENT

Die vorliegende Arbeit entstand im Zeitraum Oktober 2012 bis September 2017 am Institut für Chemie (Physikalische Chemie) der Universität Potsdam in der Arbeitsgruppe Optische Spektroskopie und Chemical Imaging unter der Anleitung von Herrn Prof. Dr. Ilko Bald.

Ihm und Herrn Prof. Dr. Hans-Gerd Löhmannsröben gilt zuallererst mein Dank dafür, dass sie mir die Möglichkeit gaben meine Doktorarbeit auf diesem spannenden und interessanten Gebiet schreiben zu können. Insbesondere möchte ich Ilko Bald dafür danken, dass er mich und mein ihm zu diesem Zeitpunkt noch fremdes Thema so bereitwillig "adoptiert" hat. Des Weiteren möchte ich mich bei ihm für die tolle Betreuung, stetige Unterstützung, und motivierende Begleitung der Arbeit bedanken.

Bei Prof. Dr. Susan J Quinn (University College Dublin) und Prof. Dr. Armin Götzhäuser (Universität Bielefeld) möchte ich mich für das Erstellen der Zweitgutachten bedanken.

Ein besonderer Dank gilt natürlich auch denjenigen, die mich und meine Arbeit durch das Bereitstellen von Chemikalien, Geräten und Fachkompetenz unterstützt haben:

- Yasemin Linde (AG Linker, Universität Potsdam) für die Elementaranalyse
- Dr. Christina Günter (Institut für Erd- und Umweltwissenschaften, Universität Potsdam) für die XRD Messungen
- Dr. Claudia Prietzel (AG Koetz, Universität Potsdam) für die TEM Aufnahmen
- M.Sc. Norman Friedrich (AG Natalio, Martin Luther University Halle-Wittenberg) für die Unterstützung bei den FTIR Messungen und der Oberflächenfunktionalisierung der CNDs
- Dr. Frank Jaiser (Institut für Physik und Astronomie, Universität Potsdam) für die EDX Messungen
- Prof. Dr. Karthaus (Chitose Institute of Science and Technology) für die EDX- und TGA Messungen
- M.Sc. Sven Schulz und M.Sc. Phillip Roder (ALS ComBi, Universität Potsdam) für die nette Einführung und stetige Hilfe bei der Einzelmolekül- und Lichtmikroskopie

Darüber hinaus möchte ich mich bei Dr. Piotr J. Cywiński für die Zusammenarbeit und die anfängliche Betreuung meiner Doktorarbeit bedanken.

Ein besonders großer Dank gilt natürlich der gesamten UPPC. Es war mir eine Ehre und wahre Freude, in dieser Gruppe zu arbeiten. Ich möchte mich bei Christian, Daniel, Eric, Jenny, Jule, Kenny, Lydia, Phillip, Robin, Steffi, Sven, Uschi und Youngeun für die schöne Atmosphäre beim

---

täglichen Mittag, beim Kaffee zwischendurch, oder dem Bier am Abend bedanken.

Ein besonders herzliches Dankeschön geht an meine Bürokollegen Eric, Stephan und Martin für die gemeinsame Zeit, die fachliche Unterstützung und dafür, dass wir es immer wieder geschafft haben ernsthafte Diskussionen mit Spaß und Vergnügen zu verbinden. Die Kombination aus unserem Büromotto (“Neun von Zehn Leuten finden Mobbing ganz in Ordnung”); der hochwertigen Ausstattung (z.B. Kaffeemaschine, Kühlschrank); stetigem Nachschub an Bier, Eis und Kaffee; und natürlich Euch, machte dieses Büro und die Arbeitsatmosphäre zu etwas ganz besonderem. Ich werde es vermissen!

Ich möchte der Gesellschaft Deutscher Chemiker e.V. (GDCh) und der Potsdam Graduate School (PoGS) für die Unterstützung bei Reisekosten für verschiedene Tagungen danken.

Des Weiteren möchte ich mich bei der Südstärke GmbH (Schrobenhausen, Deutschland) für die kostenlose Bereitstellung der modifizierten Stärken bedanken.

Natürlich möchte ich mich auch bei meinen Freunden außerhalb der Uni bedanken. Vielen Dank dafür, dass ihr immer ein offenes Ohr für die Leiden eines Doktoranden hattet, und dass ihr es immer wieder geschafft habt mich vom Arbeitsalltag abzulenken. Wir sehen uns am Donnerstag zum Stammtisch.

Ein besonders großer Dank geht an meine ganze Familie. Insbesondere meinen Eltern und meiner Schwester möchte ich für ihre motivierenden Worte, unendliche Geduld und stetige Unterstützung danken. Meiner Oma Gerda danke ich dafür, dass sie uns gezeigt hat, dass die Welt existiert um bereist zu werden und dass man nie zu alt ist um dazu zu lernen.

Mein größter Dank gilt Selina, für die gemeinsame Zeit, die stetige Unterstützung und den Mut das Experiment gewagt zu haben, gleichzeitig unsere Doktorarbeiten zu schreiben. Ich weiß die letzten Monate waren für uns beide ein einziges Chaos und eine Achterbahn aus Frust, Freude und Verzweiflung. Bei allem Streß bin ich jedoch glücklich, dass wir diesen Weg gemeinsam gegangen sind.

Und selbstverständlich danke ich allen, die sich angesprochen fühlen und die in dieser Aufzählung nicht namentlich genannt wurden. VIELEN DANK!



## AUTHOR'S DECLARATION

I declare that the work in this dissertation was carried out in accordance with the requirements of the University's Regulations and Code of Practice for Research Degree Programmes and that it has not been submitted for any other academic award. Except where indicated by specific reference in the text, the work is the candidate's own work. Work done in collaboration with, or with the assistance of, others, is indicated as such. Any views expressed in the dissertation are those of the author.

Hiermit versichere ich, dass ich die vorliegende Arbeit selbstständig verfasst und keine anderen als die angegebenen Quellen und Hilfsmittel benutzt habe, dass alle Stellen der Arbeit, die wörtlich oder sinngemäß aus anderen Quellen übernommen wurden, als solche kenntlich gemacht sind und dass die Arbeit in gleicher oder ähnlicher Form noch keiner Prüfungsbehörde vorgelegt wurde.

SIGNED: ..... DATE: .....



## TABLE OF CONTENTS

	<b>Page</b>
<b>List of Tables</b>	<b>xvii</b>
<b>List of Figures</b>	<b>xix</b>
<b>1 Introduction and Motivation</b>	<b>1</b>
<b>2 Theory</b>	<b>7</b>
2.1 The Carbon Dot Family . . . . .	7
2.1.1 Carbon Nanodots . . . . .	9
2.1.2 Graphene Carbon Quantum Dots . . . . .	10
2.1.3 Polymer Dots . . . . .	11
2.2 Synthesis of CDs . . . . .	12
2.2.1 Top-down Synthesis Methods . . . . .	12
2.2.2 Bottom-up Synthesis Methods . . . . .	13
2.2.3 Microwave Assisted Hydrothermal Treatment . . . . .	13
2.2.4 Post-Synthesis Treatment . . . . .	17
2.2.5 Starting Materials . . . . .	18
2.3 Physical and Optical Properties . . . . .	19
2.3.1 Biological Toxicity . . . . .	19
2.3.2 Introduction to Photoluminescence . . . . .	20
2.3.3 Photoluminescence Mechanisms and Processes in Carbon Dots . . . . .	31
<b>3 Materials and Experimental Methods</b>	<b>41</b>
3.1 Reagents and Materials . . . . .	41
3.1.1 Starting Materials . . . . .	41
3.1.2 Stock Solutions . . . . .	46
3.1.3 Iodine Test . . . . .	48
3.1.4 Kaiser Test . . . . .	49
3.2 Carbon Dot Synthesis Procedures . . . . .	50
3.2.1 Apparatus and Procedure . . . . .	50

## TABLE OF CONTENTS

---

3.2.2	Synthesis of Starch Derived Carbon Nanodots . . . . .	51
3.2.3	Synthesis of Starch Derived, Nitrogen-Doped Carbon Nanodots . . . . .	52
3.2.4	Synthesis of Carboxylic Acid Derived, Nitrogen-Doped Carbon Nanodots . . . . .	52
3.2.5	Post-Synthesis Treatment . . . . .	52
3.3	Experimental Methods . . . . .	53
3.3.1	Optical Characterisation . . . . .	53
3.3.2	Structural Characterisation . . . . .	56
3.4	Data Analysis . . . . .	57
<b>4</b>	<b>Results and Discussion</b>	<b>59</b>
4.1	Synthesis and Characterisation of Starch Derived Carbon Nanodots . . . . .	59
4.1.1	Influence of Starch Concentration and Reaction Time on C-CND Synthesis . . . . .	60
4.1.2	Influence of Starch Type on C-CND Synthesis . . . . .	64
4.1.3	Up-scaling . . . . .	68
4.1.4	Freeze Drying of C-CND Solutions . . . . .	70
4.1.5	Structural Characterization of C-CNDs . . . . .	71
4.1.6	Summary . . . . .	73
4.2	Synthesis and Characterisation of Starch Derived, Nitrogen-Doped Carbon Nanodots . . . . .	75
4.2.1	Influence of Various Nitrogen Additives on C/N-CND Synthesis . . . . .	75
4.2.2	Influence of Reaction Time on C/N-CND Synthesis . . . . .	77
4.2.3	Influence of Reaction Temperature on C/N-CND Synthesis . . . . .	78
4.2.4	Influence of Precursor Concentration and -Composition on C/N-CND Synthesis . . . . .	80
4.2.5	Freeze Drying of C/N-CND Solutions . . . . .	83
4.2.6	Summary . . . . .	84
4.3	Synthesis and Characterisation of Carboxylic Acid Derived, Nitrogen-Doped Carbon Nanodots . . . . .	86
4.3.1	Influence of Reaction Temperature on CA/N-CND Synthesis . . . . .	88
4.3.2	Influence of TAE Buffer Concentration on CA/N-CND Synthesis . . . . .	89
4.3.3	Influence of Acetic Acid Concentration on CA/N-CND Synthesis . . . . .	92
4.3.4	Influence of Reaction Time on CA/N-CND Synthesis . . . . .	96
4.3.5	Photophysical Properties of HAc/N-CNDs at Various pH Values . . . . .	99
4.3.6	Influence of Carboxylic Acid Type on CA/N-CND Synthesis . . . . .	100
4.3.7	Freeze Drying of CA/N-CND Solutions . . . . .	104
4.3.8	Structural Characterization of CA/N-CNDs . . . . .	105
4.3.9	Photophysical Characterization of CA/N-CNDs . . . . .	110
4.3.10	Summary . . . . .	117
<b>5</b>	<b>Summary and Outlook</b>	<b>119</b>

<b>A Abbreviations and Symbols</b>	<b>123</b>
<b>B Tables and Figures</b>	<b>127</b>
B.1 Tables . . . . .	127
B.2 Figures . . . . .	130
B.2.1 EEM- and 3DEM Measurements . . . . .	137
B.3 NMR Spectroscopy . . . . .	144
<b>C Overview of Carbon Dots from Previous Articles</b>	<b>149</b>
<b>Bibliography</b>	<b>155</b>



## LIST OF TABLES

<b>TABLE</b>	<b>Page</b>
2.1 Timescale Range for Radiative- and Non-Radiative Processes . . . . .	22
3.1 Starting Materials . . . . .	41
3.2 (Modified) Starches . . . . .	45
3.3 TAE-,TE-, and TeE Buffer Solutions . . . . .	47
3.4 PBS buffer . . . . .	48
4.1 Elemental Analysis (ELE) of Starch Types . . . . .	65
4.2 Overview of Various CA/N-CND Types . . . . .	104
4.3 Excited State Lifetimes of CNDs . . . . .	110
A.1 List of Abbreviations and Symbols . . . . .	123
B.1 Overview N-Additives . . . . .	127
B.2 Overview C-Sources . . . . .	128
B.3 Characteristic Absorption Bands of CNDs . . . . .	129
B.4 Overview N-CNDs vs QDs . . . . .	129
C.1 Overview of CDs from Previous Articles . . . . .	150





## LIST OF FIGURES

<b>FIGURE</b>	<b>Page</b>
1.1 CD Properties and Applications . . . . .	3
1.2 CND Synthesis Parameters . . . . .	4
2.1 The Carbon Dot Family . . . . .	8
2.2 GCQD Structure . . . . .	10
2.3 Electronegativity of Heteroatoms and Potential PL Emission Colors . . . . .	18
2.4 Perin-Jablonski-Diagram . . . . .	21
2.5 The Stokes Shift . . . . .	22
2.6 Franck-Condon-Principle . . . . .	24
2.7 Solvation-Energy Diagram . . . . .	27
2.8 Perrin-Jablonski Diagrams for Excited-State Processes . . . . .	29
2.9 Perrin-Jablonski Diagram for The Red-Edge Excitation Shift (REES) . . . . .	30
2.10 Edge-States and GCQD Structure . . . . .	35
2.11 The Isolated Fluorophore Effect (IFE) . . . . .	36
2.12 The Giant Red-Edge Excitation Shift (GREES) . . . . .	38
3.1 Amylose and Amylopectin . . . . .	44
3.2 The CND Synthesis . . . . .	51
4.1 Starch Types: Particles and Composition . . . . .	60
4.2 Influence of Reaction Time on C-CND Synthesis (I) . . . . .	61
4.3 Influence of Reaction Time on C-CND Synthesis (II) . . . . .	62
4.4 Influence of Reaction Time and Starch Concentration on C-CND Synthesis . . . . .	63
4.5 Influence of Starch Type on C-CND Synthesis . . . . .	66
4.6 Glucose Derived CNDs . . . . .	67
4.7 Up-scaling of C-CND Synthesis . . . . .	69
4.8 Freeze-drying of C-CNDs . . . . .	70
4.9 Structural Characterization of C-CNDs . . . . .	72
4.10 TEM Images of C-CNDs . . . . .	73
4.11 Influence of N-additives on C/N-CNDs . . . . .	76
4.12 Influence of Reaction Time on C/N-CND Synthesis . . . . .	78
4.13 Influence of Reaction Temperature on C/N-CND Synthesis . . . . .	79
4.14 Influence of C-source to N-additive Ratio on C/N-CND Synthesis . . . . .	81

4.15	Glucose Derived N-CNDs . . . . .	82
4.16	Freeze-drying of C/N-CNDs . . . . .	84
4.17	Influence of N-additives on N-CND Synthesis . . . . .	87
4.18	Influence of Reaction Temperature on CA/N-CND Synthesis . . . . .	88
4.19	Influence of TAE Buffer Concentration on CA/N-CND Synthesis (I) . . . . .	90
4.20	Influence of TAE Buffer Concentration on CA/N-CND Synthesis (II) . . . . .	91
4.21	Influence of HAc Concentration on HAc/N-CND Synthesis . . . . .	93
4.22	Influence of pH Value on HAc/N-CND Synthesis (I) . . . . .	94
4.23	Influence of pH Value on HAc/N-CND Synthesis (II) . . . . .	95
4.24	Influence of Reaction Time on HAc/N-CND Synthesis (I) . . . . .	96
4.25	Influence of Reaction Time on HAc/N-CND Synthesis (II) . . . . .	97
4.26	Influence of Reaction Time on HAc/N-CND Synthesis (III) . . . . .	98
4.27	The Effect of the Solution pH Value on the PL Properties of HAc/N-CNDs . . . . .	99
4.28	Influence of Carboxylic Acid Type on CA/N-CND Synthesis (I) . . . . .	101
4.29	Influence of Carboxylic Acid Type on CA/N-CND Synthesis (II) . . . . .	103
4.30	Structural Characterization of CA/N-CNDs (I) . . . . .	106
4.31	Structural Characterization of CNDs . . . . .	107
4.32	Structural Characterization of CA/N-CNDs (II) . . . . .	109
4.33	Photophysical Characterization of CA/N-CNDs . . . . .	111
4.34	Excitation-Emission Matrix (EEM) Measurements . . . . .	112
4.35	Influence of Excitation Wavelength on the PL Properties of HAc/N-CNDs (I) . . . . .	113
4.36	3D-Excitation Spectra Matrix (3DEM) Measurements . . . . .	114
4.37	Influence of Excitation Wavelength on the PL Properties of HAc/N-CNDs (II) . . . . .	115
4.38	Influence of Excitation Wavelength on the PL Properties of HAc/N-CNDs (III) . . . . .	116
B.1	PL Emission of PEG <sub>1500N</sub> Derived N-CNDs . . . . .	130
B.2	Calibration for Kaiser-Test . . . . .	130
B.3	Effect of Excitation Wavelength on C/N-CND PL Emission . . . . .	131
B.4	Reproducibility of C/N-CND Synthesis . . . . .	132
B.5	Oxidation of CNDs with Hydrogen Peroxide (I) . . . . .	133
B.6	Oxidation of CNDs with Hydrogen Peroxide (II) . . . . .	134
B.7	Reduction of CNDs . . . . .	135
B.8	Schematic Representation of Amidation Reaction . . . . .	136
B.9	Schematic Representation of DCC-Coupling Route . . . . .	136
B.10	Excitation-Emission Matrix (EEM) Measurements (II) . . . . .	137
B.11	Excitation-Emission Matrix (EEM) Measurements (III) . . . . .	138
B.12	Excitation-Emission Matrix (EEM) Measurements (IV) . . . . .	139
B.13	Excitation-Emission Matrix (EEM) Measurements (V) . . . . .	140
B.14	3D-Excitation Spectra Matrix (3DEM) Measurements (II) . . . . .	141

B.15 3D-Excitation Spectra Matrix (3DEM) Measurements (III) . . . . .	142
B.16 3D-Excitation Spectra Matrix (3DEM) Measurements (IV) . . . . .	143
B.17 $^1\text{H}$ -NMR Spectra of C-CNDs . . . . .	144
B.18 $^{13}\text{C}$ -NMR Spectra of C-CNDs . . . . .	145
B.19 $^1\text{H}$ -NMR Spectra of HAc/N-CNDs . . . . .	146
B.20 $^{13}\text{C}$ -NMR Spectra of HAc/N-CNDs . . . . .	147



## INTRODUCTION AND MOTIVATION

Carbon is the fourth most abundant element in the universe, after hydrogen, helium, and oxygen [43]. In particular its unique ability to form vast varieties of compounds at temperatures usually encountered on Earth [167] made it the common element of all known life [43]. Carbon atoms can bond in a variety of different ways, leading to many carbon allotropes like diamond, graphite and amorphous carbon [23]. The physical properties of these allotropes may vary widely and span a range of extremes, e.g. graphite is one of the softest and diamond the hardest (natural) material known. Furthermore, due to its nine possible oxidation states, carbon willingly forms a variety of stable covalent bonds with other suitable, multivalent (small) atoms [167]. Hence, carbon forms more compounds, approximately ten million described so far (and still counting), than any other known element [53]. For this reason, carbon provides the “backbone” of all molecules in organic compounds, making it the carrier of life [43, 53]. Over the last decades, many more allotropes of carbon have been discovered, e.g. fullerenes [72], carbon nano-foam [138] and graphene [118]. Especially with the discovery of carbon based materials for nanotechnology, e.g. carbon nanotubes [119], carbon nanobuds [115], and nanodiamonds [111], carbon once again uphold its title as “King of the Elements” [23].

In 2004, a new type of carbon analogue was described and synthesized for the first time [182] and garnered much interest over the last years [92]. These spherical nanoscale carbon particles, hence called “carbon dots,” were strongly photoluminescent with spectral features and properties comparable to those of other photoluminescent nanoparticles [157]. Nevertheless, their photoluminescence (PL) behaviour and structure distinguish carbon dots (CDs) from commonly known organic dyes, therefore, spanning from physical- and organic chemistry to traditional inorganic nanoparticle science.

Over the last decade further types of photoluminescent CDs, have been discovered, and added

to their brethren. At present, the “carbon dot family” covers three main types of carbon dots: polymer dots (PDs), graphene carbon quantum dots (GCQDs), and carbon nanodots (CNDs). Surface groups, size and intrinsic inner structure distinguish these carbon dot types, as their photoluminescence properties can be very similar (if not even identical) [16, 46, 86]. Furthermore, CDs have generated considerable attention due to their promising properties, e.g. high water solubility, chemical inertness, resistance to photobleaching, high biocompatibility and ease of functionalization [86]. These properties render them ideal for a wide range of functions, e.g. electrochemical applications [20], waste water treatment [142], (photo)catalysis [85], bio-imaging and bio-technology [4, 127, 155], as well as chemical sensing [47, 104, 155], and optoelectronic devices like LEDs [19, 49, 83, 92, 169, 196]. Moreover, CDs already made their mark in the fields of solar cells [92] and flexible photovoltaics [91].

In particular, the ability to prepare CDs from a wide range of accessible organic materials makes them a potential alternative for conventional organic dyes and semiconductor quantum dots (QDs) in various applications. However, current synthesis methods are typically expensive and depend on complex and time-consuming processes or severe synthesis conditions and toxic chemicals [4, 13, 83, 127, 155]. Typical CD preparation methods are arc-discharge [92, 182], laser ablation [90, 157], electrochemical synthesis [85, 200, 206], organic pyrolysis [44, 47, 127, 171] or hydrothermal methods [104, 140, 155]. One way to reduce overall preparation costs is the use of biological waste as starting material. Hence, natural carbon sources such as pomelo peel [104], egg white and egg yolk [171], orange juice [140] and even eggshells [68], to name a few; have been used for the preparation of CDs. While the use of waste is desirable, especially to avoid competition with essential food production [162], most starting-materials lack the essential purity and structural homogeneity to obtain homogeneous carbon dots. So far, it appears that under corresponding treatment nearly any carbon-source will form CDs.

For next generation luminescent probes foreign atom doping of CDs, especially with nitrogen, is of high interest, as it can drastically increase the overall photoluminescent quantum yield by changing the optoelectronic properties of the nitrogen-doped carbon dots [51]. However, most synthesis approaches reported to date require extensive purification steps and have resulted in carbon dots with heterogeneous photoluminescent properties and indefinite composition. For this reason, among others, the relationship between CD structure (e.g. size, edge shape, functional groups and overall composition) and photophysical properties is yet not fully understood. This is particularly true for carbon dots displaying selective luminescence (one of their most intriguing properties), i.e. their PL emission wavelength can be tuned by varying the excitation wavelength [46, 92]. Due to controversial results the origin of this behaviour is disputed and new reliable and reproducible CD synthesis ways are needed to enable comparable and meaningful experimental results in the future [92].

In order to obtain homogeneous carbon dots, a fundamental understanding of the CD formation mechanism, well-defined starting materials and deliberate use of additives are essential.

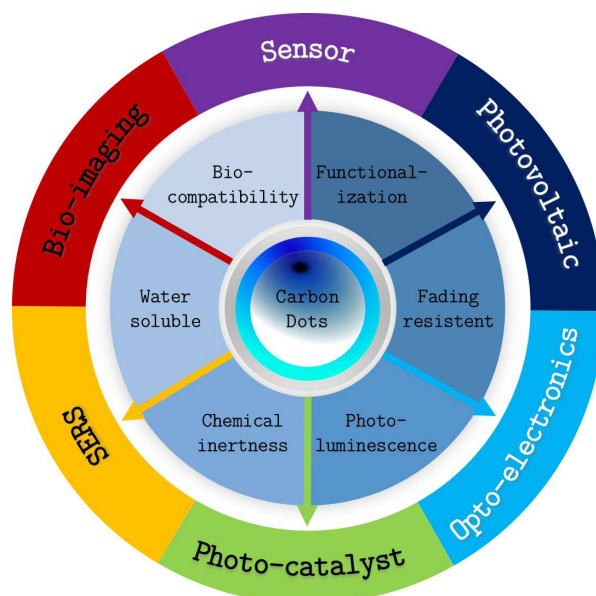


Figure 1.1: Carbon dots unique properties and their potential applications in various fields [86].

A perfect carbon source for green CD synthesis should be soluble in water (green chemistry), accessible worldwide with defined and well-known properties, should not be in direct competition with essential food production, and last but not least, be cost-effective [2, 92, 126]. While the price of additives or carbon sources plays a minor role in fundamental research, it may play a major role when commercial quantities are considered. Noticeably, the ease of the processing and no need for tedious and long purification has tremendous impact on the overall costs of the final material. Therefore, efforts have to be made to avoid today's scenario observed for semiconductor quantum dots. While having amazing properties and interesting uses, they still have not achieved their full potential in commercial applications due to significant production costs and potentially high toxicity [25, 177]. In this context CDs share common advantages with QDs, such as high photostability, large two-photon cross-sections [12] as well as suitability for bio-imaging [13, 47, 127, 140, 155]. However, in contrast to QDs, CDs are non-toxic, non-blinking and typically biocompatible [13, 47, 127, 140, 155]. Nevertheless, actual commercialisation of devices based on CDs is still pending, but their extraordinary properties (see Fig. 1.1) hold an unavoidable fascination that is likely to endure and inspire further research and discoveries for some time to come [23].

With this in mind, the aim of this work was the development of a fast, simple and cost-efficient method for the preparation of excellent and well defined CNDs at reasonable costs, thereby paving the way for future large-scale applications. For this reason, the synthesis methods presented in this work are based on microwave-assisted hydrothermal carbonization of natural precursors, which shortens the reaction time from typically hours [4, 13, 44, 155, 219] to several minutes and eliminates steps involving toxic or dangerous materials, whilst being scalable and easy to operate.

Our method involves aqueous solutions of starch or various carboxylic acids (as carbon sources) in combination with Tris and EDTA (as nitrogen additives). Starch and (most) carboxylic acids, e.g. citric- and acetic acid, meet aforementioned requirements, i.e. they can be obtained worldwide at low cost with well-defined properties in a wide variation of types and in large quantities without being in competition with food industry.

An essential part of this work was the utilization of a microwave synthesis reactor, allowing

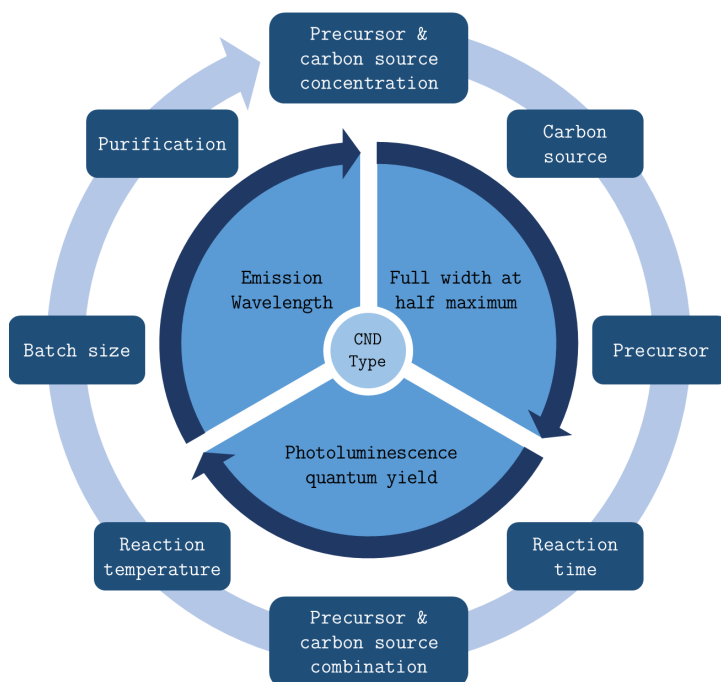


Figure 1.2: Schematic representation of investigated synthesis parameters, influencing the photophysical properties of as synthesized CNDs: emission wavelength, emission full width at half maximum and photoluminescence quantum yield.

various batch sizes (0.5 mL to 20 mL) and precise control over reaction temperature, pressure, reaction time, and heating- and cooling rate, while also being safe to operate at elevated reaction conditions (e.g. 230 °C and 30 bar). The hereby-achieved high sample throughput allowed the thorough investigation of the following synthesis parameters for the CND formation:

1. Carbon source
  - a) Starch type
  - b) Carboxylic acid type
2. Nitrogen additive (e.g. Tris, EDTA and urea)
3. Precursor concentration
4. Precursor combination
5. Reaction time and -temperature
6. Batch size (scale-up)
7. Purification steps (e.g. dialysis, freeze-drying)



---

High sample throughput further requires an assessment of obtained CND quality in a quick, but meaningful way (see Fig. 1.2). Hence, obtained CND solutions were assessed based on the following photophysical properties:

1. UV-Vis absorption spectra, as evidence for molecular structure
2. Position of emission maximum (at a given excitation wavelength)
3. Full width at half maximum (FWHM) of the (main) emission band, as means for homogeneity of obtained carbon dots
4. Photoluminescence quantum yield, as means for suitability as fluorescence marker

Of further interest was the stability of CNDs over a long period of time (at least one year), either in solution or as freeze dried powder, including the change of photophysical properties resulting from the conversion of CND solutions into dry powder and back into solution. Selected CND samples also ought to be subject to EDX, FTIR, NMR, photoluminescence lifetime, particle size (TEM), TGA and XRD analysis. In addition, the pH- and excitation dependent PL characteristics (i.e. selective luminescence) were examined for selected CND types.



Since their first discovery in 2004 [157, 182], the photoluminescence mechanisms and -processes of carbon dots have been debated controversially among researchers. At present, due to the great variety in the carbon dot family, it is highly important to summarize the different types of carbon dot materials and their possible PL mechanisms. This chapter will therefore give an introduction into the three main types of carbon dots and their ways of synthesis, and physical and optical properties. This is followed by an introduction of the basic principles of photoluminescence and subsequently a detailed view on the possible PL mechanisms of CDs.

## 2.1 The Carbon Dot Family

Carbon materials in the nanometer range, including nanodiamonds, fullerenes, carbon nanotubes (CNTs) and graphene are well known for many years [213]. In 2006 Sun *et al.* [157] showed, that by modulating the surface groups of these materials, fluorescent carbon nanoparticles could be obtained. Following this, “carbon dot” (sometimes also called carbon quantum dot) is a comprehensive term for all types of luminescent, surface-functionalized small carbon nanoparticles. All CDs show intrinsic luminescence, are at least in one dimension less than 10 nm in size and consist mainly of  $sp^2/sp^3$  hybridised carbon atoms. Furthermore, CDs can incorporate foreign atoms (e.g. oxygen, nitrogen), modified surface groups, and polymer aggregates. Simply put, all CDs consist of an inner (carbon) core surrounded by various types of surface modifications/passivations. These surface modifications not only provide solubility and colloidal stability, but also provide the possibility for further functionalization with different species for specific applications (e.g. bioimaging and -sensing) [110].

Up to now, three main types of CDs have been reported (see Fig. 2.1): carbon nanodots, graphene

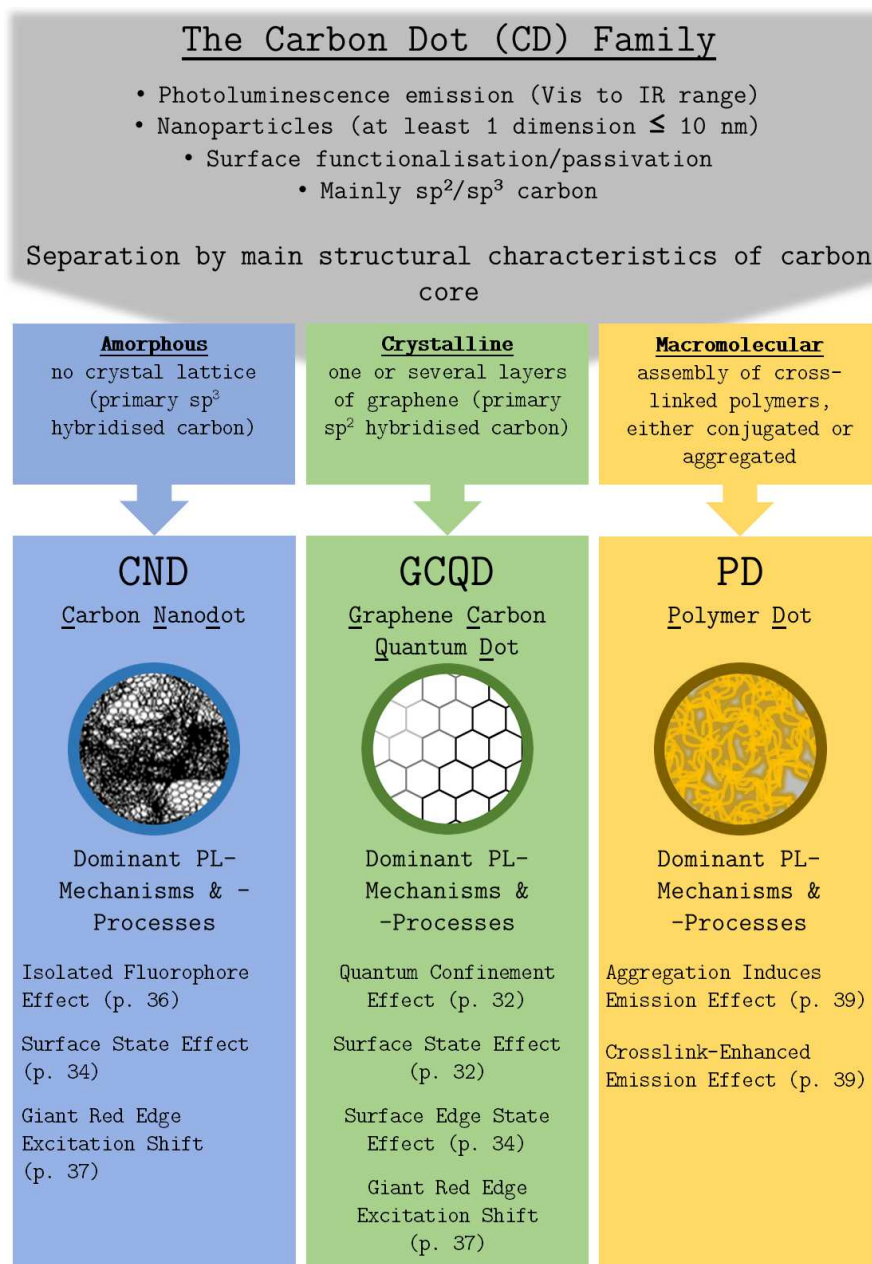


Figure 2.1: Schematic representation of the three main types of carbon dots (CDs). Their common properties and different characteristics are also presented.

carbon quantum dots and polymer dots. Other (typically larger) fluorescent carbon-based nanomaterials are fluorescent carbon nanotubes and so called fluorescent nanodiamonds, which will not be further discussed here. While these types of photoluminescent carbon nanodots can be distinguished by their surface groups, size and intrinsic inner structure, their photoluminescence properties are very much alike [46]. Various synthesis approaches to obtain CDs have been reported. This, however, also leads to diverse chemical structures for the obtained CDs.

To provide a comprehensive overview, the three main types of CDs, their potential synthesis routes, and optical, chemical and physical properties are briefly introduced in this chapter. Owing to the vast number of publications about CDs (see Table C.1, p. 150), this overview makes no claim to be complete.

### 2.1.1 Carbon Nanodots

The key difference between carbon nanodots (CNDs) and the other two CD types (PD and GCQD) is absence of near- and distant-structural order in CNDs. While GCQDs possess certain crystallinity and PDs have their repeating units, CNDs are amorphous and therefore don't have any crystal lattice. Furthermore, contrary to GCQDs, CNDs are always reported to be isotropic spherical particles.

It should be noted, that occasionally a crystalline type of CNDs is reported [213]. These so called carbon quantum dots (CQDs) are reported to have a crystal lattice corresponding to the (002) spacing of the crystalline graphite [116]. Due to their crystalline structure these CQDs should be regarded as a type of GCQDs (see Chap. 2.1.2, p. 10) rather than CNDs [213].

Due to the absence of significant conjugated  $sp^2$  domains (crystal lattice), the PL of CNDs derives from their surface states (see Chap. 2.3.3.2, p. 33). A range of functional groups have various energy levels, which may result in a series of emissive states. Depending on the excitation wavelength a single emissive surface state might dominate the emission. Most likely, these surface states do not consist of isolated chemical (surface) groups but rather of a hybridization of the chemical (surface) groups and the carbon backbone (CND core). As a consequence surface passivation plays a key role in CND PL processes. This becomes clear, e.g. from a red-shifted emission due to higher degrees of surface defects, either due to surface oxidation or other effective modifications. To date, it has been proven that many organic molecules can provide surface passivation [157], e.g. amino-polyethylene glycol (PEG), poly(propionyl ethyleneimine-co-ethyleneimine) (PPEI-EI) [92], and branched polyethyleneimine (BPEI) [204].

The origin of PL in CNDs is still not entirely understood, yet there is increasing evidence that PL emission arises from extrinsic photoluminescence resulting from surface states that can be either directly excited or excited by energy transfer from the CND core (carbon backbone). Thus, tuning the PL emission (bandwidth) could be achieved by modifying the chemical groups on the CND surfaces. However, this proves to be quite challenging (see Chap. 2.2, p. 12), as multiple PL processes appear to be intertwined. Depending on the synthesis routes (starting materials, reaction conditions etc.) different types of CNDs can be obtained. Therefore possible PL processes for CNDs include the surface state effect (see Chap. 2.3.3.2, p. 33) [175], the giant red-edge excitation shift GREENS (see Chap. 2.3.3.4, p. 37) [21], the isolated fluorophore effect (see Chap. 2.3.3.3, p. 36) [32, 212] or any combination of the above.

The unclear origin of PL of CNDs is counterbalanced by their many advantages over other CDs (GCQDs and PDs). So far CNDs have not only shown the highest PLQYs ever reported for CDs

(approx. 80 % [212]), but also their production costs can be considerably lower (e.g. wider range of raw materials, time- and energy consumption).

### 2.1.2 Graphene Carbon Quantum Dots

As their name implies, graphene carbon quantum dots (GCQDs) consist of one or several layers (usually  $< 10$ ) of graphene complemented by modified (surface) groups on the edges [110]. Hence, they are anisotropic with lateral dimensions larger than their height. Owing to the existence of its graphene like (single-)layered carbon core, GCQDs possess certain crystallinity. Similar to the corresponding (100) spacing of graphene the average lattice parameter is about 240 pm [94, 204, 213]. Their simple structure (see Fig. 2.2) makes GCQDs an ideal model to investigate the PL mechanisms and PL processes of CDs. However, a second crystalline type is described as carbon quantum dots (CQDs) with a typical crystal lattice interlayer distance of about 340 pm, which corresponds to the (002) spacing of the crystalline graphite [116]. Often these CQDs are regarded as CNDs [213], but due to their crystallinity they should be regarded as a type of GCQDs.

Graphene oxide (GO) is an important “first layer” GCQD and an important raw material for the

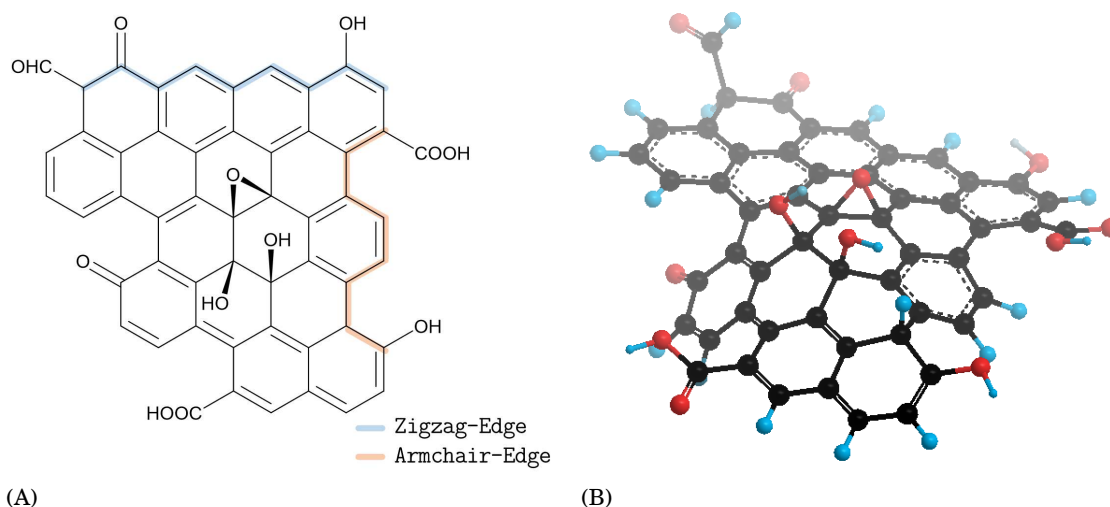


Figure 2.2: Exemplary presentation of a typical GCQD structure, including surface edge states and most common functional groups: (A) skeletal formula and (B) corresponding 3D model (at state of least energy). The 3D model illustrates the presence of bond distortions and out-of-plane strain, which may modify the PL of GCQDs (see Chap. 2.3.3.4, p. 37) [21, 107]. Atom color assignments: carbon (black), oxygen (red) and hydrogen (blue).

preparation of “higher layer” GCQDs. Therefore, GO and GCQDs possess similar chemical structures (see Fig. 2.2). Beside its carbon core, GO contains oxygen-based functional (surface) groups, either on the basal plane or at its edges. That is, that the aromatic  $sp^2$  domains are surrounded by an epoxy and hydroxyl-based  $sp^3$  carbon-oxygen matrix [92]. Whereas the oxygen-based sur-

face groups provide electrostatic and steric stabilization, the photoluminescent properties are determined by the  $\pi$  states of the about 2 nm to 3 nm sized  $sp^2$  domains (see Chap. 2.3.3.1, p. 32). Simply put, the PL properties of GOs/GCQDs depend on the size of the band-gap, determined by the size of their respective  $sp^2$  domains. Because of the existence of a wide size distribution of  $sp^2$  domains in GO/GCQDs, the band gaps of different sizes cover a wide range, leading to potential broad PL emission spectra from the visible range to near infrared. It is worth noting that the graphene oxide (GO) is sometimes classified as an independent type of CDs [213]. In this work GO is considered as a sub-type of GCQDs, due to its structural characteristics.

Apart from the quantum confinement effect (QCE) (see Chap. 2.3.3.1, p. 32), induced by conjugated (aromatic)  $sp^2$  domains, also other potential PL mechanisms for GCQDs are discussed. For example, potential PL mechanisms/processes are associated with (localized) electronically excited states of surface functional groups (see Chap. 2.3.3.2, p. 33) [48], with different edge states on the GCQD surface (see Chap. 2.3.3.2, p. 34), and with the emission of quasi-molecular fluorophores in GCQDs (see Chap. 2.3.3.3, p. 36) [45]. Furthermore it was proposed that also bond distortions and out-of-plane strain (see Chap. 2.3.3.4, p. 37) may modify the PL of GCQDs [21, 107]. This wide variation of potential PL mechanisms/processes is typical for CDs, due to their complex and sometimes uncertain chemical structure. Thus, it is possible that in a single type of GCQD, multiple PL mechanisms/processes are contributing and influencing each other at the same time. This makes the clarification of the exact PL mechanisms and PL processes very difficult. Up to now, GCQDs obtained from currently employed synthesis routes (see below) still suffer from many drawbacks, such as high cost, comparably low PLQYs and low control of specific chemical structure. Especially the latter still leads to GCQD mixtures with broad emission bands due to the wide range of  $sp^2$  domain sizes (on both intra- and intermolecular level).

### 2.1.3 Polymer Dots

The so called polymer dots (PDs) are an assembly of cross-linked polymers prepared from linear monomers or polymers. Two types of PDs are known, conjugated PDs, which are obtained from conjugation of fluorescent polymers; and non-conjugated PDs, which possess an aggregated polymer structure. A specific feature of PDs is, that they do not necessarily possess a carbonized carbon core. Furthermore, the inner (carbon) core and the connected polymer chains can self-assemble into PDs [213]. Hence, in PDs the photoluminescence is either attributed to the formed inner (carbon) core or the fluorophores of the conjugated polymers. A special characteristic of PDs is their ease of surface modification, making them very promising fluorescent materials. Non-conjugated PDs can be synthesized by dehydration, condensation, carbonization, or other polymer assembly routes. To cite a few examples, PDs have been synthesised by hydrothermal treatment of grass route [100], by polymerisation of carbon tetrachloride and ethylenediamine [130] and by a general transformation route of linear non-conjugated polymers into fluorescent

PDs [218].

So far a preliminary investigation of PL behavior was conducted for several types of PDs. The evident PL process seems to be the crosslink-enhanced emission (CEE) [215], which amplifies the PL properties of potential fluorescent centers (chromophores). Another (controversially discussed) potential PL process for PDs is the so called aggregation-induced emission (AIE), which relegates to (small) organic molecules exhibiting physical or supramolecular aggregation [55, 56]. For a detailed explanation of both effects see Chapter 2.3.3.5 (p. 39).

## 2.2 Synthesis of CDs

The synthesis of CDs can be achieved in many ways and with an almost infinite variety of starting materials. Generally the CD synthesis approaches are divided into two basic processes: “top-down” (nano-cutting) methods and “bottom-up” (organic) synthesis methods. While “top-down” methods commonly include cutting different (large size) carbon sources (e.g. graphene oxide, carbon fiber, carbon nanotubes, fullerenes and graphite) into nano sized carbon dots, “bottom-up” approaches generally utilize different methods, like carbonization of carbohydrates, self-assembly of polycyclic aromatic hydrocarbons and organic synthesis from small molecules [152, 213]. An overview of common starting materials in CD synthesis will be given at the end of this section.

### 2.2.1 Top-down Synthesis Methods

Generally, the materials used in the “top-down” (nano-cutting) methods already possess perfect  $sp^2$  carbon structures but lack efficient band gaps to show PL. Materials meeting aforementioned requirements, include graphite powder [131], carbon rods [85], carbon fibers [124], carbon nanotubes [147, 182], carbon black [31], and candle soot [98]. To make these carbon sources photoluminescent, both their size and surface chemistry must be modulated accordingly. One of the most common methods is the application of strong and concentrated oxidizing acids (e.g.  $HNO_3$ ,  $H_2SO_4$  or a mixture of both) [159]. During this process the bulk carbon source is cut into smaller and nano-sized pieces while their surfaces are modified by oxygen-based groups. Further “top-down” synthesis approaches include chemical routes, such as catalysed cage-opening of fullerenes [102], electrochemistry methods [102, 203], hydrothermal/solvothermal or more unusual oxidation methods [122, 216], metal-graphite intercalation [94]; and physical routes, such as arc discharge [8], laser ablation [157], and nanolithography [40, 82].

In a typical electrochemical cutting approach, a graphite electrode is fragmented by the electric field, through graphite layer intercalation and/or a radical reaction, into nano-sized carbon particles (GCQDs). Applied electrolytes may contain ethanol [85], ionic liquids [102], monosodium phosphate ( $NaH_2PO_4$ ) [200], tetrabutylammonium perchlorate (TBAP) [5], aqueous phosphate buffered saline (PBS) [24, 91] and so on.

In hydrothermal/solvothermal oxidation methods already oxidized carbon sources with defect-



based chemical groups (oxygen-based groups), e.g. GO or oxidized CNTs are fragmented into pieces at high temperatures and pressures [122, 216]. Certain unusual oxidation methods, such as a photo-Fenton reaction [209], can also lead to GCQDs.

Especially nanolithography techniques, e.g. mask-assisted reactive-ion etching (RIE), proved to be an efficient approach for precise size and surface chemistry control of resulting CDs [82], thereby providing good model systems for inquiring PL mechanisms in CDs.

“Top-down” (nano-cutting) methods have already proven to lead to high quality GCQDs, but still suffer from major drawbacks, as they are mostly time and/or cost intensive and often use toxic/hazardous chemicals.

## 2.2.2 Bottom-up Synthesis Methods

Materials used in the “bottom-up” (organic) synthesis methods are carbon-based but have no further specific requirements, contrary to above mentioned starting materials for “top-down” methods (see Chap. 2.2.1, p. 12). Due to this flexibility nearly any carbon-based material has been used to synthesise CDs via “bottom-up” methods. Hence, the exact synthesis routes can differ widely and are as versatile as their starting materials [92, 213]. For example, small molecules and polymers may undergo dehydration/polymerisation and further carbonization to form CNDs and PDs. In many cases applied starting materials (molecules) possess alcohol –OH, carboxyl –COOH, carbonyl –C=O and/or amine –NR<sub>2</sub> groups, which can dehydrate at elevated temperatures.

Many approaches to accomplish dehydration/polymerisation and carbonization have been exploited, such as (classic) hydrothermal- [189], microwave-assisted- [211] and plain combustion [9] methods. Further methods also include pyrolysis in concentrated acid [123], carbonization in microreactors [220] and enhanced hydrothermal (microwave assisted-hydrothermal [158] and plasma-hydrothermal [171]) methods. Often it is difficult to control polydispersity and chemical purity (structure and composition) in these approaches. Although certain “bottom-up” (organic) synthesis methods can be time and/or cost consuming and sometimes utilize toxic/hazardous chemicals, it has to be noted that “bottom-up” methods are the most efficient routes to produce photoluminescent CDs, especially on a large scale. It remains, however, a primary aim to increase the stability of CDs and the reproducibility of CD synthesis routes [193].

## 2.2.3 Microwave Assisted Hydrothermal Treatment

### 2.2.3.1 Microwave Theory

Microwave irradiation, with its frequency range from 0.3 GHz to 300 GHz (corresponding to 1 m - 1 mm wavelength), lies between the infrared and radio frequencies. The main applications of microwaves (MWs) are either the transmission of information (e.g. telecommunication, RADAR) or energy (e.g. heating). Therefore, all commercially available domestic microwave ovens and

microwave reactors (MWRs) for chemical synthesis have to operate at 2.45 GHz (corresponding to a wavelength of 12.25 cm) to avoid interference with telecommunication, wireless networks, RADAR and cellular phone frequencies. Due to its low photon energy of 1.6 meV at 2.45 GHz a microwave photon can not cleave molecular bonds (e.g. hydrogen bond has an energy of 0.04 eV to 0.44 eV); i.e. MW irradiation (at 2.45 GHz) can not lead to chemical reactions by direct absorption of MW electromagnetic energy, as opposed to photochemistry with UV-Vis radiation (approx. 4.1 eV to 2.5 eV).

Microwave chemistry must therefore rely on “microwave dielectric heating effects” for efficient heating of materials [67]. In turn, microwave dielectric heating strongly depends on the ability of the material in question (e.g. a solvent or reagent) to convert absorbed microwave energy into heat. Heating by the electric component of an electromagnetic field can be caused by three main mechanisms: dipolar polarization, ionic conduction and resistance (ohmic) heating.

For a substance to be able to generate heat under MW irradiation it must possess a dipole moment. Therefore the interaction of the electric field component with the substance (matrix) is called “dipolar polarization mechanism.” Under MW irradiation, the dipoles of the matrix (substances) align in the applied electric field and constantly attempt to adjust themselves with the oscillating electric field. As the dipoles reorient to align themselves with the electric field, the electric field is already changing, hence, generating a phase difference between the field and the dipole. This phase difference gives rise to dielectric heating as energy is lost from the molecular dipoles by molecular friction and collisions. In other words, electrical energy is converted into kinetic or thermal energy (and ultimately into heat) as field energy is transferred to the medium. It should be noted that transitions between quantized rotational bands are not involved under MW irradiation and that energy transfer is not a property of a specific molecule but a result of a collective phenomenon involving the bulk [67]. Further should be noted that gases are MW transparent, i.e. they cannot be heated under microwave irradiation since the inter-molecular distances are too long. Similarly, due to the constrained dipoles in the crystal lattice, ice is also (nearly) MW transparent since the water dipoles cannot move as freely as in the liquid state.

For substances containing dissolved charged particles a second major heating mechanism, “ionic conduction mechanism,” occurs. Under MW irradiation, the dissolved charged particles oscillate back and forth under the influence of the MW field and simultaneously collide with the neighbouring molecules or atoms causing agitation or motion. Regarding the heat-generating capacity, the ionic conduction mechanism proves to be much stronger than the dipolar polarization mechanism [67].

For strongly conducting or semiconducting materials (e.g. metals, graphite), a third (related) heating mechanism exists. In those materials microwave (MW) irradiation can induce a flow of electrons on the surface. This flow of electrons can heat the material through ohmic heating mechanisms [67]. This mechanism becomes important for heating strongly microwave absorbing materials, such as graphite.

Obviously the heating characteristics of a substance (e.g. solvent) under MW irradiation depend on the dielectric properties of the substance. The ability of a substance to convert electromagnetic energy into heat (at a given frequency and temperature) is given by the so-called loss tangent ( $\tan \sigma$ ).

$$(2.1) \quad \tan \sigma = \frac{\epsilon''}{\epsilon'}$$

The loss tangent is determined by the ratio (see Eq. 2.1) between the dielectric loss ( $\epsilon''$ ), expressing the efficiency with which electromagnetic radiation is converted into heat, and the dielectric constant ( $\epsilon'$ ) describing the polarizability of the molecule in the electric field. Therefore, solvents without a permanent dipole moment (e.g. carbon tetrachloride, benzene and dioxane) are more or less MW transparent. As a rule of thumb, the higher the loss tangent of a medium, the more efficient and suitable it is for rapid heating under MW irradiation. Generally, substances can be classified in three categories: high ( $\tan \sigma > 0.5$ ), medium ( $\tan \sigma = 0.1$  to  $0.5$ ), and low microwave absorbing ( $\tan \sigma < 0.1$ ). Apparently, high dielectric constants not necessarily lead to high tangent loss values. Indeed, ethanol with a significantly lower dielectric constant ( $\epsilon' = 24.3$  at  $25^\circ\text{C}$ ) than water ( $\epsilon' = 80.4$  at  $25^\circ\text{C}$ ) heats much more rapidly under MW irradiation than water, due to its higher loss tangent ( $\tan \sigma_{\text{ethanol}} = 0.941$ ;  $\tan \sigma_{\text{water}} = 0.123$ ) [67].

As both the dielectric constant ( $\epsilon'$ ) and the dielectric loss ( $\epsilon''$ ) are both frequency and temperature dependent, the loss tangent values are as well. Hence, the heating of distilled water (measured by  $\epsilon''$ ) reaches its maximum at around 18 GHz. The reason for the use of the much lower frequency (2.45 GHz) of all domestic microwave ovens and laboratory MW reactors is the higher penetration depth, i.e. the efficient heating of the sample throughout its interior (volume).

The penetration depth denotes the point where 37 % of the initial MW irradiation power is still present [67]. Since the penetration depth is inversely proportional to tangent loss, it consequently depends both on the temperature and irradiation frequency. For example, water ( $\tan \sigma_{\text{water}} = 0.123$  at  $25^\circ\text{C}$  and 2.45 GHz) has a penetration depth of only a few centimetres (1.4 cm at  $25^\circ\text{C}$  and 5.7 cm at  $95^\circ\text{C}$ ). The increasing penetration depths of water with increasing temperature (see above) is due to a decreasing absorption of MW irradiation. As a matter of fact the dielectric loss and loss tangent of most solvents decrease with increasing temperature [67].

### 2.2.3.2 Microwave Assisted and Conventional Heating

For the most part organic synthesis are carried out by conventional conductive heating with external heat sources, e.g. an oil-bath or heating mantle. Comparatively this is a slow and energy inefficient method for energy-transfer into a system since it depends on convection currents and the thermal conductivity of the various materials that must be penetrated. Generally, it results in a higher temperature for the reaction vessel than for the reaction mixture [67, 71]. Specifically under reflux conditions, where the temperature of the bath fluid is kept at around  $10^\circ\text{C}$  to  $30^\circ\text{C}$  above the boiling point of the solvent, in order to ensure an efficient reflux. Hence, a temperature

gradient can develop within the reaction mixture and local overheating (e.g. on the reaction vessel wall) can lead to product, substrate or reagent decomposition and unintentional by-products [67, 71].

Microwave irradiation (as mentioned above), however leads to efficient internal heating (volumetric heating) raising the temperature of the whole volume simultaneously (bulk heating) [67, 71]. If reaction vessels out of (nearly) MW transparent materials are used (e.g. borosilicate glass, quartz or Teflon) an inverted temperature gradient as compared to conventional heating can be observed.

Since the introduction of MW assisted heating observed differences to comparable conventionally heated experiments, e.g. rate-accelerations and sometimes altered product distributions, have led to speculations about the existence of so-called “specific” or “non-thermal” microwave effects [67]. But nowadays it is generally agreed upon, that (in most standard cases) the observed enhancements are the result of purely thermal/kinetic effects; i.e. they are a consequence of high reaction temperatures which can rapidly be attained by polar materials (reaction mixtures) under closed vessel conditions in a microwave field. Still the following, so-called “specific microwave effects,” which arise from the uniqueness of the microwave heating mechanisms and cannot be duplicated by conventional heating, remain undisputed [67]. For example the superheating effect of solvents at atmospheric pressure, the elimination of reaction vessel wall effects (due to inverted temperature gradients) and the selective heating of strongly microwave absorbing heterogeneous materials (e.g. catalysts or reagents) in a less polar reaction medium (e.g. solvent).

### 2.2.3.3 Hydrothermal Treatment

Both terms “hydrothermal” (Ancient Greek: *water* and *heat*) and “hydrothermal synthesis” are of geologic origin while the latter describes a method of single crystal growth depending on the solubility of minerals in hot water and high pressure. In order to avoid confusion, the term “hydrothermal treatment” shall be used to describe chemical processing in water under superheated conditions ( $T > 100\text{ }^{\circ}\text{C}$ ) in sealed vessels and therefore high pressures [67].

Under superheated conditions, the chemical and physical properties of water undergo some favorable changes. Specifically the subcritical (or near-critical) region of water (between  $150\text{ }^{\circ}\text{C}$  to  $300\text{ }^{\circ}\text{C}$ ) is of great interest for organic synthesis; as with increasing temperature, water exhibits properties like polar organic solvents and thus organic compounds become soluble in high-temperature water [67, 79]. For example, at  $250\text{ }^{\circ}\text{C}$  water exhibits a similar density and polarity as acetonitrile at room temperature ( $25\text{ }^{\circ}\text{C}$ ) and also the dielectric constant of water drops rapidly from 78.5 ( $25\text{ }^{\circ}\text{C}$ ) to 27.5 ( $250\text{ }^{\circ}\text{C}$ ). Furthermore, the dissociation constant (ionic product) of water increases by three orders of magnitude, decreasing the  $\text{pK}_{\text{W}}$  from 14 to 11.2 (at  $250\text{ }^{\circ}\text{C}$ ). Hence water can act as an acid, base, or acid-base bi-catalyst, as water becomes both a stronger acid and stronger base at the same time [67]. The application of supercritical water at

temperatures  $> 374\text{ }^{\circ}\text{C}$  is therefore limited due to its degenerative properties.

Despite its comparably low  $\tan\sigma$  water can easily and rather effectively be heated from room temperature to  $100\text{ }^{\circ}\text{C}$  by MW irradiation (2.45 GHz), but it is significantly more difficult to further heat it (in a sealed vessel) to  $200\text{ }^{\circ}\text{C}$  and beyond. In fact, supercritical water ( $T > 374\text{ }^{\circ}\text{C}$ ) is microwave transparent [67].

### 2.2.4 Post-Synthesis Treatment

Independent of the used synthesis method, prepared CDs possess numerous reactive (surface) groups. Therefore, post-synthesis passivation and functionalisation can be used (if necessary) to enhance the photoluminescence quantum yield (PLQY), modify the photoluminescence emission wavelength, or meet the requirements for a specific application (e.g. bioimaging) [92, 213].

**Functionality and Surface Passivation** Especially for CDs with very low PLQY, due to non-radiative surface defects, the surface passivation with organic or polymeric materials, such as PEG [12, 144, 157], PPEI-EI [92], and BPEI [204], can enhance the PL emission significantly [12, 92, 144, 157]. Furthermore, these surface modifications (depending on their type) can change the solubility of CDs drastically, making them better soluble in polar or non-polar solvents (e.g. water or organic solvents), respectively. However, these surface passivations also increase the overall particle size, which can limit possible applications [204].

Other modifications control the degree of CD surface oxidation [204] by oxidation or reduction of existing surface groups and edge-sites [202]. Generally, oxidation/reduction of CDs leads to a blue-shift/red-shift of the PL emission, respectively [59, 148, 151, 217]. Also various electron-donating (functional) groups can be introduced after synthesis, e.g. diamine, thiol [128], hydrazide [194], alkylamine [217], often preventing non-radiative recombination (i.e. enhancing PLQY), and causing significant wavelength shifts [204].

**Separation Techniques** Harsh, and non-selective carbon dot synthesis often need post-synthesis separation techniques to reduce the variation of particle sizes. These techniques include dialysis, gel electrophoresis [98], ultra-filtration [121, 121, 205], column chromatography [85], and anion-exchange high-performance liquid chromatography [165], to name a few. Especially (ultra-) centrifugation is widely used for size separation, to separate soluble CDs from their solvent or non-soluble by-products.

Especially size-separation (i.e. monodispersity) is of utmost importance for subsequent characterization and future applications. Very often initially observed excitation dependent behaviour (in the bulk) vanished in fractionated samples, because of size uniformity [85].

### 2.2.5 Starting Materials

As mentioned before, nearly any carbon-based material can be used to synthesize CDs. Carbon dots have therefore the potential to provide (multicoloured) highly luminescent chromophores (for multiple applications) made out of environmentally friendly and cost-efficient resources which are not in competition with food resources.

Currently used starting materials can be divided into 3 categories: natural resources (e.g. starch, plant matter, various proteins), (purified) commercial chemicals (e.g. citric acid, EDTA, polymers) and graphite based materials (e.g. electrodes, coal, candle soot). Especially the latter are often used in top-down synthesis methods: e.g. carbon fibres [124], carbon nanotubes [159], graphene oxide [173] and reduced graphene oxide (rGO) films [91], soot [98], coal [190], graphite rods [85], 3-dimensional chemical vapour deposition (CVD) grown graphene [204], carbon black [31], and activated carbon [131]. CDs can even be synthesized from fullerenes through (ruthenium-)catalyzed cage-opening [103].

Commercially available chemicals are mostly used in bottom-up synthesis and include benzene derivatives, glycerol graphene oxide [77], and various polymers or their respective monomers like various types of PEG or PEI [92]. Quite common is the use of various carboxylic acids or their respective salts, e.g. octadecylammonium citrate or diethylene glycolammonium citrate [9], L-glutamic acid [180], ascorbic acid [63], and citric acid [34, 65].

Over the last decade various publications have shown that CDs can also be obtained from a wide range of natural resources, e.g. camphor [44], coffee grounds [57, 64], cow milk [51], green tea [178], orange juice [140], pomelo peel [104], strawberry juice [61], urine [39], watermelon peel [208], whole chicken eggs [68, 171], and many more (see Table C.1, p. 150).

**Heteroatom Doping** Notably heteroatom doping, most commonly nitrogen (N) doping, can profoundly affect the photoluminescence behavior (e.g. FWHM, Stokes shift, PLQY and photoluminescence lifetime) and/or catalytic properties of CDs [46, 92, 204]. Other heteroatoms

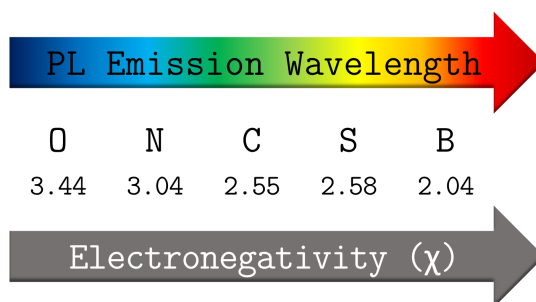


Figure 2.3: Electronegativity (Pauling scale) of various heteroatoms and resulting potential emission colors for (heavily) doped CDs [46].

introduced into CDs include silicon (Si) [129], selenium (Se) [186], phosphorus (P) [125], sulfur (S) [33, 75, 132], and boron (B) [27, 41]. So far there is mounting evidence that specifically the

electronegativity ( $\chi$ ) of heteroatoms plays the crucial role; heteroatoms can either function as electron donors (lower  $\chi$ ) or electron acceptors (higher  $\chi$ ); in affecting the PL emission wavelength of (heavily) doped CDs (see Fig. 2.3) [153, 185, 186, 210]. Heteroatoms are in most cases introduced by corresponding precursors, e.g. ethylenediaminetetraacetic acid (EDTA) and its disodium salt [204], various amino acids [179], and various thiols [33, 75].

## 2.3 Physical and Optical Properties

To this day, the mechanisms and processes behind the PL of CDs are still not fully understood. Unravelling the underlying concepts behind the PL properties of CDs is significantly hindered by the large variety of CDs and their often unclear assignment in the literature [92, 204]. To give a thorough summary, the chemical and physical properties of CDs are briefly introduced in advance, followed by the fundamental principles of PL in general and the potential PL mechanisms and -processes for CDs. So far six PL mechanisms and -processes are being considered: (1) the quantum confinement or conjugated  $\pi$ -domains effect (see Chap. 2.3.3.1, p. 32), (2) the surface state or surface group effect (see Chap. 2.3.3.2, p. 33), (3) the isolated fluorophore or molecule state effect (see Chap. 2.3.3.3, p. 36), (4) the giant red-edge excitation shift (see Chap. 2.3.3.4, p. 37), (5) and the crosslink-enhanced- and (6) aggregation induced emission effects (see Chap. 2.3.3.5, p. 39).

### 2.3.1 Biological Toxicity

Generally, photoluminescent nanoparticles (aka. nanosized contrast agents) are of high interest for bio-imaging and other bio-based applications, as they can overcome many of the limitations of conventional contrast agents (organic dyes), e.g. poor photostability, low photoluminescent quantum yields, insufficient *in vitro* and *in vivo* stability. Therefore, the implementation of new types of nanosized contrast agents is anticipated to accelerate the advancements in understanding biological processes at the molecular level and furthermore lead to new progress in the development of diagnostic tools and innovative therapies.

Hence, the toxicity and biocompatibility of nanoparticles is of extraordinary concern in bio-imaging applications (*in vitro* and *in vivo*) [154]. Contrary to metal-based photoluminescent quantum dots (QDs), which often consist of intrinsically toxic elements such as cadmium and other rare earth metals [25, 92], CDs are composed of intrinsically non-toxic carbon [204]. Various studies concerning the (cyto-)toxicity of different CD types have been conducted in various model organisms, e.g. cell-viability assays [47, 165, 168, 172], zebrafish [68, 139] and various rodents [42, 159, 187]. All studies so far agree that CDs appear to have low (cyto-)toxicity *in vitro* and *in vivo* and that all types of CDs (PDs, GCQDs and CNDs) possess excellent biocompatibility [12, 35, 97, 128, 159, 160, 216, 218].

### 2.3.2 Introduction to Photoluminescence

Photoluminescence describes the form of luminescence after photoexcitation (excitation by photons). Depending on the nature of the excited state from which the emission occurs (see Fig. 2.4) it is further divided into two categories, fluorescence and phosphorescence. In the case of the former, the emission of a photon occurs rapidly from an excited singlet state. This is due to the fact that in excited singlet states (e.g.  $S_1$ ) the electron in the excited orbital has the opposite spin compared to the unpaired electron in the ground-state orbital. The return to the ground state is therefore spin allowed.  $10^8 \text{ s}^{-1}$  is a typical fluorescence emission rate, resulting in a typical fluorescence lifetime of 10 ns ( $10 \times 10^{-9} \text{ s}$ ). The term lifetime ( $\tau$ ) of a fluorophore must be understood as the average time between the fluorophores excitation and its subsequent return to the ground state. Phosphorescence on the other hand describes the emission of a photon from triplet excited states (e.g.  $T_1$ ), in which case the electron in the excited orbital has the same spin orientation (parallel spin) as the electron in the ground-state orbital. The transition to the ground state is therefore forbidden and the typical emission rates are slow ( $10^3 \text{ s}^{-1}$  to  $1 \text{ s}^{-1}$ ), resulting in phosphorescence lifetimes of typically milliseconds to seconds, but even longer lifetimes are possible. Usually phosphorescence is not observed in fluid solutions at room temperature, due to the existence of many deactivation processes competing with the emission process, e.g. non-radiative decay and quenching processes.

To illustrate the absorption and emission (of light) and the various molecular processes that can occur in excited states Perrin-Jablonski diagrams are used. In a typical Perrin-Jablonski diagram (see Fig. 2.4) the electronic states are vertically arranged by energy, e.g. ground (0), first (1) and second (2) electronic state; and grouped horizontally by their spin multiplicity, e.g. singlet (S) and triplet (T) states. Therefore the singlet ground, first, and second electronic states are depicted by  $S_0$ ,  $S_1$ , and  $S_2$ , respectively. In each of these electronic states the fluorophores can exist in a number of vibrational energy levels ( $n = 0, 1, 2$ , etc.). The transitions between states, due to light absorption, are represented as vertical arrows to illustrate their direction and near instantaneous nature. These fast transition times of about  $< 10^{-15} \text{ s}$  are insufficient for significant displacement of nuclei, leading to the Franck-Condon principle (see Chap. 2.3.2.2, p. 23). Generally absorption and emission occur from molecules in the lowest vibrational energy level ( $n = 0$ ) of the electronic states, as at room temperature (RT) thermal energy is not sufficient to significantly populate the higher vibrational levels ( $n \geq 1$ ). Commonly the fluorophore, depending on the energy of the photon, is excited to one of the higher vibrational levels of either  $S_1$  or  $S_2$ . Subsequently several processes can occur. The process of non-radiative transition between two electronic states of equal spin multiplicity (e.g.  $S_2 \rightarrow S_1$ ) is called internal conversion (IC). Internal conversion occurs typically in between  $10^{-11} \text{ s}$  to  $10^{-9} \text{ s}$  and directly competes with luminescence. However, due to the larger energy gap, IC from  $S_1$  to  $S_0$  is generally less efficient than IC from  $S_2$  to  $S_1$ .

In most cases molecules in condensed phases rapidly relax (within  $10^{-12} \text{ s}$  to  $10^{-10} \text{ s}$ ) to the lowest vibrational energy level of the electronic state via vibrational relaxation. Therefore, vibrational



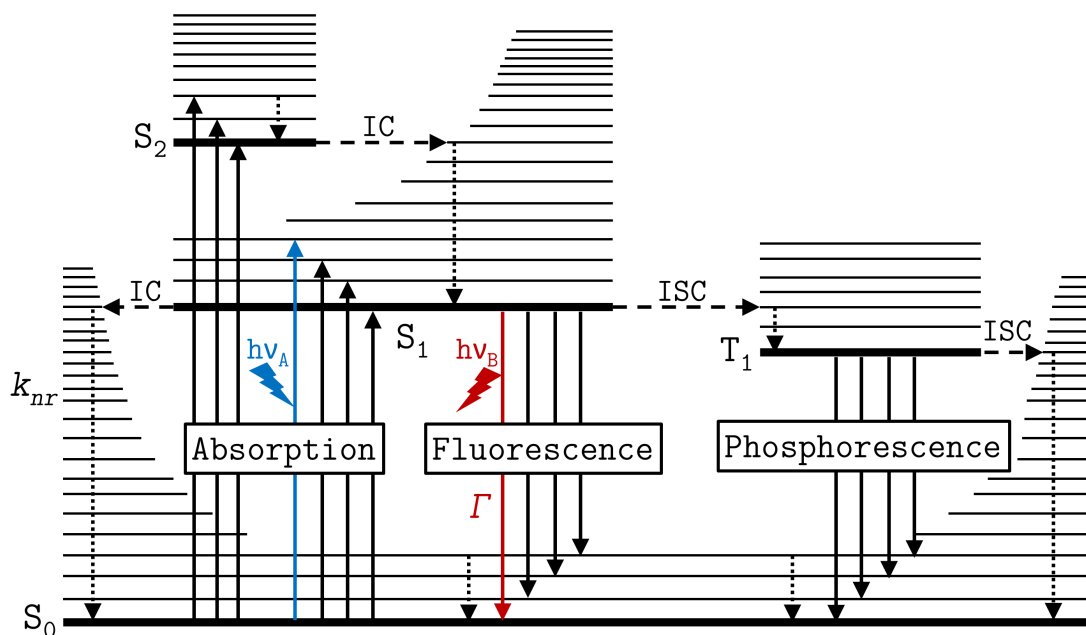


Figure 2.4: Perrin-Jablonski-Diagram for the simplified representation of radiative and non-radiative processes within molecules. Presented are those rate constants characterizing the excited-state decay of the fluorophore to the ground state ( $S_0$ ); the rate of radiative decay of the fluorophore ( $\Gamma$ ) and its rate of non-radiative decay (as sum of all possible non-radiative decay processes) to  $S_0$  ( $k_{nr}$ ).

relaxation (and IC) is generally complete prior to emission, since most fluorescence lifetimes are typically near  $10^{-8}$  s. Thus, fluorescence emission generally occurs from a thermally equilibrated excited state, in other words, the lowest energy vibrational state of  $S_1$ . Radiative deactivation (emission) generally leads to a higher vibrational energy level of the ground state, which then, due to vibrational relaxation, quickly reaches thermal equilibrium (see Fig. 2.4). Thus, the energy of the emitted photon is typically lower than the energy of the absorbed photon. In other words the photoluminescence occurs at lower energy or longer wavelength than the absorption. This phenomenon of energy loss between excitation and emission is called the Stokes shift (see Fig. 2.5), named after its discoverer Sir G. G. Stokes. Normally the spacings of the vibrational energy levels of the excited states are similar to that of the ground state. Hence, the emission spectrum is typically a mirror image of the absorption spectrum of the  $S_0 \rightarrow S_1$  transition. In addition to the above mentioned effects, fluorophores can exhibit further Stokes shifts due to solvent effects, excited-state reactions, complex formations, and/or energy transfer.

Besides IC and/or fluorescence, molecules in the first excited singlet state ( $S_1$ ) can undergo a spin conversion to the first triplet state  $T_1$ . This slightly slower conversion ( $10^{-10}$  s to  $10^{-8}$  s) between two states of different spin multiplicity (e.g.  $S_1 \leftrightarrow T_1$ ) is called intersystem crossing (ISC). Relative to fluorescence, emission from the  $T_1$  (termed phosphorescence) is commonly shifted to lower energies (longer wavelength). Furthermore, as the transition from  $T_1$  to singlet ground

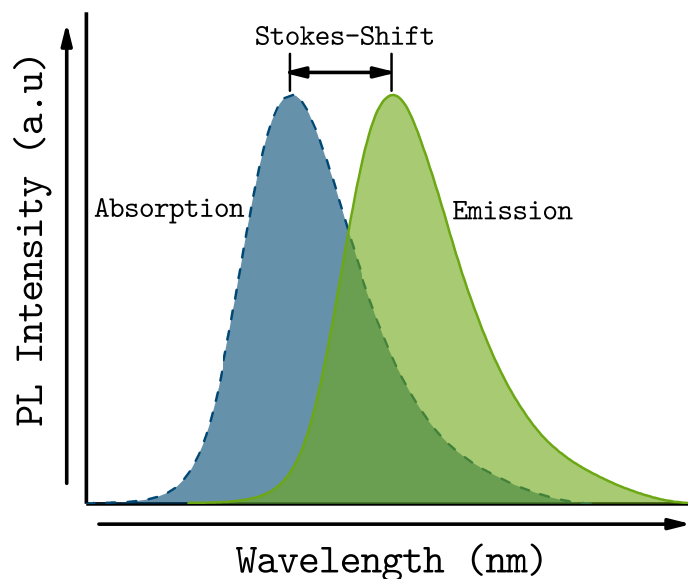


Figure 2.5: Schematic representation of stokes shift between positions of the absorption and emission spectra of a fluorophore.

state  $S_0$  is forbidden the rate constants for triplet emission are several orders of magnitude smaller (see Table 2.1) than those for fluorescence [78, 164].

Table 2.1: Overview of characteristic times for possible radiative and non-radiative processes between electronic states in a chromophore [164].

Process	Characteristic Times
Absorption	$10^{-15}$ s
Vibrational relaxation	$10^{-12}$ s - $10^{-10}$ s
Lifetime of the excited electronic state $S_1$	$10^{-10}$ s - $10^{-7}$ s → Fluorescence
Intersystem crossing (ISC)	$10^{-10}$ s - $10^{-8}$ s
Internal conversion (IC)	$10^{-11}$ s - $10^{-9}$ s
Lifetime of the excited electronic state $T_1$	$10^{-6}$ s - 1 s → Phosphorescence

### 2.3.2.1 Kasha's and Vavilov's Rule

Typically, photoluminescence spectra are independent of the excitation wavelength. In other words, the same fluorescence/phosphorescence emission spectrum is generally observed regardless of the excitation wavelength. Named Kasha's rule, it states that emission of a photon (either by fluorescence or phosphorescence) occurs in appreciable yield only from the lowest excited

electronic state of a given spin multiplicity (e.g.  $S_1$  &  $T_1$ ). The underlying reason for this is, that upon photon absorption a molecule in its electronic ground state (e.g.  $S_0$ ) can be excited (depending on the photons energy/wavelength) into any set of higher electronic states and vibrational levels ( $S_x$ , where  $x \geq 1$ ). Enabled by presumably strong overlaps among numerous states of nearly equal energy, vibrational relaxation (and IC) quickly dissipates this excess energy (see Chap. 2.3.2, p. 20), leaving the molecule in the lowest vibrational level of its lowest excited electronic state (e.g.  $S_1$ ). As a result of this rapid relaxation, only the lowest vibrational level of the lowest excited electronic state is expected to yield emission. An equivalent statement of the rule is therefore that the emission wavelength (Kasha's Rule) and the photoluminescence quantum yield (Vavilov's Rule) are independent of the excitation wavelength. Of course exceptions exist, e.g. if the relaxation is hindered (see Chap. 2.3.2.4, p. 30 and Chap. 2.3.3.4, p. 37); if large energy gaps exist between excited states (e.g. QDs); or for fluorophores that exist in multiple ionization states (e.g. Fluorescein), each of which displays distinct absorption and emission spectra.

### 2.3.2.2 The Franck-Condon Principle

A good way to explain Kasha's rule is by the Franck-Condon factors for vibronic transitions. The basis of the Franck-Condon principle is the Born-Oppenheimer approximation, i.e. the assumption, that the motion of atomic nuclei and electrons in a molecule can be separated, due to their different momentum. Characteristic transition times for light absorption (about  $10^{-15}$  s) prove to be too fast for significant nuclei displacement, i.e. molecular vibrations ( $10^{-12}$  s to  $10^{-10}$  s). Hence, for the electronic transition of the molecule, the new vibrational level must be instantaneously compatible with the nuclear positions and momenta of the vibrational level in the originating electronic state, if the molecule is to move to the new vibrational level (see Fig. 2.6A). The vibrational levels and vibrational wavefunctions are either those of quantum harmonic oscillators or of more complex approximations to the potential energy of molecules (Morse potential). The illustration of the Franck-Condon principle for vibronic transitions with Morse-like potential energy functions in both the ground and excited electronic states of a molecule is shown in Figure 2.6A. The vibronic transition is indicated by a vertical transition (blue arrow) due to the assumption of constant nuclear coordinates during the transition (see above). The resulting state is called a Franck-Condon state [164].

Nevertheless, the electron configuration of the new (excited) state may result in a shift ( $q_{01}$ ) of the equilibrium position of the nuclei constituting the molecule. For a basic diatomic molecule, the axis of nuclear coordinates would therefore refer to the internuclear separation.

The probability of transition (of the molecule) into any particular vibrational level is proportional to the square of the (vertical) overlap of the vibrational wavefunctions of the original and final state. For any given combination of energy levels that differ both in electronic and vibrational quantum number, the Franck-Condon factor signifies the degree of overlap between their vibrational wavefunctions (see Fig. 2.6A).

After quick relaxation into the vibrationless level of the lowest electronic excitation state (Kasha's

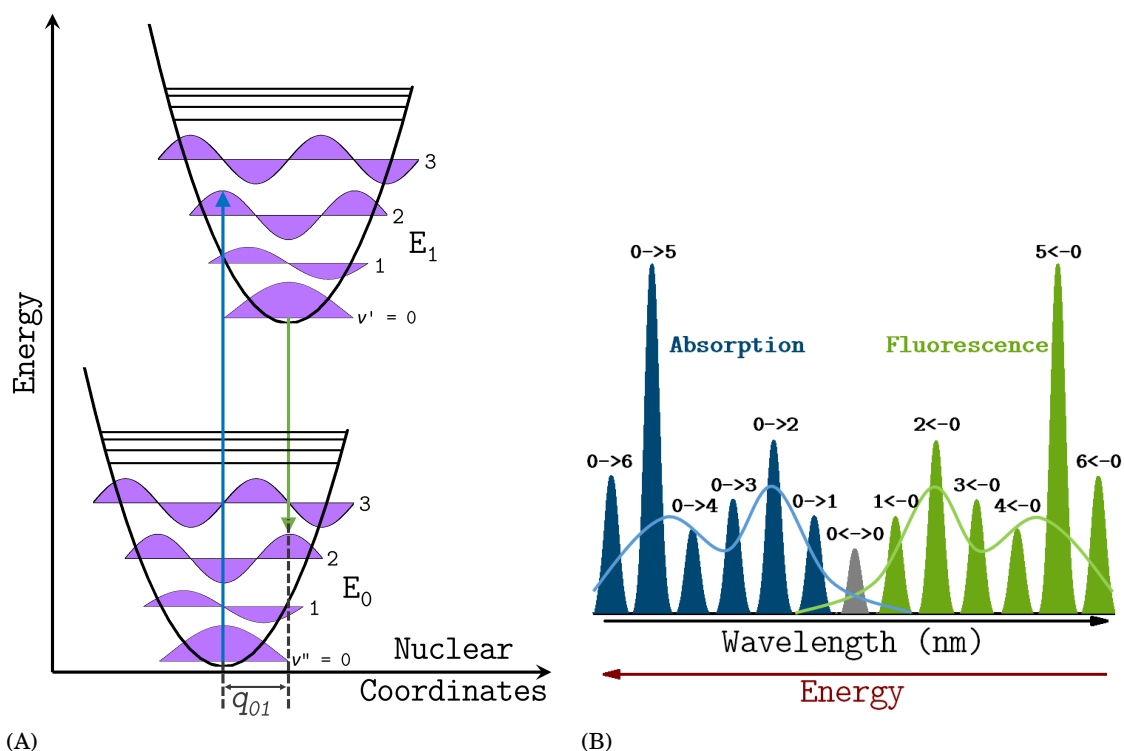


Figure 2.6: Schematic representation of (A) Franck-Condon principle energy diagram and (B) the corresponding absorption (blue) and emission (e.g. fluorescence) spectra (green). The symmetry between absorption and emission spectra is due to ground and excited state potential wells being equally shaped. Narrow lines can usually only be observed in the spectra of dilute gases. The curves (solid lines) represent the inhomogeneous broadening of the same transitions as occurs in liquids and solids. The 0-0 transition (grey) between the lowest vibrational levels of the electronic states has the same energy in both absorption and fluorescence [78, 164].

rule), e.g.  $S_1$ , the molecule can decay to the electronic ground state. Fluorescence occurs (green arrow), if the energy gap between the lowest excited state and the ground state ( $S_1 \rightarrow S_0$ ) is great, since this process is now kinetically competitive with internal conversion (IC). In summary, the Franck-Condon principle states: The higher the overlap of two vibrational wave functions, the more likely an electronic transition between one vibrational energy level to another will occur. Obviously the Franck-Condon principle does apply both for non-radiative (vibrational relaxation) and radiative (e.g. absorption, fluorescence and phosphorescence) transitions. This applicability of the Franck-Condon principle in both absorption and emission (along with Kasha's rule) leads to the afore mentioned (approximate) mirror symmetry shown in Figure 2.6B.

In a cold, sparse gas, due to the absence of inhomogeneous broadening of the individual transitions, the vibrational structure of molecules are most clearly visible. Equal spacing between vibrational levels, as shown in Figure 2.6B, is only the case for the parabolic potential of simple harmonic oscillators; while in more realistic potentials (see Fig. 2.6A) energy spacing decreases

with increasing vibrational energy. Transitions from and to the vibrational ground states, often referred to as zero zero (0 – 0) transitions, have the same energy in both absorption and fluorescence (Fig. 2.6B; black Lorentzian lineshape).

### 2.3.2.3 Photoluminescence Lifetimes and Photoluminescence Quantum Yields

Besides their emission- and absorption spectra, the PL (fluorescence) lifetimes and PLQYs are perhaps the most important quantities to characterize fluorophores. In its wider meaning, the term quantum yield is the number of events relative to the number of absorbed photons. Hence, in the area of optical spectroscopy, the photoluminescence quantum yield ( $\Phi$ ) describes the ratio between the number of emitted photons ( $N_E$ ) relative to the number of absorbed photons ( $N_A$ ):

$$(2.2) \quad \Phi = \frac{\text{Number of events}}{\text{Number of absorbed photons}} = \frac{N_E}{N_A}$$

In other words: The larger the photoluminescence quantum yield ( $\Phi$ ) of the fluorophore, the brighter its emission.

Shown in Figure 2.4 (p. 21) are those rate constants characterizing the excited-state decay of the fluorophore to the ground state ( $S_0$ ); the rate of radiative decay of the fluorophore ( $\Gamma$ ) and its rate of non-radiative decay (as sum of all possible non-radiative decay processes) to  $S_0$  ( $k_{nr}$ ). Both constants ( $\Gamma$  and  $k_{nr}$ ) signify a depopulation of the excited state (e.g.  $S_1$ ), therefore the fraction of excited fluorophores decaying through emission (and hence the  $\Phi$ ) can be expressed by:

$$(2.3) \quad \Phi = \frac{\Gamma}{\Gamma + k_{nr}}$$

Whereas the PLQY can reach unity (when  $k_{nr} \ll \Gamma$ ), the energy yield of PL is always less than unity due to relaxation processes (Stokes losses).

The average time  $t$  a molecule spends in its excited state, prior to its return to the ground state, is called the PL lifetime ( $\tau$ ) of the excited state and can be expressed by the following equation.

$$(2.4) \quad \tau = \frac{1}{\Gamma + k_{nr}}$$

The lifetime of a fluorophore in the absence of non-radiative processes (either prevented or orders of magnitude longer than the radiative decay) is called the natural (sometimes intrinsic) lifetime ( $\tau_n$ ).

$$(2.5) \quad \tau_n = \frac{1}{\Gamma}$$

The natural lifetime can be calculated from the absorption spectra, extinction coefficient and emission spectra of the fluorophore. However, calculating the natural lifetime from the measured PL lifetime and PLQY is much simpler and proves much more reliable [78]. Alteration of PLQY and PL lifetime can be due to modifications of either of the two rate constants ( $\Gamma$  and/or  $k_{nr}$ ). A molecule may be non-fluorescent as a result of a large rate of internal conversion or a slow

rate of emission. High PLQYs are a result of large  $\Gamma$  values, which in turn leads to generally short PL lifetimes. The importance of the PL lifetime is due to the fact, that it determines the time available for the excited fluorophore to interact with or diffuse in its environment (see Chap. 2.3.2.4, p. 28).

In general PLQYs of phosphorescence are extremely small in fluid solutions at room temperature. Based on the (symmetry) forbidden triplet-to-singlet transition for phosphorescence the rates of spontaneous emission are about  $10^3 \text{ s}^{-1}$  or smaller. Considering the above mentioned conditions and that  $k_{nr}$  values are near  $10^9 \text{ s}^{-1}$ , the phosphorescence quantum yields have to be around  $10^{-6}$ , i.e. comparably small at room temperature.

**Timescale of Molecular Processes in Solution** If a fluorophore is surrounded by solvent molecules, both species may interact with each other, particularly if the solvent molecules (and fluorophore) are polar. Solvation, i.e. the association between solvent and solute, is a stabilizing interaction, meaning the solvent molecules can move and rotate until the energy of the interaction (with the solute/fluorophore) is minimized. This form of intermolecular interaction can involve hydrogen bonds, van der Waals- and electrostatic forces. Furthermore, only immediately adjacent solvent molecules will affect the fluorophore and therefore its spectral characteristics (e.g. absorption- and emission spectra).

The interactions between the fluorophore and the surrounding solvent molecules can be different in the ground and in the excited electronic state, e.g. due to different dipole moments in these two states. Most fluorophores have larger dipole moments in the excited electronic state than in the electronic ground state. The electronic transition is very fast compared with the rearrangement of solvent molecules in the case of solvation. Due to the fast transition times, absorption spectroscopy can only yield information on the average ground state of the absorbing species. In other words, absorption spectra are not sensitive to molecular dynamics, but can provide information on the average solvent shell adjacent to the absorbing species.

In order to minimize the interaction energy, the solvent molecules will immediately try to rearrange themselves around the fluorophore. Hence, the solvent relaxation rates depend on the viscosity of the solvent. If solvent relaxation times are much shorter than the lifetime of the electronic excited state, the emission will occur from the lowest solvent energy state of the excited electronic state. For example, for small-molecule solvents such as water or methanol solvent relaxation times are on the order of  $10^{-11} \text{ s}$  to  $10^{-10} \text{ s}$  in fluid solution [78], whereas excited state lifetimes range from  $10^{-12} \text{ s}$  to  $10^{-9} \text{ s}$ . The excited states lifetime of the fluorophore provides therefore an opportunity for interactions with other molecules in solution, e.g. oxygen [78]. It is these interactions that result in the high sensitivity of emission spectra to solvent polarity compared to the smaller spectral changes seen in absorption spectra. Solvent relaxation can therefore also result in substantial Stokes shifts.

The Franck-Condon principle for solvation is illustrated in Figure 2.7. Unlike classical potential energy diagrams, in this case the horizontal coordinate axis represents the solvent-solute interac-

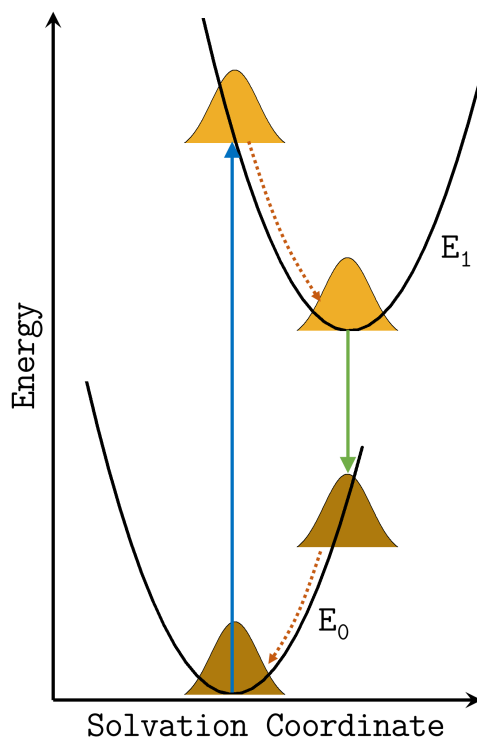


Figure 2.7: Schematic representation of Franck-Condon principle applied to the solvation of chromophores. The parabolic potential curves in the energy diagram illustrate the interaction energy between the fluorophores and the solvent molecules. The Gaussian curves (orange) represent the distribution of this solvent-solute interaction energy.

tion space. Labelled “Solvation Coordinate” it represents all of the relevant dimensions of motion for all of the interacting solvent molecules.

Upon excitation with light of corresponding energy/wavelength to the electronic transition, part of the fluorophores will progress to the excited state (blue vertical arrow). Obviously there will be a statistical distribution of solvent-solute interaction energies, here represented by a (orange) Gaussian distribution function (see Fig. 2.7). The solvent-solute interaction is drawn as a parabolic potential in both ground ( $E_0$ ) and excited electronic state ( $E_1$ ). As mentioned before, the collection of excited state fluorophores is (after excitation) immediately far from equilibrium and will therefore undergo rearrangement of the solvent molecules according to the new potential energy curve (curved orange arrow). And this of course also applies after the transition to the electronic ground state (green arrow), where the solvent molecules must again immediately rearrange themselves to accommodate the new electronic configuration of the fluorophore (curved orange arrow). The energy difference between absorbed and emitted photons can therefore be seen as the solvation contribution to the Stokes shift.

As to be expected, in Figure 2.7 emission (green arrow) is depicted as occurring from the minimum of the excited state solvent-solute interaction potential. However, in cases where the excited state lifetime is short and/or the viscosity of the solvent is high (see below), significant emission can

take place before the equilibrium between solvent-solute is reached. It should be mentioned, that in this example (see Fig. 2.7) the electronic transitions are quantized, while (due to the large number of molecules involved) the solvent-solute interaction energy is treated as a classical continuum.

#### 2.3.2.4 Overview of Excited-State Processes

In the preceding sections it was shown that emission spectra can be affected by solvent polarity and specific solvent effects. Furthermore, fluorophores can also display charge separation and/or conformational changes while in their excited electronic state. The excited-state lifetime gives the average time a molecule spends in its excited state (see Chap. 2.3.2.3, p. 25). Therefore, depending on the corresponding dynamic process rate constant (e.g. solvent reorientation, charge separation and conformational changes), it also determines if a fluorophore emits after, during or prior to the dynamic process (see see Fig. 2.8).

These time-dependent spectral changes can be divided into two categories: a continuous spectral relaxation model (CRM) and a two-state model (2SM). In case of the CRM the emission spectrum shifts with time but does not change its spectral shape (i.e. continuous spectral shift); and in case of the 2SM there are distinct emission spectra from two forms of the fluorophore. While the CRM is usually appropriate for general solvent effects, the latter is usually appropriate for excited-state reactions or formation of internal charge-transfer (ICT) states. Excited-state processes can be studied by measurement of time-resolved emission spectra (TRES), which are emission spectra observed at several distinct points in time following pulsed excitation. Figure 2.8A shows a schematic for the CRM model, in which the fluorophore is excited to a Franck-Condon (or unrelaxed) state (**F**). Following the excitation the solvent molecules reorient around the excited-state dipole moment with a solvent relaxation rate  $k_s$ . This relaxation rate can also be expressed as the solvent relaxation time  $\tau_s = k_s^{-1}$ . In almost all cases of a fluid solvent, the relaxation time will be less than the photoluminescence lifetime ( $\tau_s \ll \tau$ ) and emission occurs from the relaxed (**R**) state. However, at low temperatures, solvent relaxation time can be much slower than the photoluminescence lifetime ( $\tau_s \gg \tau$ ) resulting in emission occurring from the **F** state. When both times are equal ( $\tau_s = \tau$ ), in case of intermediate temperatures, emission will be occurring during the relaxation process and an intermediate spectrum between **F** and **R** will be observed (dashed curve in Fig. 2.8A). Hence, the emission spectrum represents a weighted average of the photoluminescence emission spectra at each point in time during the solvent relaxation process. The intermediate emission spectra should have the same shape and half width as the **F**- and **R**-state emission spectra. However, fluorophores with varying extents of relaxation contribute and the intermediate spectrum can therefore be much broader. It is important to note that the **F** and **R** state are considered to be similar, i.e. the fluorophore is emitting from the same electronic state. Therefore, the PL lifetimes for the fluorophore in the **F** and **R** state can ( $\tau_F \neq \tau_R$ ), but do not have to be different ( $\tau_F = \tau_R$ ).



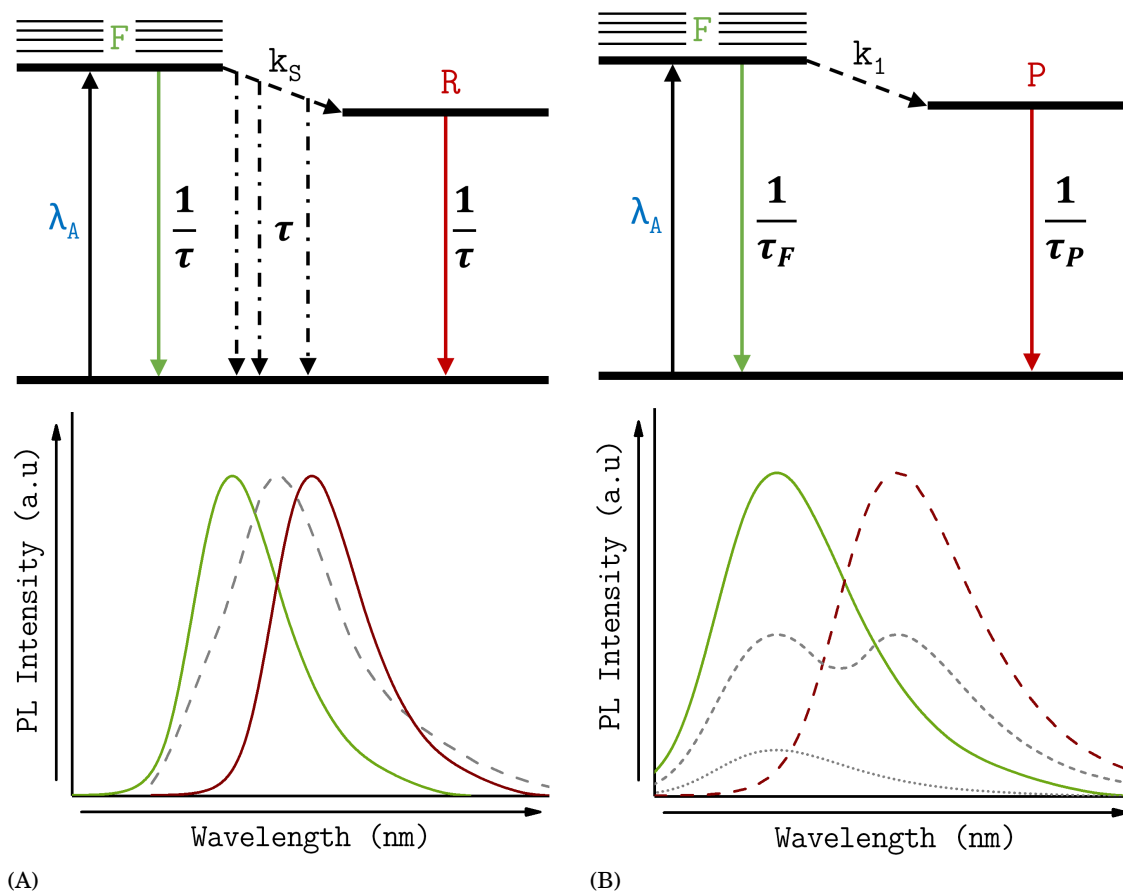


Figure 2.8: Simplified Perrin-Jablonski diagrams for (A) the continuous spectral relaxation model (CRM) and (B) for an excited-state reaction of the two-state model (2SM).

In cases of the 2SM, where spectral relaxation occurs in a stepwise manner, there are two distinct emitting species: the initially excited Franck-Condon state (**F**) and, resulting from the excited-state reaction, the molecular (product) state (**P**). Consequently the photoluminescence lifetimes ( $\tau_F$  and  $\tau_P$ ) and emission spectra of both states are different, as emission is occurring from two different molecular species (see Fig. 2.8B) whose electronic states and/or chemical structures are different. Both states (**F** and **P**) are linked by an (ir)reversible reaction with the rate constant  $k_1$ , making it a chemical rate constant that is determined by solvent composition and chemical structures. If  $k_1$  is smaller than the radiative decay rate of the **F** state ( $k_1 < \tau_F^{-1}$ ) the emission occurs primarily from the **F** state. If  $k_1$  is greater than the radiative decay rate of the **F** state ( $k_1 > \tau_F^{-1}$ ) the emission occurs primarily from the **P** state. Consequently, if  $k_1$  and radiative decay rates are comparable ( $k_1 = \tau_F^{-1}$  and  $\tau_P^{-1}$ ) the emission occurs from both the **F**- and **P**-state. In cases, where the emission spectra of the **F**- and **P**-state are well separated, two distinct components will be seen in the emission spectrum. But if the emission spectra of both states overlap, the (intermediate) emission spectra may show a shoulder or be wider than the

individual emission spectra (dashed curves in Fig. 2.8B).

**The Red-Edge Excitation Shift** In the preceding discussions it was assumed that emission spectra and PLQYs are independent of the excitation wavelength (see Chap. 2.3.2.1, p. 22). However, this assumption is no longer valid in viscous and moderately viscous solvents. Especially the emission of polar fluorophores, under conditions where solvent relaxation is not

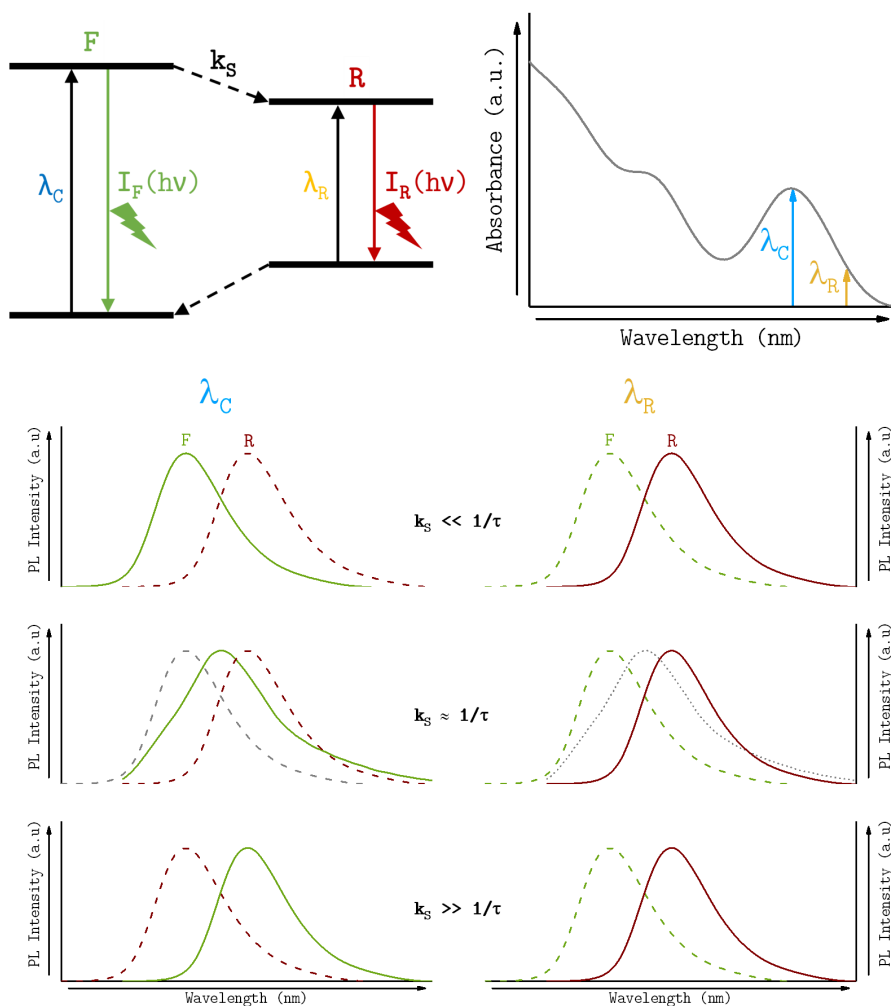


Figure 2.9: Schematic representation of the effects of red-edge excitation on emission spectra. Simplified Perrin-Jablonski diagram (top left) and schematic absorption spectra (top right) are given for better understanding. The term  $\lambda_C$  (blue) indicates excitation in the center of the last absorption band of the fluorophore. The term  $\lambda_R$  (orange) indicates excitation on the red edge of the absorption band. Possible results of REES, depending on excitation wavelength, are given in the lower emission spectra. Solid lines represent observed spectra and dashed lines represent the emission spectra of either the F or R state (for comparison). The grey dotted line (middle emission panel) represents a possible consequence of reverse relaxation.

complete, shifts to longer wavelengths when the excitation is on the long-wavelength edge of the

absorption spectrum (see Fig. 2.9). This effect, known as the red-edge excitation shift (REES), can be rather substantial and can be observed for a variety of fluorophores [78]. The origin of this unusual behaviour of polar molecules with red-edge excitation can be understood by examining a Perrin-Jablonski diagram including spectral relaxation (see Fig. 2.9).

Interactions of a fluorophore (in solution) with its surrounding molecules induce many possible solvent-solute configurations. This distribution of solvent-solute configurations leads to a variation in the local electric field and results in a statistical distribution of electronic transition energies [164]. Any population of fluorophores, therefore, not only consists of molecules with a solvent configuration similar to that of the Franck-Condon state (**F**), but also to a certain extend of some molecules with a solvent configuration similar to that of the relaxed **R** state. Typically those molecules are more tightly hydrogen bonded to the solvent.

In case of a fixed fluorophore, e.g. in a frozen solvent, which is excited in the center of its last absorption band ( $\lambda_C$ ) the conventional (thawed) emission from the Franck-Condon state (**F**) is observed. Whereas excitation with the red edge (i.e. long wavelength edge) of its absorption band ( $\lambda_R$ ) selects for those fluorophores that have absorption at lower energy, i.e. higher wavelength ( $\lambda_C < \lambda_R$ ). Due to the frozen surrounding (of the solution) the fluorophore-solvent configurations persist during the intensity decay, resulting in a display of red-shifted emission.

Therefore it is clear, that an increasing temperature must lead to a disappearance of the REES, as it enables rapid reorientation of the solvent ( $k_S \ll \tau^{-1}$ ). This means, even if a potentially red-emitting fluorophore is initially excited, the fluorophore (and therefore its emission spectra) reach equilibrium prior to emission. In fact, this reverse relaxation to higher energies from the **R** state (red-shifted emission) to the equilibrium conditions of the **F** state, as shown in the middle panel for  $k_S \approx \tau^{-1}$  (see Fig. 2.9), has been observed for red-edge excitation [78]. Usually REES should only be observed if solvent relaxation is hindered (i.e. not complete) as the magnitude of the REES strongly depends on the rate of spectral relaxation. Furthermore, excitation-wavelength dependence at the red edge of the absorption band has also been observed for other parameters, e.g. PL lifetime, PLQY and apparent rotational rate [164].

### 2.3.3 Photoluminescence Mechanisms and Processes in Carbon Dots

The PL properties of CDs are of utmost importance for the exploration of CDs for novel applications. Emission spectra of CDs can vary widely between types and synthesis approaches [204]. Typically, their PL emission spectra are (roughly) symmetrical and usually wide on the wavelength scale. Most CDs possess strong PL emission in the blue, rarely green wavelength region. Only a small fraction of CDs possesses optimal PL emission in long-wavelength regions [7, 85, 98]. Compared with organic dyes, CDs show large Stokes shifts and for certain CDs the emission peak (i.e. emission maximum) is related to the excitation wavelength, which is either called wavelength-dependent behaviour or selective luminescence [46, 213].

So far six PL mechanisms and -processes are being considered: (1) the quantum confinement or

conjugated  $\Pi$ -domains effect (see Chap. 2.3.3.1, p. 32), (2) the surface state or surface group effect (see Chap. 2.3.3.2, p. 33), (3) the isolated fluorophore or molecule state effect (see Chap. 2.3.3.3, p. 36), (4) the giant red-edge excitation shift (see Chap. 2.3.3.4, p. 37), (5) and the crosslink-enhanced- and (6) aggregation induced emission effects (see Chap. 2.3.3.5, p. 39). Despite their chemical diversity, certain optical properties of CDs are similar in terms of absorption and even photoluminescence [46]. Therefore, a summary of the common optical properties, rather than specific examples, are given here.

UV-Vis absorption spectra of CDs typically exhibit two strong separate absorption bands: the first at around 230 nm to 320 nm (sometimes with a tail extending into the visible range) can be assigned to the carbon core. A peak at approximately 230 nm is ascribed to the  $\pi - \pi^*$  transition within C-C bonds in aromatic  $sp^2$  domains. In addition, connected chemical groups may contribute to the absorption in the UV-Vis region. For example, nitrogen-doping often leads to a strong absorption peak at around 225 nm, which can be assigned to C-N bonds located either on the CD surface or in the CD core. A shoulder at around 300 nm to 400 nm is attributed to the  $n - \pi^*$  transition of C=O bonds or other similar groups. The observed deviations in UV-Vis absorption spectra, to some extent, can therefore indicate differences in the CD compositions or structures of different synthesis approaches [204, 213].

### 2.3.3.1 The Quantum Confinement Effect in GCQDs

QCE in carbon dots arise from the graphene like structure of the GCQDs. For GCQDs with an intact graphene core and few surface groups (see below), the band gap originating from conjugated  $\pi$ -domains is thought to be the intrinsic PL emission center. QCE is a major feature of QDs, which occurs when QDs are smaller than their corresponding exciton Bohr radius [15]. Normally, the zero optical band gap deriving from the Dirac cone prevents graphene from being luminescent [22], but in graphene excitons have an infinite Bohr radius and for this reason graphene fragments of any size will show quantum confinement effects. Consequently, GCQDs possess a non-zero band gap, meaning the photoluminescent properties are determined by the  $\pi$  states of the  $sp^2$  domains. Under these conditions, recombination of electron-hole (e-h) pairs in these  $sp^2$  domains can facilitate fluorescence [18].

In contrast to QDs, GCQDs consist of light atoms, and thus their dielectric constant and spin-orbit coupling are small and weak, respectively [213]. However, these characteristics lead to strong carrier-carrier interactions and electronic states with well defined spin multiplicity. Thus, GCQDs have much larger energy bands than inorganic semiconductor QDs of comparable size. It has been reported that absorption of one photon, due to aforementioned strong carrier-carrier interactions, can lead to the generation of more than one exciton [114]. GCQDs with this process can be particularly useful for improving the efficiency of photon-generated carriers.

Density functional theory (DFT) calculations have shown that the band gap for one aromatic

ring (benzene) is about 7 eV and decreases to approximately 2 eV in GCQDs consisting of 20 aromatic rings [38]. This means, the extent of the band gap can be tuned by modifying the size of the GCQD's conjugated  $\pi$ -domains [204, 214]. Depending on the synthesis approach and subsequent purification methods, the size distribution of aforementioned  $sp^2$  domains can vary significantly. This leads to the existence of band gaps of different sizes; covering a wide range of the PL emission spectrum, from visible light to near infrared [85, 204].

Furthermore, it seems that due to changes to the edges, the QCE no longer holds if the GCQDs diameters exceed 17 nm [70]. For diameters < 17 nm, the bulk of GCQDs have mixed zigzag and armchair edges and a circular/elliptical shape. When the diameters exceed 17 nm the GCQDs exhibit polygonal shape with mostly armchair edges. The greater number of armchair edges compared to zigzag edges results in larger energy gaps for graphene materials [137]; as a result the PL emission blue-shifts while the peak energy increases with increasing diameter (> 17 nm).

### 2.3.3.2 The Surface State Effect

As described in the previous chapter, surface states (i.e. surface chemistry) of CDs can have a strong influence on the PL properties of CDs. First of all, the difference between the surface and molecule state should be noted. The surface state is the PL center, not consisting of isolated chemical groups but rather synergetically constituted by the hybridization of the CD surface groups and the CD carbon core (backbone). Often the molecule state is the emerging PL center for CDs prepared by small-molecule carbonization (bottom-up route). Surface groups (i.e. functional groups) can have various energy levels, which may result in various emissive states. When light of a matching excitation wavelength illuminates the CDs, the corresponding surface emissive state will dominate the PL emission. Often a higher degree of surface oxidation or further effective modification can result in more surface defects, resulting in a (red-)shifted emission. Since the first discovery of CDs in 2004 [157, 182] most reported PL centers of CDs were proven to be surface state related. This is particularly significant as many organic molecules can provide surface passivation and thereby alter the PL emission of CDs. Especially in the case of CDs with intact  $sp^2$  domains, the absorption is due to the band-gap, but the resulting PL emission is controlled by the surface state effect [175].

For example, the band gap can also be tuned by the surface chemistry of the GCQDs [204]. Lau *et al.* reported that, if oleylamine ligands are used, the PL emission peak is blue-shifted by around 25 nm upon increasing the GCQDs size from 1.5 nm to 3.5 nm. The oleylamine ligands, which act as auxochromes, reduce the extent of certain energy gaps and thus large GCQDs with relatively small ligand/ $sp^2$ -ratios possess larger band gaps than smaller GCQDs [74, 76].

Generally, the surface states are only loosely defined, due to the diversity of the exact CD structure [46]. Furthermore, owing to the variety of possible surface states, some of these could also be non-radiative surface states. Hence, the competition between various emissive states and non-emissive trap states dominates the optical properties of carbon nanodots (especially CNDs).

As a rule of thumb, red-shifted PL emission can be observed for CNs with a high degree of surface oxidation, while blue-shifted emission (for CNs) can be observed after surface reduction [202].

To summarise, after photoexcitation the generated carriers are first stored in the carbon backbone. Subsequently they transfer either into any possible emissive state (hybridized structure of carbon backbone and surface groups) or into a non-emissive trap state. In the latter graphitic crystallinity can act as a temporary reservoir. Therefore an increased degree of graphitic crystallinity (i.e. carbonization) will lead to better photostability but lower the PLQYs, due to a higher number of different non-radiative relaxation channels created by the carbon structures (e.g. the layered structure of the graphite). Furthermore, this process suggests that a single carbon dot can possess multiple PL units of various PL emission wavelengths [213].

**Influence of Amine Groups** Among the relevant surface groups for CDs, amines (besides oxygen-based groups) are the most common and studied. It was shown, that GCQD edge-termination by primary amines allowed a modification of the electronic structure due to effective orbital resonance between amine moieties and the graphene core [160]. Amine functionalized GCQDs possess higher PLQYs, due to the reduction of non-radiative electron-hole recombination centers (e.g. carboxylic and epoxide groups) and their emission wavelength increases with increasing numbers of amine groups (for GCQDs of comparable size). Ab initio calculations further showed, that strong orbital interaction with the  $-NH_2$  groups leads to a higher HOMO at the GCQD edges, compared to hydrogen-terminated groups. Furthermore, the resonance between the delocalized  $\pi$ -orbital and the molecular orbitals of the amine groups results in a narrowing of the optical band gap. This means that with amine-functionalisation the band gap of GCQDs can be tuned and narrowed, as the band gap gradually decreases with increasing numbers of amine groups. Furthermore, surface functionalisation with amines (e.g. 1,2-ethylenediamine) can lead to enhancement of fluorescence in GCQDs due to promoted proton transfer from the ammonium moiety to the conjugated carbon structure [128]. Similar effects (e.g. enhanced PLQY) can be observed for amine-functionalized (amorphous) CNs, although the underlying mechanism is not yet understood. The PL emission of amine-functionalized CDs is pH sensitive, attributed to the protonation and deprotonation of the functional amine-groups.

**The Surface Edge State Effect** A special case of surface state emission is due to surface edge state effects or short SESE, which can often be observed for GCQDs. When graphene is broken down into GCQDs it can be cut along various crystallographic directions leading to different types of surface edges, e.g. armchair and zigzag-edges (see Fig. 2.10A). These edge types play an important role in the resulting electronic, magnetic and optical properties of the GCQD. For example, predominantly zigzag-edge GCQDs with diameters of 7 nm to 8 nm are metallic (due to the presence of zigzag-edge states) and graphene nanoribbons (GNRs) with

higher fractions of zigzag-edges exhibit smaller energy gaps than comparable GNRs with a predominantly armchair-edge ribbon [137]. Furthermore the type of edge sites directly influences the type of ground state, i.e. zigzag sites are carbene-like with a triplet ground state being the most common; and armchair sites are carbyne-like with a singlet ground state being the most common [135]. Nevertheless, the ground states of carbenes contain both triplet and singlet states (see Fig. 2.10). The triplet ground state is described as  $\sigma^1\pi^1$ , indicating that the two orbitals  $\sigma$  and  $\pi$  are singly occupied. In contrast the singlet state is described as  $\sigma^2$ , indicating that the  $\pi$  orbital is unoccupied and two non-bonding electrons are paired in the  $\sigma$  orbital [46]. The energy difference ( $\delta E \approx 0.96$  eV) between the triplet and singlet state, i.e. between the  $\sigma$  and  $\pi$  orbitals, causes a carbene ground-state multiplicity. Therefore, the blue PL emission of certain GCQDs can be attributed to the radiative recombination of excited electrons between the LUMO and the HOMO of free zigzag sites, with a carbene-like triplet/singlet ground state [46, 122]. Additionally, these surface edge states can be pH sensitive. Under acidic conditions, the free zigzag sites form a reversible complex with the protons leading to PL quenching (breaking of the emissive triplet carbene state). Under alkaline conditions the PL emission recovers because the free zigzag sites are restored (deprotonation). The major distinction between the two major PL mechanisms for GCQDs, surface edge state effect and the quantum confinement effect, is that the latter is defined by the size of the GCQDs (or better their  $sp^2$  domain size), whereas the first is independent of the GCQD size and the PL properties are determined by the triplet carbene at the zigzag edges [46, 94].

DFT and time-dependent density functional theory (TDDFT) calculations, showed that PL

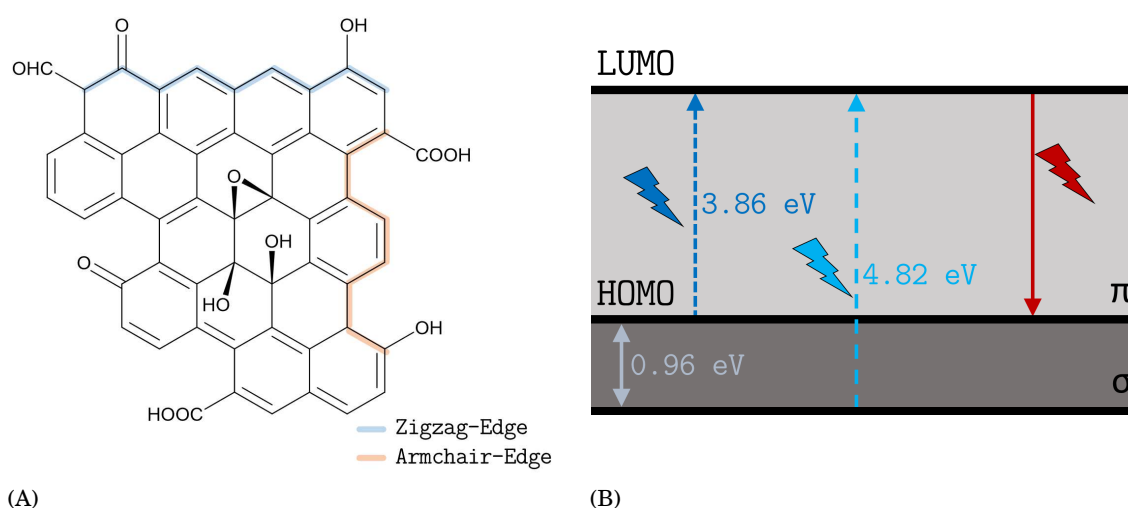


Figure 2.10: Schematic representation of (A) a typical GCQD structure, including surface edge states and most common functional groups and (B) the electronic transitions of triplet carbenes at zigzag sites [46].

emission of zigzag-edged GCQDs can cover the entire visible light spectrum by varying the average

diameter in the range from 0.89 nm to 1.80 nm [106]. Furthermore, the results revealed that armchair edges and pyrrolic nitrogen-doping (N-doping) induce a blue-shift, whereas chemical functionalities and defects cause a red-shift. It was also suggested, that isolated inhomogeneous  $sp^2$  domains can widen the PL emission peaks of GCQDs. Furthermore, the discrete excitonic energy levels can significantly slow down the relaxation of highly excited states in GCQDs, owing to a phonon bottleneck. In one case [88], due to a low energy-level offset between the intrinsic (QCE driven) state and the surface edge state, the offset between singlet- and triplet state was determined to be approx. 175 meV, making ISC efficient enough that it competes with IC among states with the same multiplicity. These GCQDs, as a result, emitted both fluorescence and phosphorescence. This could greatly affect the chemical reactivity and other processes (e.g. charge transfer, exciton migration) in the GCQD system, due to the triplet state's longer lifetimes. In summary, the PL emission of GCQDs not only depends on their  $sp^2$  domains size, it also derives from the surface- and edge-states. Furthermore, the surface- and edge-state derived PL emission is comparably brighter [73]. As a result, much of the reported (experimentally observed) PL emission of GCQDs in the literature was probably surface- and edge-state related.

### 2.3.3.3 The Isolated Fluorophore Effect

First of all, the difference between the surface and molecule state should be noted. The surface state is the PL center synergistically constituted by the hybridization of the CD surface groups and the CD carbon core (backbone). In contrast, the molecule state is the PL center solely constituted by an (isolated) organic fluorophore. Often the molecule state is the emerging PL center for CNDs prepared by small-molecule carbonization (bottom-up route) or by introduction of a strong (photoluminescent)  $sp^2$  conjugation unit like rhodamine B ( $sp^2$ -doping) [32].

The PL properties of CDs exploiting the isolated fluorophore effect (IFE) can be tuned by

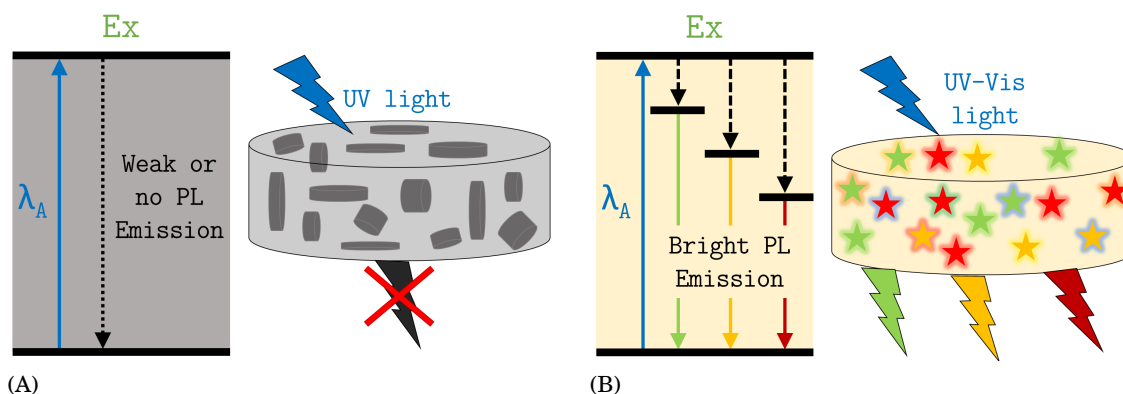


Figure 2.11: Schematic representation of: (A) CDs with strong absorption in the UV region, high photostability and weak emission (low PLQY). (B) CDs with weak absorption in the UV-vis region but strong multicolour emissions in the visible region (high PLQY).



the applied reaction temperature during the synthesis. At low reaction temperatures small fluorophore molecules are either formed (bottom-up route) and incorporated or the provided fluorophore is incorporated into the CD structure ( $sp^2$ -doping), while maintaining/contributing most of its PL properties (e.g. absorption and emission band) to the carbon dot. Upon increased reaction (carbonization) temperatures a carbon core is formed by either dehydration of the starting materials or consumption of the formed/present fluorophores (leading to a loss of the fluorophores original PL properties). Depending on the starting material used, the PL emission can therefore either red- or blue-shift with increasing reaction temperature (i.e. increasing contribution of the carbon core). While the isolated fluorophores show (similar to single fluorophores) strong PL emission with high PLQY, the carbon-core only possesses weak PL but with high photostability (see Fig. 2.11). Therefore a balance needs to be struck, while CDs showing a strong IFE show strong PL emission, their PL intensity decreases dramatically after high-power UV exposure [212]. On the other hand, CDs showing a weaker IFE have weaker PL emission (due to increased reaction temperatures) but a larger carbon core, providing higher photostability. A drawback of CDs showing an IFE is their broad PL emission bandwidth. Nevertheless, synthesis routes implementing the  $sp^2$ -doping technique are one of the most promising ways to obtain CDs with high PLQY and PL emission in the longer wavelength regions (red emission).

#### 2.3.3.4 The Giant Red-Edge Excitation Shift

One of the most controversial PL processes for CNDs is the so called “Giant Red-Edge Excitation Shift” or short GREES, because it contradicts partially the current knowledge of fluorophore behaviour. GREES derives from the aforementioned “Red-Edge Excitation Shift” (see Chap. 2.3.2.4, p. 30). The difference is that in GREES the solvation dynamics (approx.  $10^{-12}$  s) are slowed by a factor of one thousand until the same time scale as that of fluorescence is reached (approx.  $10^{-9}$  s) [21, 22]. This means that during the fluorescence process the energy levels of the excited- and ground state are changing and so is the emission energy (i.e. emission wavelength). Often the emission is tunable over a range of about 200 nm, for which the same emission band is replicated independent of the excitation wavelength, but with a constant offset [21, 22]. While the static PL properties of CNDs are controlled by their structure and chemical composition (e.g. functional groups), the selective luminescence was found independent of chemical composition and inter-layer forces (in multilayer GCQDs). Nevertheless, defects and  $sp^3$  hybridised carbon atoms can lead to in- and out-of-plane deformations (see Fig. 2.2, p. 10), thereby causing significant plane distortions and strain in the surrounding lattice. In particular, out-of-plane strain (as an intra-layer reorganization potential) was shown to be responsible for the selective luminescence behaviour of GCQDs [21].

After photoexcitation, the dipole of the excited state (i.e. of the functional group responsible for the emission) is no longer aligned with the other functional groups (neighbours) and solvent dipoles in its surrounding. Without out-of-plane strain the dipole of the excited state does not feel

intra-layer reorganization potentials and relaxes (with respect to the solvent dipoles), i.e. the PL emission is independent of the excitation wavelength (see Chap. 2.3.2.1, p. 22). If out-of-plane strain is present, the re-orientation of the excited state dipole and the neighbouring functional groups is much slower than the re-orientation of the surrounding solvent dipoles. Thus, the relaxation of the excited state dipole moment is slowed down (by intra-layer interactions) to the same time scale as the fluorescence, resulting in selective luminescence (see Fig. 2.12).

As soon as the excitation wavelength is increased, excitation within the same absorption band

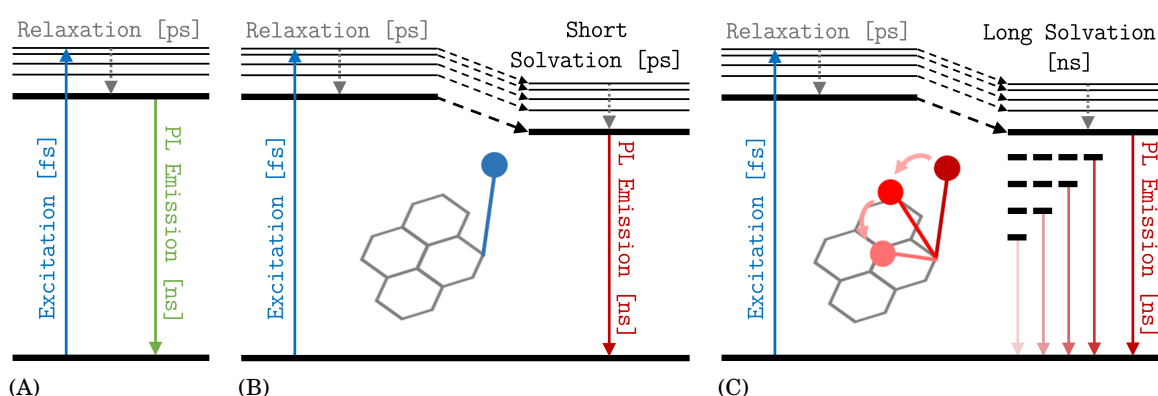


Figure 2.12: Schematic representation of the “Giant Red-Edge Excitation Shift” (GREES), i.e. the wavelength-dependent PL emission behaviour due to solvent environment. (A) Fluorescence in a nonpolar solvent proceeds through excitation in femtoseconds ( $10^{-15}$  s), thermal relaxation of carriers in picoseconds ( $10^{-12}$  s), and emission in nanoseconds ( $10^{-9}$  s). (B) In a polar solvent, solvent relaxation acts to lower the energy of the excited state and red-shift the emission. However, the solvation duration is much shorter than the PL lifetime ( $\tau$ ). (C) If the solvent interactions are on the same time scale as the fluorescence lifetime, a time-dependent emission is created, resulting in a red-edge tail. The insets are simplified representation of the excited state dipoles: (B) Without strain; the excited state dipole does not feel intra-layer reorganization potentials. (C) With strain; due to intra-layer reorganization potentials the relaxation of the excited state dipole moment is slowed to the same time scale as the fluorescence [21].

occurs but at a lower energy. Hence, solvation still occurs during the emission process, leading to an emission ranging from the shifted excitation wavelength to the same final solvated energy. This results in an identical red-shifted emission spectrum, starting at the identical, but red-shifted new excitation wavelength. As this process occurs constantly during emission, the emission bandwidth can be broadened. It is important to underline that tuning the relaxation time of the solvent, either via pH, polarity or temperature, can modify the GREES, but can not create it. Furthermore, there is evidence that the higher this strain is the more pronounced the GREES will be, but with a constant offset [21].

### 2.3.3.5 The Crosslink-Enhanced Emission- and the Aggregation Induced Emission Effects

The crosslink-enhanced emission (CEE) effect determines the PL emission in PDs [215]. The CEE leads to an amplification of the PL properties of potential photoluminescent centers (e.g. secondary and tertiary amines). Amplification is discussed to originate from the decreased vibrational and rotational freedom of fluorophores, as can be achieved by a crosslinked skeleton (e.g. crosslinked polyethylenimin). Consequently, the PL is temperature-dependent, meaning that high temperatures quench the PL to some degree, as higher temperatures enhance the vibration and rotation, thus increasing the non-radiative processes. Furthermore, PDs also show pH-dependent fluorescence as acidic conditions result in much more rigid and compact conformations.

For bare PEI the recombination (after excitation) to the ground state mainly occurs via a non-radiative process. Only a fraction of excited electrons are trapped by the amino-based states and returns to the ground state via the radiative route (weak PL emission). For PDs, due to their crosslinked skeleton, the vibration and rotation of the amino-based fluorophores is hindered (CEE effect), increasing the percentage of trapped (excited) electrons and thus enhancing the radiative process (strong PL emission). One of two special cases are CND-PD hybrids, where the PEI chains are immobilized by an amorphous carbon core. In CND-PD hybrids PL enhancement occurs both through the immobilization of the PEI chains and the antenna effect of the carbon core. The second special case are GCQD-PD hybrids, where the PEI chains are coated around a carbon core with a (multilayer) crystal carbon lattice. Because the PEI chains are fixed, the amine-based PL is enhanced by the CEE effect, but the carbon core with its (multilayer) crystal lattice possesses non-radiative trap states (structures). In sum the radiative process is neutralized and limited.

Finally it should be noted that the CEE effect is a different concept than the so called aggregation induced emission (AIE). The latter refers to small organic molecules exhibiting physical and/or supramolecular aggregation PEI [55, 56]. Especially fluorophores with freely-rotating groups, that promote radiation-less decay, are subject to AIE in solution. When these fluorophores aggregate/crystallize, the rotation of aforementioned groups is restricted. Hence the photoluminescence intensity (e.g. PLQY) becomes higher in the solid-state than in the solution phase.



## MATERIALS AND EXPERIMENTAL METHODS

**3.1 Reagents and Materials****3.1.1 Starting Materials**

Besides double deionized water, obtained from a Milli-Q water system (Merck Millipore, Billerica, MA, USA), the following starting materials were used (without further purification) throughout this work:

Table 3.1: Overview of starting materials, listed in alphabetical order, used during this study.

Name	CAS Number	Purity	Notes	Supplier
1,26-Diamino-3,6,9,12,15,18,21,24-octaoxahexacosane	82209-36-7	98 %	i.e. NH <sub>2</sub> -PEG(8)-NH <sub>2</sub>	Iris Biotech GmbH (Marktredwitz, Germany)
1,2,3,4-Butanetetracarboxylic acid	1703-58-8	99 %		Sigma-Aldrich Chemie GmbH (Munich, Germany)
Acetic acid (glacial)	64-19-7	100 %	i.e. HAc	Sigma-Aldrich Chemie GmbH (Munich, Germany)
Acetone	67-64-1	≥99.9 %		Carl Roth GmbH + Co. KG (Karlsruhe, Germany)
Ammonia solution	7664-41-7	NDA	30 % in H <sub>2</sub> O	Carl Roth GmbH + Co. KG (Karlsruhe, Germany)

NDA: no data available

Table 3.1: Continued on next page

*Table 3.1: Continued from previous page*

Name	CAS Number	Purity	Notes	Supplier
Benzylamine	100-46-9	≥99 %		Sigma-Aldrich Chemie GmbH (Munich, Germany)
Chitosan 100	9012-76-4	NDA	NDA	WKGP Karthaus; CIST (Chitose, Japan)
Citric acid	77-92-9	≥99.5 %	anhydrous	Carl Roth GmbH + Co. KG (Karlsruhe, Germany)
Dimethyl sulfoxide	67-68-5	≥99.9 %		Merck KGaA (Darmstadt, Germany)
Dimethyl sulfoxide-d6	2206-27-1	NDA	99.9 At.% D	Sigma-Aldrich Chemie GmbH (Munich, Germany)
Disodium phosphate	7558-79-4	≥98 %		Carl Roth GmbH + Co. KG (Karlsruhe, Germany)
Ethylenediamine-tetraacetic acid	60-00-4	99.995 %	i.e. EDTA	Sigma-Aldrich Chemie GmbH (Munich, Germany)
Ethanol (absolute)	64-17-5	≥99.9 %		Sigma-Aldrich Chemie GmbH (Munich, Germany)
Fluorescein sodium salt	518-47-8	NDA		Merck KGaA (Darmstadt, Germany)
Glucose monohydrate	50-99-7	≥99.5 %	i.e. $\alpha$ -D(+)-Glucose monohydrate	Carl Roth GmbH + Co. KG (Karlsruhe, Germany)
Glycerine	56-81-5	≥99 %		Sigma-Aldrich Chemie GmbH (Munich, Germany)
Hexane	110-54-3	≥97 %		Sigma-Aldrich Chemie GmbH (Munich, Germany)
Hydrochloric acid	7647-01-0	NDA	1 M in H <sub>2</sub> O	Carl Roth GmbH + Co. KG (Karlsruhe, Germany)
Hydrogen peroxide	7722-84-1	NDA	30 wt.% in H <sub>2</sub> O	Sigma-Aldrich Chemie GmbH (Munich, Germany)
Iodine	7553-56-2	≥99.8 %	solid	Sigma-Aldrich Chemie GmbH (Munich, Germany)
Magnesium chloride	7791-18-6	≥98 %	anhydrous	Sigma-Aldrich Chemie GmbH (Munich, Germany)
Melamine	7791-18-6	≥99 %		Sigma-Aldrich Chemie GmbH (Munich, Germany)

NDA: no data available

*Table 3.1: Continued on next page*

## 3.1. REAGENTS AND MATERIALS

Table 3.1: Continued from previous page

Name	CAS Number	Purity	Notes	Supplier
Methanol	67-56-1	≥99.5 %		Carl Roth GmbH + Co. KG (Karlsruhe, Germany)
<i>n</i> -Hexane	110-54-3	95 %	anhydrous	Sigma-Aldrich Chemie GmbH (Munich, Germany)
N-Fmoc-L-glutamic acid 5-benzyl ester	123639-61-2	≥98.0 %	Fmoc-Glu(OBzl)-OH	Sigma-Aldrich Chemie GmbH (Munich, Germany)
Ninhydrin	108-78-1	≥99 %		Sigma-Aldrich Chemie GmbH (Munich, Germany)
<i>N,N</i> -Dimethylformamid	68-12-2	99.8 %	anhydrous	Sigma-Aldrich Chemie GmbH (Munich, Germany)
Phenol	108-95-2	≥99.0 %		Sigma-Aldrich Chemie GmbH (Munich, Germany)
Poly(vinyl alcohol)	9002-89-5	NDA	average MW 31,000 - 50,000; 87 % - 89 % hydrolyzed	Sigma-Aldrich Chemie GmbH (Munich, Germany)
Potassium cyanide	151-50-8	≥98 %		Sigma-Aldrich Chemie GmbH (Munich, Germany)
Potassium dihydrogen phosphate	7778-77-0	≥98 %		Carl Roth GmbH + Co. KG (Karlsruhe, Germany)
Potassium iodide	7681-11-0	≥99 %		Sigma-Aldrich Chemie GmbH (Munich, Germany)
Poly(ethylene glycol) bis(3-aminopropyl) terminated	34901-14-9	NDA	$M_n \sim 1500$	Sigma-Aldrich Chemie GmbH (Munich, Germany)
Pyridine	110-86-1	≥99.8 %	anhydrous	Sigma-Aldrich Chemie GmbH (Munich, Germany)
Qdot 525 ITK carboxyl quantum dots		NDA	CdSe/ZnS QDs	Invitrogen Corporation (Carlsbad, CA, USA)
Silver nitrate	7761-88-8	≥99.9 %		Carl Roth GmbH + Co. KG (Karlsruhe, Germany)
Sodium acetate trihydrate	6131-90-4	≥99.5 %		Carl Roth GmbH + Co. KG (Karlsruhe, Germany)
Sodium borohydride	16940-66-2	≥96 %		Sigma-Aldrich Chemie GmbH (Munich, Germany)

NDA: no data available

Table 3.1: Continued on next page

Table 3.1: Continued from previous page

Name	CAS Number	Purity	Notes	Supplier
Sodium hydrogen carbonate	144-55-8	NDA		Sigma-Aldrich Chemie GmbH (Munich, Germany)
Sodium hydroxide	1310-73-2	≥99 %		Carl Roth GmbH + Co. KG (Karlsruhe, Germany)
Succinic acid	110-15-6	≥99.5 %		Carl Roth GmbH + Co. KG (Karlsruhe, Germany)
Thionyl chloride	7719-09-7	≥99 %		Sigma-Aldrich Chemie GmbH (Munich, Germany)
Tris-Acetate-EDTA buffer		NDA	10X concentrate; i.e. TAE buffer	Sigma-Aldrich Chemie GmbH (Munich, Germany)
Tris-EDTA buffer		NDA	Stock 100X; i.e. TE buffer	Carl Roth GmbH + Co. KG (Karlsruhe, Germany)
Tris-(hydroxymethyl)-aminomethane	77-86-1	≥99.7 %	i.e. Tris	Carl Roth GmbH + Co. KG (Karlsruhe, Germany)

### 3.1.1.1 Starch

Starch is produced by nearly any known green plant (e.g. potato, corn and algae) as an energy storage. Especially modified starches have found wide applications as additives in the paper-, textile-, pharmaceutical- and food industry. Today the worldwide production of starch and its modified derivatives is approx. 127 million tonnes per year (MTPA) [1].

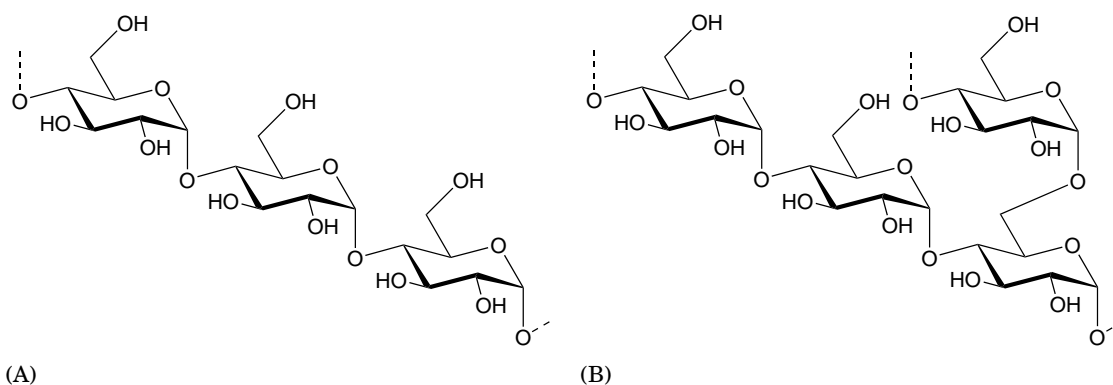


Figure 3.1: Structure of the two major types of starch molecules: (a) amylose and (b) amylopectin.



**Properties of Starch** Starch is a polymeric carbohydrate formed from a large number of glucose units (GU) joined by glycosidic bonds. This polysaccharide consists of two major types of molecules, distinguished by their structural disparities: the branched amylopectin and the linear (and helical) amylose [37], whereby, amylose molecules prove to be much smaller than amylopectin molecules (see Fig. 3.1). Generally, starch molecules are stored in plants in semi-crystalline granules, whose size (diameter: 1  $\mu\text{m}$  to 200  $\mu\text{m}$ ), shape and amylose/amylopectin ratio are unique for each plant species [87, 96, 143].

When in contact with cold water starch only swells. But it becomes quite soluble in water when heated, thereby losing its semi-crystalline structure, forming an colloidal dispersion and increasing the mixture's viscosity [50, 87]. This process is called starch gelatinization, as during cooking, starch becomes a paste and further increases the mixtures viscosity. When the paste is cooled or stored for a prolonged time retrogradation occurs, i.e. the semi-crystalline structure (mainly caused by amylose) partially recovers and the starch paste thickens, expelling water. Contrary, amylopectin tends not to undergo retrogradation, i.e. the higher the amylopectin content, the higher the stability of the aqueous starch solution/mixture [50, 87]. See Table 3.2 for an overview of starch types used in this study.

Table 3.2: Overview of starches ( $(\text{C}_6\text{H}_{10}\text{O}_5)_n$ ) and modified starches, listed in alphabetical order, used during this study.

Name	CAS Number	Purity	Notes	Supplier
Alimentamyl 2002*	NDA	$\geq 99\%$	distarch phosphate (E 1412)	Südstärke GmbH (Schrobenhausen, Germany)
Amylex 20/20*	NDA	$\geq 99\%$	depolymerized potato starch	Südstärke GmbH (Schrobenhausen, Germany)
Corn starch (wild type)	9005-25-8	$\geq 99\%$	27 wt.% amylose	Sigma-Aldrich Chemie GmbH (Munich, Germany)
Fibraffin K105*	56780-58-6	$\geq 99\%$	cationic starch ether	Südstärke GmbH (Schrobenhausen, Germany)
Licocat P*	56780-58-6	$\geq 99\%$	quaternary cationic starch solution	Südstärke GmbH (Schrobenhausen, Germany)
Low amylose corn starch	9005-25-8	$\geq 99\%$	0 wt.% - 1 wt.% amylose	Sigma-Aldrich Chemie GmbH (Munich, Germany)

NDA: no data available

Table 3.2: Continued on next page

Table 3.2: Continued from previous page

Name	CAS Number	Purity	Notes	Supplier
Potato starch	9005-25-8	≥99 %	20 wt.% amylose	Sigma-Aldrich Chemie GmbH (Munich, Germany)
Sobocat*	56780-58-6	≥99 %	quaternary starch ether	Südstärke GmbH (Schrobenhausen, Germany)
Sobotex 5305 NN*	NDA	≥99 %	starch acetate	Südstärke GmbH (Schrobenhausen, Germany)
Sobotex CM*	009063-38-1	≥99 %	starch ether	Südstärke GmbH (Schrobenhausen, Germany)
Undefined starch	NDA	NDA	food-grade	Supermarket (Potsdam, Germany)
Waxy corn starch	9005-25-8	≥99 %	76 wt.% amylose	Sigma-Aldrich Chemie GmbH (Munich, Germany)
Wheat starch	9005-25-8	≥99 %	28 wt.% amylose	Sigma-Aldrich Chemie GmbH (Munich, Germany)

\* Amount of modifications ≤0.1 %.

### 3.1.2 Stock Solutions

#### 3.1.2.1 TAE buffer solutions

Tris Acetate-EDTA buffer (TAE buffer) of various concentrations were obtained from a TAE100X buffer solution. For a TAE100X buffer solution Tris(hydroxymethyl)aminomethane (Tris: 484 g, 4 mol, 4 M), Ethylenediaminetetraacetic acid (EDTA: 29.224 g, 100 mmol, 100 mM) and glacial acetic acid (HAc: 114.2 mL, 2 mol, 2 M) were dissolved in water to a total volume of 1 L. If needed, this stock solution could be further diluted with water in various ratios to obtain either TAE50X- (01:02), TAE10X- (01:10), TAE05X- (01:20) or TAE01X (01:100) buffer solutions (see Table 3.3).

#### 3.1.2.2 TE buffer solutions

1 L of Tris-EDTA buffer (TE buffer) 100X stock solution (pH 8.0) contains Tris(hydroxymethyl)aminomethane (Tris: 121 g, 1 mol, 1 M), Ethylenediaminetetraacetic acid (EDTA: 29.224 g, 100 mmol, 100 mM) and water. If needed, this stock solution (TE100X) could be further diluted with water in various ratios to obtain either TE50X- (01:02), TE10X- (01:10), TE05X- (01:20) or TE01X (01:100) buffer solutions (see Table 3.3).

**TeE buffer solutions** TE buffer solutions enriched with Tris (TeE buffer) were obtained by dissolving 363 g (3 mol) of Tris(hydroxymethyl)aminomethane in 1 L of TE100X (see above). 1 L of the resulting TeE100X buffer (pH 8.0) contains Tris (484 g, 4 mol, 4 M), EDTA (29.224 g, 100 mmol, 100 mM) and water. If needed, this stock solution (TeE100X) could be further diluted with water in various ratios to obtain either TeE50X- (01:02), TeE10X- (01:10), TeE05X- (01:20) or TeE01X (01:100) buffer solutions (see Table 3.3).

Table 3.3: Various TAE-, TE- and TeE buffer solutions, their respective composition and compound concentrations; i.e. typical concentrations of starting materials.

Name (short)	Tris	EDTA	HAc	pH
TAE100X	4 M	0.1 M	2 M	8.3
TAE50X	2 M	50 mM	1 M	8.3
TAE10X	0.4 M	10 mM	0.2 M	8.3
TAE05X	0.2 M	5 mM	0.1 M	8.3
TAE01X	40 mM	1 mM	20 mM	8.3
TE100X	1 M	0.1 M	-	8.0
TE50X	0.5 M	50 mM	-	8.0
TE10X	0.1 M	10 mM	-	8.0
TE05X	50 mM	5 mM	-	8.0
TE01X	10 mM	1 mM	-	8.0
TeE100X	4 M	0.1 M	-	8.0
TeE50X	2 M	50 mM	-	8.0
TeE10X	0.4 M	10 mM	-	8.0
TeE05X	0.2 M	5 mM	-	8.0
TeE01X	40 mM	1 mM	-	8.0

### 3.1.2.3 PBS buffer for pH values from 4.8 to 8.0

All PBS buffer solutions (pH range from 4.8 to 8.0) used in this work were prepared according to the following protocol (see Table 3.4) [136]:

#### Stock Solutions

1. Solution A:  $c_{\text{KH}_2\text{PO}_4} = \frac{1}{15} \text{M}$

2. Solution B:  $c_{\text{Na}_2\text{HPO}_4} = \frac{1}{15} \text{ M}$

Table 3.4: Preparation of PBS buffer with defined pH values [136]: Take  $(100 - X)$  mL of Solution A and add  $X$  mL of Solution B.

pH	Solution A (mL)	Solution B (mL)	pH	Solution A (mL)	Solution B (mL)
4.8	99.65	0.35	6.6	62.80	37.20
5.0	99.05	0.95	6.8	50.80	49.20
5.2	98.20	1.80	7.0	38.80	61.20
5.4	97.00	3.00	7.2	27.40	72.60
5.6	95.10	4.90	7.4	18.20	81.80
5.8	92.10	7.90	7.6	11.50	88.50
6.0	87.90	12.10	7.8	6.40	93.60
6.2	81.60	18.40	8.0	3.10	96.90
6.4	74.60	26.40			

for 100 mL buffer solution

### 3.1.3 Iodine Test

The iodine test is used as a qualitative colorimetric indicator for the presence of starches in solutions or organic compounds. The test is based on the formation of a complex between the polyiodide anions ( $\text{I}_3^-$ ,  $\text{I}_5^-$ , aso.) and the starch molecules (especially the amylose helix) leading to an intense blue/purple colour. The exact color of the complex depends both on the amylose/amylopectin content and the chain length of the amylose. Beyond a length of 45 glucose units (GU) the solution will be intense blue, at ca. 30 GU purple, at 30 GU to ca. 20 GU red and below approx. 12 GU the solution will be yellow. A negative iodine test is characterized by its brown color and therefore, positive and negative tests are easy to distinguish. Lugol's iodine solution will not detect simple sugars such as glucose and fructose, but other complexing agents (e.g. PEG) can lead to false positive results.

However, It should be noted that the intensity of the color of a positive test decreases or disappears with increasing temperature or with the presence of water-miscible organic solvents such as ethanol. Furthermore, at very low pH values the test cannot be performed, due to the complete hydrolysis of the starch under these conditions (i.e. no formation of amylose helix).

**Lugol's Iodine Solution** The Lugol's iodine solution (10 %) used in this work was prepared according to the following protocol [30]: For 100 mL of Lugol's iodine solution 10 g of potassium iodide (KI) were dissolved in 25 mL of deionized water and the solution was heated slightly under

constant stirring. Subsequently 5 g of iodine were added and after all iodine was dissolved, 75 mL of deionized water were added. The solution was filled into an amber bottle and stored in cool and dark (chemical refrigerator).

**Procedure for the Iodine Test** In order to verify total starch conversion, 50  $\mu$ L of Lugol's Iodine solution (10 %) were added to 0.5 mL of the obtained carbon nanodot solution at room temperature and vigorously shaken. Total starch conversion was confirmed if no color change was observed (see above).

### 3.1.4 Kaiser Test

The Kaiser test [66] (i.e. ninhydrin test), is a qualitative colorimetric test for the presence or absence of free primary amino groups. In solid phase peptide synthesis (SPPS) and solid-phase organic synthesis (SPOS) the Kaiser test is commonly used for detection of free terminal amino groups, i.e. indication about the completeness of a coupling step. The test is based on the reaction of primary amines with ninhydrin, forming a characteristic dark blue color (Ruhemanns blue). The advantages of the test are its fast reaction time (completed within minutes), its minimal sample consumption and its high level of sensitivity. It should be noted that with the Kaiser test neither secondary amines, aromatic amines or tertiary amines can be detected.

Jarre *et al.* presented a modified Kaiser test [62] for the quantitative detection of primary amines on nanoparticle surfaces, which was further adjusted in this study to enable the use of a Monowave 300 synthesis microwave oven (Anton Paar GmbH, Graz, Austria) as heating source. All solutions needed for the Kaiser test were prepared according to the following protocol [66]:

#### Solution No.

1. *Buffer pH 5.5*: 36 g of sodium acetate were dissolved in 6.9 mL of glacial acetic acid, subsequently distilled water was added until a total volume of 100 mL was reached.
2. *Ninhydrin (5 %) solution*: 2.5 g of ninhydrin were dissolved in 50 mL of pure ethanol.
3. *KCN pyridine reagent*:
  - a) KCN solution (0.03 M): 9.768 mg of potassium cyanide (KCN) were dissolved in 5 mL of distilled water.
  - b) 1 mL of above KCN solution (0.03 M) was diluted with pyridine to a total volume of 50 mL.
4. *Phenol solution*: 200 g of phenol were dissolved in 50 mL of pure ethanol under constant stirring while being gently heated.
5. *Aqueous ethanol*: 135 mL of pure ethanol were diluted with 90 mL of distilled water.
6. *Benzylamine stock solution (0.002 M)*: 4.286 mg of benzylamine were dissolved in 25 mL of distilled water.

**Procedure for the Quantification of Primary Amino Groups on Carbon Nanodots**

1. 250  $\mu\text{L}$  of sample solution (e.g. CND, benzylamine) were put into microwave vial G10 with a stirring bar.
2. 750  $\mu\text{L}$  of *Solution No.1* (buffer pH 5.5) was added and shaken vigorously.
3. 500  $\mu\text{L}$  of *Solution No.3* (KCN pyridine reagent) and 500  $\mu\text{L}$  of *Solution No.4* (phenol solution) were added.
4. The vial was sealed, put into the microwave and heated to 110 °C for 10 minutes with the following program:
  - a) Heat as fast as possible to 110 °C.
  - b) Hold temperature (110 °C) for 10 minutes.
  - c) Cool as fast as possible to 75 °C.
5. The vial was opened and 500  $\mu\text{L}$  of *Solution No.2* (5% ninhydrin solution) were added.
6. The vial was sealed again, placed into the microwave and heated to 110 °C for 10 minutes with the following program:
  - a) Heat as fast as possible to 110 °C.
  - b) Hold temperature (110 °C) for 10 minutes.
  - c) Cool as fast as possible to 50 °C.
7. The vial was removed and stored until the sample reached room temperature.
8. After 40 minutes 2 mL of *Solution No.5* (aqueous ethanol) were added and the UV-Vis absorption spectrum was recorded.

The absolute values (primary amine concentration) were obtained from a benzylamine calibration curve (see *Solution No.6*) measured earlier. For the benzylamine calibration curve see Fig. B.2, p. 130.

## 3.2 Carbon Dot Synthesis Procedures

### 3.2.1 Apparatus and Procedure

All following synthesis have been performed as a microwave-assisted hydrothermal precursor carbonization (MiW-hPC). This means that the carbon- and foreign atom source (e.g. nitrogen) were processed in aqueous solutions under superheated conditions ( $T > 100\text{ }^\circ\text{C}$ ) in a sealed vessel and therefore high pressures (see subsubsec:Hydrothermal). The utilization of a Monowave 300 synthesis microwave oven (Anton Paar GmbH, Graz, Austria) enabled simultaneous reaction temperature, -time and pressure control and monitoring, while also providing necessary safety precautions for high pressure reactions. Depending on the total sample volume ( $V$ ) needed, three (3) different vessels were used, giving a total volume range from 0.5 mL to 20 mL.

Unless otherwise stated, the following synthesis program was used:

1. Heat as fast as possible to chosen reaction temperature (e.g. 230 °C).
2. Hold temperature for chosen reaction time (e.g. 45 minutes).

3. Cool as fast as possible to 50 °C.

It should be noted that for security reasons the highest achievable pressure in a Monowave 300 reaction vessel is 30 bar (by factory default), thus limiting the highest possible reaction temperature for water to 230 °C. In the following, examples of synthesis for starch derived carbon nanodots (C-CNDs), starch derived nitrogen doped carbon nanodots (C/N-CNDs) and carboxylic acid derived nitrogen doped carbon nanodots (CA/N-CNDs) will be presented. Throughout this work, batch size, starch type, carboxylic acid type, starting material concentration and ratio, pH value of starting solution, reaction temperature and -time were varied for various CND synthesis (see Fig. 3.2).

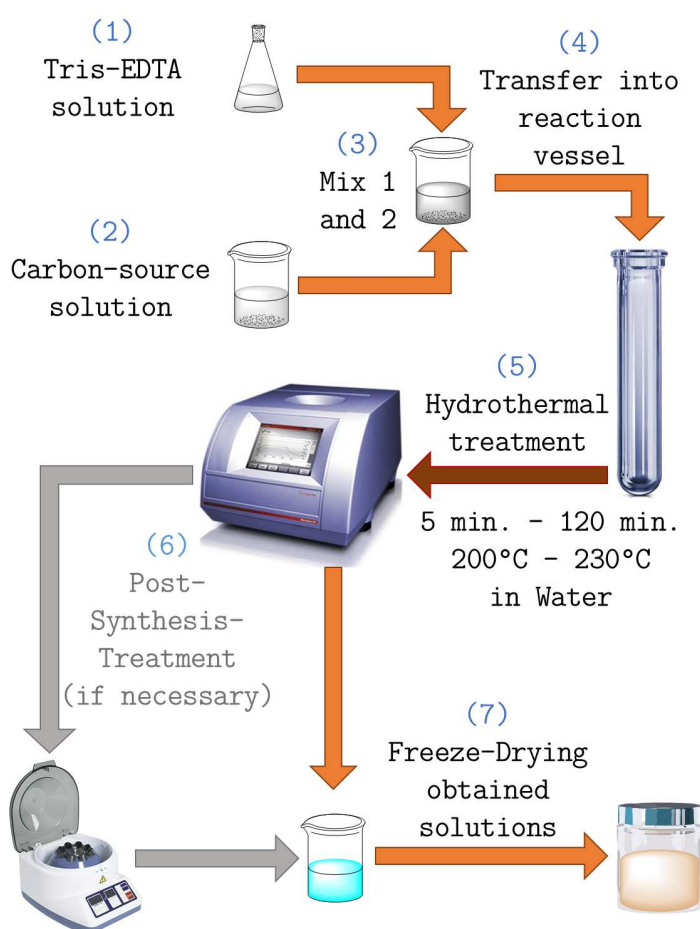


Figure 3.2: Schematic illustration of a typical carbon nanodot synthesis.

### 3.2.2 Synthesis of Starch Derived Carbon Nanodots

In a typical C-CND synthesis 4 mg starch were dispersed in 4 mL of deionized water at room temperature (RT) for several minutes under vigorous shaking. The as-prepared precursor solution was then transferred into a pressure resistant glass vial and heated up to 200 °C for 45 minutes

in the synthesis microwave oven. After cooling down to RT, the resulting clear light yellow to brown aqueous solution was prepared for further purification, storage and characterization.

### **3.2.3 Synthesis of Starch Derived, Nitrogen-Doped Carbon Nanodots**

In a typical C/N-CND synthesis 4 mg starch were dispersed in 4 mL of TAE buffer at room temperature (RT) for several minutes under vigorous shaking. The applicable TAE buffer originated from a TAE50X stock solution containing 242 g Tris (2 M), 57.1 mL glacial acetic acid (1 M) and 14.612 g of EDTA (50 mM) dissolved in 1 L of water. Subsequently the as-prepared precursor solution was transferred into a pressure resistant glass vial and heated up to 200 °C for 45 minutes in the synthesis microwave oven. After cooling down to RT, the resulting clear light yellow to brown aqueous solution was prepared for further purification, storage and characterization.

### **3.2.4 Synthesis of Carboxylic Acid Derived, Nitrogen-Doped Carbon Nanodots**

In a typical CA/N-CND synthesis 1.537 g citric acid (2 M) were dissolved in 4 mL of TeE buffer at RT for several minutes under vigorous shaking. The applicable TeE buffer originated from a TeE50X stock solution containing 242 g Tris base (2 M) and 14.612 g of EDTA (50 mM) dissolved in 1 L of water. Subsequently the as-prepared precursor solution was transferred into a pressure resistant glass vial and heated up to 230 °C for 45 minutes in the synthesis microwave oven. After cooling down to RT, the resulting clear light yellow to brown aqueous solution was prepared for further purification, storage and characterization.

### **3.2.5 Post-Synthesis Treatment**

Generally the as-prepared aqueous CND solutions needed no further purification and were ready for further optical characterization. In cases of strong carbonisation and consequent precipitation, resulting precipitates were separated by centrifugation or filtration. Finally, highly volatile by-products and excess solvent were removed either by evaporation under reduced pressure (rotary evaporator) or via freeze drying with a LYOVAC GT2 (Finn-Aqua Santasalo-Sohlberg GmbH, H"urth, Germany) Freeze-Dryer and a TRIVAC B D16 BCS rotary vane vacuum pump (Leybold Vacuum GmbH, Cologne, Germany). In case of incomplete material conversion, remaining starting material (non-volatile) was removed by recrystallization and/or precipitation, either in water or ethanol.

#### **3.2.5.1 Surface Functionalization of Carbon Nanodots**

In order to assess the suitability of as-synthesized C-CNDs and HAc/N-CNDs for future applications, two different surface functionalization routes were employed, targeting the CNDs respective surface groups (see below).



**Functionalization of C-CNDs with PEG** C-CNDs were functionalized with PEG (NH<sub>2</sub>-PEG(8)-NH<sub>2</sub>) under amidation reaction conditions, hence targeting the carboxylic acid groups on the C-CNDs surface. Freeze dried C-CNDs (120 mg) and 2 mL thionyl chloride were added in 50 mL DMF. The mixture was stirred for 2h under reflux (approx. 80 °C), followed by adding 200 mg of NH<sub>2</sub>-PEG(8)-NH<sub>2</sub> (poly(ethylene glycol) bis(3-aminopropyl) terminated) and the reaction mixture was kept stirring for 24h under reflux, wherein the solution turned red. The solution was cooled down to 60 °C, then neutralized (pH 7) with sodium hydrogen carbonate (NaHCO<sub>3</sub>). The obtaining brown solution was filtered to retain the supernatant. The raw product was further purified via solvent extraction with DCM, yielding the PEG-conjugated C-CNDs as a brown/yellow solid.

**Functionalization of HAc/N-CNDs with Glutamic Acid** HAc/N-CNDs were functionalized with glutamic acid (Fmoc-Glu(OBzl)-OH) by a DCC-coupling route, hence targeting the primary amines on the HAc/N-CNDs surface. Freeze dried HAc/N-CNDs (200 mg) and protected glutamic acid (N-Fmoc-L-glutamic acid 5-benzyl ester) were added in dried DMF under nitrogen protection. The mixture was stirred for 6h at room temperature. After the DMF was removed by rotary evaporator, the obtained solid was dissolved in EtOH to remove insoluble reagents via centrifugation. The EtOH solution was mixed with ice-cold n-hexane to retain the surface functionalized HAc/N-CNDs as a white precipitate (i.e. solid).

### 3.3 Experimental Methods

#### 3.3.1 Optical Characterisation

##### 3.3.1.1 Stationary UV-Vis Absorption Spectroscopy

Stationary UV-Vis absorption spectra were collected either on a Perkin-Elmer Lambda 750 (PerkinElmer, Waltham, MA, USA) or a Nanodrop 2000c spectrophotometer (Thermo Fisher Scientific Inc., Waltham, MA, USA). For the former 1.0 cm × 1.0 cm PMMA cuvettes (Carl Roth GmbH + Co. KG, Karlsruhe, Germany) or 1.0 cm × 1.0 cm quartz cuvettes (Hellma GmbH Co. KG, Müllheim, Germany) were used. All measurements were performed against the respective solvent of the samples. For every series of measurements, all relevant solvents were measured against air and samples with high optical density (OD) were diluted as follows: Solutions of fresh synthesized CNDs at two different concentrations, pure and diluted a hundredfold (01:100), were prepared and their absorbance spectra were recorded. If necessary, depending on the absorption spectra obtained, further solutions with varying dilution (e.g. 01:20, 01:200) were prepared and their absorbance spectra were recorded.

### 3.3.1.2 Stationary Emission Spectroscopy

Steady-state photoluminescence emission spectra were collected using a FluoroMax-P and a FluoroMax-4 fluorescence spectrometer (HORIBA Jobin Yvon GmbH, Munich, Germany). Samples were placed in 1.0 cm  $\times$  1.0 cm PMMA cuvettes (Carl Roth GmbH + Co. KG, Karlsruhe, Germany) or quartz cuvettes (Hellma GmbH Co. KG, Müllheim, Germany) and measured in a 90° setup. To avoid filter effects and other effects that might distort the signal readout, the PL emission measurements were carried out at an OD equal to 0.1 at the corresponding excitation wavelength. Unless otherwise stated all emission spectra were taken at pH 7.0 to account for the potential pH sensitivity of carbon nanodots and therefore assure comparability between measurements.

**Excitation-Emission Matrix Measurements** For excitation-emission matrix (EEM) measurements, the excitation wavelength was varied in the range of 250 nm to 650 nm in 20 nm steps (e.g. 250 nm, 270 nm, ..., 650 nm). The measured emission wavelength range was shifted accordingly (in 20 nm steps) to avoid detection of excitation light. To account for possible filter- or other effects that might distort the signal readout, the EEM measurements were carried out for each of two sample groups: (a) samples with an OD equal to 0.1 at the corresponding excitation wavelength and (b) for samples with an fixed OD (e.g. OD 0.1 at 340 nm). Steady-state photoluminescence emission spectra were collected using a FluoroMax-P fluorescence spectrometer (HORIBA Jobin Yvon GmbH, Munich, Germany) in a 90° setup and samples were placed in 1.0 cm  $\times$  1.0 cm PMMA cuvettes (Carl Roth GmbH + Co. KG, Karlsruhe, Germany). Unless otherwise stated all spectra were taken at pH 7.0 to account for the potential pH sensitivity of carbon nanodots and therefore assure comparability between measurements.

**3D-Excitation Spectra Measurements** For 3D-excitation spectra matrix (3DEM) measurements the observed PL emission wavelength (i.e. observed  $\lambda_{Em}$ ) was varied in the range of 410 nm to 599 nm in arbitrary steps (e.g. 410 nm, 417 nm, ..., 599 nm) based on PL emission peaks obtained by EEM measurements. In contrast, the excitation wavelengths were kept constant in the range of 250 nm to 575 nm for all measurements. To account for possible filter- or other effects that might distort the signal readout, the 3DEM measurements were carried out for each of two sample groups: (a) samples with an OD equal to 0.1 at the corresponding excitation wavelength and (b) for samples with an fixed OD (e.g. OD 0.1 at 340 nm). Steady-state photoluminescence excitation spectra were collected using a FluoroMax-P fluorescence spectrometer (HORIBA Jobin Yvon GmbH, Munich, Germany) in a 90° setup and samples were placed in 1.0 cm  $\times$  1.0 cm PMMA cuvettes (Carl Roth GmbH + Co. KG, Karlsruhe, Germany). Unless otherwise stated all spectra were taken at pH 7.0 to account for the potential pH sensitivity of carbon nanodots and therefore assure comparability between measurements.

### 3.3.1.3 Photoluminescence Quantum Yield Measurements

Photoluminescence quantum yield (PLQY) measurements were carried out on a modular C9920-02/-03 (Hamamatsu Photonics, Japan) including an integrating sphere, a PMA-12 Photonic Multi-Channel-Analyser C10027-01 (Hamamatsu Photonics, Japan) as detector and a 150 W/CW Xe lamp L10092 (Hamamatsu Photonics, Japan) as excitation source. Samples were placed in a 1.0 cm × 1.0 cm quartz cuvette and measurement data was collected, processed, visualized and analysed automatically by built-in software. To avoid filter effects and other effects that might distort the signal readout, the PLQY measurements were carried out at an OD equal to 0.1 at the corresponding excitation wavelength. Unless otherwise stated all measurements were taken at pH 7.0 to account for the potential pH sensitivity of carbon nanodots and therefore assure comparability between measurements.

### 3.3.1.4 Photoluminescence Lifetime Measurements

Photoluminescence lifetimes were determined by TCSPC (Time-correlated single photon counting) measurements on a FLS920 Fluorescence spectrophotometer (Edinburgh Instruments, UK). The samples were measured in a 90° setup using a white light source (SC-400-PP supercontinuum-source, Fianium: 0.5 MHz to 20 MHz, 400 nm <  $\lambda$  < 24 000 nm, pulse width: ca. 30 ps) as excitation source and a Multi-Channel-Plate (ELDY EM1-132/300, Europhoton GmbH, Berlin, Germany) as detector. To avoid filter effects and other effects that might distort the signal readout, the TCSPC measurements were carried out at an OD equal to 0.1 at the corresponding excitation wavelength. Unless otherwise stated all measurements were taken at pH 7.0 to account for the potential pH sensitivity of carbon nanodots and therefore assure comparability between measurements.

### 3.3.1.5 Single-Particle Fluorescence Microscopy

Single-particle fluorescence microscopy (SPFM) was performed using a home-build total internal reflection fluorescence (TIRF) setup. The total internal reflection fluorescence microscope (TIRFM) was a Zeiss Axio Observer Z1 (Carl Zeiss AG, Oberkochen, Germany). The microscope was equipped with a 100x/NA 1.45 oil immersion objective and four different filter cubes for separation of excitation and emission light at  $\lambda_{\text{Exc}} = 457$  nm and  $\lambda_{\text{Em}} = 495$  nm; at  $\lambda_{\text{Exc}} = 488$  nm and  $\lambda_{\text{Em}} = 535$  nm; at  $\lambda_{\text{Exc}} = 568$  nm and  $\lambda_{\text{Em}} = 630$  nm; and at  $\lambda_{\text{Exc}} = 647$  nm and  $\lambda_{\text{Em}} = 700$  nm. After excitation with a 3 W Ar-Kr-Ion cw-Laser Innova 70C (Coherent Inc., Santa Clara, CA, USA):  $\lambda_{\text{Exc}} = 456$  nm, 488 nm, 514 nm, 568 nm and 647 nm, image acquisition occurred with an iXon 888 EMCCD camera (Andor Technology, Belfast, United Kingdom) using the MetaMorph software (Molecular Devices, Sunnyvale, CA, USA).

**Sample Preparation for Single-Particle Fluorescence Microscopy** In order to perform SPFM measurements CND stock solutions were diluted multiple times with a saturated aqueous

solution of poly(vinyl alcohol), resulting in samples with an altogether dilution of approximately 1:10000 to 1:100000 (depending on initial stock solution). Prior to SPFM measurements multiple coverslips were evenly coated with approx. 200  $\mu\text{L}$  of above mentioned solutions (i.e. fixative) and left to dry (approx. 6h) until the PVAL/CND mixture was consolidated.

### **3.3.2 Structural Characterisation**

#### **3.3.2.1 Energy-dispersive X-ray Spectroscopy**

Energy-dispersive X-ray spectroscopy (EDX) was either performed on a Zeiss ULTRA55 PLUS scanning electron microscope (Carl Zeiss Microscopy GmbH, Jena, Germany), operating at 5 kV to 10 kV, a working distance of 10 mm, an acquisition time of 20 - 30 minutes and a Quantax 400 (Bruker Corporation, Billerica, MA, USA) as detector; or on an JSM-7800F (JEOL Ltd, Tokyo, Japan) with an attached EDX equipment. The elemental quantitative analysis (on both systems) used an automatic background subtraction and a correction has been used to calculate the elemental composition in weight percentages and atomic percentages.

EDX microanalyses was performed on the Zeiss ULTRA55 Plus for C-CND and HAc/N-CND and on the JSM-7800F for CiA/N-CND.

#### **3.3.2.2 Elemental Analysis**

Elemental analysis (ELE) was performed on Elementar Vario EL III (Elementar Analysensysteme GmbH, Hanau, Germany).

#### **3.3.2.3 Fourier Transform Infrared Spectroscopy**

Fourier transform infrared spectroscopy (FTIR) was performed using a Bruker Tensor 27 FTIR spectrometer (Bruker Optics, Billerica, MA, USA) using diamond in attenuated total reflection (ATR) in the range of  $400\text{ cm}^{-1}$  to  $4000\text{ cm}^{-1}$ .

#### **3.3.2.4 Nuclear Magnetic Resonance**

Nuclear magnetic resonance (NMR) measurements, both  $^1\text{H}$ - and  $^{13}\text{C}$ -NMR, were performed in deuterated dimethyl sulfoxide (DMSO- $d_6$ ) on a Bruker Avance 300 MHz NMR-spectrometer (Bruker Corporation, Billerica, MA, USA).

#### **3.3.2.5 Laser Diffraction Particles Size Analysis**

Laser diffraction particles size analysis, i.e. static light scattering (SLS), was performed on LS 13 320 Laser Diffraction Particle Size Analyser (Beckman Coulter Inc., Brea, CA, USA).

### 3.3.2.6 Transmission Electron Microscopy

Transmission electron microscopy (TEM) images were recorded on a JEOL JEM 1011 microscope (JEOL Germany GmbH, Freising, Germany) operated at 200 kV with samples prepared on 400 mesh, SiO<sub>2</sub> coated copper grids (Plano GmbH, Wetzlar, Germany).

### 3.3.2.7 Thermogravimetric Analysis

Thermogravimetric analysis (TGA) was performed on a TGA-50 (Shimadzu Corporation, Tokyo, Japan) and a connected TA-60WS Thermal Analysis Workstation (Shimadzu Corporation, Tokyo, Japan). Measurements were performed in alumina (Al<sub>2</sub>O<sub>3</sub>) cells under atmospheric pressure and air as flow gas, heating occurred from room temperature (approx. 25 °C) up to 1000 °C with a linear heating rate of 10 K/min.

### 3.3.2.8 X-ray Diffraction

X-ray diffraction (XRD) patterns were recorded on an EMPYREAN diffractometer (PANalytical B.V., Almelo, Netherlands) equipped with CuK $\alpha$  ( $\lambda = 0.15405$  nm) radiation at scanning speed of 0.47 °/min in the range from 4° to 70°.

## 3.4 Data Analysis

Generally, if not stated otherwise, Origin 2017 (OriginLab Corporation, Northhampton, MA, USA) and Microsoft Excel 2010 (Microsoft Corporation, Redmond, WA, USA) were used for data analysis, mathematical calculations, curve fitting and graphic display.

Evaluation of obtained TEM images (particle recognition; measurement and analysis of corresponding particle sizes) was performed using Pebbles and PebbleJuggler [112]. Photoluminescence decay times were fitted using the FAST software (Edinburgh Instruments, UK). NMR spectra were analysed using ACDLabs 2012 LSM software (Advanced Chemistry Development Inc., Toronto, Canada). ChemDraw and ChemOffice 16 (PerkinElmer, Waltham, MA, USA) were used for representations of chemical structures and their corresponding 3D models. TIRFM images were analysed and presented using ImageJ ver. 1.50i (Wayne Rasband, National Institute of Health, USA).



## RESULTS AND DISCUSSION

Each of the following sections is dedicated to one of the three major types of carbon nanodots synthesised in this study, namely: (1) starch derived carbon nanodots (C-CNDs), (2) starch derived-nitrogen doped carbon nanodots (C/N-CNDs) and (3) carboxylic acid derived-nitrogen doped carbon nanodots (CA/N-CNDs). Each section addresses the influence of various reaction conditions (e.g. time and temperature) on the photophysical properties (e.g. absorption- and PL emission spectra), and the structural characterization (e.g. NMR, Raman and XRD) of as-synthesized CNDs, by various means.

### 4.1 Synthesis and Characterisation of Starch Derived Carbon Nanodots

A key element for obtaining homogeneous CNDs is the careful selection of starting materials. Thus, a perfect carbon source (for green CND synthesis) needs to fulfil certain requirements: it should be soluble in water (green chemistry), accessible worldwide with defined and well known properties and composition, should not be in direct competition with essential food production, and last but not least, be cost effective [2, 92, 126].

Starch, as a worldwide accessible mass product with over 127 MTPA [1], meets the aforementioned requirements since nearly any known green plant (e.g. potato, corn and algae) produces starch as an energy storage. In plants starch is stored in so called starch particles which contain (depending on the plants species and variety) mainly amylose and amylopectin, apart from minor quantities of other substances (e.g. proteins) [37]. Like all natural products, starch undergoes seasonal changes and particularly the amylose/amylopectin ratio is influenced by plant species (see Fig. 4.1) and area of plant cultivation [37], which could influence the CND formation and

their photophysical properties. Nevertheless, due to its widespread use in the food-, textile- and paper industry starch can be obtained worldwide at low cost with well-defined properties in a wide variation of types.

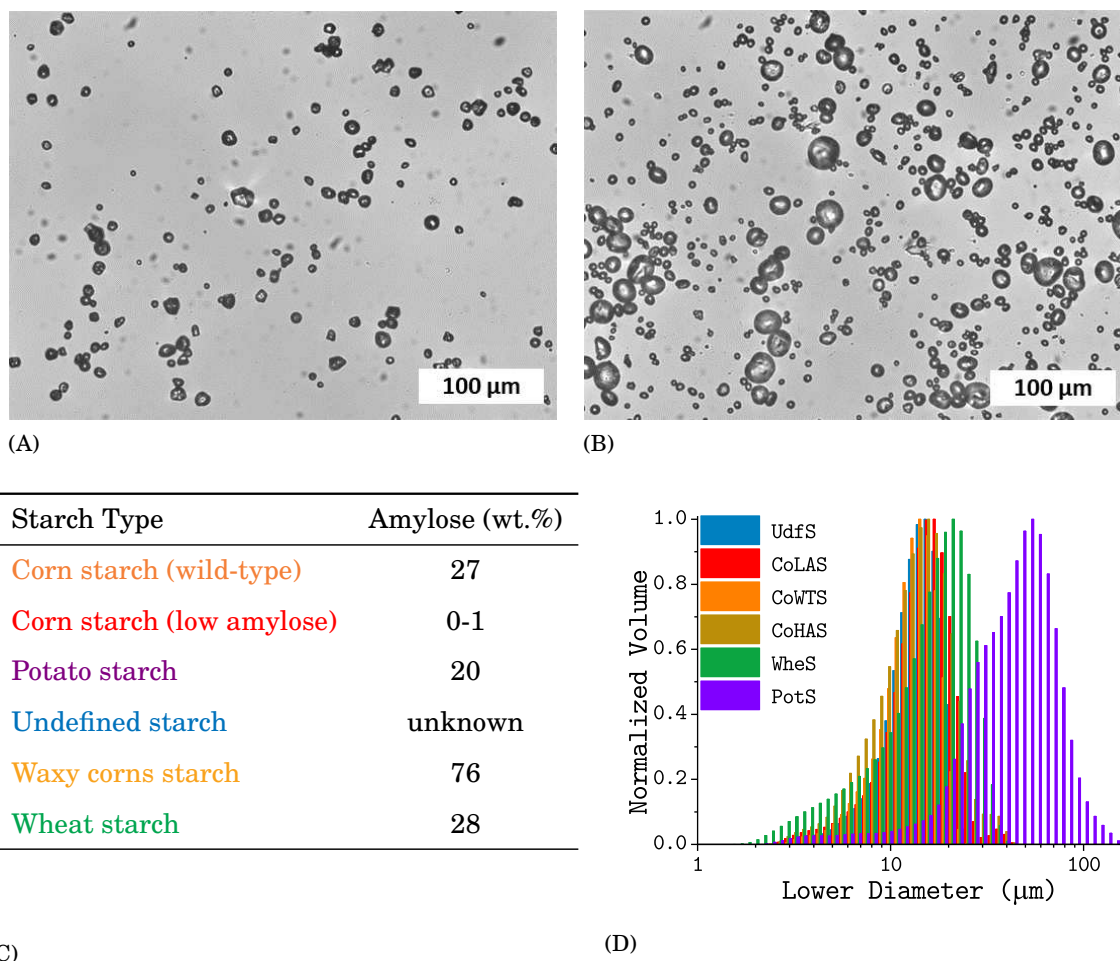


Figure 4.1: Light microscope images of starch particles from (A) potato starch and (B) corn starch. (C) Amylose content (wt%) for the used natural starches; and (D) their starch particle size distributions obtained by laser diffraction particles size analysis (SLS). UdfS: undefined starch; CoLAS: low amylose corns starch; CoWTS: wild type corn starch; CoHAS: (high amylose) waxy corn starch; WheS: wheat starch; and PotS: potato starch.

#### 4.1.1 Influence of Starch Concentration and Reaction Time on C-CND Synthesis

In order to gain initial insight into the formation of starch derived carbon nanodots (C-CNDs) various amounts of starch were dispersed in water (0.14 mg/mL, 0.28 mg/mL and 1.0 mg/mL) and subsequently heated to 200 °C for 5 to 120 minutes in the MiWR. Throughout the ongoing reaction the initially transparent colorless liquid sample turned into a yellow clear solution after



#### 4.1. SYNTHESIS AND CHARACTERISATION OF STARCH DERIVED CARBON NANODOTS

15 minutes, and became deep orange to brown as the reaction progressed. After 45 minutes blue emission could be observed for all samples when exposed to UV-light ( $\lambda_{\text{Exc}} = 312 \text{ nm}$ ). The influence of reaction time and starch concentration on the C-CND formation is illustrated in Figure 4.2 to Figure 4.4.

In Figure 4.2A, UV-Vis absorption spectra exhibit two strong separate absorption bands: the

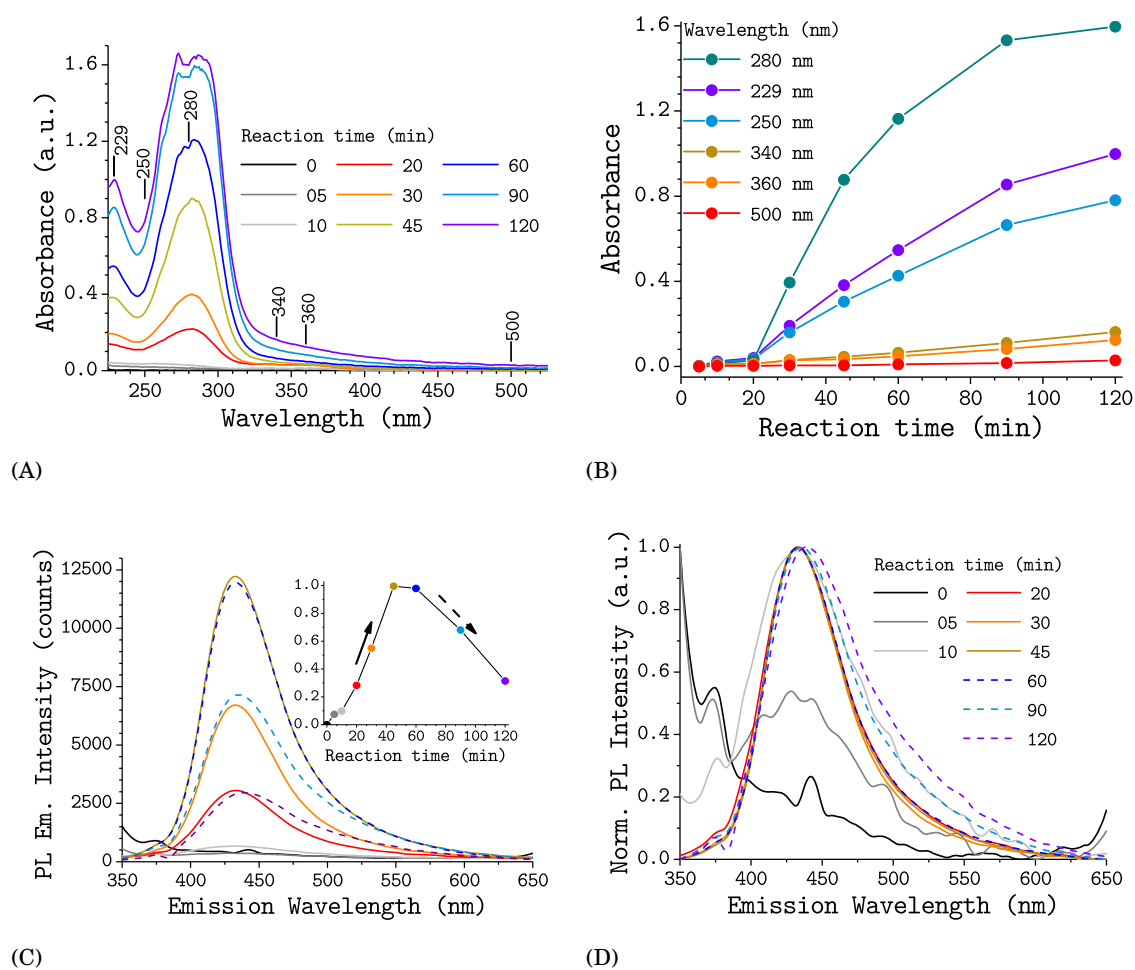


Figure 4.2: Effect of reaction time on the optical properties of C-CNDs derived from aqueous starch dispersion (1.0 mg/mL): (A) UV-Vis absorption spectra; (B) absorbance at six selected wavelengths as a function of reaction time; (C) PL emission spectra for different reaction times under excitation at 340 nm (OD 0.1), the inset is the PL Intensity as a function of reaction time; and (D) their corresponding normalized PL emission spectra.

first with the peak at around 229 nm (Peak 1) is assigned to  $n-\sigma^*$  transitions within C-O bonds (e.g. alcohols), while the second peak at around 250 nm to 280 nm (Peak 2) is assigned to the  $n-\pi^*$  transitions within conjugated carbonyl compounds. The band with the peak at around 300 nm to 400 nm (Peak 3) can presumably be attributed to  $n-\pi^*$  transitions within the C=O bonds of carbonyl groups, located either on the C-CND surface or within the C-CND core [69]. Aromatic

$\pi$ -systems, which also absorb in the range of Peak 2 (250 nm to 280 nm) and Peak 3 (300 nm to 400 nm), can be excluded as XRD and Raman measurements (see Fig. 4.9, p. 72) show that C-CNDs consist mainly of amorphous carbon (up to 99.9 %).

The spectra shown in Figure 4.2 were taken for ten C-CND samples obtained from ten synthesis attempts, for each reaction time, of aforementioned C-CND precursor solution with a fixed starch concentration (undefined starch: 1.0 mg/mL). The intensities of Peak 1 to Peak 3 increase with the reaction time due to increasing C-CND concentration, reaching their maximum after 120 minutes (see Fig. 4.2B). The corresponding PL and normalized PL emission spectra collected with excitation at 340 nm are shown in Figure 4.2C and Figure 4.2D, respectively. After 5 minutes

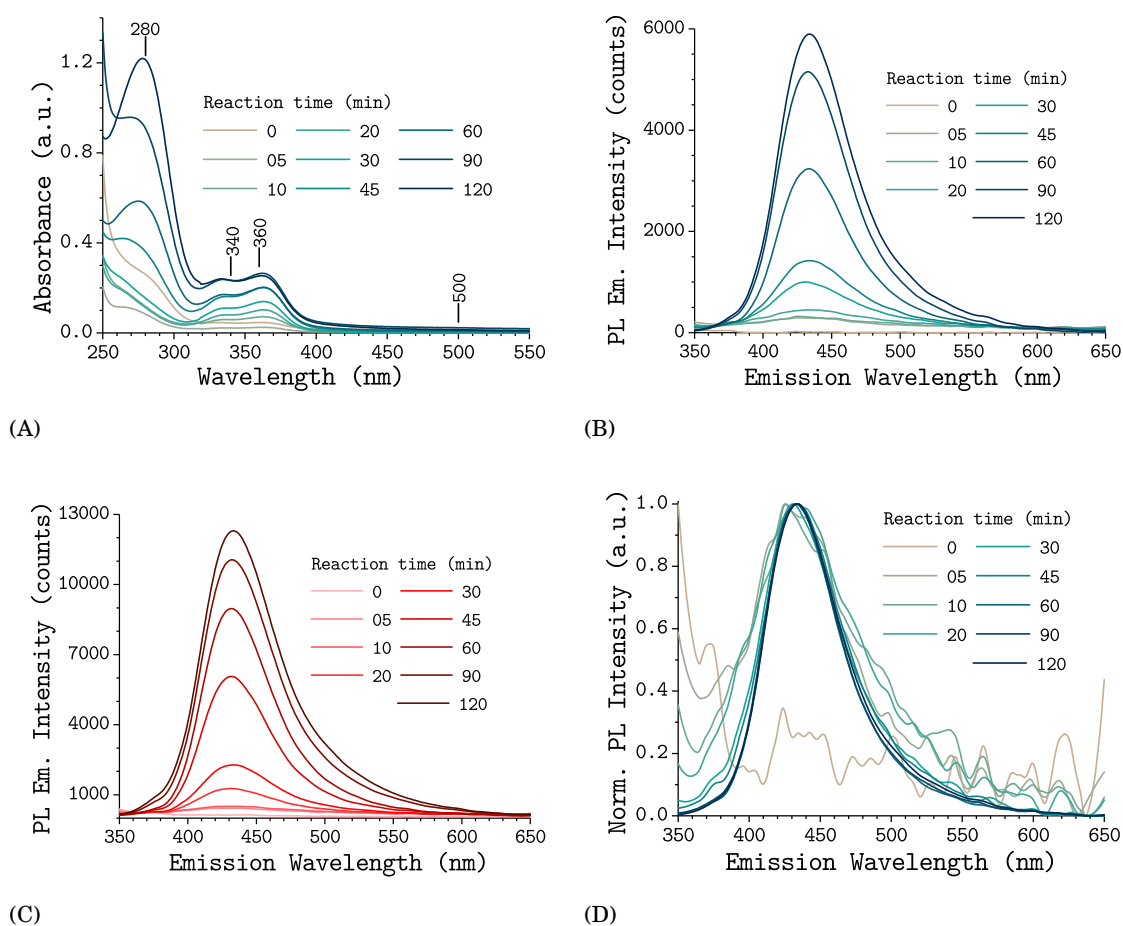


Figure 4.3: Effect of reaction time on the optical properties of C-CNDs derived from aqueous starch dispersion. Two distinctive initial starch concentrations, 0.14 mg/mL (top) and 0.28 mg/mL (bottom), are represented: (A,C) UV-Vis absorption spectra; and (B,D) PL emission spectra for different reaction times under excitation at 340 nm (OD 0.1), respectively.

reaction time no clear emission band can be observed as the C-CND formation has just started, but after 10 minutes, a weak emission band (see Fig. 4.2C) at around  $(433 \pm 2)$  nm, with a FWHM

#### 4.1. SYNTHESIS AND CHARACTERISATION OF STARCH DERIVED CARBON NANODOTS

of  $(67 \pm 4)$  nm and an average PL lifetime of 2.22 ns (see Table 4.3, p. 110) starts to emerge. The low standard deviation of  $\pm 2$  nm indicates the high reproducibility of the presented synthesis method. PL emission intensity increases as the reaction time increases, reaching its maximum after 45 minutes (inset in Fig. 4.2C). Subsequently, the overall PL intensity decreases (dashed line) and a slight emission red-shift from 433 nm to 438 nm can be observed simultaneously. Additionally, a loss in colloidal stability occurs after 120 minutes. The observed decreasing PL

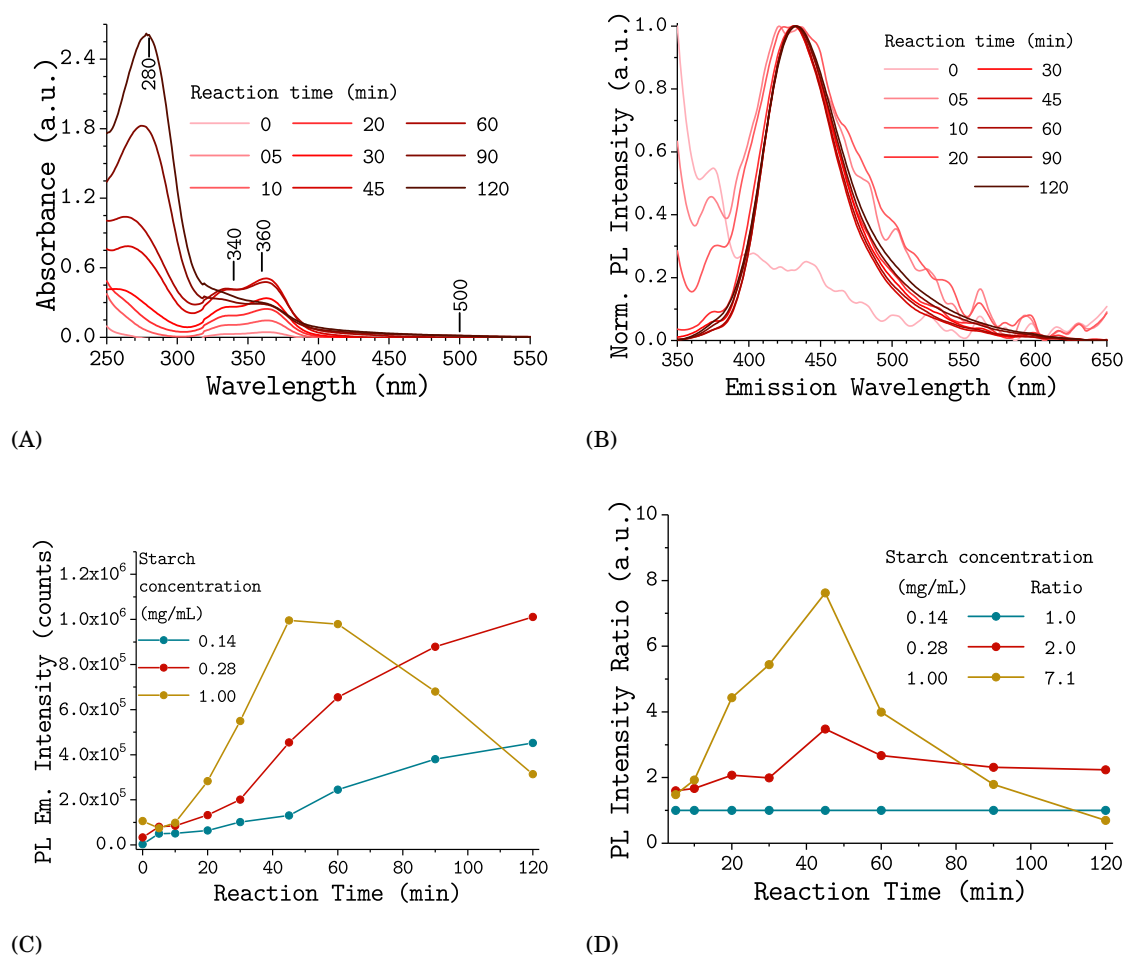


Figure 4.4: Effect of reaction time on the optical properties of C-CNDs derived from aqueous starch dispersion. Normalized PL emission spectra for different reaction times under excitation at 340 nm (OD 0.1) for: (A) 0.14 mg/mL of initial starch concentration (blue); and (B) 0.28 mg/mL of initial starch concentration (red). Effect of reaction time and initial starch concentration on the C-CND synthesis. (C) Cumulated PL emission intensities, and (D) normalized cumulated PL emission intensities for different reaction times under excitation at 340 nm (OD 0.1). The normalization is carried out by relating the samples cumulated PL emission intensities to the cumulated PL emission intensity of the lowest initial starch concentration, at any given reaction time. The samples are depicted according to their initial starch concentration: 1.0 mg/mL (yellow), 0.28 mg/mL (red) and 0.14 mg/mL (blue).

intensities and subsequent red-shift result either from the destruction of stabilizing surface groups and/or C-CND aggregation e.g. due to stacking. This is supported by centrifugation of remaining starch and Iodine tests [166], which showed total starch conversion after 45 minutes. Thus, the changes in the absorption spectra at reaction times longer than 45 minutes can only result from further changes in the molecular structure or assembly of C-CNDs. In summary the C-CNDs carbon core (where absorption presumably takes place) [213] stays intact and grows, while the emissive surface states are quenched. Further PL measurements demonstrated that the PLQY was below 1% and that it was independent of the reaction time.

The same measurements were executed for starch concentrations at 0.14 mg/mL and 0.28 mg/mL (see Fig. 4.3 and Fig. 4.4). Both measurement series led to similar results with regard to emission band and FWHM, but with much lower reaction rates (see Fig. 4.4). For both concentrations the highest PL intensity was observed after 120 minutes, at the end of the selected reaction time run (see Fig. 4.4C). One can expect, given an extended reaction time run, a further increase of PL intensity. Furthermore, the observed maximal PL intensities directly correlate with the initial starch concentration of (a) 0.14 mg/mL, (b) 0.28 mg/mL and (c) 1.0 mg/mL (1:2:7.1), i.e. after 120 minutes and 45 minutes both concentration **b** and **c** have approximately twice and seven times higher PL intensities, respectively, than concentration **a** at that given time (see Fig. 4.4D).

During hydrolysis starch undergoes depolymerisation, which ultimately leads to the formation of two main products:  $\alpha$ -D-glucose and organic acids (e.g. acetic acid) [10, 163]. Hence, the carbonization of starch by hydrothermal treatment is probably an autocatalysis process based on the formation of carboxylic acids, which increase the hydrolysis rate significantly (see Fig. 4.4D). Furthermore, above results demonstrate that the formation of C-CNDs is independent of the starch concentration, but most efficient at high starch concentrations due to the stronger autocatalysis process (see Fig. 4.4), enabling larger amounts of C-CNDs to be synthesized in shorter time.

### 4.1.2 Influence of Starch Type on C-CND Synthesis

In order to assess the suitability of various starch types as carbon source for C-CND synthesis, their influence on the resulting C-CNDs PL properties has been investigated using UV-Vis absorption as well as PL steady-state and PLQY measurements. All samples had a starting concentration of 1.0 mg/mL and were heated to 200 °C for 45 minutes.

There are two categories of starch types: (A) natural starches of different plant species and (B) modified starches for food-, textile- and paper industry. While natural starches mainly differ with respect to starch particle size and -structure, amylose/amylopectin ratio (see Fig. 4.1, p. 60) and water solubility, they are not distinguishable by their elemental composition (see Table 4.1). Modified (industrial) starches, on the other hand, can vary widely in their physical properties, even though in most cases the amount of modification is less than 0.1% (see Table 3.2).

As it can be seen in Figure 4.5 the optical properties of C-CNDs stay unaffected for different starch types, even when modified starches are used. The only exception is the UV-Vis absorption

#### 4.1. SYNTHESIS AND CHARACTERISATION OF STARCH DERIVED CARBON NANODOTS

Table 4.1: Overview of the elemental content (according to elemental analysis) of 6 different natural starches ((C<sub>6</sub>H<sub>10</sub>O<sub>5</sub>)<sub>n</sub>); MW: n · 162.14 g/mol) used during this study, listed in alphabetical order.

Name	Abbreviation	C (wt%)	H (wt%)	O (wt%)
Theoretical value*	-	44.44	6.23	≤ 49.34
Corn starch (wild type)	CoWTS	39.75	6.39	≤ 53.86
Corn starch (low amylose)	CoLAS	39.72	6.53	≤ 53.75
Potato starch	PotS	37.90	6.40	≤ 55.70
Undefined starch	UdfS	39.46	6.34	≤ 54.20
Waxy corn starch	CoHAS	39.84	6.41	≤ 53.70
Wheat starch	WheS	39.37	6.33	≤ 54.31
Mean value		39.3 ± 0.73	6.40 ± 0.072	54.3 ± 0.74

\* calculated from molecular formula (C<sub>6</sub>H<sub>10</sub>O<sub>5</sub>)<sub>n</sub>

spectra of LicocatP (Lic) derived C-CNDs, which are missing the prominent  $n-\pi^*$  transition peak at around 250 nm to 300 nm (e.g. conjugated carbonyl compounds). Nevertheless, independently of starch type the C-CND show PL emission peaking at around (433 ± 3) nm and a FWHM of (72 ± 5) nm, when excited at 340 nm. The PLQY for all C-CND solutions was found to be below 1 %, similar to previous results. Hence, it can be concluded, that nearly any commercial starch currently available on the market can be used to produce similar C-CNDs via microwave-assisted hydrothermal precursor carbonization.

##### 4.1.2.1 Glucose as Starting Material for C-CND Synthesis

As already stated, starch (as a polymeric carbohydrate) undergoes depolymerisation during the hydrothermal treatment [10, 163] prior to or during C-CND formation. However, it has not yet been clarified if as-synthesized C-CNDs thereby derive from starch monomers ( $\alpha$ -D-glucose) or starch oligomers (e.g. maltodextrin).

The application of  $\alpha$ -D-glucose (i.e. sugar or D-(+)-glucose) meets the aforementioned requirements for a suitable carbon source, and its high level of water solubility surpasses by far the solubility of starch. In order to gain deeper insight into the C-CND formation, and to assess the suitability of  $\alpha$ -D-glucose as a carbon source, various amounts of glucose were dispersed in water (0.14 mg/mL, 1.0 mg/mL and 10 mg/mL) and subsequently heated to 200 °C for 45 minutes in the MiWR. Similar to starch derived samples, the initially transparent colorless liquid sample turned into a yellow clear solution after 15 minutes, and became deep orange to brown as the reaction

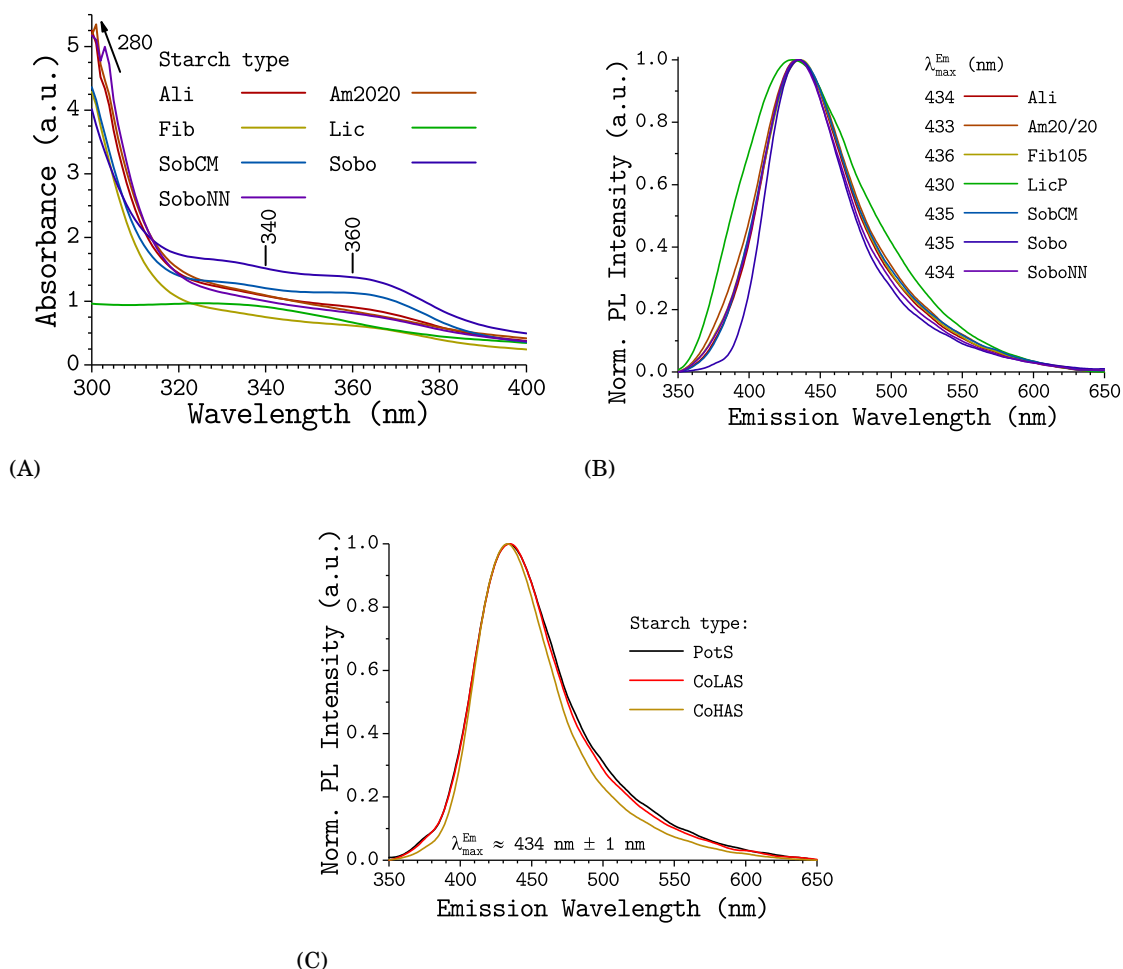


Figure 4.5: Influence of starch type on the optical properties of C-CNDs derived from aqueous starch dispersion (1.0 mg/mL): (A) UV-Vis absorption spectra; and (B,C) normalized PL emission spectra for various modified- and natural starch types, respectively. PL emission spectra were taken under excitation at 340 nm (OD 0.1) for all samples. Ali: Alimentamyl 2002; Am20/20: Amylex 20/20; Fib105: Fibraffin K105; LicP: Licocat P; SobCM: Sobotex CM; Sobo: Sobocat; SoboNN: Sobotex 5305 NN; CoLAS: low amylose corns starch; CoHAS: (high amylose) waxy corn starch; and PotS: potato starch.

progressed. After 45 minutes blue emission could be observed for all samples when exposed to UV-light ( $\lambda_{\text{Exc}} = 312 \text{ nm}$ ).

The influence of glucose concentration and ageing on the CND PL properties is illustrated in Figure 4.6. The UV-Vis absorption spectra (see Fig. 4.6A) exhibit two strong separate absorption bands with a peak at around 229 nm (Peak 1), assigned to  $n\text{-}\sigma^*$  transitions (e.g. C-O bonds), and a second peak at around 250 nm to 310 nm (Peak 2), assigned to  $n\text{-}\pi^*$  transitions within conjugated carbonyl compounds (see Table B.3, p. 129). Contrary to C-CNDs, Peak 1 is much stronger than Peak 2, implying a difference in structure between starch- and glucose derived CNDs. The broad absorption band at around 310 nm to 450 nm can be attributed to  $n\text{-}\pi^*$  transitions within the

#### 4.1. SYNTHESIS AND CHARACTERISATION OF STARCH DERIVED CARBON NANODOTS

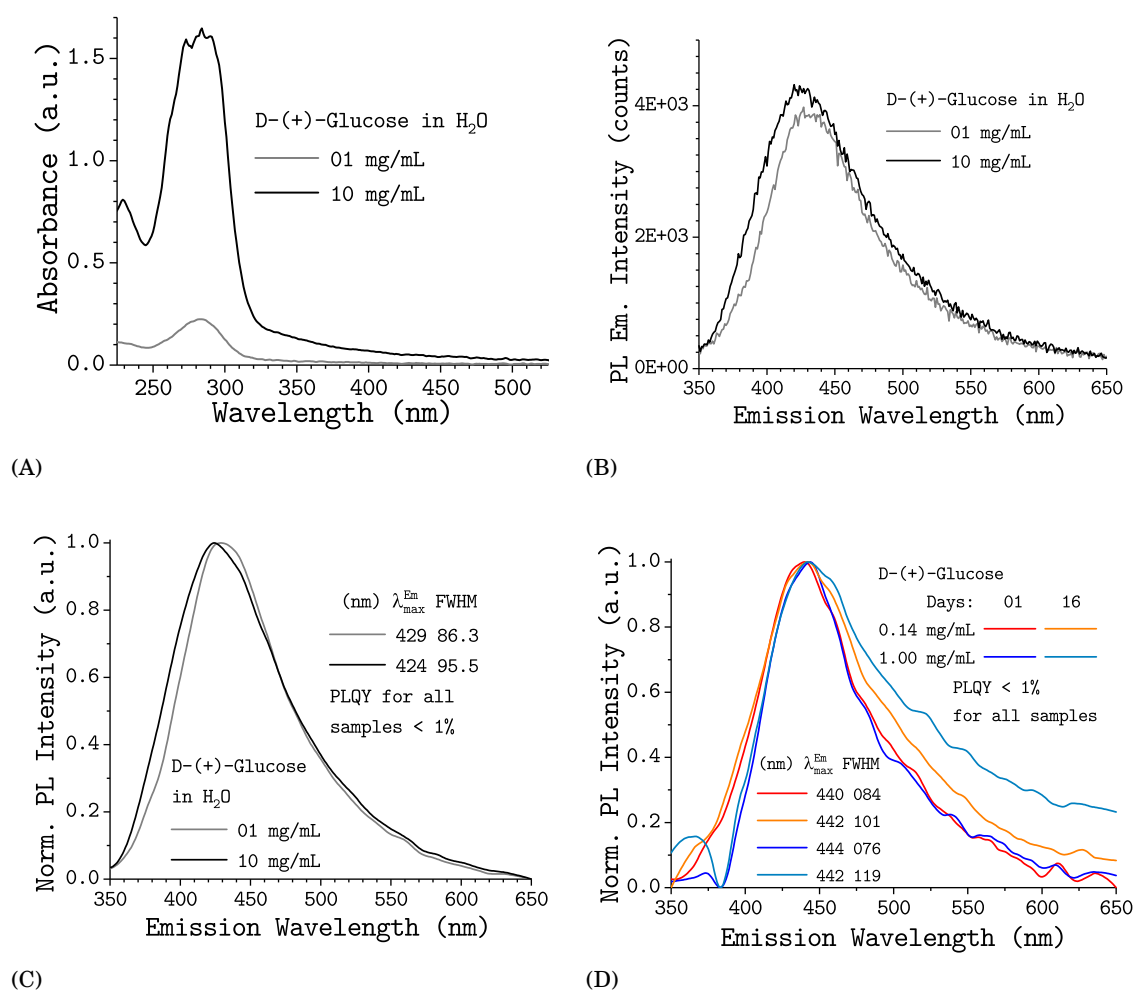


Figure 4.6: Optical properties of CNDs derived from individual aqueous  $\alpha$ -D-glucose solutions at various dates: (A) UV-Vis absorption spectra; (B) PL emission spectra under excitation at 340 nm (OD 0.1); and (C) their corresponding normalized smoothed-out PL emission spectra, for two different initial glucose concentrations (1.0 mg/mL and 10 mg/mL). (D) Effect of loss in colloidal stability (i.e. ageing) on the normalized smoothed-out PL emission spectra of glucose derived CNDs.

C=O bond (either on the C-CND surface or -core) [69].

While the absorption spectra of glucose derived CNDs are similar to starch derived C-CNDs, the same can not be said for the PL emission properties; except the PLQY which was found to be below 1%, similar to previous results. The observed PL and normalized PL emission spectra collected with excitation at 340 nm are shown in Figure 4.6B to Figure 4.6D, respectively. Contrary to C-CNDs, the observed PL emission bands of glucose derived CNDs vary widely from batch to batch (either due to starting concentration and/or date). Hence, the observed PL emission band for a given starting concentration (e.g. 1.0 mg/mL) range from around 429 nm up to 444 nm (see Fig. 4.6C and Fig. 4.6D), accompanied by comparably broad FWHM of around 86 nm to 100 nm,

respectively. This clear dependency of PL properties on batch and date (i.e. glucose derived PL properties are not reproducible) show that C-CND formation is fundamentally different between starch and glucose. Furthermore, glucose derived CNDs show increased precipitation, i.e. are unstable over time and are subject to ageing. Hence, it can be concluded, that the depolymerisation of starch during MiW-hPC is not complete and stable, reproducible C-CNDs are formed from glucose oligomers/polymers of unknown chain length. Apart from this, the inability of glucose to form stable CNDs may be an indicator for the origin of C-CND stabilization. It is conceivable, that incomplete depolymerisation and carbonisation (of starch) leads to starch fragments (e.g. oligomers), either covalently bound or adsorbed on the C-CND surface. This provides colloidal stabilization for the C-CNDs, either by sterical and/or electrostatic effects.

### 4.1.3 Up-scaling

Since starch to C-CND transformation appears to be an autocatalytic process and solubility of starch in water is limited, up-scaling C-CND synthesis needs to account for these challenges. Especially the use of natural (i.e. unmodified) starches in aqueous systems is restricted due to starch grain swelling and gelification. Both processes result in very high viscosities due to retrogradation, phase separation and gelification effects. Hence, the initial starch concentration is limited to 10 mg/mL by the ability of the magnetic stirrer incorporated into the MiWR.

Such high starch concentrations lead to very high reaction rates (see Chap. 4.1.1, p. 60). Hence, an aqueous starch dispersion of 10 mg/mL needs less than 5 minutes (at 200 °C) to transform from an initially white turbid dispersion into a dark brown solution with high amounts of black precipitate. Although the precipitate can be removed via centrifugation and C-CNDs can be extracted from the supernatant, the overall loss of starting material (in form of precipitate) makes this process highly inefficient. A simple way to control reaction rates is the use of buffer solutions as solvent, as they stabilize the pH value during the synthesis and thereby lower the reaction rate during C-CND formation. Buffer solutions need to fulfil certain requirements to be considered suitable for C-CND synthesis. First of all, they need to be stable at high reaction temperatures (e.g. 200 °C) second, be available in a wide range of pH values to account for various starting concentrations (e.g. < 10 mg/mL), and last but not least, they should not react with the starch, i.e. alter the chemical-, physical- and PL properties of resulting C-CNDs. Phosphate-buffered saline fulfils all aforementioned requirements and proved to be ideal for high throughput C-CND synthesis in the course of this study.

The spectra shown in Figure 4.7 were taken from six C-CND synthesis attempts, of six C-CND precursor solutions. Each solution contained 10 mg/mL starch in 20 mL of PBS buffer (pH 8.0) and was heated to 200 °C for 10 minutes. Total starch conversion was verified via Iodine test and post synthesis centrifugation (see Chap. 3.1.3, p. 48).

Similar to previous results (see above), the UV-Vis absorption spectra (see Fig. 4.7A) exhibit two strong separate absorption bands: the first at around 229 nm (Peak 1) and the second peak at



#### 4.1. SYNTHESIS AND CHARACTERISATION OF STARCH DERIVED CARBON NANODOTS

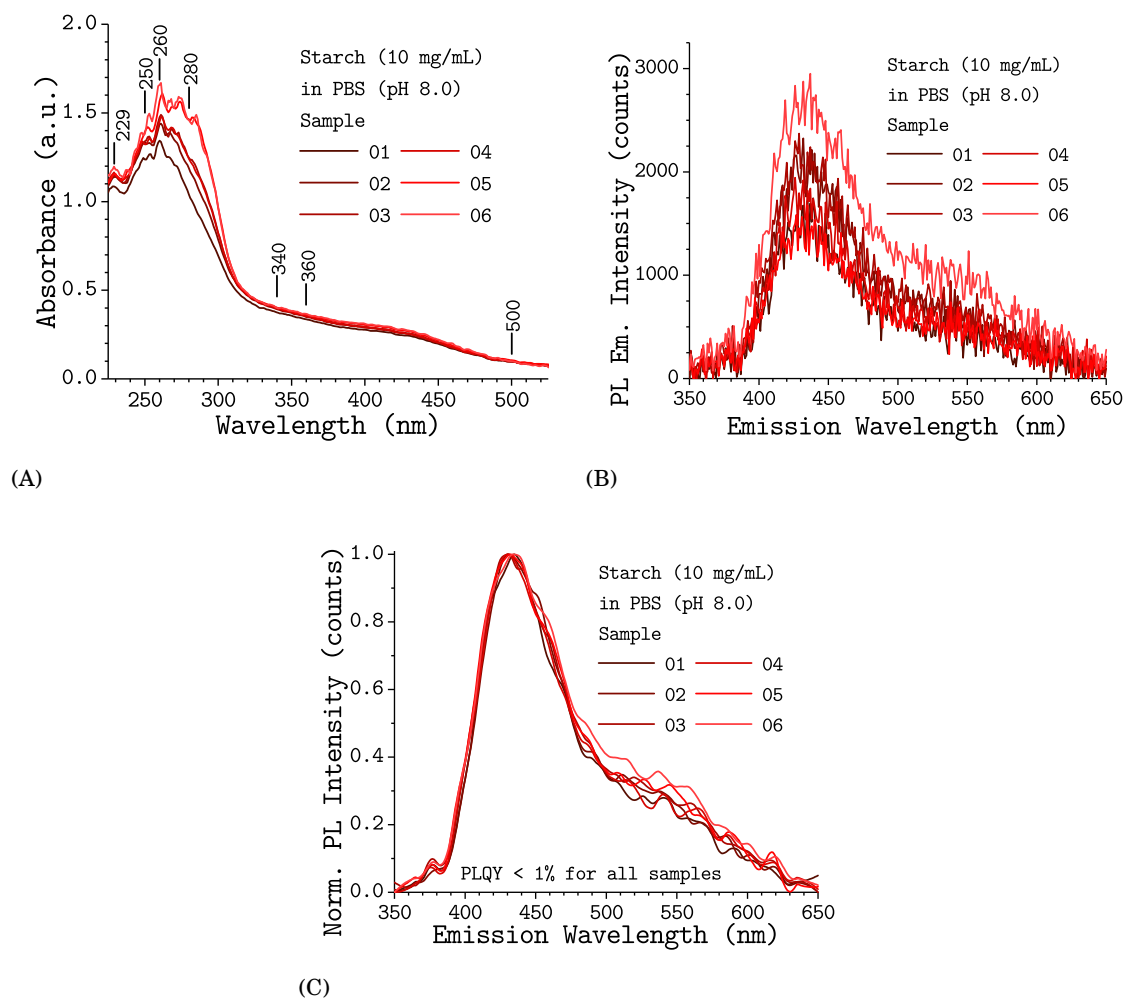


Figure 4.7: Effect of high initial starch concentrations (10 mg/mL) and PBS buffer (pH 8.0) on the C-CND synthesis and the level of reproducibility for the presented high throughput synthesis method. The following spectra were taken from six independent synthesis batches (01 - 06): (A) UV-Vis absorption spectra; (B) PL emission spectra under excitation at 340 nm (OD 0.1); and (C) the corresponding normalized smoothed-out PL emission spectra.

around 250 nm to 280 nm (Peak 2) followed by a shoulder at around 300 nm to 500 nm (Peak 3). The corresponding PL and normalized PL emission spectra collected with excitation at 340 nm are shown in Figure 4.7B and Figure 4.7C, respectively. After 5 minutes reaction time a clear emission band can be observed at around  $(432 \pm 2)$  nm, with a FWHM of  $(75 \pm 4)$  nm and a PLQY below 1%. The obtained C-CND solutions were stable over time and no difference to C-CNDs obtained from lower starch concentrations was detected. Furthermore, the low standard deviations indicate the high level of reproducibility for the presented high throughput synthesis method.

It shall be noted that the separation of PBS buffer and C-CNDs requires greater efforts of post synthesis purification. Hence, the use of high starch concentrations in combination with PBS

buffer must be based on a balance between the needed quantities (e.g. high throughput due to high concentrations and short reaction times), the overall cost (e.g. purification and overall preparation time) and the required purity of the C-CNDs (e.g. depending on expected application).

#### 4.1.4 Freeze Drying of C-CND Solutions

Initial results indicated that dried C-CNDs, contrary to most QDs, are stable over a long period of time (see Fig. 4.8A) and can be re-dispersed without loss in colloidal stability and PL properties. In

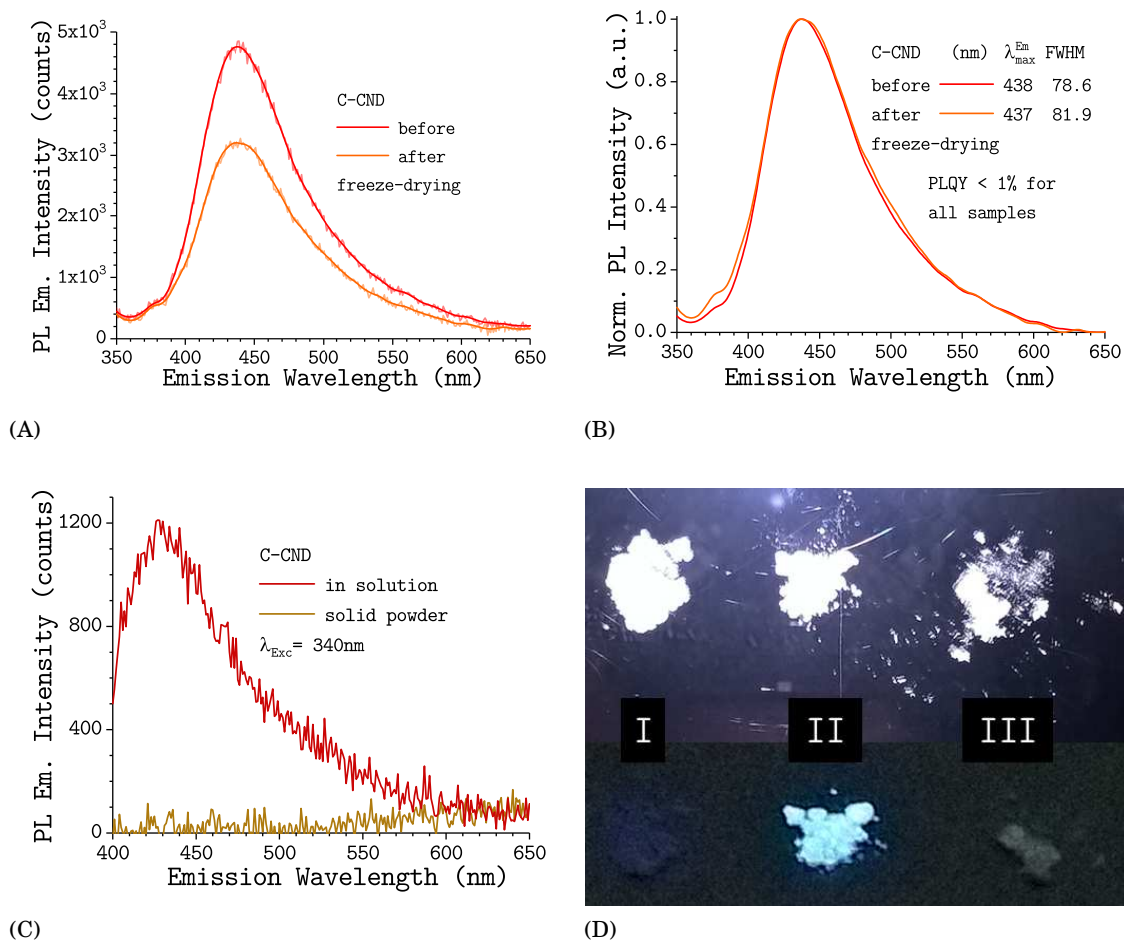


Figure 4.8: Effect of freeze-drying on the optical properties of C-CNDs: (A) PL emission spectra under excitation at 340 nm (OD 0.1) and (B) the corresponding normalized smoothed-out PL emission spectra for unmodified C-CND solution (before) and re-dispersed C-CND powder (after). (C) PL emission spectra of C-CND as dried solid powder (brown) and the same sample as aqueous solution (red) in PBS (pH 7.0). (D) Comparison between (I) starch powder; (II) dry starch powder, dyed with C-CNDs; and (III) C-CND powder after freeze-drying, under white light (top) and under 312 nm UV-light (bottom), respectively.

order to assess the stability of C-CNDs as a solid, 1 L of aqueous C-CND solution was freeze-dried

and characterised via PL steady-state and PLQY measurements. After freeze-drying for three days the former dark brown solution turned into a white to slightly brown C-CND powder. The powder did not exhibit any PL under UV-light (see Fig. 4.8C and Fig. 4.8D). PL properties recurred without any changes (see Fig. 4.8A) upon dissolving the C-CND powder in polar solvents (e.g. water, ethanol and acetone). Nevertheless, provided they have been incorporated into a matrix, e.g. paper and starch powder (see Fig. 4.8D), C-CNDs maintain their PL emission properties even when dried. Observed differences in PL emission maximum and FWHM remain within the error tolerances established by earlier findings (see above). Hence, C-CNDs can be easily stored and transported as freeze-dried powder, giving them a distinct advantage over today's quantum dots. Freeze-drying enabled the determination of the overall yield of C-CNDs, obtained out of starch via hydrothermal treatment, at around 80 % (w/w). These excellent yields show the high efficiency of the here presented C-CND synthesis via MiW-hPC of starch.

##### 4.1.5 Structural Characterization of C-CNDs

The functional groups within C-CNDs were characterized using FTIR spectroscopy (see Fig. 4.9A). The broad peak at around  $3290\text{ cm}^{-1}$  can be attributed to OH stretching vibrations, indicating the presence of carboxyl- and hydroxyl groups [80, 149], which enable good water solubility and long-term stability. The broad absorption band present at  $2700\text{ cm}^{-1}$  (C-H stretching),  $1357\text{ cm}^{-1}$  (rock alkanes),  $1150\text{ cm}^{-1}$  (C-H wag) and  $860\text{ cm}^{-1}$  (C-H bend in alkenes) indicate C-H bonds [80, 149]. The peak at  $1597\text{ cm}^{-1}$  can be correlated with C=C double bonds in alkene [80, 149]. Further carboxyl groups are confirmed by the peaks at  $1076\text{ cm}^{-1}$  and  $1026\text{ cm}^{-1}$  (which can both be ascribed to C-O stretching), and the peak at  $936\text{ cm}^{-1}$ , which is ascribed to O-H bending in carboxylic acids [80, 149].

Elemental composition of C-CNDs was analyzed by energy-dispersive X-ray spectroscopy (see Fig. 4.9B). The as-synthesized C-CNDs consist mostly of C- and O-atoms (56.6 At.%; 40.9 At.%) with minor traces of nitrogen (1.27 At.%) and sodium chloride (Na 0.46 At.%; Cl 0.77 At.%). These traces may be caused by minor components associated with starch granules (e.g. proteins, enzymes, amino acids and nucleic acids) [11].

The structural composition of C-CNDs was characterized using XRD and Raman measurements (see Fig. 4.9C and Fig. 4.9D) of the freeze-dried powder. The broad XRD pattern centered at  $16^\circ$  reveals that the as-prepared C-CNDs consist mainly of amorphous carbon (up to 99.9 %) without any aromatic  $\pi$ -systems present. This is further proven by Raman spectroscopy, showing the two major peaks for (amorphous) carbon materials at  $1580\text{ cm}^{-1}$  and  $1360\text{ cm}^{-1}$ , while simultaneously missing the typical spectral features of graphite and related  $\text{sp}^2$  carbon materials at  $2700\text{ cm}^{-1}$  (D' band) and  $3248\text{ cm}^{-1}$  (G' band) [29, 54, 176]. The presence of both the D band at  $1580\text{ cm}^{-1}$  and the G band at  $1360\text{ cm}^{-1}$  are due to the  $\text{sp}^2$  sites, but peak positions and intensities can vary for various reasons (e.g. bond disorder, clustering of the  $\text{sp}^2$  phase and  $\text{sp}^2/\text{sp}^3$  ratio) [54]. The G band rises from bond stretching of all pairs of  $\text{sp}^2$  carbons in aromatic and olefinic molecules, and

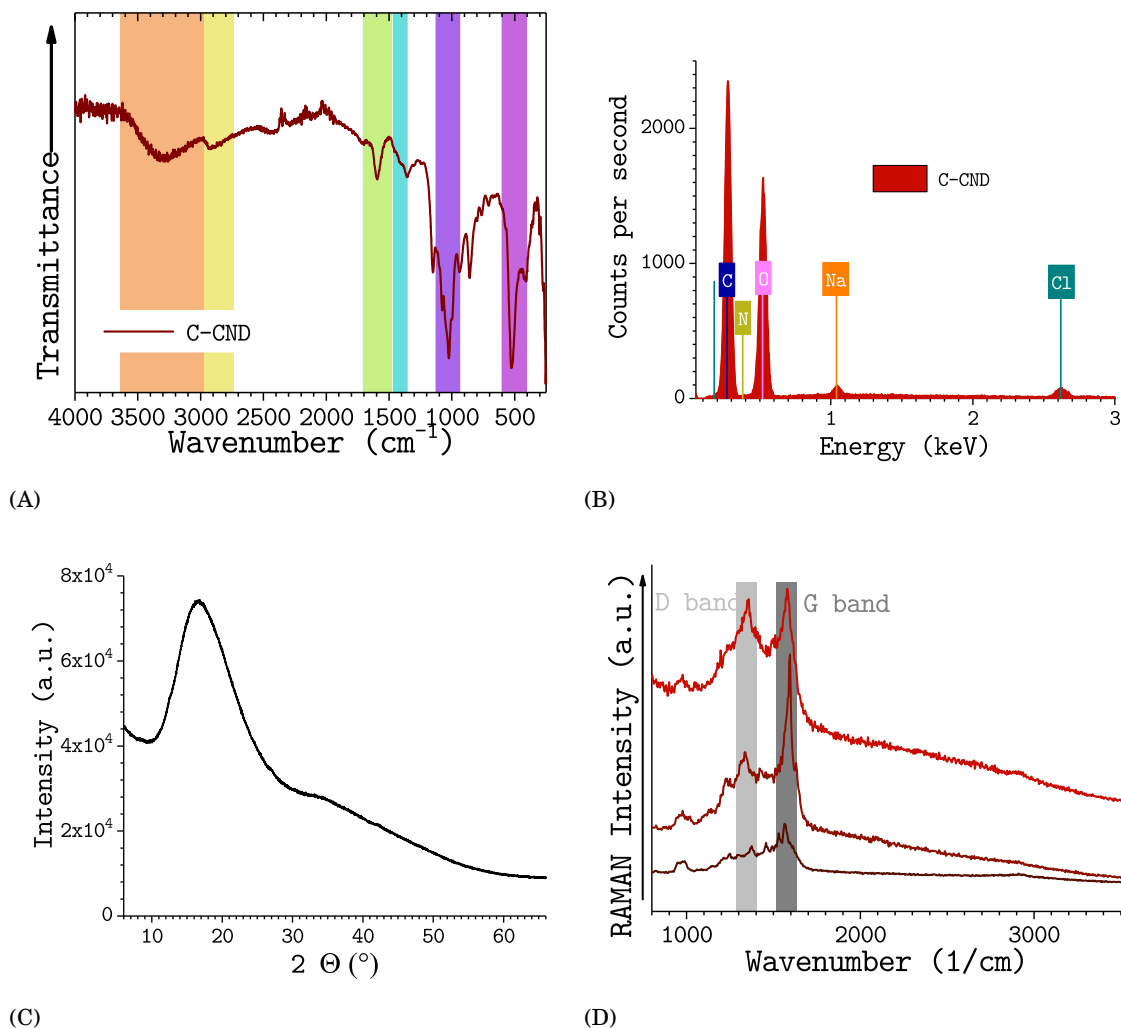


Figure 4.9: Structural characterization of C-CNDs: typical (A) FTIR spectra; (B) EDX spectra; (C) XRD pattern; and (D) Raman spectra of C-CNDs prepared by MiW-hPC of starch.

does not require the presence of benzene-like structures. The origin of the D band is often related to bond-angle disorder in the  $\text{sp}^2$  graphite like microdomains induced by binding with  $\text{sp}^3$  atoms. This mode is forbidden in perfect graphite and only becomes active in the presence of disorder [54].

NMR spectroscopy (see Chap. B.3, p. 144) was employed for further structural elucidation by means of separation of  $\text{sp}^2$ - and  $\text{sp}^3$ - hybridized carbon atoms. The  $^1\text{H}$ -NMR spectrum (see Fig. B.17, p. 144) gives rise to various signals: (a) strong signals in the range of 2 ppm to 4 ppm, stemming from  $\text{sp}^2$  carbon atoms (i.e. aliphatic compounds), (b) weak peaks in the range of 4 ppm to 6 ppm, attributed to carbonyls (e.g. carboxylates and amides), (c) weak signals in the range of 6 ppm to 7 ppm, attributed to unsaturated  $\text{sp}^2$  carbon atoms, and (d) weak signals in the range of 8 ppm to 10 ppm, originating from aromatic ring hydrogen. The  $^{13}\text{C}$ -NMR (see Fig. B.18, p. 145)

#### 4.1. SYNTHESIS AND CHARACTERISATION OF STARCH DERIVED CARBON NANODOTS

is dominated by very strong signals at around 39 ppm and medium signals at 55 ppm to 100 ppm, suggesting the presence of  $sp^3$  hybridized carbon atoms in aliphatic- and carbonyl compounds [150, 212]. In conflict with the  $^1H$ -NMR, no signals beyond 100 ppm, which are indicative for  $sp^2$  hybridized carbon atoms, carboxyl- and amide groups [150] are observed. Hence the structural characterization of C-CNDs by means of NMR spectroscopy remains inconclusive.

TEM images (see Fig. 4.10A), in accordance with the XRD- and Raman data, gave no indication

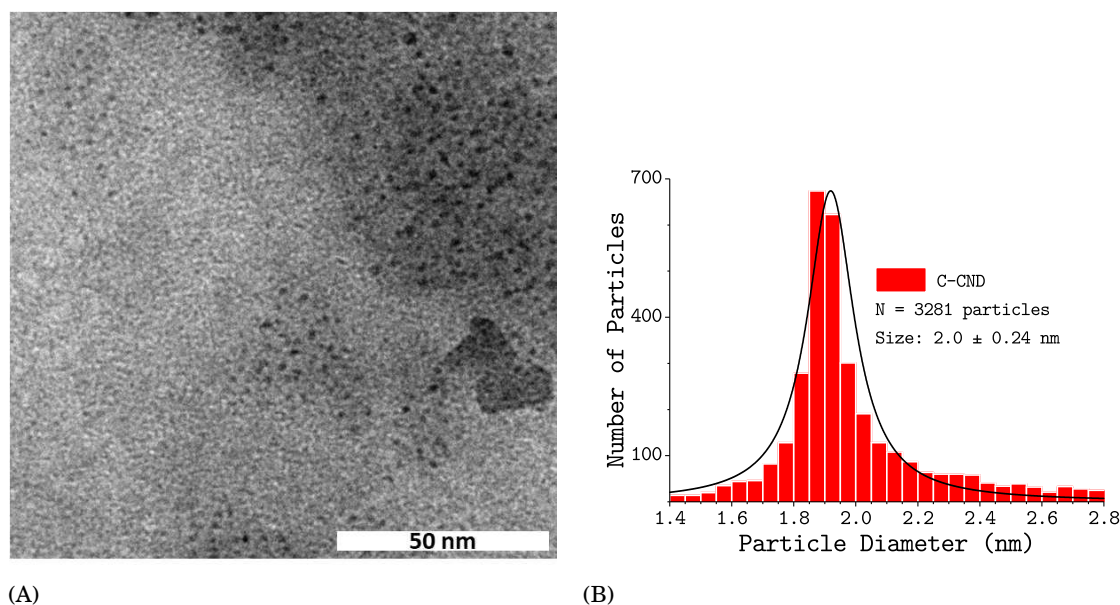


Figure 4.10: (A) Transmission electron microscopy (TEM) images of C-CNDs and (B) the corresponding particle size distributions and Lorentzian curves obtained from the fitted data. Obtained from multiple Images the average particles sizes are reported at the 99 % confidence interval. Total number of evaluated particles and the resulting average particle size are given in the inset.

of crystalline particles. Nevertheless, the particle size of as-synthesized C-CNDs was determined to be comparatively small ( $2.00 \pm 0.24$  nm); with a narrow size distribution (see Fig. 4.10B).

For TGA analysis and further characterisation see Chap. 4.3.8, p. 105.

#### 4.1.6 Summary

A new reliable, one-step C-CND synthesis based on hydrothermal treatment of starch, with a low environmental footprint, a high yield of approximately 80 % (w/w) and at reasonable costs is presented. The as-prepared C-CNDs are highly homogeneous in their photoluminescence properties and size distribution, and are ready to use without need for further purification, modification or surface passivation agents (e.g. PEG). Furthermore, PL measurements demonstrated that the PLQY was below 1 % and that the photophysical properties of C-CNDs are independent of reaction time. The same measurements executed for various starch concentrations led to similar results, but different reaction rates. In other words, higher starch concentrations lead to higher

reaction rates. Hence, the carbonization of starch by hydrothermal treatment is probably an autocatalysis process. This autocatalysis is most likely based on the formation of carboxylic acids (during starch hydrolysis), which increase the hydrolysis rate significantly. Above results demonstrate that the formation of C-CNDs is independent of the starch concentration, but most efficient at high starch concentrations due to stronger autocatalysis process, enabling larger amounts of C-CNDs to be synthesized in shorter time. Noticeably, the optical properties stayed unaffected for different starch types, even when modified starch was used. Independently of seasonal changes and origin starch provides C-CNDs with highly reproducible PL properties. Hence, nearly any commercial starch currently available on the market can be used to produce C-CNDs by means of MiW-hPC. Additionally, in comparison to other methods used to prepare C-CNDs, the hydrothermal starch decomposition leads to barely any impurities or by-products, and thus starch can be considered as superior over other carbon sources. The C-CNDs are comparatively small (C-CND:  $2.00 \pm 0.24$  nm); with narrow size distributions; are stable over a long period of time, either in solution or as freeze dried powder and maintain their photoluminescence properties when re-dispersed in solution.

Although not suited as fluorescence marker (due to the low PLQY) C-CNDs can have a great impact on various other nanoparticle applications, e.g. photocatalysts [20, 59], Ag-NP CND composites [19, 20, 145], waste water treatment [142] and printing [171].

## 4.2 Synthesis and Characterisation of Starch Derived, Nitrogen-Doped Carbon Nanodots

The only, but major drawback limiting the application of C-CNDs in life sciences is their low PLQYs, since brighter CNDs improve the contrast against tissue background (e.g. in vivo), promising better opportunities for bioimaging [13].

Three approaches are usually employed to improve the PLQY of CNDs, surface passivation and -modification (e.g. oxidation, reduction), and element doping [89, 182, 188]. Often these applied modification processes prove to be time-consuming, harsh and/or impractical on a large scale [17, 73, 113, 156, 157, 183, 187]. Furthermore, modifications often lead to increased particle sizes of the modified CNDs, restricting their further application [156, 161]. Nevertheless, nitrogen-doped carbon nanodots (N-CNDs) have emerged to be complementary to C-CNDs due to their high PLQYs [101, 108, 146, 183, 212], making them promising luminescent materials for various applications.

Herein, the effects of TAE buffer (i.e. EDTA: ethylenediaminetetraacetic acid; Tris: tris(hydroxymethyl)aminomethane) and urea (as nitrogen additives), on the photophysical properties of starch derived nitrogen-doped CNDs (C/N-CNDs) are reported. The presented synthesis method is based on MiW-hPC, without the need of sophisticated post synthesis treatment and/or additional surface passivation.

Urea and TAE buffer were chosen for a number of reasons: both are highly water soluble, can be obtained worldwide with high purity and well-defined composition, and are cost effective. Furthermore, urea already has been successfully used in nitrogen-doped carbon dot synthesis [68, 134].

### 4.2.1 Influence of Various Nitrogen Additives on C/N-CND Synthesis

In order to gain initial insight into the suitability of selected N-additives for C/N-CND synthesis, various amounts of starch (0.14 mg/mL, 0.28 mg/mL and 1.0 mg/mL) and N-additives (urea: 0.75 mg/mL, 0.0125 mmol/mL; and TAE10X) were dissolved in water and subsequently heated to 200 °C for 5 to 45 minutes in the MiWR. Throughout the ongoing reaction the initially transparent colorless liquid samples turned into a yellow clear solution, and became deep orange to brown as the reaction progressed. After the reaction finished blue emission could be observed for all samples when exposed to UV-light ( $\lambda_{Exc} = 312$  nm). While blue PL emission could be observed in all cases, the PL, the PL emission maximum and the overall quantum yield varies considerably depending on N-additive and starch combination (see Fig. 4.11).

The PL and normalized PL emission spectra for urea derived C/N-CNDs, collected with excitation at 340 nm, are shown in Figure 4.11A and Figure 4.11B, respectively. After 5 minutes reaction time a clear emission band at around 431 nm, with a FWHM of around 71.4 nm and a PLQY of 2% can be observed. With advancing reaction time the PLQY stays constant, but the overall

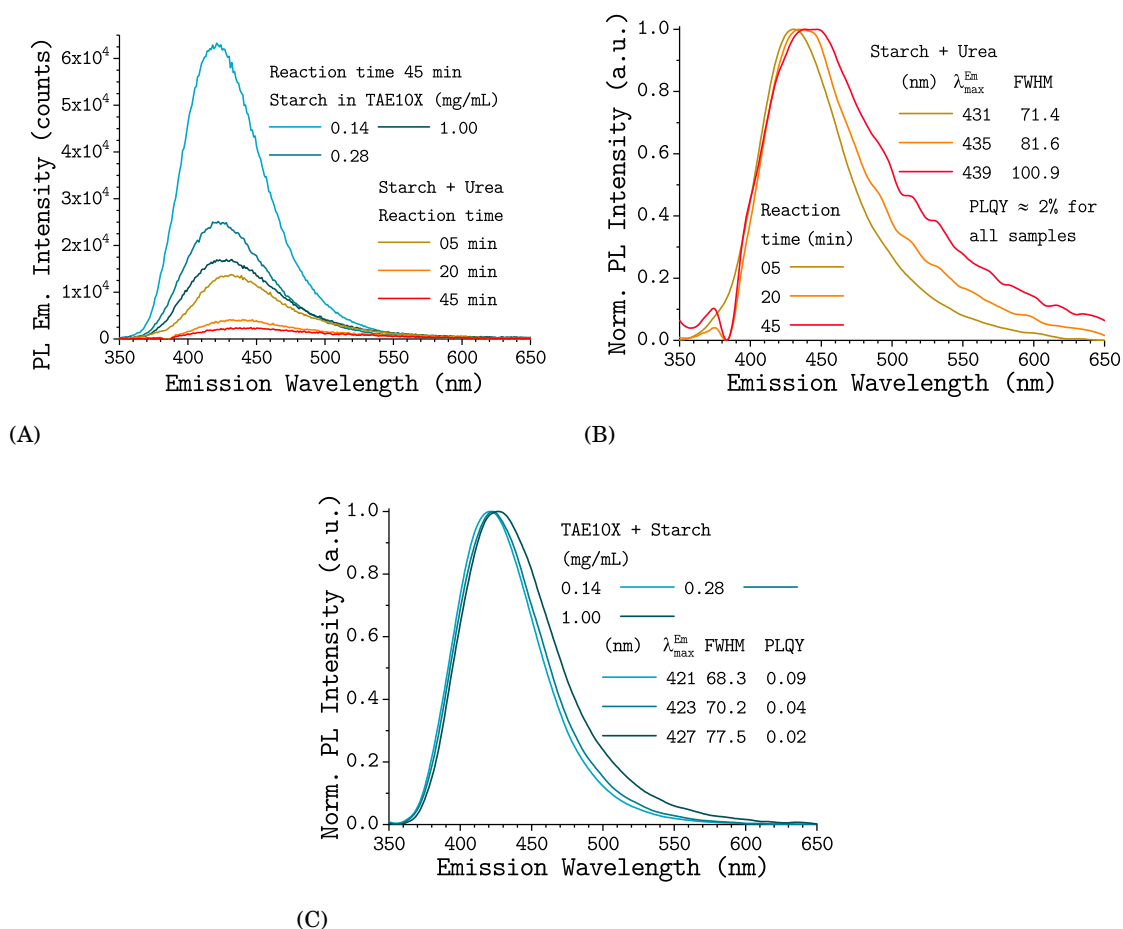


Figure 4.11: Effect of different N-additives (urea and TEA10X buffer solution) and starch combinations on the optical properties of C/N-CNDs (prepared at 200 °C using a reaction time of 5 to 45 minutes): (A) PL emission spectra (under excitation at 340 nm (OD 0.1)); and (B,C) the corresponding normalized PL emission spectra for urea and TEA10X derived C/N-CNDs, respectively.

PL intensity decreases (see Fig. 4.11A) and a slight emission red-shift to 439 nm, along with an increase in FWHM to 101 nm, can be observed. This behaviour, very similar to C-CNDs (see Chap. 4.1.1, p. 60), indicates that the formation of urea derived C/N-CNDs is finished after 5 minutes and the observed decreasing PL intensities and subsequent red-shift result either from the destruction of stabilizing surface groups and/or C/N-CND aggregation e.g. due to stacking. In summary, urea has to be considered unsuitable as N-additive for starch derived C/N-CNDs. While not affecting the PL emission properties (compared to C-CNDs, see Fig. 4.2, p. 61) and increasing the reaction rate significantly (due to its alkaline properties), the obtained increase in PLQY was insignificant.

Substantially better results were achieved with starch dispersed in aqueous TAE10X buffer



solution (see Fig. 4.11A and Fig. 4.11C). With increasing initial starch concentration (0.14 mg/mL, 0.28 mg/mL and 1.0 mg/mL) a slight emission red-shift from 421 nm to 427 nm, along with a slight increase in FWHM from around 68 nm to 78 nm, can be observed (see Fig. 4.11A and Fig. 4.11C). Furthermore, the overall PL intensity decreases in accordance with the PLQY, descending from around 9% to 2%. This clear dependence of N-additives on the PL properties (PL emission bandwidth and PLQY) of C/N-CNDs are in accordance with the theory and previous findings (see

#### 4.2.2 Influence of Reaction Time on C/N-CND Synthesis

As shown earlier, the reaction time can have a significant impact on the obtained PL properties of CNDs (see Chap. 4.1.1, p. 60). Hence, in order to gain deeper insight into formation of C/N-CNDs, TAE10X buffer solutions with a fixed starch concentration (undefined starch: 0.14 mg/mL) were heated to 200 °C for 45 to 120 minutes in the MiWR. As stated before, the initially transparent colorless liquid sample turned into a deep orange to brown clear solution as the reaction progressed. After 45 minutes blue emission could be observed for all samples when exposed to UV-light ( $\lambda_{\text{Exc}} = 312 \text{ nm}$ ). The influence of reaction time on the C/N-CND formation is illustrated in Figure 4.12.

As presented in Figure 4.12A, the UV-Vis absorption spectra exhibit three strong separate absorption bands: the first peak at around 231 nm (Peak 1) is assigned to  $n\text{-}\sigma^*$  transitions in C-N- (e.g. amides) and/or C-O bonds (e.g. alcohols), respectively. The second peak at around 250 nm (Peak 4) is assigned to  $n\text{-}\sigma^*$  transitions in amines, located either on the C/N-CND surface or within the C/N-CND core. The band with the peak at around 300 nm to 400 nm (Peak 3) can presumably be attributed to  $n\text{-}\pi^*$  transitions within the C=O bonds. Noticeably, the typical peak at around 250 nm to 300 nm (see Fig. 4.2A, p. 61) deriving from  $n\text{-}\pi^*$  transitions in conjugated carbonyl compounds, couldn't be observed any more (see Table B.3, p. 129). This is either due to high C-N signal intensities or missing  $sp^2$  domains in C/N-CNDs. The intensities of Peak 1 to Peak 3 increase with proceeding reaction time due to increasing C/N-CND concentration, reaching their maximum after 120 minutes (see Fig. 4.12A).

The corresponding PL and normalized PL emission spectra collected with excitation at 340 nm are shown in Figure 4.2B and Figure 4.2C, respectively. After 45 minutes reaction time a strong emission band can be observed, but with proceeding reaction time (45 to 120 minutes) the overall PL intensity decreases in accordance with the PLQY (descending from around 11% to 6%), and a slight emission red-shift from 419 nm to 427 nm, along with a slight increase in FWHM from 69 nm to 77 nm, can be observed.

The formation of TAE buffer derived C/N-CNDs is supposedly finished after 45 minutes. Hence, subsequent changes in the absorption- and PL emission spectra result from further changes in the molecular structure or assembly of C/N-CNDs; e.g. destruction of stabilizing surface groups and/or C/N-CND aggregation. In other words, while the C/N-CNDs carbon core (where absorption presumably takes place) stays intact and grows, the emissive surface states are quenched.

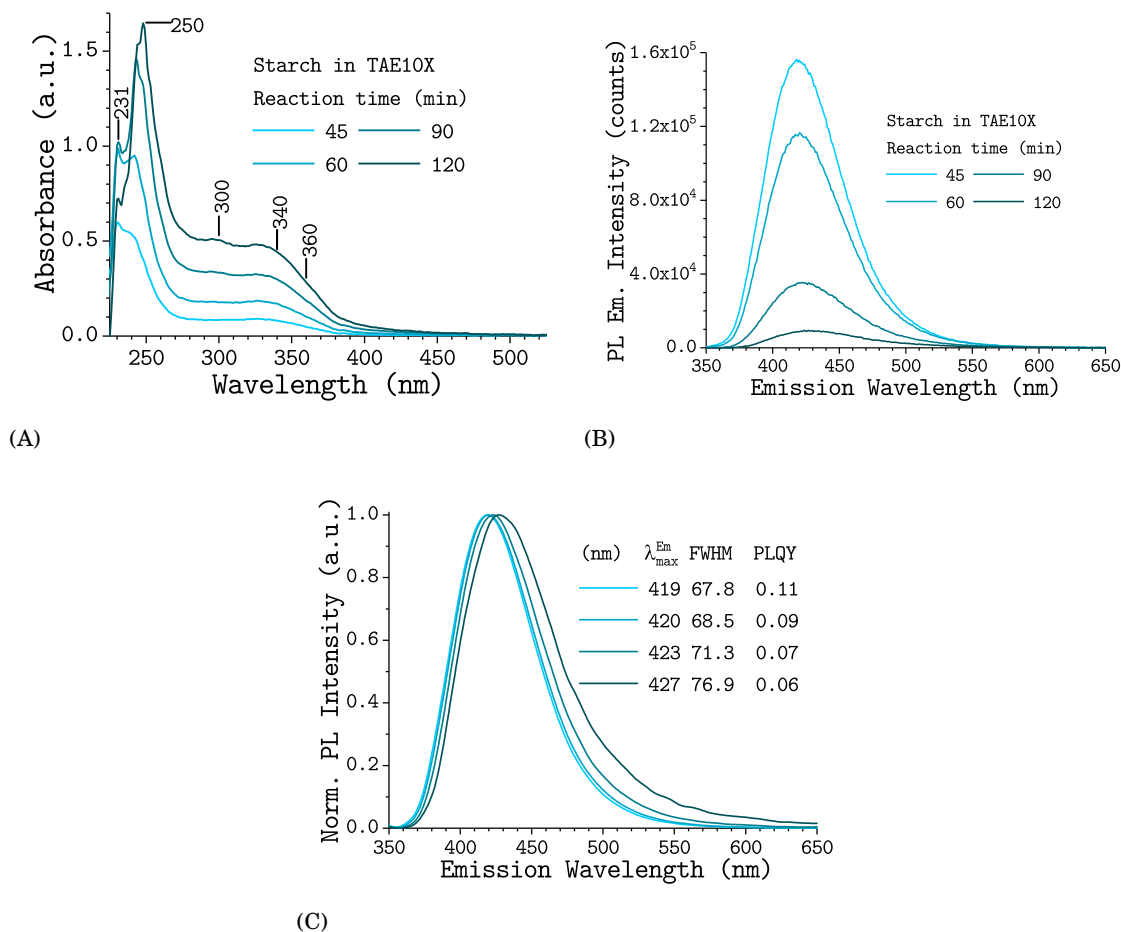


Figure 4.12: Effect of reaction time on the optical properties of C/N-CNDs derived from aqueous TAE10X buffer-starch dispersion (0.14 mg/mL): (A) UV-Vis absorption spectra; (B) PL emission spectra for different reaction times under excitation at 340 nm (OD 0.1); and (C) their corresponding normalized PL emission spectra.

### 4.2.3 Influence of Reaction Temperature on C/N-CND Synthesis

A potential way for PLQY enhancement in nitrogen doped CNDs are increased reaction temperatures, as it was shown that higher reaction temperatures can lead to improved nitrogen incorporation into carbon structures [51, 146]. The influence of reaction temperature on the PL properties of C/N-CNDs is presented in Figure 4.13. The spectra shown were taken for three C/N-CND samples obtained from three synthesis attempts, for each reaction temperature, using C/N-CND precursor solutions with a fixed starch concentration (undefined starch: 0.14 mg/mL) in aqueous TAE10X buffer.

As presented in Figure 4.13A, the UV-Vis absorption spectra exhibit the same strong absorption bands already reported for C/N-CNDs (see Chap. 4.2.2, p. 77): the first two peaks at around 231 nm (Peak 1) and at around 250 nm (Peak 4), and the third peak at around 300 nm to 400 nm

## 4.2. SYNTHESIS AND CHARACTERISATION OF STARCH DERIVED, NITROGEN-DOPED CARBON NANODOTS

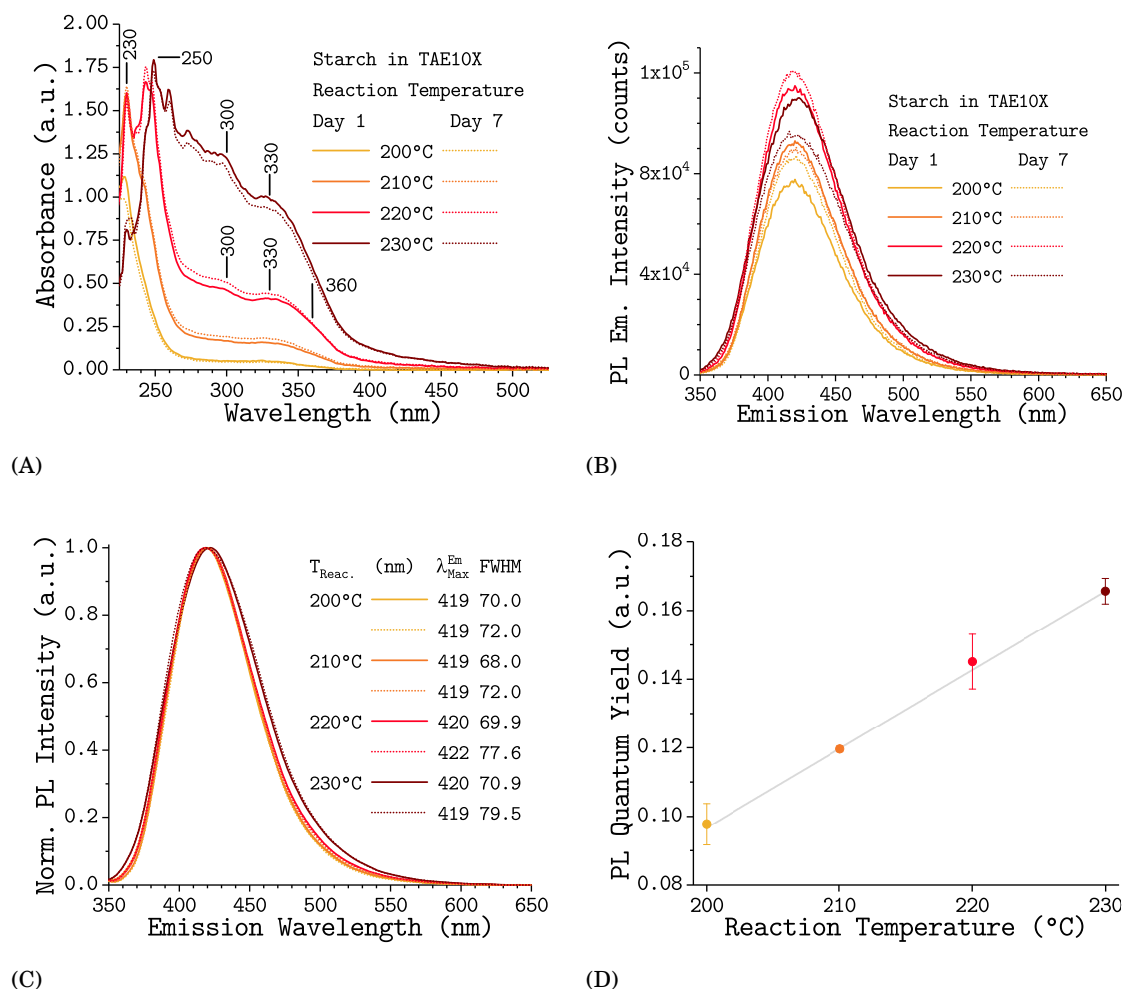


Figure 4.13: Effect of reaction temperature and ageing on the optical properties of C/N-CNDs derived from aqueous TAE10X buffer-starch dispersion (0.14 mg/mL): (A) UV-Vis absorption spectra; (B) PL emission spectra for different reaction times under excitation at 340 nm (OD 0.1); (C) their corresponding normalized PL emission spectra; and (D) PLQY at 340 nm as a function of reaction temperature.

(Peak 3). With increasing reaction temperature the general shape of the spectra remains similar, while the total absorption increases drastically.

The corresponding PL and normalized PL emission spectra collected with excitation at 340 nm (see Fig. 4.13B and Fig. 4.13C) show that the emission band, despite different reaction temperatures, is always positioned at around  $(419 \pm 1)$  nm when excited at 340 nm. Furthermore, only a slight increase in FWHM, from around 70 nm at 200 °C to 80 nm at 230 °C was noticed. This result supports the notion that for CNDs the nature of the surface states determines the emission wavelength (see Chap. 2.3.3, p. 31). In addition, the strong linearity between PLQY and synthesis temperature (see Fig. 4.13D) suggests that a further increase in PLQYs could potentially be achieved with much higher reaction temperatures [155]. This can be explained by the formation

of favourable N-doping architecture [51] and/or higher surface to volume ratios without a clear correlation between nitrogen content of the precursors and the resulting N-doped CNDs [51]. Regarding stability over time, as-synthesized C/N-CNDs proved to be highly stable after an initial consolidation period of around seven days (see Fig. 4.13A). During this period a slight increase in FWHM of C/N-CNDs emission band was observed for all samples (independent of reaction temperature), while the remaining PL properties (e.g. absorption, PL emission bandwidth and PLQY) stayed unaffected. Additionally, some precipitation was observed. Nevertheless, after this consolidation period no further precipitation or changes in PL properties were observed.

#### 4.2.4 Influence of Precursor Concentration and -Composition on C/N-CND Synthesis

Another potential way for PLQY enhancement in nitrogen doped CNDs is to increase the nitrogen content by means of increased N-additive concentration in the precursor solution. The impact of various precursor solutions was investigated by a combination of varying starch concentrations (0.00 mg/mL, 0.14 mg/mL, 1.0 mg/mL and 5.0 mg/mL) dispersed in various aqueous TAE buffer solutions (TAE100X, TAE50X, TAE10X, TAE05X and TAE01X). All precursor solutions were subsequently heated to 230 °C for 45 minutes in the MiWR.

As presented in Figure 4.14A, the UV-Vis absorption spectra also exhibit the same strong absorption bands already reported for C/N-CNDs (see Chap. 4.2.2, p. 77 and Table B.3, p. 129): the first two peaks at around 230 nm (Peak 1) and at around 250 nm (Peak 4), and the third peak at around 300 nm to 400 nm (Peak 3). The strong increase in Peak 1 is ascribed to increased nitrogen doping (C-N bonds), due to increased N-additive concentrations. Noticeably, the typical peak at around 270 nm to 280 nm (see Fig. 4.2A, p. 61) deriving from  $n-\pi^*$  transitions in conjugated carbonyl compounds, can only be observed for C/N-CNDs derived from precursor solutions with both high C-source- and N-additive concentrations (e.g. starch 1.0 mg/mL and TAE100X). Independent of precursor solution the general shape of the absorption spectra remains similar, while the total absorption increases with increasing starting material concentrations. Regarding the initial concentrations two different trends can be observed: (1) the absorption increases only slightly with increasing starch concentration and (2) the absorption increases drastically with increasing TAE buffer concentration (see Fig. 4.14A).

The corresponding normalized PL emission spectra collected with excitation at 340 nm (see Fig. 4.13B) and 360 nm (see Fig. 4.13C) show excitation wavelength dependent behaviour. Nevertheless, the emission bands are still independent of precursor solution, and positioned at around  $(420 \pm 2)$  nm and around  $(426 \pm 3)$  nm for excitation at 340 nm and 360 nm, respectively. In line with this, the FWHM is also constant:  $(76 \pm 2)$  nm and  $(75 \pm 2)$  nm for excitation at 340 nm and 360 nm, respectively.

Regarding the PLQY, four tendencies are emerging: (1) the PLQY increases with increasing initial N-additive concentration; (2) N-additive concentrations higher than TAE50X have no

## 4.2. SYNTHESIS AND CHARACTERISATION OF STARCH DERIVED, NITROGEN-DOPED CARBON NANODOTS

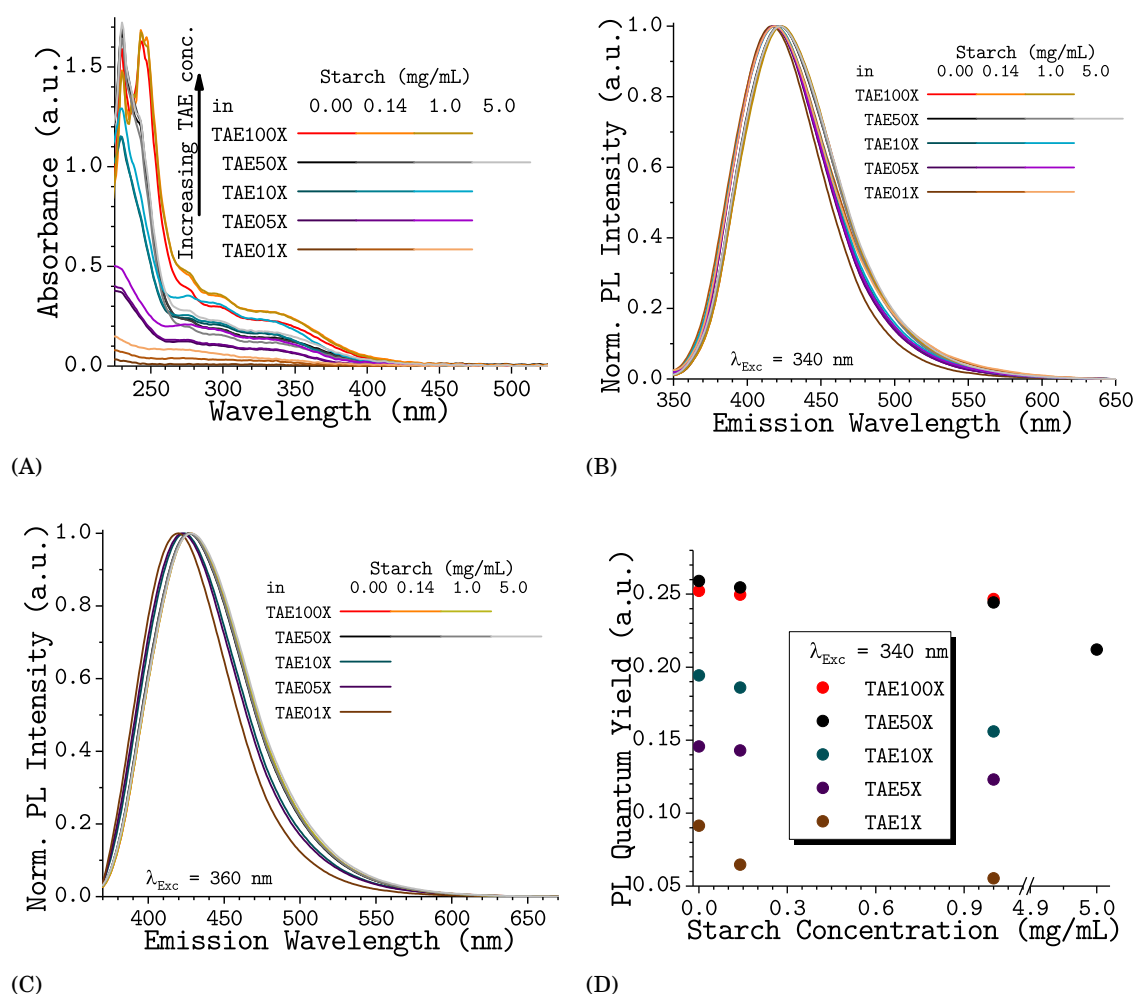


Figure 4.14: Effect of precursor solutions with varying C-source to N-additive ratio on the optical properties of C/N-CNDs derived from various aqueous TAE buffer-starch dispersions: (A) UV-Vis absorption spectra; (B) normalized PL emission under excitation at 340 nm (OD 0.1); (C) their corresponding normalized PL emission spectra under excitation at 360 nm (OD 0.1); and (D) PLQY at 340 nm as a function of initial starch concentration (C-source) in various TAE buffer solutions (N-additive).

further impact (e.g. TAE100X) on the PLQY; (3) the PLQY decreases with increasing initial starch concentration; and (4) the PLQY of as-synthesized C/N-CNDs is excitation wavelength dependent. On average, and independent of precursor solution, PLQYs with excitation at 360 nm are about three percentage points higher than PLQYs with excitation at 340 nm (see Fig. B.3, p. 131). Furthermore, pure TAE derived C/N-CNDs (starch: 0.00 mg/mL) show the highest PLQYs (approx. 26%) for all nitrogen-doped CNDs presented so far.

This result further underlines the notion that for CNDs the nature of the surface states determines the emission wavelength but not necessarily the efficiency of radiative recombination (see

Chap. 2.3.3, p. 31).

#### 4.2.4.1 Glucose as Starting Material

As established earlier (see Chap. 4.1.2.1, p. 65) CND formation is fundamentally different with starch and glucose. Therefore, further insight into the relation between initial C-source and N-additive concentration (i.e. precursor solution) on the C/N-CNDs photoluminescence properties can be gained through replacing starch by  $\alpha$ -D-glucose (as carbon source). For this

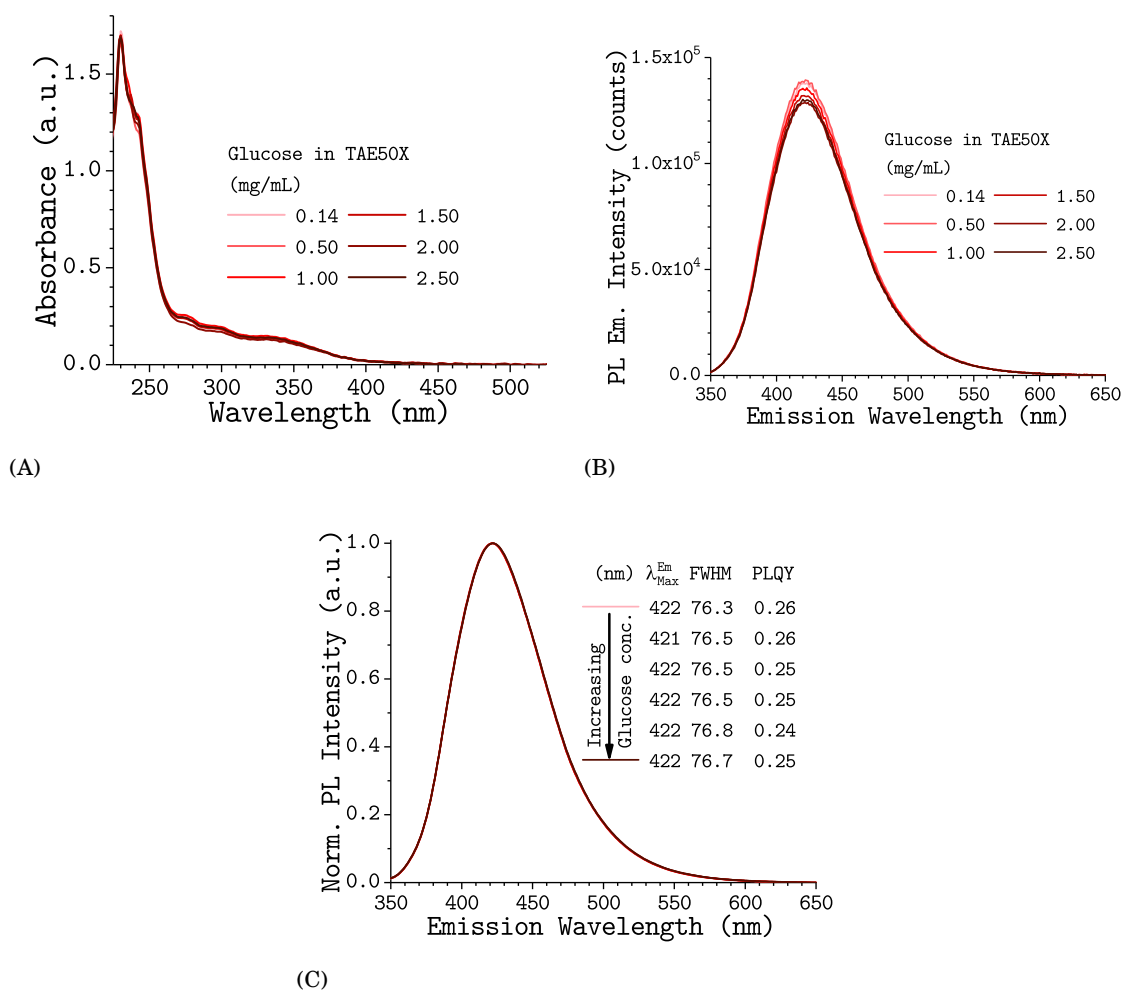


Figure 4.15: Optical properties of N-CNDs derived from individual aqueous TAE50X buffer solutions with various  $\alpha$ -D-glucose concentrations: (A) UV-Vis absorption spectra; (B) PL emission spectra under excitation at 340 nm (OD 0.1); and (C) their corresponding normalized PL emission spectra, for six different initial glucose concentrations (0.14 mg/mL, 0.5 mg/mL, 1.0 mg/mL, 1.5 mg/mL, 2.0 mg/mL and 2.5 mg/mL).

measurement series various amounts of glucose were dispersed in aqueous TAE50X buffer (0.14 mg/mL, 0.5 mg/mL, 1.0 mg/mL, 1.5 mg/mL, 2.0 mg/mL and 2.5 mg/mL) and subsequently heated to 230 °C for 45 minutes in the MiWR. In line with the foregoing, the initially transparent

colorless liquid sample (depending on glucose concentration) turned into a yellowish-orange to brown clear solution after 45 minutes; and blue emission was observed for all samples when exposed to UV-light ( $\lambda_{Exc} = 312$  nm).

As presented in Figure 4.15A, the UV-Vis absorption spectra for glucose derived N-CNDs are not distinguishable from starch derived C/N-CNDs (see Fig. 4.14A, p. 81 and Table B.3, p. 129): the first two peaks at around 230 nm (Peak 1) and at around 250 nm (Peak 4), and a third broad absorption band at around 300 nm to 400 nm (Peak 3). But in contrast to starch, an increased initial glucose concentration has virtually no effect on the absorption intensity.

This is also true for the PL emission properties of glucose derived N-CNDs, as can be seen in Figure 4.15B and Figure 4.15C. The observed PL emission bands are positioned at around  $(421.8 \pm 0.4)$  nm, with a FWHM of  $(76.5 \pm 0.2)$  nm and an PLQY of  $(25.2 \pm 0.7)$  % for excitation at 340 nm. The presented low standard deviations show that the observed variations in PL emission bands of glucose derived N-CNDs are negligible, i.e. are independent of starting concentration and/or date. Furthermore, glucose derived N-CNDs proved to be highly reproducible, contrary to glucose derived CNDs (see Chap. 4.1.2.1, p. 65). Nevertheless, like their undoped derivative, glucose derived N-CNDs are unstable over time and are subject to ageing, which manifests itself in a fluffy precipitate. Surprisingly, the precipitation is not reflected in the optical properties (e.g. absorption, PL emission and PLQY), which stay unaffected by the ageing process.

These results show again, that CND formation is fundamentally different between starch and glucose and that results in CND synthesis are hard to predict.

#### 4.2.5 Freeze Drying of C/N-CND Solutions

In order to assess the long time stability of C/N-CNDs as a solid powder, 260 mL of an C/N-CND solution were synthesized from a starch (0.14 mg/mL) TAE10X buffer solution via MiW-hPC for 45 minutes at 230 °C (see Fig. B.4, p. 132). Obtained aqueous C/N-CND solution was subsequently freeze-dried and characterised via PL steady-state and PLQY measurements. After freeze-drying for three days the former dark brown solution turned into a white to slightly brown C/N-CND powder. The powder did not exhibit any PL under UV-light. PL properties recurred without any changes (see Fig. 4.16) upon dissolving the C/N-CND powder in water.

Observed differences in PL emission maximum and FWHM remain within the error tolerances established by earlier findings (see above). Hence, C/N-CNDs can, similar to C-CNDs, be easily stored and transported as freeze-dried powder, giving them a distinct advantage over today's quantum dots. It should be noted that C/N-CND powder, is more hygroscopic than C-CND powder. The previously white to slightly brown C/N-CND powder turns into a dark brown highly viscous compound when stored in air.

Nevertheless, freeze-drying enabled the determination of the overall yield of C/N-CNDs, obtained from starch and TAE buffer via hydrothermal treatment, to be around 80 % (w/w). These excellent yields show the high efficiency of the here presented C/N-CND synthesis via MiW-hPC of starch

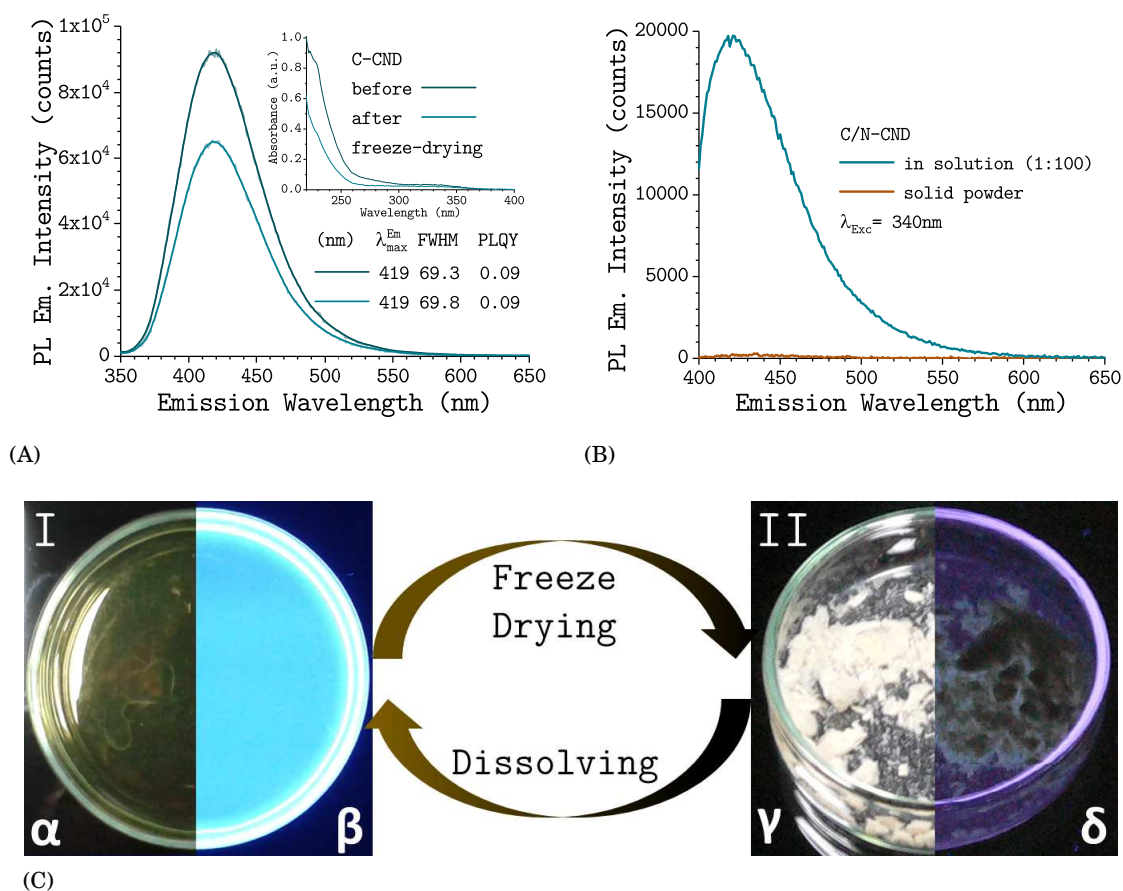


Figure 4.16: Effect of freeze-drying on the optical properties of C/N-CNDs: (A) PL emission spectra under excitation at 340 nm (OD 0.1) for C/N-CND solution (before) and re-dispersed C/N-CND powder (after), the inset is the absorption spectra. (B) PL emission spectra of C/N-CND as dried solid powder (brown) and the same sample (diluted 1:100) as aqueous solution (blue) in PBS (pH 7.0). (C) A comparison between C/N-CND emission in solution (I) and as dried powder (II) under white light ( $\alpha$ ;  $\gamma$ ) and under 312 nm UV-light ( $\beta$ ;  $\delta$ ), respectively.

and TAE buffer.

#### 4.2.6 Summary

A first step towards a one-step synthesis of nitrogen doped carbon nanodots was presented. The synthesis shown is based on microwave-assisted hydrothermal precursor carbonisation of a combination of starch and TAE buffer solutions, resulting in a high yield of approximately 80 % (w/w), matching the results from previous C-CND synthesis. The as-prepared C/N-CNDs are highly homogeneous in their photoluminescence properties and are ready to use without need for further purification, modification or surface passivation. Furthermore, PL measurements demonstrated that the photophysical properties of C/N-CNDs are independent of reaction time and that the



PLQY (of as-synthesized C/N-CNDs) can be considerably enhanced, to as high as 25 %, by means of increased reaction temperatures and enhanced nitrogen doping. This chapter also addressed the following issues and their influence on the C/N-CND formation: influence of (1) reaction time and -temperature, (2) precursor concentration, and (3) type of N-additives. Furthermore, the stability of C/N-CNDs over time, both in solution and as dry powder was investigated. Noticeably, the photophysical properties of starch derived C/N-CNDs stayed unaffected during conversion of C/N-CND solution into dry powder and back into solution. The obtained results further support the notion that for CNDs the nature of the surface states determines the emission wavelength. Regarding the nitrogen-additives used, urea proved to be unsuitable for nitrogen-doping of starch derived CNDs, whereas TAE buffer (i.e. EDTA: ethylenediaminetetraacetic acid; Tris: tris-(hydroxymethyl)-aminomethane) demonstrated rather more encouraging nitrogen-doping capabilities. The highest PLQYs for C/N-CNDs of 25 % (TAE50X + starch: 0.14 mg/mL) were obtained for a reaction temperature of 230 °C, which is lower than the recently reported PLQY for an alginate/tryptophan mixture (47.9 %) [219], but higher than the PLQY values previously reported for N-doped CNDs obtained from citric acid and urea (14 %) [134], EDTA (17.5 %) [146], and waste chicken eggshell and urea (7.8 %) [68]. The strong linearity between PLQY and synthesis temperature (see Fig. 4.13D, p. 79) suggests that even higher PLQYs could be achieved with much higher reaction temperatures [155]. This can be explained by the formation of favourable N-doping architecture [51] and/or higher surface to volume ratios without a clear correlation between nitrogen content of the precursors and the resulting N-CNDs [51].

C/N-CNDs share many advantages with C-CNDs, such as good solubility in water, high colloidal stability and high photostability either in solution or as dried white powder. However, nitrogen doping also leads to significant differences in the photophysical- and chemical properties. Compared to C-CNDs, C/N-CNDs have significantly higher PLQYs, blue-shifted PL emission spectra and an increased hygroscopicity.

Like their analogues, C/N-CNDs may be interesting for a wide range of applications and further comparative studies are needed, shedding light on the nature of CND emission properties (e.g. influence of chemical structure and elemental composition). Although well suited as fluorescence markers, PLQYs of C/N-CNDs are still comparably low and need to be improved (see Table C.1, p. 150). Furthermore, there is evidence, that MiW-hPC of pure TAE buffer solutions (see Fig. 4.13, p. 79) may lead to equivalent or even better results.

### 4.3 Synthesis and Characterisation of Carboxylic Acid Derived, Nitrogen-Doped Carbon Nanodots

Encouraged by previous findings (see Chap. 4.2.4, p. 80), the suitability of TAE buffer as starting material for nitrogen-doped carbon nanodots is tested. Special attention is paid towards the following issues regarding their influence on CA/N-CND formation and photophysical properties: (1) reaction time, (2) reaction temperature, (3) precursor concentration, (4) precursor composition and (5) type of carbon source (i.e. carboxylic acid). This work also addresses the issues of excitation wavelength and pH dependence of the photophysical properties (e.g. PL emission and -excitation spectra as well as PLQY) of CA/N-CNDs.

To the best of one's knowledge, the combined use of EDTA and Tris as N-additives in CND synthesis has not been reported to date. The physical properties (e.g. molar mass, structure) of the N-additives and C-sources used in this work, can be found in the Appendix (see Table B.2, p. 128 and Table B.1, p. 127).

In order to gain initial insight into the formation of nitrogen-doped carbon nanodots (N-CNDs) comparable concentrations (EDTA: 0.01 M, 2.9 mg/mL; Tris: 0.2 M, 48.25 mg/mL; and starch 48.25 mg/mL) of various combinations of N-additives were dissolved in water (EDTA; Tris; EDTA + Tris; EDTA + starch; and Tris + starch) and subsequently heated to 230 °C for 45 minutes in the MiWR. While blue PL emission could be observed for all samples when exposed to UV-light ( $\lambda_{\text{Exc}} = 312 \text{ nm}$ ), the PL emission properties and the overall PLQY varies considerably depending on N-additive combination (see Fig. 4.17). The results shown in Figure 4.17A were taken for independent N-CND samples, obtained from three to five synthesis attempts per N-additive combination.

As presented in Figure 4.17A, the UV-Vis absorption spectra of as-synthesized N-CNDs are comparable to earlier findings (see Fig. 4.13A, p. 79 and Table B.3, p. 129), but still distinctive: the first peak at around 230 nm (Peak 1) is assigned to  $n-\pi^*$  transitions in C-N- and/or C-O bonds, located either on the N-CND surface or within the N-CND core. Noticeably, the typical second peak at around 250 nm (Peak 4) assigned to  $n-\sigma^*$  transitions in C-N bonds (amines), couldn't be observed for any N-CND type. In accordance with previous results the band at around 300 nm to 400 nm (Peak 3), attributed to  $n-\pi^*$  transitions within the C=O bonds, is presented in all samples, but strongest in N-CNDs obtained from starch (as main carbon- and oxygen-source). Apparently, Peak 2 at around 250 nm to 280 nm (see Fig. 4.2A, p. 61) deriving from  $n-\pi^*$  transitions within conjugated carbonyl compounds, could only be observed for N-CNDs obtained from a combination of EDTA and starch.

Compared to pure N-additive derived samples (e.g. EDTA, Tris and EDTA + Tris), the addition of starch leads to a strong red-shift in the PL emission (see Fig. 4.17B and Fig. 4.17C), but has nearly any effect on the overall PLQY (see Fig. 4.17D). While low PLQYs were observed for the EDTA derived samples, much higher PLQYs were obtained for samples derived from Tris. The

### 4.3. SYNTHESIS AND CHARACTERISATION OF CARBOXYLIC ACID DERIVED, NITROGEN-DOPED CARBON NANODOTS

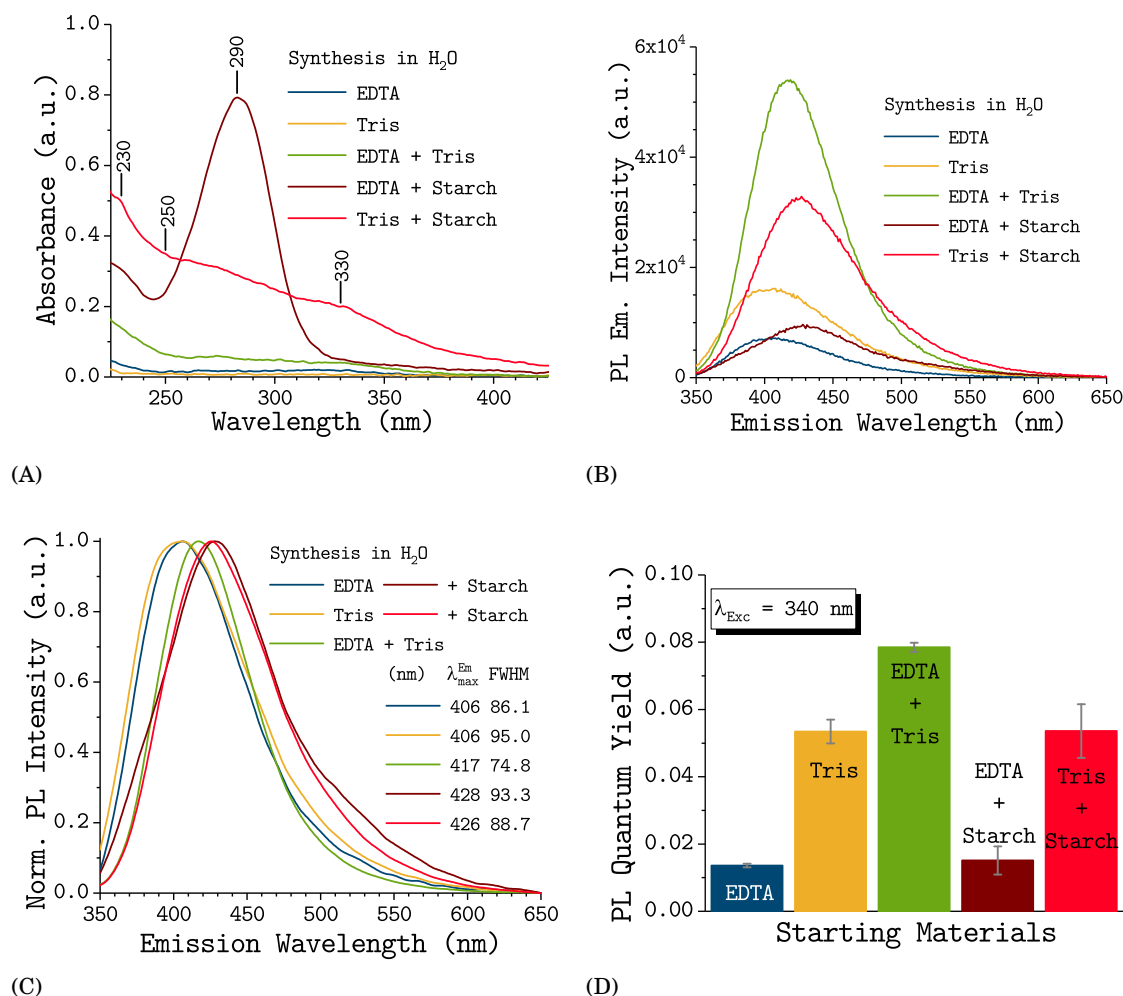


Figure 4.17: Influence of nitrogen-additive on the optical properties of N-CNDs derived from aqueous solutions of various N-additive combinations: (A) UV-Vis absorption spectra; and (B) PL emission spectra under excitation at 340 nm (OD 0.1); (C) their corresponding normalized PL emission spectra; and (D) PLQY at 340 nm for five different N-additive combinations (EDTA; Tris; EDTA + Tris; EDTA + starch; and Tris + starch) of comparable concentrations (EDTA: 0.01 M, 2.9 mg/mL; Tris: 0.2 M, 48.25 mg/mL; and starch 48.25 mg/mL).

highest PLQYs were observed for the combination of Tris and EDTA.

Based on the above mentioned results, the reason for PL enhancement in N-CNDs (compared to C-CNDs) cannot solely be attributed to nitrogen groups on the N-CNDs surface. Both EDTA and Tris have nitrogen groups (see Table B.1, p. 127), and therefore, are potential N-additives on their own, but only when combined they reach their full potential. Especially in combination with acetic acid (as TAE50X buffer) they have provided the highest PLQYs (approx. 28%) observed in this work so far (see Chap. 4.2.4, p. 80). It can even be argued that EDTA and Tris fulfil rather different functions. EDTA facilitates the N-CND formation and is responsible for the incorporation of nitrogen into the carbon core; reflected in the high concentrations but low PLQYs

of EDTA derived N-CNDs. Tris, on the other hand, barely forms N-CNDs on its own, but provides the essential nitrogen containing surface groups for N-CNDs; reflected in low concentrations but significantly higher PLQYs for Tris derived N-CNDs.

### 4.3.1 Influence of Reaction Temperature on CA/N-CND Synthesis

As it was shown earlier, higher reaction temperatures can lead to enhanced PLQYs, without altering the photoluminescence properties of N-CNDs (see Chap. 4.2.3, p. 78). Hence, the impact of reaction temperature on the PL properties of CA/N-CNDs are presented in Figure 4.18. The

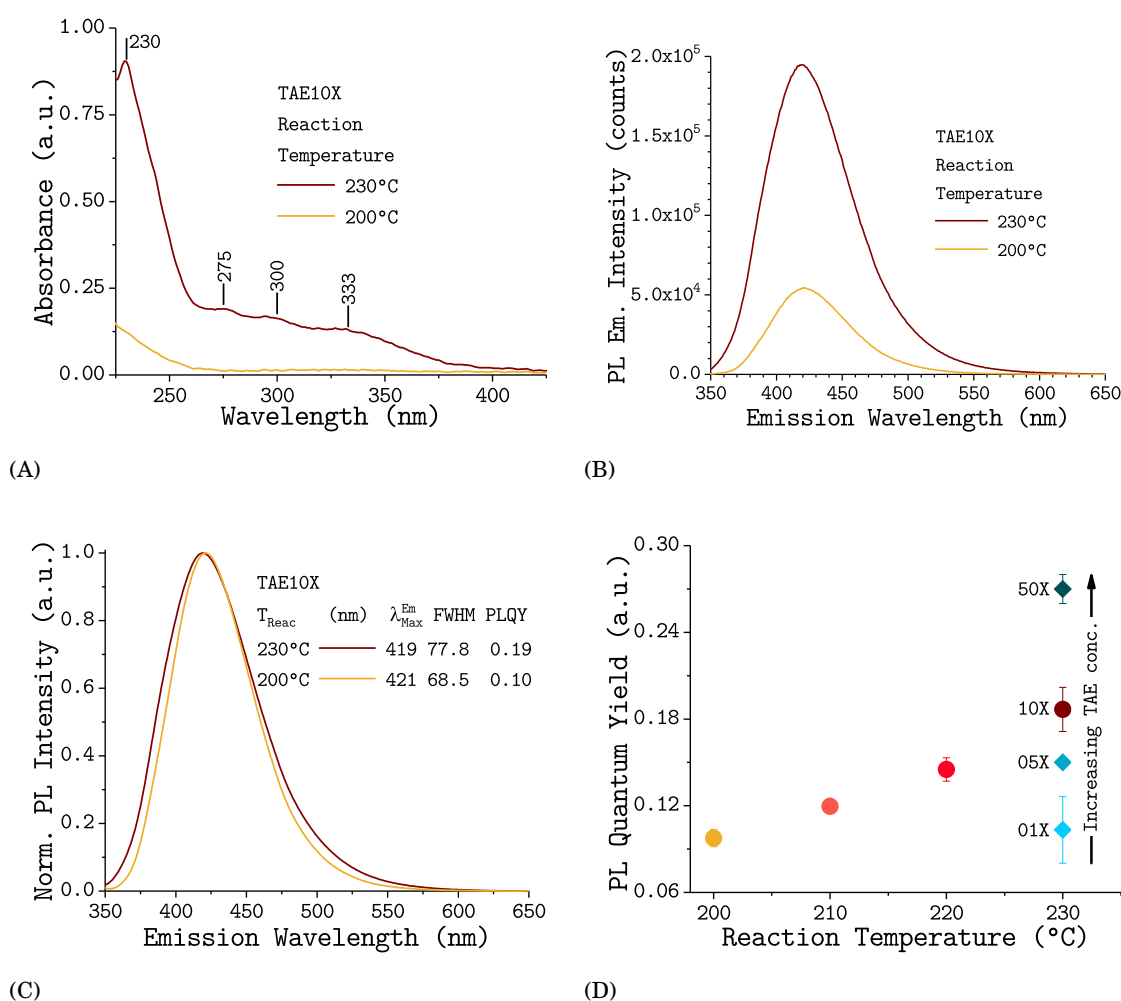


Figure 4.18: Effect of reaction temperature on the optical properties of CA/N-CNDs derived from an aqueous TAE10X buffer solution (EDTA: 0.01 M; Tris: 0.2 M; HAC: 0.4 M; pH 8.3): (A) UV-Vis absorption spectra; (B) PL emission spectra for different reaction temperatures under excitation at 340 nm (OD 0.1); (C) their corresponding normalized PL emission spectra; and (D) PLQY at 340 nm as a function of reaction temperature and TAE concentration (TAE01X to TAE50X).

spectra shown were taken for three C/N-CND samples obtained from three synthesis attempts for

each reaction temperature of an aqueous TAE10X buffer solution (EDTA: 0.01 M; Tris: 0.2 M; HAc: 0.4 M; pH 8.3). As presented in Figure 4.18A, the UV-Vis absorption spectra of as-synthesized N-CNDs are comparable to earlier findings but still distinctive in certain characteristics (see Table B.3, p. 129). The first peak at around 230 nm (Peak 1) is very pronounced and assigned to  $n-\pi^*$  transitions either in C-N bonds and/or C-O bonds; while the second Peak at around 250 nm (Peak 4), assigned to  $n-\sigma^*$  transitions in amines, is much less pronounced. The peak at around 275 nm (Peak 5) is attributed to  $n-\pi^*$  transitions in C=O bonds in ketones. Apparently, the generally broad band at around 300 nm to 400 nm, (attributed to  $n-\pi^*$  transitions within the C=O bonds) includes two distinctive peaks at around 300 nm (Peak 6) and at around 333 nm (Peak 7). With increasing reaction temperature the general shape of the spectra remains similar, while the total absorption increases drastically.

The corresponding PL and normalized PL emission spectra collected with excitation at 340 nm (see Fig. 4.18B and Fig. 4.18C) show that the emission band, despite different reaction temperatures, is always positioned at around  $(420 \pm 1)$  nm when excited at 340 nm. Furthermore, only a slight increase in FWHM, from around 70 nm at 200 °C to 80 nm at 230 °C was noticed. These results are consistent with earlier findings (see Chap. 4.2.3, p. 78), and hence support the notion that the nature of the surface states determines the PL emission bandwidth of CNDs (see Chap. 2.3.3, p. 31).

Furthermore, CA/N-CNDs share the same strong linearity between PLQY and synthesis temperature as C/N-CNDs (see Fig. 4.18D and Fig. 4.13D, 79). This suggests a further increase in PLQYs with much higher reaction temperatures, due to the formation of favourable N-doping architecture [51] and/or higher surface to volume ratios under higher reaction temperatures [51]. Regarding stability over time, as-synthesized CA/N-CNDs proved to be highly stable and no precipitation or changes in PL properties were observed over a period of one year.

### 4.3.2 Influence of TAE Buffer Concentration on CA/N-CND Synthesis

Thus far, when excited at 340 nm, CA/N-CNDs exhibited strong blue PL emission centred at around  $(420 \pm 2)$  nm, with a FWHM of around  $(76 \pm 2)$  nm, independent of initial TAE-buffer concentration. Initial indications suggest that this is not true for the PLQY, which increased drastically from 9 % for TAE01X to 26 % for TAE50X (see Chap. 4.2.4, p. 80).

In order to gain a deeper insight into this behaviour, various TAE buffer concentrations (TAE01X, TAE05X, TAE10X, TAE50X, and TAE100X) with a constant pH value of 8.3 were dissolved in water and subsequently heated to 230 °C for 45 minutes in the MiWR. Throughout the ongoing reaction the initially transparent colorless liquid samples turned into a yellow to orange to brown solution, in accordance with increasing initial TAE buffer concentration. After the reaction finished blue emission could be observed for all samples when exposed to UV-light ( $\lambda_{Exc} = 312$  nm). The influence of TAE buffer concentration on the CA/N-CND formation is illustrated in Figure 4.19 to Figure 4.20. The presented results were obtained from five to ten synthesis

attempts, for each TAE buffer concentration.

As presented in Figure 4.19A, the UV-Vis absorption spectra of as-synthesized CA/N-CNDs are

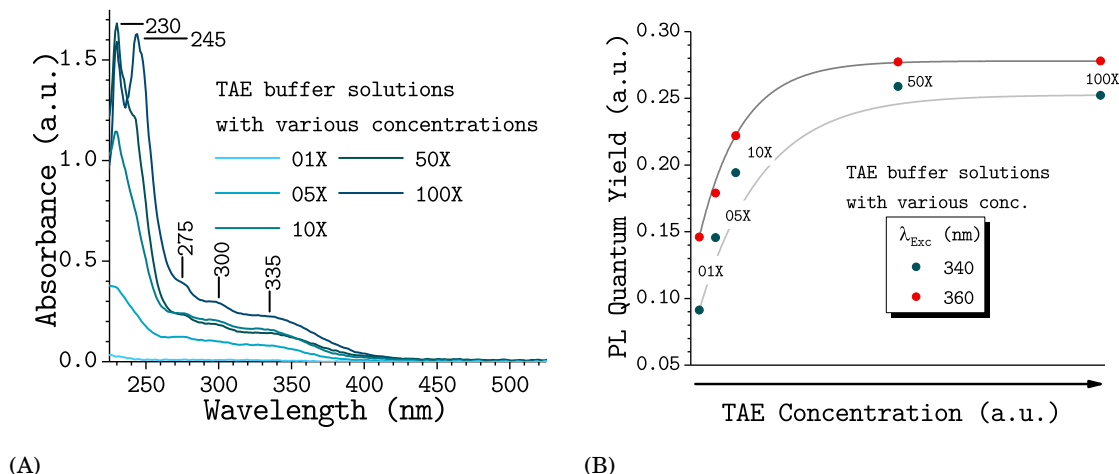


Figure 4.19: Effect of TAE buffer concentration on the optical properties of CA/N-CNDs derived from an aqueous TAE buffer solutions: (A) UV-Vis absorption spectra; and (B) PLQY at 340 nm as a function of initial TAE buffer concentration (TAE01X to TAE50X). It should be noted, that while the TAE buffer concentration, and hence its components (EDTA, Tris, HAc) concentrations change, their ratio (1:40:20) remains the same.

comparable to earlier findings (see Table B.3, p. 129): the two first peaks at around 230 nm (Peak 1) and at around 245 nm (Peak 4) are assigned to  $n-\pi^*$  transitions in C-N and C-O bonds, respectively, located either on the CA/N-CND surface or within the CA/N-CND core. The peak at around 275 nm (Peak 5) is attributed to  $n-\pi^*$  transition in C=O bonds in ketones. The broad band at around 300 nm to 400 nm (attributed to  $n-\pi^*$  transitions within the C=O bonds) includes two distinctive peaks at around 300 nm (Peak 6) and at around 335 nm (Peak 7). With increasing TAE buffer concentration the general shape of the spectra remains similar, while the total absorption increases drastically. The strong increase in Peak 4 (with increasing TAE buffer concentration) may indicate a change in CA/N-CND structure and/or composition due to increased incorporation of oxygen and/or nitrogen (for further information, see Chap. 4.3.3, p. 92).

Regarding the PLQY (see Fig. 4.20B), three tendencies can be observed: (1) the PLQY increases exponentially with increasing initial TAE buffer concentration; (2) concentrations higher than TAE50X have no further impact (e.g. TAE100X) on the PLQY; and (3) the PLQY of as-synthesized CA/N-CNDs is excitation wavelength dependent. On average, PLQYs with excitation at 360 nm are about three percentage points higher than PLQYs with excitation at 340 nm (see Fig. 4.20B).

The corresponding PL and normalized PL emission spectra collected with excitation at 340 nm and 360 nm (see Fig. 4.14) indicate excitation wavelength dependent behaviour of as-synthesized CA/N-CNDs. Nevertheless, the emission bands are almost independent of initial precursor concentration, and positioned at around  $(420 \pm 3)$  nm and around  $(424 \pm 3)$  nm for excitation at

### 4.3. SYNTHESIS AND CHARACTERISATION OF CARBOXYLIC ACID DERIVED, NITROGEN-DOPED CARBON NANODOTS

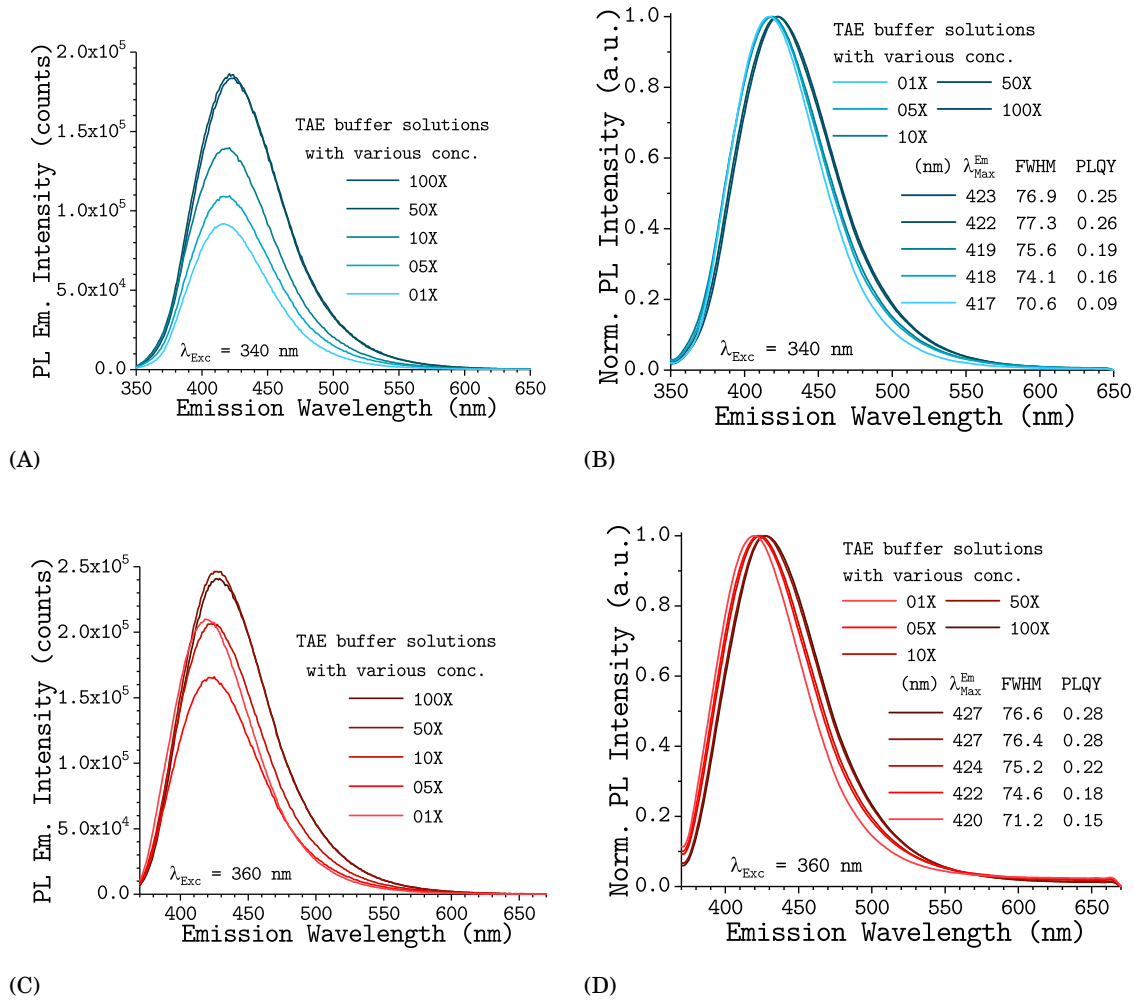


Figure 4.20: Effect of TAE buffer concentration on the optical properties of CA/N-CNDs derived from an aqueous TAE buffer solutions: (A,C) PL emission spectra for various initial TAE buffer concentrations (TAE01X to TAE50X); and (B,D) their corresponding normalized PL emission spectra under excitation at 340 nm (OD 0.1) and 360 nm (OD 0.1), respectively. It should be noted, that while the TAE buffer concentration, and hence its components (EDTA, Tris, HAC) concentrations change, their ratio (1:40:20) remains the same.

340 nm and 360 nm, respectively. In line with this, the FWHM is also constant:  $(75 \pm 3)$  nm and  $(75 \pm 2)$  nm for excitation at 340 nm and 360 nm, respectively.

This result proves again the notion that for CNDs the nature of the surface states determines the emission wavelength but not necessarily the efficiency of radiative recombination (see Chap. 2.3.3, p. 31).

### 4.3.3 Influence of Acetic Acid Concentration on CA/N-CND Synthesis

As shown earlier (see above), the TAE buffer concentration can have significant impact on the obtained PLQYs of CA/N-CNDs. More specifically, increased TAE buffer concentrations lead to significantly higher PLQYs. According to the obtained absorption spectra (see Fig. 4.19A, p. 90), a potential cause for this behaviour is a change in CA/N-CND structure and/or composition due to increased incorporation of oxygen. The main provider of oxygen in TAE buffer solutions, due to its high concentrations, is acetic acid. Furthermore, earlier findings already indicated its crucial role in the formation of N-CNDs (see Chap. 4.2.4, p. 80). To avoid confusion between different types of carboxylic acid derived nitrogen-doped carbon nanodots (i.e. CA/N-CNDs), acetic acid derived nitrogen-doped carbon nanodots will from now onwards be referred to as HAc/N-CNDs.

In order to gain deeper insight into formation of HAc/N-CNDs, various amounts of acetic acid (0.00 M to approx. 9.75 M) were dissolved in TeE- and TE buffer solutions with fixed EDTA- (0.05 M) and Tris concentrations (0.5 M and 2.0 M), respectively. The precursor solutions thus obtained were subsequently heated to 230 °C for 45 minutes in the MiWR. Throughout the ongoing reaction the initially transparent colorless liquid samples turned into deep orange to brown solutions. After 45 minutes blue emission could be observed for all samples when exposed to UV-light ( $\lambda_{\text{Exc}} = 312 \text{ nm}$ ). The influence of HAc concentration on the HAc/N-CND formation is illustrated in Figure 4.21 to Figure 4.7. The data shown in Figure 4.21 was taken for five to twenty HAc/N-CND samples obtained from five to twenty synthesis attempts, for each acetic acid concentration of aforementioned HAc/N-CND precursor solutions.

As presented in Figure 4.21A and Figure 4.21B, the acetic acid concentration has a significant impact on the overall PLQY of as-synthesized HAc/N-CNDs. The PLQY increases drastically from about 9 % (without HAc) to the highest PLQYs observed, about 17 % for TE buffer (HAc: 2.0 M) and about 50 % for TeE buffer (HAc: 7.0 M). Regarding the PLQY, five tendencies are emerging: (1) the initial Tris concentration plays a crucial role in the HAc/N-CND formation; (2) PLQY rises with increasing initial Tris concentration; (3) without acetic acid the initial Tris concentration has no impact; (4) the PLQY rises strongly with increasing initial acetic acid concentration (i.e. dynamic range); and (5) acetic acid concentrations larger than four times the initial Tris concentration have no further impact on the PLQY. In spite of the drastic increase in PLQY, the PL emission properties stay virtually unaffected (see Fig. 4.22C).

As presented in Figure 4.21C, Figure 4.21D and Figure 4.22, the PL emission maximum and -FWHM of HAc/N-CNDs are virtually unaffected by increasing initial precursor concentration. The emission bands are positioned at around  $(422.0 \pm 0.6) \text{ nm}$  and around  $(421 \pm 1) \text{ nm}$  for TeE- and TE buffer derived HAc/N-CNDs, respectively. In line with this, the FWHM values are also constant: around  $(75 \pm 2) \text{ nm}$  and around  $(79.0 \pm 0.7) \text{ nm}$  for TeE- and TE buffer derived HAc/N-CNDs, respectively. Nevertheless, increased initial acetic acid concentrations appear to promote lower FWHM and slightly blue-shifted emission maxima, in particular for TeE buffer derived HAc/N-CNDs (see Fig. 4.21C).



### 4.3. SYNTHESIS AND CHARACTERISATION OF CARBOXYLIC ACID DERIVED, NITROGEN-DOPED CARBON NANODOTS

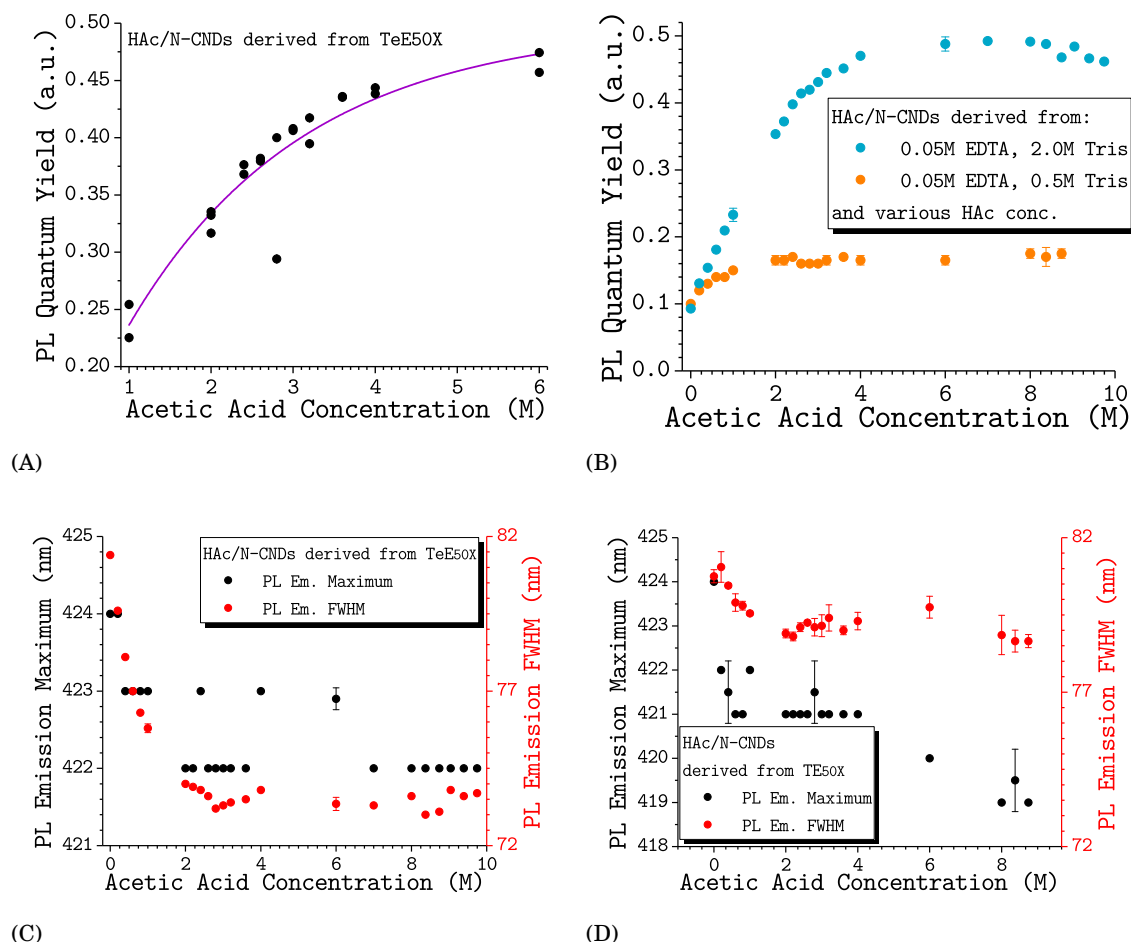


Figure 4.21: Effect of acetic acid concentration on the optical properties of HAC/N-CNDs derived from aqueous TeE- and TE buffer solutions: (A) PLQY as a function of acetic acid concentration for TeE buffer derived HAC/N-CNDs (dynamic range); (B) PLQY; and (C,D) PL emission maximum and its corresponding FWHM, under excitation at 340 nm (OD 0.1), as a function of acetic acid concentration for TeE- and TE buffer derived HAC/N-CNDs, respectively. TeE buffer: 0.05 M EDTA, 2.0 M Tris; and TE buffer: 0.05 M EDTA, 0.5 M Tris.

#### 4.3.3.1 Influence of pH Value on CA/N-CND Synthesis

Increasing acetic acid concentrations are accompanied by decreasing pH values. In order to confirm or exclude decreasing pH values as the origin of increased PLQYs in as-synthesized HAC/N-CNDs (see above) the following precursor solutions were prepared: (a) various amounts of acetic acid (1.0 M to 5.0 M; pH 8.3 to 4.16) were dissolved in a TeE50X buffer solution (EDTA: 0.05 M; Tris: 2.0 M); and (b) hydrochloric acid (HCl) was used for the adjustment of pH of a TAE50X buffer solution (EDTA: 0.05 M; Tris: 2.0 M; and HAC: 1.0 M) to equivalent values (pH 8.3

to 4.16). The precursor solutions thus obtained were subsequently heated to 230 °C for 45 minutes in the MiWR. Throughout the ongoing reaction the initially transparent colorless liquid samples turned into deep orange to brown solutions. In the case of acidified TAE50X buffer derived HAC/N-CNDs, strong precipitation of a black solid was observed for all samples with lower pH values ( $\text{pH} \leq 6.0$ ). After 45 minutes blue emission could be observed for all samples when exposed to UV-light ( $\lambda_{\text{Exc}} = 312 \text{ nm}$ ). The influence of pH value on the HAC/N-CND formation is illustrated in Figure 4.22 to Figure 4.23.

As presented in Figure 4.22A and Figure 4.22B, the UV-Vis absorption spectra, independent of

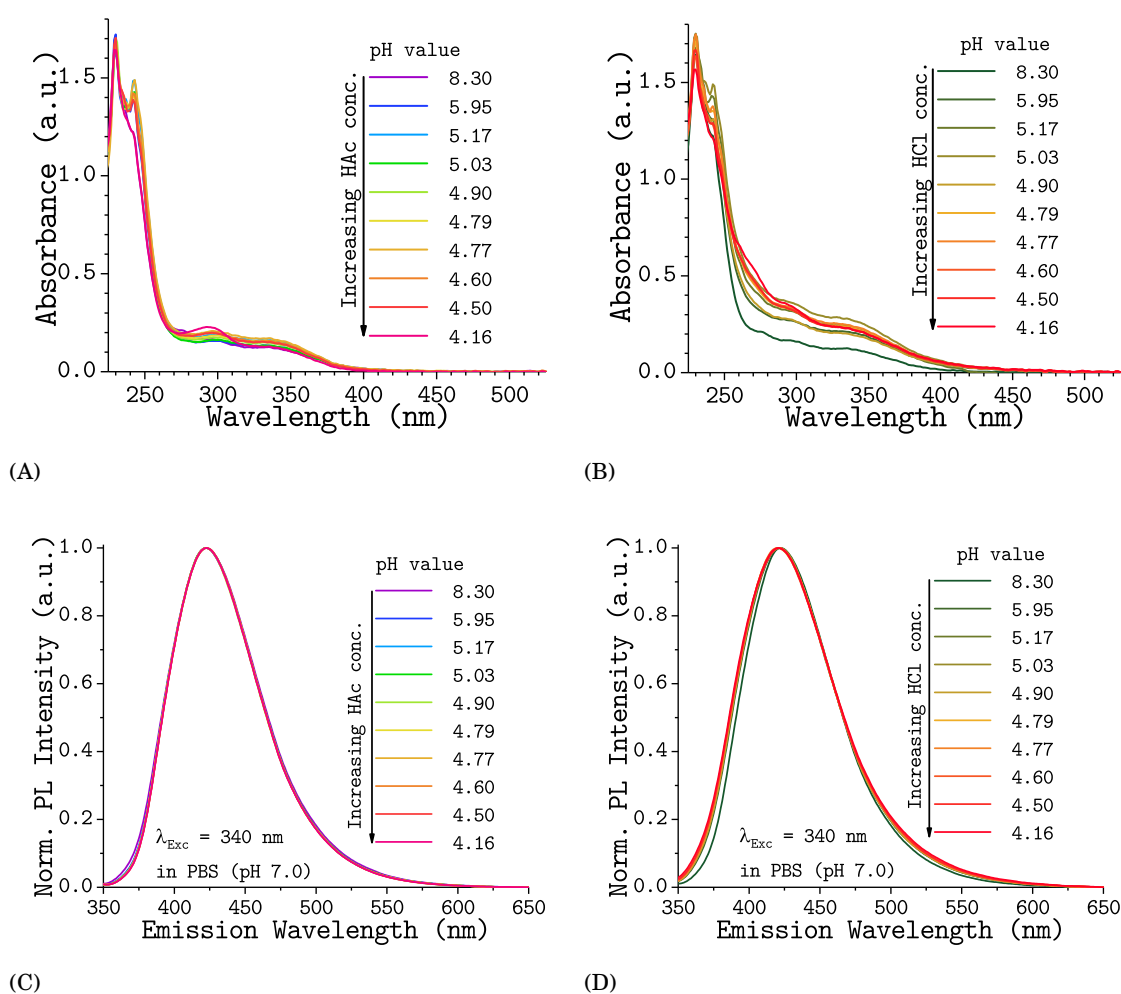


Figure 4.22: Effect of pH value on the optical properties of HAC/N-CNDs derived from aqueous TeE- and TAE50X buffer solutions: (A,B) UV-Vis absorption spectra; and (C,D) their corresponding normalized PL emission spectra under excitation at 340 nm (OD 0.1) at various pH values for TeE- (Type 1) and acidified TAE50X buffer (Type 2) derived HAC/N-CNDs, respectively. TeE buffer: 0.05 M EDTA, 2.0 M Tris, HAC: varies; and TAE50X buffer: 0.05 M EDTA, 2.0 M Tris, 1.0 M HAC.

precursor and pH value, exhibit the same absorption bands already reported for HAC/N-CNDs

#### 4.3. SYNTHESIS AND CHARACTERISATION OF CARBOXYLIC ACID DERIVED, NITROGEN-DOPED CARBON NANODOTS

(see Chap. 4.3.1, p. 88 and Chap. 4.3.2, p. 89): the first two peaks at around 230 nm (Peak 1) and 245 nm (Peak 4); followed by a weak peak at around 275 nm (Peak 5). The broad band at around 300 nm to 400 nm, includes two distinctive peaks at around 300 nm (Peak 6) and at around 335 nm (Peak 7). With increasing pH values and/or acetic acid concentration the general shape of the spectra remains similar, while the total absorption increases slightly.

The corresponding normalized PL emission spectra collected at pH 7.0 and with excitation at 340 nm are presented in Figure 4.22C and Figure 4.22D. The PL emission bands prove to be independent of pH values, and are positioned at around  $(422.0 \pm 0.5)$  nm and around  $(421 \pm 1)$  nm; with FWHM at around  $(74 \pm 1)$  nm and around  $(81 \pm 2)$  nm for TeE- (Type 1) and acidified TAE50X buffer (Type 2) derived HAc/N-CNDs, respectively (see Fig. 4.23A and Fig. 4.23B). Despite the constant PL emission properties of HAc/N-CNDs Type 2, it should be noted that a drastic increase in precipitation and loss of long time stability was observed for decreasing pH values. Conversely, HAc/N-CNDs Type 1 proved to be highly stable over a long period of time (at least one year).

The results of the corresponding PLQY measurements (see Fig. 4.23) can be summarised as

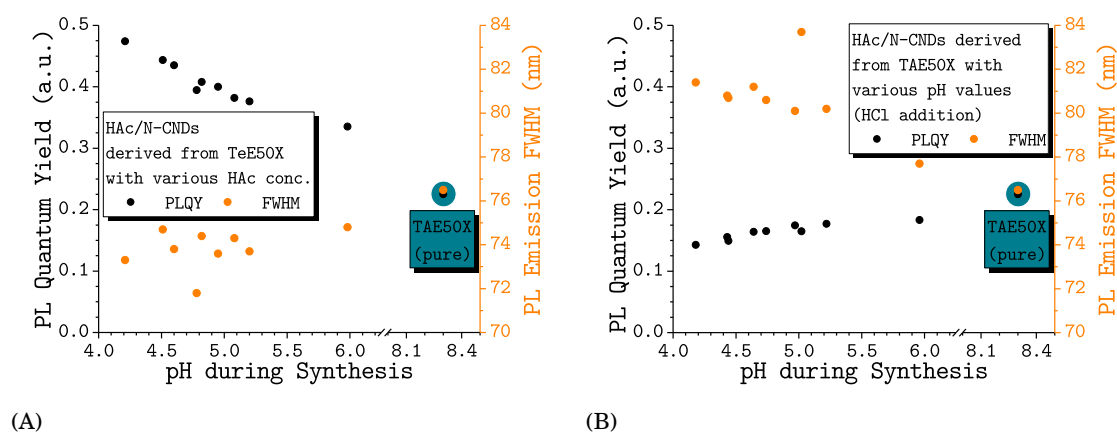


Figure 4.23: Effect of pH value on the PLQY and FWHM of HAc/N-CNDs derived from aqueous TeE- and TAE50X buffer solutions: (A) PLQY and PL emission FWHM under excitation at 340 nm (OD 0.1) as a function of pH values for TeE buffer derived HAc/N-CNDs (Type 1); and (B) PLQY and PL emission FWHM under excitation at 340 nm (OD 0.1) as a function of pH values for acidified TAE50X buffer derived HAc/N-CNDs (Type 2). The results for HAc/N-CNDs obtained from unmodified TAE50X buffer are marked in blue. TeE buffer: 0.05 M EDTA, 2.0 M Tris, HAc: varies; and TAE50X buffer: 0.05 M EDTA, 2.0 M Tris, 1.0 M HAc.

follows: (1) for Type 1 HAc/N-CNDs the PLQY increases drastically with increasing initial acetic acid concentration (despite the corresponding decrease in pH values); (2) for Type 2 HAc/N-CNDs the PLQY decreases significantly with decreasing pH values; and (3) at their highest value Type 1 HAc/N-CNDs (48 %) have at least a more than three times higher PLQY than Type 2 HAc/N-CNDs (14 %).

The obtained results support the notion that decreasing pH values can be excluded as the origin

of increased PLQYs in as-synthesized HAC/N-CNDs. More specifically, the influence of decreasing pH values on the formation of HAC/N-CNDs seems to be detrimental. It must therefore be presumed that the true cause of increased PLQYs lies in a (yet to be understood) interaction of Tris and acetic acid during HAC/N-CND formation.

#### 4.3.4 Influence of Reaction Time on CA/N-CND Synthesis

In order to assess the influence of reaction time on the formation of HAC/N-CNDs, the influence on the resulting HAC/N-CNDs PL properties has been investigated using UV-Vis absorption as well as PL steady-state and PLQY measurements. A TAE50X- (HAC: 1.0 M) and TeE50X buffer

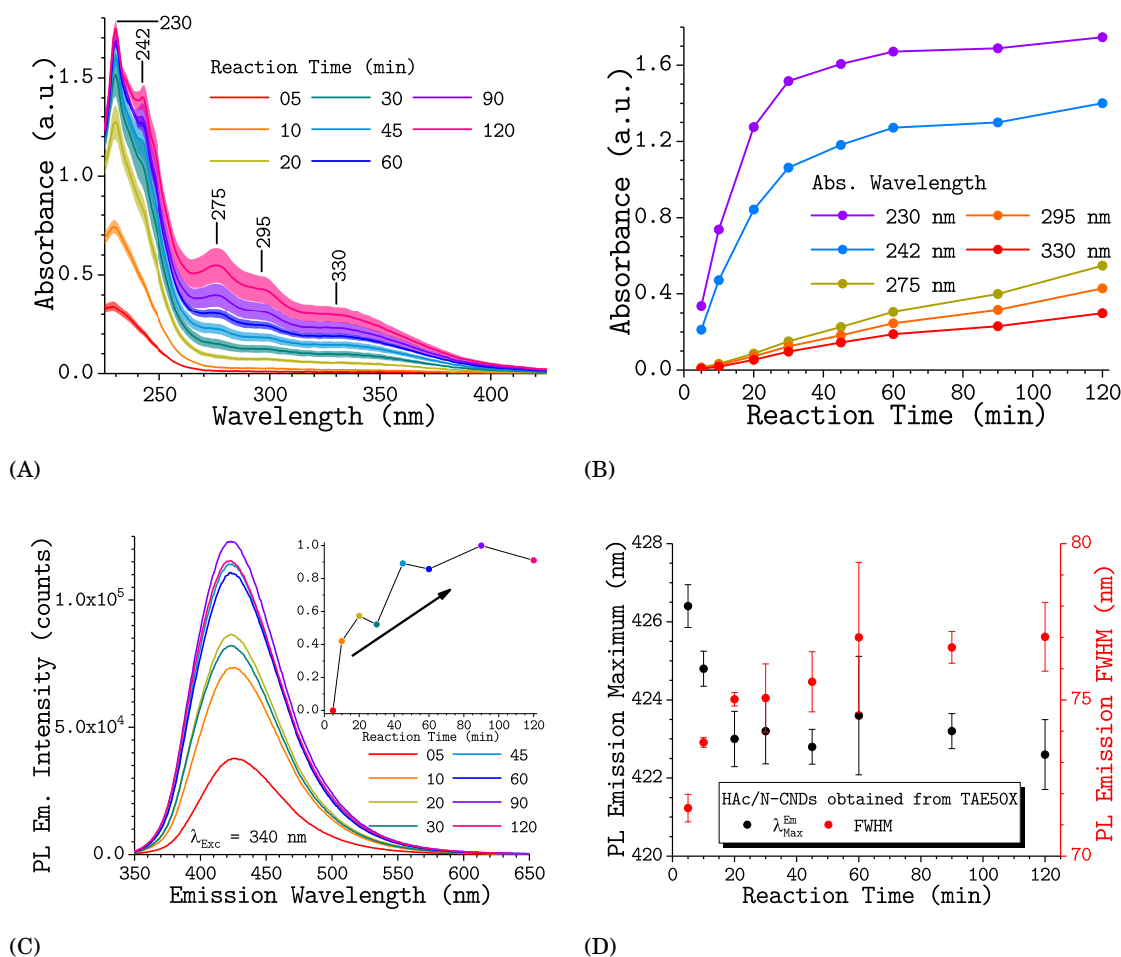


Figure 4.24: Effect of reaction time on the optical properties of HAC/N-CNDs derived from aqueous TAE50X buffer solution (Type 3): (A) UV-Vis absorption spectra (shaded regions represent the standard deviation obtained from ten synthesis attempts); (B) absorbance at five selected wavelengths as a function of reaction time; (C) PL emission spectra for different reaction times under excitation at 340 nm (OD 0.1), the inset is the PL Intensity as a function of reaction time; and (D) the PL emission maximum ( $\lambda_{Max}^{Em}$ ) and -FWHM as a function of reaction time. TAE50X buffer: 0.05 M EDTA, 2.0 M Tris, 1.0 M HAC.

### 4.3. SYNTHESIS AND CHARACTERISATION OF CARBOXYLIC ACID DERIVED, NITROGEN-DOPED CARBON NANODOTS

solution (HAc: 7.0 M) with comparable EDTA and Tris concentrations were heated to 230 °C for 5 to 120 minutes in the MiWR. As stated before, the initially transparent colorless liquid sample turned into a deep orange to brown clear solution as the reaction progressed. After 5 minutes blue emission could already be observed when exposed to UV-light ( $\lambda_{Exc} = 312$  nm). The influence of reaction time on the HAc/N-CND formation is illustrated in Figures 4.24 to 4.26. The data shown in aforementioned figures were obtained from ten independent HAc/N-CND samples obtained from ten synthesis attempts, for each reaction time, of aforementioned precursor solutions.

As presented in Figure 4.24A and Figure 4.25A, the UV-Vis absorption spectra, independent of

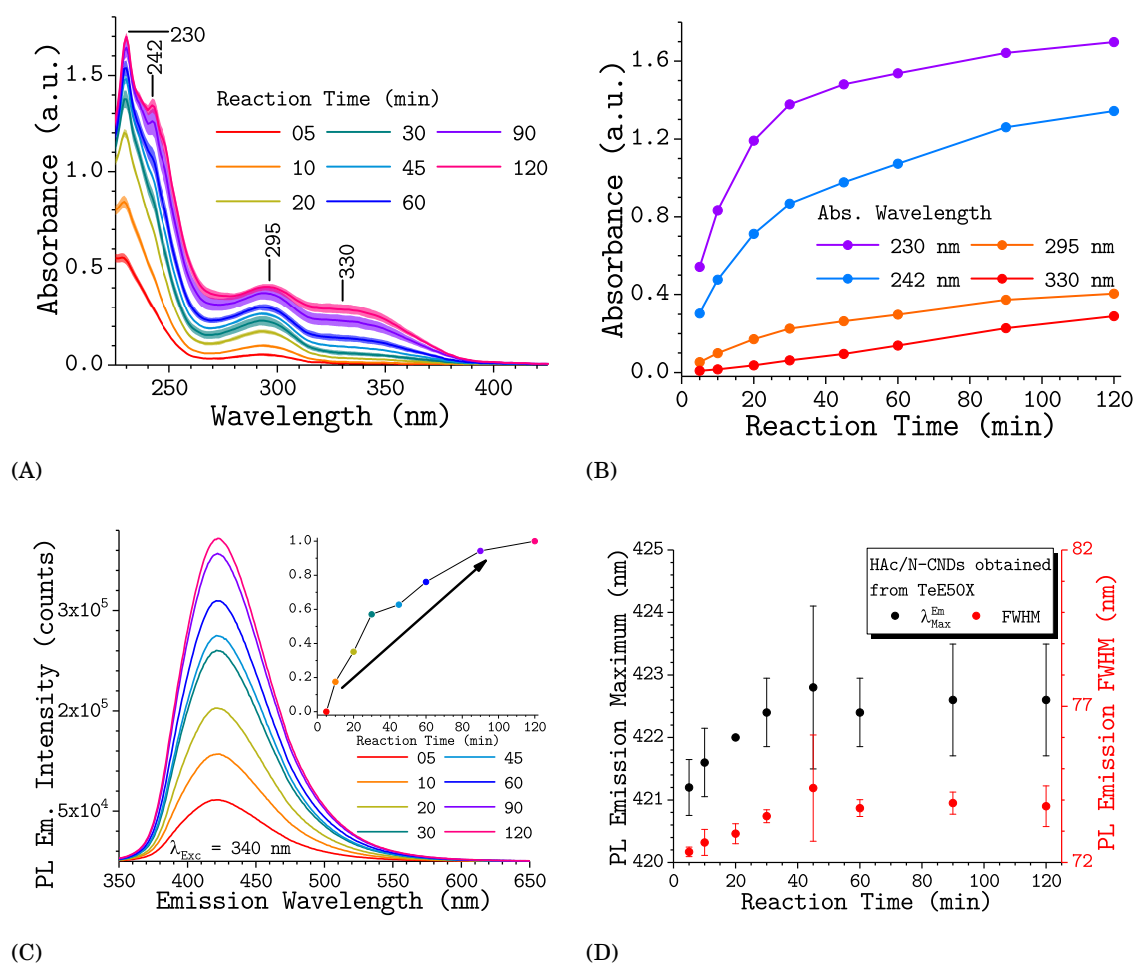


Figure 4.25: Effect of reaction time on the optical properties of HAc/N-CNDs derived from aqueous TeE50X buffer solution (Type 4): (A) UV-Vis absorption spectra (shaded regions represent the standard deviation obtained from ten synthesis attempts); (B) absorbance at five selected wavelengths as a function of reaction time; (C) PL emission spectra for different reaction times under excitation at 340 nm (OD 0.1), the inset is the PL Intensity as a function of reaction time; and (D) the PL emission maximum and -FWHM as a function of reaction time. TeE50X buffer: 0.05 M EDTA, 2.0 M Tris, 7.0 M HAc.

precursor solution, exhibit the same absorption bands already reported for HAc/N-CNDs (see

Table B.3, p. 129). With proceeding reaction time the general shape of the absorption spectra remain similar, while the total absorption increases steadily, reaching its maximum after 120 minutes (see Fig. 4.24B and Fig. 4.25B).

The corresponding PL emission spectra collected with excitation at 340 nm are shown in Figure 4.24C and Figure 4.25C, respectively. Already after 5 minutes of reaction time a strong emission band can be observed. With proceeding reaction time the general shape of the PL emission spectra remain similar, while the overall PL intensity rises substantially, reaching its maximum after 120 minutes (see inset in Fig. 4.24C and inset in Fig. 4.25C). The emission bands are almost independent of reaction time, and positioned at around  $(423 \pm 1)$  nm and around  $(422 \pm 1)$  nm; with FWHM at around  $(75 \pm 2)$  nm and around  $(74 \pm 1)$  nm for TAE50X- (Type 3) and TeE50X buffer (Type 4) derived HAc/N-CNDs, respectively. However, a closer look reveals that with proceeding reaction time a slight emission red-shift, along with a slight increase in FWHM, can be observed (see Fig. 4.24D and Fig. 4.25D). Furthermore, the low standard deviations indicate once again the high level of reproducibility for the presented N-CND synthesis method. The results of the corresponding PLQY measurements (see Fig. 4.26) can be summarised as

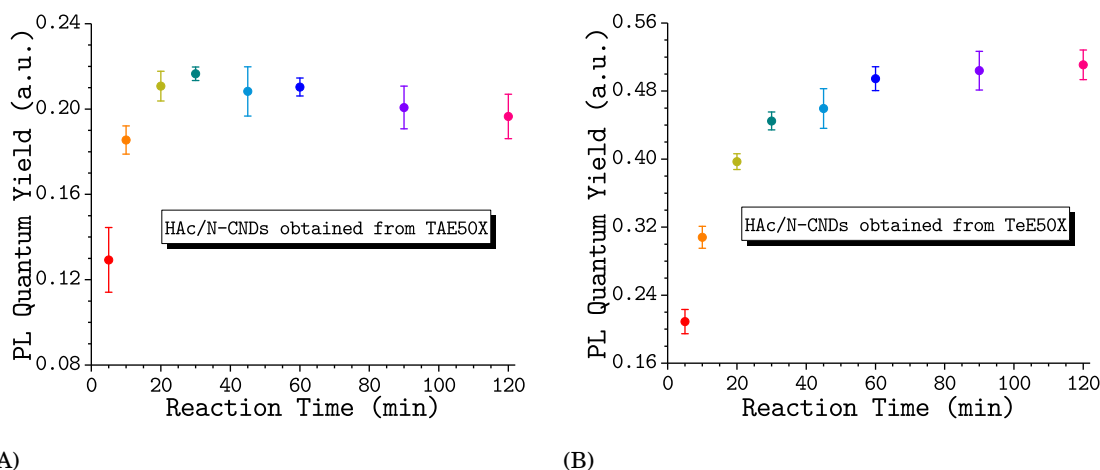


Figure 4.26: Effect of reaction time on the photoluminescence quantum yield of HAc/N-CNDs derived from aqueous TAE50X- (Type 3) and TeE50X buffer (Type 4) solution: (A) PLQY under excitation at 340 nm (OD 0.1) as a function of reaction time for TAE50X buffer derived HAc/N-CNDs; and (B) PLQY under excitation at 340 nm (OD 0.1) as a function of reaction time for TeE50X buffer derived HAc/N-CNDs. TAE50X buffer: 0.05 M EDTA, 2.0 M Tris, 1.0 M HAc; TeE50X buffer: 0.05 M EDTA, 2.0 M Tris, 7.0 M HAc.

follows: (1) independent of precursor solution the PLQY increases drastically with proceeding reaction time; (2) the maximum PLQY for Type 3 HAc/N-CNDs (approx. 22 %) is reached at about 30 to 45 minutes; (3) for Type 3 HAc/N-CNDs the PLQY drops slightly at reaction times higher than 60 minutes (see Fig. 4.26A); (4) the maximum PLQY for Type 4 HAc/N-CNDs (approx. 51 %) is reached at about 90 to 120 minutes; and (5) at their highest value Type 4 HAc/N-CNDs have

about twice the PLQY of Type 3 HAc/N-CNDs.

The obtained results show once again that many factors play a crucial role in CND synthesis and therefore precise reaction control (e.g. starting materials, reaction time and -temperature) is needed to obtain CNDs with highly homogeneous photophysical properties.

#### 4.3.5 Photophysical Properties of HAc/N-CNDs at Various pH Values

Another interesting phenomenon often associated with CDs is the pH sensitivity of their PL behaviour [58, 104, 141]; not to be confused with the influence of pH values on CA/N-CND synthesis (see Chap. 4.3.3.1, p. 93). However, the kind of pH sensitivity is not always the same and depends strongly on CD type and synthesis [58, 104, 141]. Especially, as the differences in pH sensitivity may be related to the surface chemistry of CDs (see Chap. 2.3.3, p. 31).

In order to assess the pH-dependent PL behaviour of as-synthesized HAc/N-CNDs, the influence of three pH values on the HAc/N-CNDs PL properties has been investigated for a range of HAc/N-CND types using UV-Vis absorption as well as PL steady-state and PLQY measurements. Aforementioned HAc/N-CND types were synthesized via MiW-hPC (230 °C for 45 minutes) of TeE10X buffer solutions with varying acetic acid concentrations (0.2 M to 1.89 M). The obtained HAc/N-CND solutions were processed (see Chap. 3.2.5, p. 52) and subsequently dissolved in pH 4, pH 7 and pH 8 PBS buffer solutions.

As presented in Figure 4.27A, the PL emission maximum and -FWHM of HAc/N-CNDs are

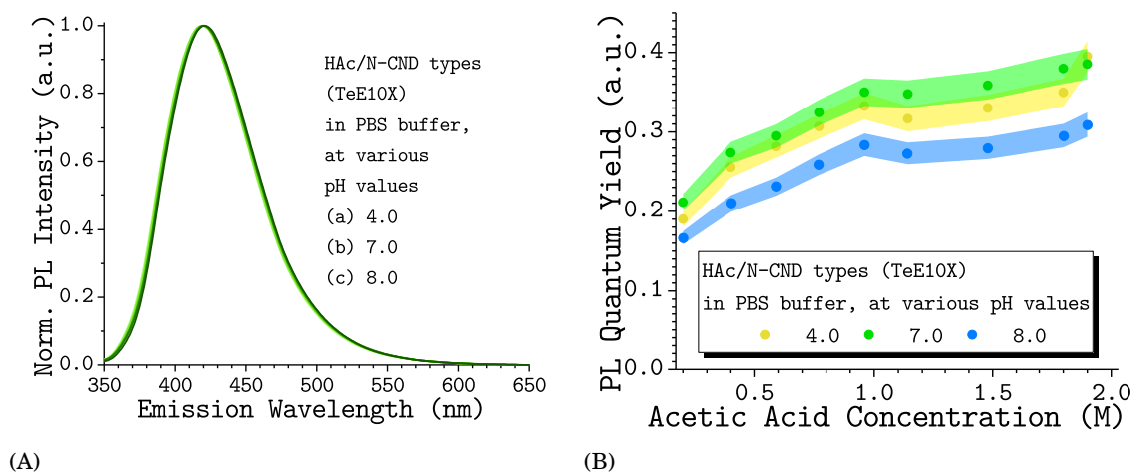


Figure 4.27: The effect of the solution pH value on the photophysical properties of HAc/N-CNDs derived from aqueous TeE10X buffer solution: (A) normalized PL emission spectra for different solution pH values under excitation at 340 nm (OD 0.1); and (B) PLQY for different solution pH values under excitation at 340 nm as a function of initial acetic acid concentration for TeE10X buffer derived HAc/N-CNDs (shaded regions represent error bars). TeE10X: 0.01 M EDTA, 0.5 M Tris, HAc: varies.

absolutely unaffected by varying solution pH values. The emission bands of all TeE10X buffer



derived HAc/N-CNDs are positioned at around  $(422.0 \pm 0.6)$  nm with a FWHM around  $(75 \pm 2)$  nm independent of initial acetic acid concentration and set solution pH value. However, the set pH value has a significant impact on the overall PLQY of as-synthesized HAc/N-CNDs. The results of the corresponding PLQY measurements (see Fig. 4.27B) can be summarised as follows: (1) the PLQY increases with increasing initial acetic acid concentration, as to be expected (see Chap. 4.3.3, p. 92); (2) the highest PLQYs are observed at neutral solution pH value, independent of HAc/N-CND type; (3) under acidic (pH 4.0) conditions the PLQYs are generally two percentage points lower than PLQYs at neutral pH; (4) under basic (pH 8.0) conditions the PLQYs are generally seven percentage points lower than PLQYs at neutral pH; and (5) all HAc/N-CND types show similar long time stability under all solution pH values covered by this work (i.e. extended pH range stability).

The results shown above support the notion that high initial acetic acid concentrations may increase the PLQY (in an as yet unknown way), but do not alter the surface chemistry of as-synthesized HAc/N-CNDs. Hence, the PL emission and pH sensitivity of HAc/N-CNDs are independent of HAc/N-CND type, i.e. the initial acetic acid concentration. It can therefore be concluded, that the surface chemistry is identical or at least very similar for all types of HAc/N-CNDs presented in this work.

### 4.3.6 Influence of Carboxylic Acid Type on CA/N-CND Synthesis

Citric acid is one of the most common carbon sources in CD synthesis and used in a wide range of synthesis methods, resulting in a vast range of (citric acid derived) CD types with a multitude of different photophysical properties [6, 28, 46, 60, 93, 120, 141, 150, 168, 170] (see Table C.1, p. 150). Hence, among other things, citric acid derived carbon dots can cover a wide range of PLQYs, ranging from as low as 3 % [192] to as high as 83 % [84, 174, 212].

In order to assess the suitability of citric acid and other carboxylic acid types as carbon source for CA/N-CND synthesis, their influence on the resulting CA/N-CND PL properties has been investigated using UV-Vis absorption as well as PL steady-state and PLQY measurements. All samples were prepared by dissolving the respective carboxylic acid (CiA: citric acid; BtA: 1,2,3,4 butane-tetracarboxylic acid; McA: malonic acid; OxA: oxalic acid; and SuA: succinic acid) in an aqueous TeE50X buffer solution and subsequently heated between 180 °C and 230 °C for 5 to 45 minutes in the MiWR. The differences in reaction temperature are caused by safety precautions to account for different decomposition temperatures and concentration (i.e. reaction pressure) of the carboxylic acids used. For example, increasing citric acid concentrations (e.g. 2.0 M to 7.0 M) must be accompanied by a reduction in reaction temperature (200 °C to 180 °C), due to increased gas evolution during MiW-hPC. As concerns carboxylic acid types, they can (among others) be classified according to their number of carboxyl groups (see Table 4.2) and chemical structures (e.g. straight-chain, saturated, aromatic etc.).

As presented in Figure 4.28A and Figure 4.28B, the UV-Vis absorption spectra (independent



### 4.3. SYNTHESIS AND CHARACTERISATION OF CARBOXYLIC ACID DERIVED, NITROGEN-DOPED CARBON NANODOTS

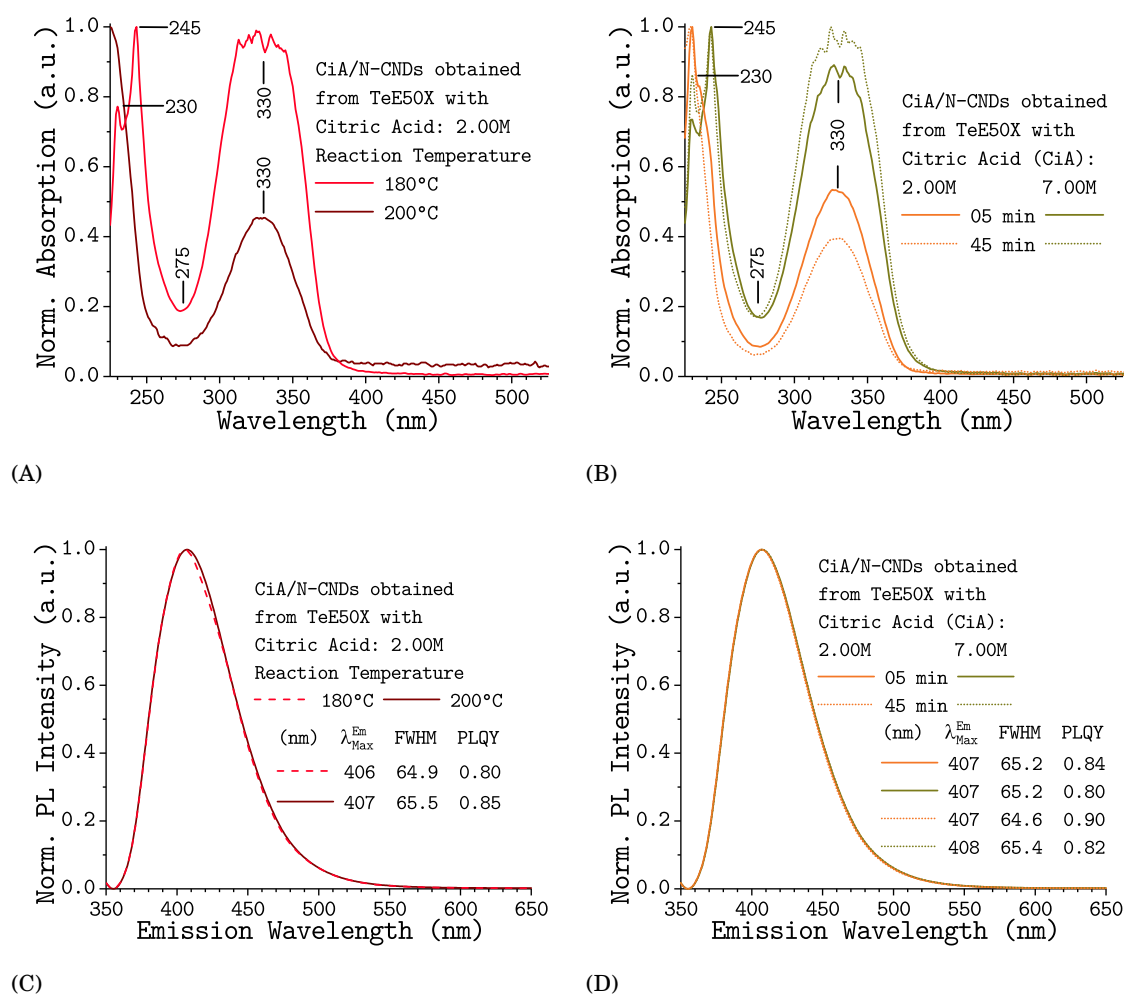


Figure 4.28: Effect of citric acid concentration, reaction time and -temperature on the optical properties of CiA/N-CNDs derived from aqueous TeE50X buffer solution: (A;B) normalized UV-Vis absorption spectra; and (C,D) their corresponding normalized PL emission spectra under excitation at 340 nm (OD 0.1), for two reaction temperatures (180 °C and 200 °C), and two citric acid concentrations (2.0 M and 7.0 M) at two reaction times (5 and 45 minutes), respectively. Furthermore, CiA/N-CNDs show the highest PLQYs (80 % to 90 %) of all (nitrogen-doped) CNDs presented in this work (see inset). CiA: citric acid; and TeE50X buffer: 0.05 M EDTA, 2.0 M Tris.

of initial citric acid concentration) are complementary to HAc/N-CNDs (see Chap. 4.3.3, p. 92 and Chap. 4.3.4, p. 96) but still distinctive in certain characteristics. The first two peaks at around 230 nm (Peak 1) and at around 245 nm (Peak 4) are very pronounced and assigned to  $n-\pi^*$  transitions in C-N and C-O bonds, and  $n-\sigma^*$  transitions in amines (C-N bonds), respectively. Apparently, the generally broad (Peak 3) and less pronounced band at around 330 nm (Peak 7), attributed to  $n-\pi^*$  transitions within the C=O bonds, is very pronounced for CiA/N-CNDs. This indicates an increased incorporation of oxygen, presumably resulting in a difference in structure

and/or composition between acetic- and citric acid derived CA/N-CNDs (for further information, see Chap. 4.3.8, p. 105). With increasing reaction temperature and -time the general shape of the spectra remains similar, while the total absorption increases drastically. The initial citric acid concentration, on the other hand, has no significant impact on neither spectral shape nor intensity of the UV-Vis absorption spectra.

As presented in Figure 4.28C and Figure 4.28D, the PL emission maximum and -FWHM of CiA/N-CNDs are virtually unaffected by increasing initial citric acid concentration, reaction time and -temperature. The emission bands are positioned at around  $(407 \pm 1)$  nm, with a FWHM around  $(65 \pm 1)$  nm. Compared to HAc/N-CNDs a distinctively blue-shifted PL emission can be observed.

Regarding the PLQY, four tendencies are emerging: (1) the PLQY increases with increasing reaction temperature, (2) the PLQY increases with proceeding reaction time, (3) citric acid concentrations larger than the initial Tris concentration have no further impact on the PLQY, and (4) a large excess of initial citric acid concentration (compared to initial Tris concentration) has a highly detrimental impact on the obtained PLQY. Furthermore, CiA/N-CNDs show the highest PLQYs (90 %) of all (nitrogen-doped) CNDs presented in this work (see Table 4.2); making them the highest PLQY values for N-CNDs obtained by a microwave-assisted one-pot synthesis so far (see Table C.1, p. 150). The results obtained for the remaining carboxylic acids (BtA, McA, OxA, and SuA) are illustrated in Figure 4.29.

As presented in Figure 4.29A, the UV-Vis absorption spectra are complementary to previous CA/N-CNDs, but still distinctive for each carboxylic acid type. All CA/N-CNDs (with one exception) show at least two or more of the characteristic peaks at around 230 nm (Peak 1), around 245 nm (Peak 4), and the broad band at around 300 nm to 400 nm (Peak 3), including the two distinctive peaks at around 300 nm (Peak 6) and at around 335 nm (Peak 7).

In particular the UV-Vis absorption spectra of oxalic acid derived CA/N-CNDs (i.e. OxA/N-CNDs) sets itself apart from all other CA/N-CNDs as most of the characteristic peaks (except for the broad band at around 300 nm to 400 nm) can not be observed. Apparently, the peak at around 267 nm deriving from  $n-\pi^*$  transition in C=O bonds in ketones, dominates the OxA/N-CNDs UV-Vis absorption spectrum. In accordance with earlier findings, no indications could be found that the reaction temperature and -time as well as the initial carboxylic acid concentration alter the general shape of the UV-Vis absorption or PL emission spectra.

As presented in Figure 4.29B and Figure 4.29C, the PL emission maximum and -FWHM of as-synthesized CA/N-CNDs can vary extensively, based on carboxylic acid type. The emission bands, PL emission FWHM and corresponding PLQYs, for each respective carboxylic acid type, are represented in Table 4.2.

In summary: The utilization of different carboxylic acids types in CA/N-CND synthesis leads to the formation different CA/N-CND types. They can vary significantly with respect to their UV-Vis absorption spectra (see Table B.3, p. 129); PL emission properties (e.g. emission bandwidth,

### 4.3. SYNTHESIS AND CHARACTERISATION OF CARBOXYLIC ACID DERIVED, NITROGEN-DOPED CARBON NANODOTS

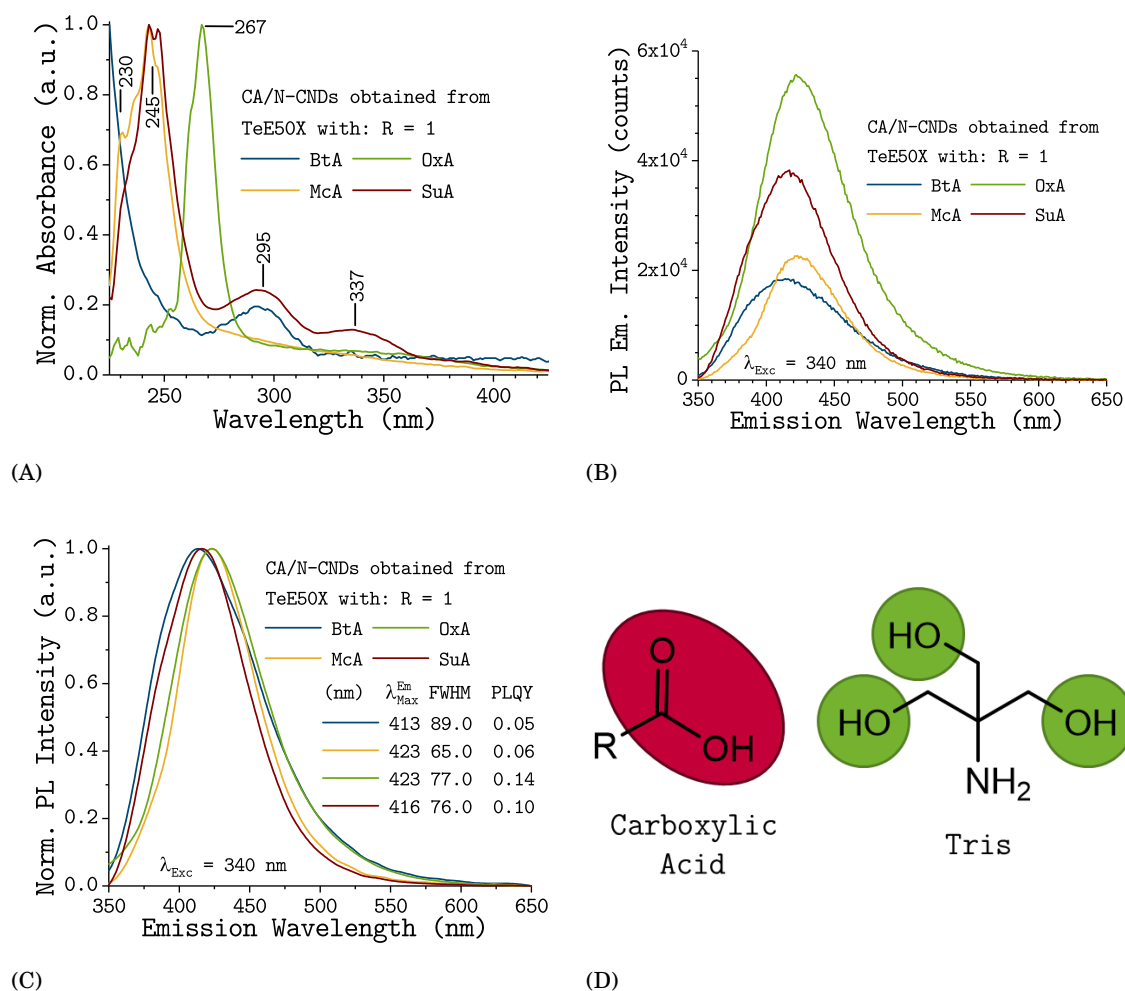


Figure 4.29: Effect of carboxylic acid type on the optical properties of CA/N-CNDs derived from aqueous TeE50X buffer solution: (A) UV-Vis absorption spectra; (B) PL emission spectra under excitation at 340 nm (OD 0.1); and (C) their corresponding normalized PL emission spectra for four carboxylic acid types. (D) Schematic representation of the basic rule for CA/N-CND synthesis developed in this study. Where  $R$  is the ratio between the amount of carboxylic acid groups  $\#COOH$  (red) and the amount of Tris based alcohol groups  $\#OH$  (green). BtA: 1,2,3,4 butane-tetracarboxylic acid; McA: malonic acid; OxA: oxalic acid; and SuA: succinic acid; and TeE50X buffer: 0.05 M EDTA, 2.0 M Tris.

FWHM and PLQY); and their overall reaction yield (w/w). But all carboxylic acids (independent of type) examined in this work seem to abide the following basic rule (see Fig. 4.29D): The highest possible PLQY is achieved when the ratio ( $R$ ) between the amount of carboxylic acid groups  $\#COOH$  and the amount of Tris based alcohol groups  $\#OH$  is equal to one (1).

$$(4.1) \quad R = \frac{\#COOH}{\#OH} = \frac{N_{COOH} \cdot c_{CA}}{N_{OH} \cdot c_{Tris}} = 1$$

Where  $N_{\text{COOH}}$  and  $N_{\text{OH}}$  are the number of active carboxylic acid- and alcohol sides; and  $c_{\text{CA}}$  and  $c_{\text{Tris}}$  are the carboxylic acid- and Tris concentration, respectively. This support the notion that the CA/N-CND formation, to a large extent, is based on a condensation reaction of Tris and carboxylic acids [109].

At present it is not fully understood why certain carboxylic acids are more suited to efficiently form N-CNDs with very high PLQYs than others (see Table 4.2).

Table 4.2: Overview of various carboxylic acid types: the number of active carboxylic acid sides; and the PL properties (PL emission maximum  $\lambda_{\text{Max}}^{\text{Em}}$ , FWHM and PLQY) of resulting CA/N-CNDs are given.

Name	Abbreviation	$N_{\text{COOH}}$	$\lambda_{\text{Max}}^{\text{Em}}$ (nm)	FWHM (nm)	PLQY (a.u.)
1,2,3,4-butane-tetracarboxylic acid	BtA	4	413	89	0.05
Acetic acid	HAc	1	422	75	0.50
Citric acid	CiA	3	407	65	0.90
Malonic acid	McA	2	423	65	0.06
Oxalic acid	OxA	2	423	77	0.14
Succinic acid	SuA	2	416	76	0.10

### 4.3.7 Freeze Drying of CA/N-CND Solutions

In order to determine the overall yield of CA/N-CNDs obtained by Miw-hPC and to assess the long time stability of CA/N-CNDs as a solid powder, 250 mL of various types of CA/N-CND solutions were synthesized (e.g. HAc/N-CND Type 1 and Type 4; and CiA/N-CNDs) and subsequently freeze-dried. After freeze-drying for three days, obtained results varied widely. Subsequently further attempts, by means of different drying methods (e.g. vacuum desiccator, rotary evaporator and heating under ultra high vacuum), were undertaken. The results can be summarised as follows: (1) nitrogen-doping leads to increased hygroscopy; (2) differences in hygroscopy seem to be linked to the PLQY of CA/N-CNDs; i.e. high PLQYs go hand in hand with high hygroscopy; (3) the drying stage can be monitored through a change in colour as former dark brown solutions turn into a white to slightly yellowish-white solid (and vice versa); and (4) fully dried samples do not exhibit any PL under UV-light, but regain their PL properties upon dissolving in polar solvents (e.g. water, ethanol and acetone). Hence, depending on their hygroscopicity, "dried" CA/N-CNDs can be obtained in three forms (and everything in between): (1) a white to yellowish-white powder (PLQY  $\leq 15\%$ ); (2) a yellowish-white waxy solid (PLQY  $\leq 50\%$ ); and (3) a yellow-brown highly

viscous compound (PLQY  $\geq 80\%$ ). Because of their affinity for atmospheric moisture, CA/N-CNDs require storage in sealed containers, but are nevertheless stable either in solution or as a "dried" solid, giving them a distinct advantage over today's quantum dots. Similar to C-CNDs (see Chap. 4.1.4, p. 70), CA/N-CNDs maintain their PL emission properties when incorporated into a solid and dry matrix (e.g. paper and PVAL).

Wherever possible, the overall yield of CA/N-CNDs, obtained by MiW-hPC was assessed to be around 80 % (w/w), matching the results from previous CND synthesis [68, 109, 146, 219]. These excellent yields show the high efficiency of the here presented CA/N-CND synthesis via MiW-hPC of carboxylic acids, EDTA and Tris.

### 4.3.8 Structural Characterization of CA/N-CNDs

The functional groups within HAc/N-CNDs were characterized using FTIR spectroscopy, and as shown in Figure 4.30A C-CNDs and HAc/N-CNDs share some IR bands, thus revealing similar chemical compositions and structures. Noticeably, due to nitrogen doping, new characteristic peaks and a drastically changed fingerprint region emerged. Increasing peak intensity and peak broadening at  $3700\text{ cm}^{-1}$  to  $3000\text{ cm}^{-1}$  (spectral region marked in orange) is due to N-H stretching vibrations (from primary and secondary amines) appearing in addition to C-H- and O-H stretching vibrations (see Chap. 4.1.5, p. 71). The broad bands at  $3000\text{ cm}^{-1}$  to  $2500\text{ cm}^{-1}$  (aliphatic C-H stretch in alkanes and aldehydes) are much stronger for HAc/N-CNDs than for C-CNDs, due to less unsaturated structures in HAc/N-CNDs. The strong peaks at  $1568\text{ cm}^{-1}$  (N-H bend in primary amines) and  $1020\text{ cm}^{-1}$  (aliphatic amines) indicate successful nitrogen-doping. The band at  $1398\text{ cm}^{-1}$  (bend/rock vibrations in alkanes) further underline the saturated character of HAc/N-CND structures [80, 149]. Additionally, the strong peaks at  $900\text{ cm}^{-1}$  to  $625\text{ cm}^{-1}$  can be assigned to N-H wag vibrations.

Elemental composition of HAc/N-CNDs and CiA/N-CNDs was analyzed by energy-dispersive X-ray spectroscopy (see Fig. 4.30B and Fig. 4.31A). The as-synthesized HAc/N-CNDs consist mostly of C- and O-atoms (56.35 At.%; 33.07 At.%) and a significant amount of nitrogen (10.57 At.%). As shown in Figure 4.31A, HAc/N-CNDs and CiA/N-CNDs have a similar N-content (10.96 At.%), but differ in their carbon- (60.65 At.%) and oxygen-content (27.83 At.%).

The structural composition of HAc/N-CNDs and CA/N-CNDs could not be characterized by means of XRD and Raman measurements due to the lack of dry samples (see Chap. 4.3.7, p. 104). Furthermore, the strong luminescence background of HAc/N-CNDs and CiA/N-CNDs generally interfered with Raman scattering. NMR spectroscopy was employed for structural elucidation by means of separation of  $sp^2$ - and  $sp^3$ - hybridized carbon atoms in HAc/N-CNDs. The  $^1\text{H}$ -NMR spectra (see Fig. B.19, p. 146) gives rise to various signals: (a) strong signals in the range of 1 ppm to 4 ppm, stemming from  $sp^2$  carbon atoms (i.e. aliphatic compounds) and amines ( $\text{R}_2\text{NH}$ ); and (b) weak signals in the range of 8 ppm to 10 ppm, originating from aromatic ring hydrogen. Notably, no signals at 4 ppm to 6 ppm, attributed to carbonyls (e.g. carboxylates and amides),

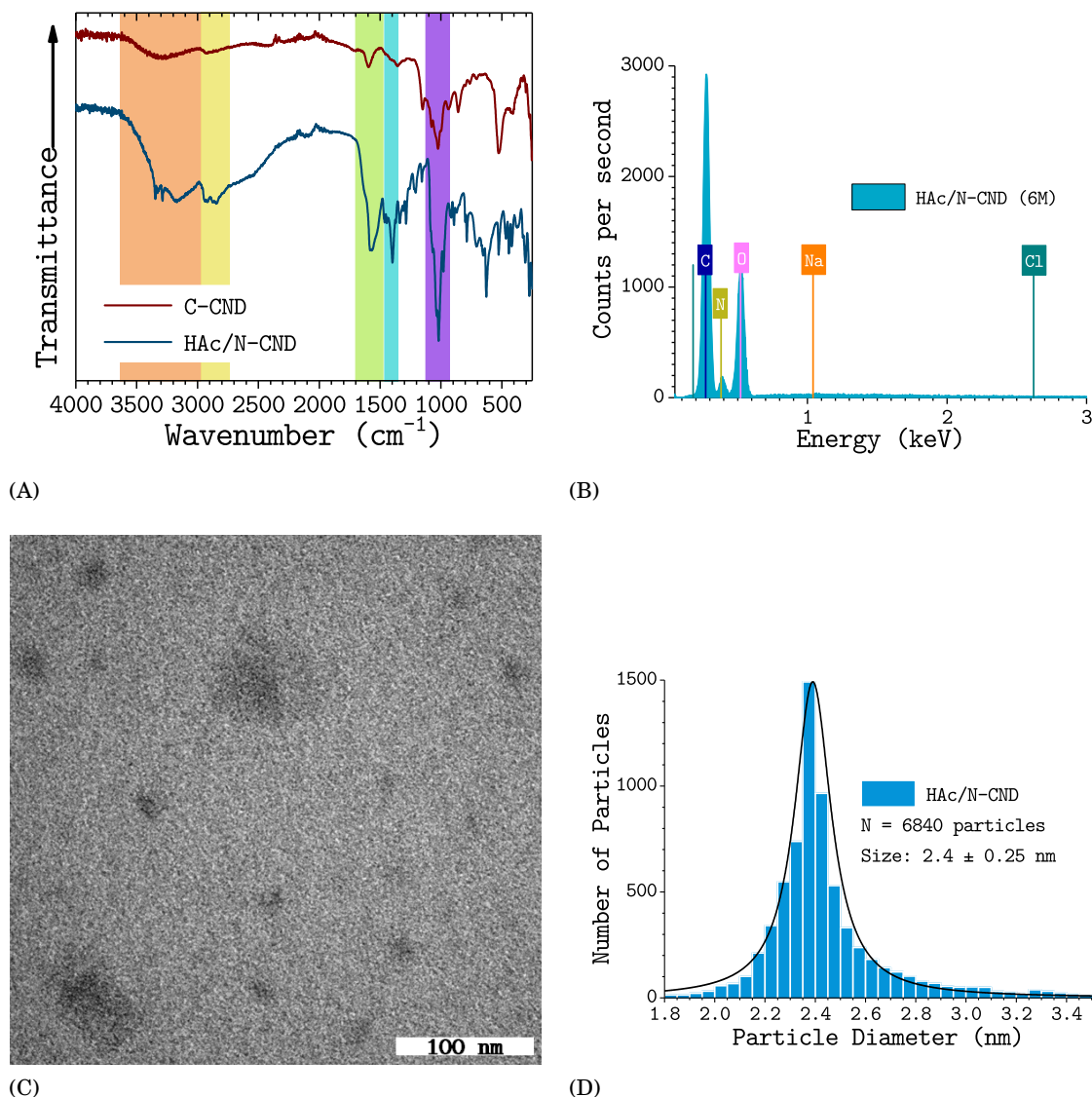


Figure 4.30: Structural characterization of HAC/N-CNDs: typical (A) FTIR spectra; (B) EDX spectra; (C) Transmission electron microscopy (TEM) images of HAC/N-CNDs and (D) the corresponding particle size distributions and Lorentzian curves obtained from the fitted data. Obtained from multiple Images the average particles sizes are reported at the 99% confidence interval. Total number of evaluated particles and the resulting average particle size are given in the inset.

were detected. The  $^{13}\text{C}$ -NMR (see Fig. B.20, p. 147) is dominated by very strong signals at around 39 ppm and medium signals at 55 ppm to 100 ppm, suggesting the presence of  $\text{sp}^3$  hybridized carbon atoms in aliphatic- and carbonyl compounds [150, 212]. In conflict with the  $^1\text{H}$ -NMR, weak signals beyond 100 ppm, which are indicative for  $\text{sp}^2$  hybridized carbon atoms, carboxyl- and amide groups [150], were observed. Hence the structural characterization of HAC/N-CNDs by means of NMR spectroscopy remains inconclusive.

TEM images (see Fig. 4.30C) gave no indication of crystalline particles. Nevertheless, the particle

### 4.3. SYNTHESIS AND CHARACTERISATION OF CARBOXYLIC ACID DERIVED, NITROGEN-DOPED CARBON NANODOTS

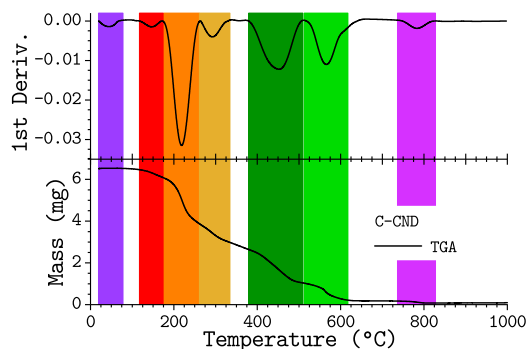
size of as-synthesized HAc/N-CNDs was determined to be comparatively small ( $2.40 \pm 0.25$ ) nm; with a narrow size distribution (see Fig. 4.30D).

As presented in Figure 4.31, the TGA analysis shows considerably different results for C-CNDs, HAc/N-CNDs and CiA/N-CNDs.

The behaviour of C-CNDs when heated in air is divided into seven main stages based on the

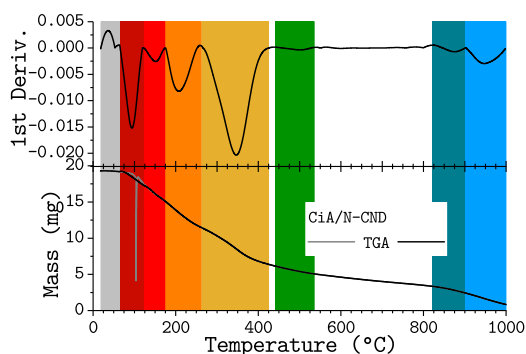
Sample	C (At.%)	N (At.%)	O (At.%)
C-CND*	56.6	1.26	40.09
HAc/N-CND	56.35	10.57	33.07
CiA/N-CND	60.65	10.96	27.83

also contains traces of:  
Na (0.46 At.%) and Cl (0.77 At.%)

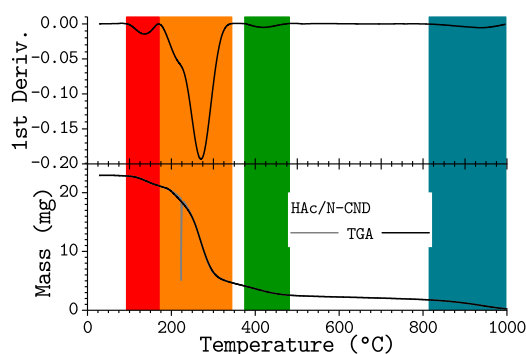


(A)

(B)



(C)



(D)

Figure 4.31: Structural characterization of CNDs obtained during this work: (A) Elemental content; (B) thermogravimetric analysis (TGA) of C-CNDs; (C) TGA analysis of HAc/N-CNDs; and (D) TGA analysis of CiA/N-CNDs. The grey curve indicates the original measurement and the black curve the corrected TGA curve to accommodate for buoyancy due to bubble formation.

TGA analysis. The first (20 °C to 70 °C) and second stage (114 °C to 172 °C) are accompanied by a 1.5 % mass loss each, largely associated with the release of water. The third (172 °C to 264 °C) and fourth stage (264 °C to 329 °C) are characterised by a mass loss of 42 % and 4.5 %, respectively. Both stages are associated with the release of carbon dioxide, due to decarboxylation of carboxylic surface groups and anhydride structures. The fifth (380 °C to 518 °C) and sixth stage (518 °C to 640 °C) are accompanied by significant mass losses of 27.8 % and 18.3 %, respectively. Both stages are associated with the combustive oxidation of C-CND remnants in air. The seventh stage (748 °C to 824 °C) is accompanied by a 2.3 % mass loss and yields a residual mass of about 2.1 %,

indicating completed combustion. The residual mass can be completely attributed to inorganic ash, due to traces of sodium chloride (NaCl; approx. 2.7 wt.%) in C-CNDs (see Chap. 4.1.5, p. 71). The behaviour of HAc/N-CNDs when heated in air is divided into four main stages based on the TGA analysis. The first step (91 °C to 169 °C) is accompanied by a 4.2 %, associated with the release of water. The second (169 °C to 340 °C) and third step (380 °C to 471 °C) are accompanied by a 89.3 % and 1.7 %, respectively. Both stages are associated with the release of carbon dioxide, water and nitrogen oxide, due to decarboxylation and combustive oxidation of HAc/N-CNDs. The fourth step (791 °C to 1000 °C) is accompanied by a 4.0 % mass loss and yields a residual mass of less than 1.0 %, indicating total combustion.

The behaviour of CiA/N-CNDs when heated in air is divided into eight main stages based on the TGA analysis. The first stage (19 °C to 53 °C) is characterized by a 2.8 % increase of mass, largely associated with the adsorption of water, due to CiA/N-CNDs high hygroscopicity (see Chap. 4.3.7, p. 104). The following four steps (2 to 5) lie very closely together and are accompanied by significant mass losses (87.4 % in total) and therefore are considered various steps during the decarboxylation and combustive oxidation of CiA/N-CNDs. The second (53 °C to 120 °C), third (120 °C to 175 °C), fourth (176 °C to 266 °C) and fifth step (266 °C to 425 °C) are accompanied by a 16.7 %, 2.7 %, 13.7 %, and 54.3 % mass loss, respectively. The sixth step (460 °C to 527 °C) is accompanied by a 0.5 % mass loss. The seventh (843 °C to 904 °C) and eighth step (904 °C to 1000 °C) are accompanied by a 1.1 % and 6.4 % mass loss, respectively. Both stages are associated with the combustive oxidation of CiA/N-CND remnants in air. The residual mass is very high at 7.4 % and may indicate hard-combustible residues, due to the absence of inorganic content in CiA/N-CNDs (see Fig. 4.31).

For the quantification of primary amino groups on the HAc/N-CND surface a modified photometric assay based on the Kaiser test, developed by Jarre *et al.* [62], was used. This colorimetric method is characterized by its ease of use and high selectivity for primary amines; since secondary-, tertiary- and aromatic amines do not yield positive test results (see Chap. 3.1.4, p. 49) [62]. As presented in Figure 4.32A and Figure 4.32B, the Kaiser test proved to be a valuable tool for primary amine detection on the HAc/N-CND surface. The obtained results can be summarized as follows: (1) after 5 minutes the free primary amine concentration is reduced to about 12.5 % of its initial concentration (Tris: 2.0 M), due to rapid HAc/N-CND formation (see Chap. 4.3.4, p. 96); (2) prim. amine concentration undergoes a gradual but steady decline with proceeding synthesis reaction time; and (3) after 120 minutes of synthesis reaction time the prim. amine concentration is about 0.1M, i.e. about 5 % of its initial concentration provided by Tris (2.0 M). These findings indicate a high number of free primary amine sides per HAc/N-CND particle, making them a promising material for functionalization and wide range of applications (e.g. FRET-sensors, bio-technology and bio-imaging).

In order to assess the suitability of as-synthesized C-CNDs and HAc/N-CNDs for future applications, two different functionalization routes were employed, targeting the CNDs respective



### 4.3. SYNTHESIS AND CHARACTERISATION OF CARBOXYLIC ACID DERIVED, NITROGEN-DOPED CARBON NANODOTS

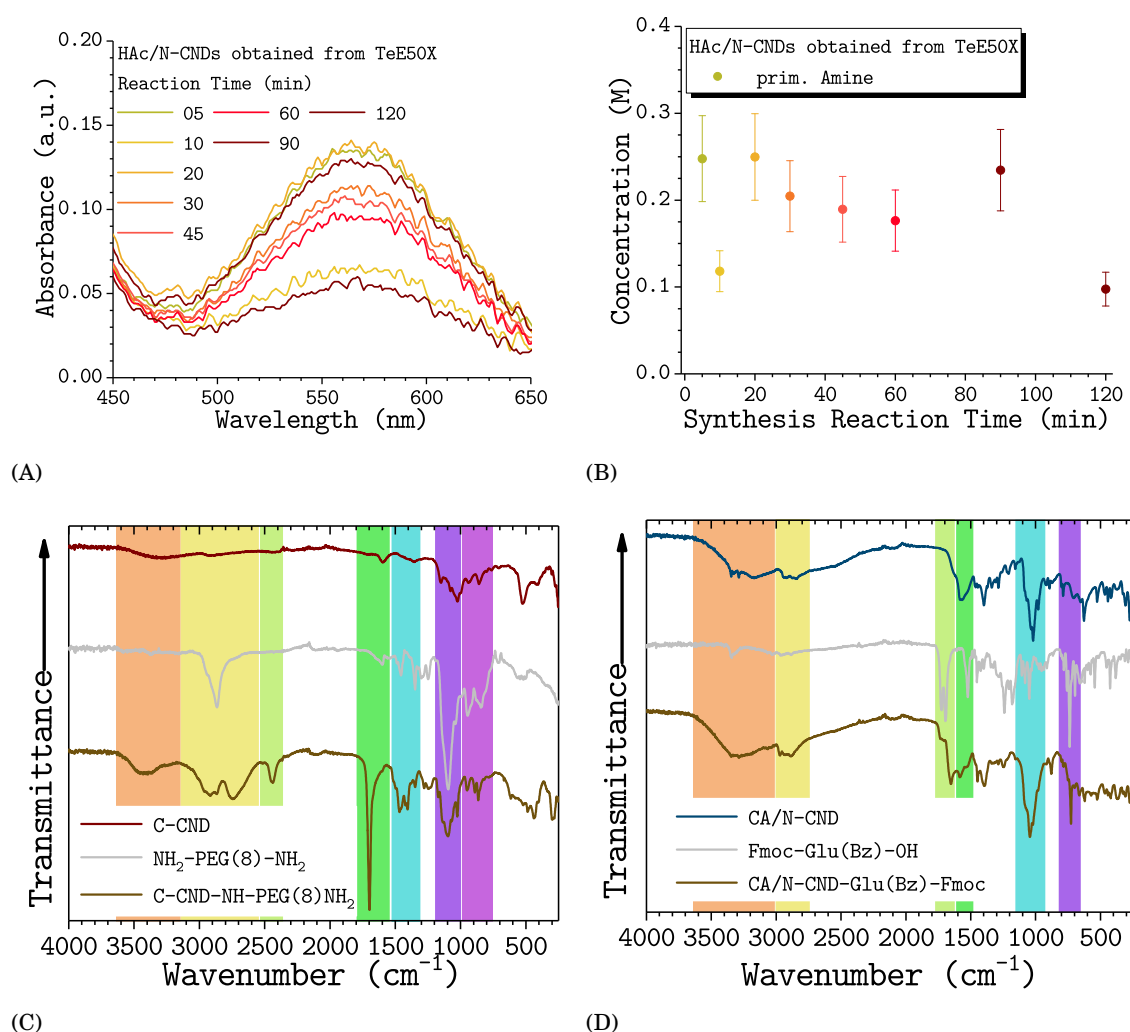


Figure 4.32: Structural characterization of HAC/N-CNDs (derived from TeE50X buffer solution) via modified Kaiser test according to Jarre *et al.* [62]: (A) UV-Vis absorption spectra of various HAC/N-CND types after successful Kaiser test; and (B) the obtained corresponding primary amine concentrations as a function of HAC/N-CND synthesis reaction time. FTIR spectra of (C) C-CNDs functionalized with PEG ( $\text{NH}_2\text{-PEG}(8)\text{-NH}_2$ ) via a thionyl chloride assisted route; and (D) HAC/N-CNDs functionalized with glutamic acid via DCC-coupling. The upper and lower curves represent the CNDs prior to (top) and after (bottom) functionalization, respectively. The grey curve represents the agents used for functionalization prior to conjugation. TeE50X buffer: 0.05 M EDTA, 2.0 M Tris, 7.0 M HAc

surface groups. C-CNDs were functionalised with PEG ( $\text{NH}_2\text{-PEG}(8)\text{-NH}_2$ ) via a thionyl chloride assisted route, targeting the carboxylic acid groups on the C-CNDs surface (see Fig. B.8, p. 136). In the case of HAC/N-CNDs, functionalization with glutamic acid was performed via a DCC-coupling route, targeting the primary amines on the HAC/N-CNDs surface (see Fig. B.9, p. 136). Successful functionalization was confirmed through FTIR spectroscopy (see Fig. 4.32C

and Fig. 4.32D). The results do not only show that the targeted surface groups (C-CNDs: carboxylic acids; HAc/N-CNDs: prim. amines) are present in as-synthesised CNDs, but also facile functionalization for future applications and adjustment of physicochemical properties.

### 4.3.9 Photophysical Characterization of CA/N-CNDs

Single-particle fluorescence microscopy (see Chap. 3.3.1.5, p. 55) was employed to assess whether or not as-synthesised CNDs are subject to fluorescence intermittency (i.e. blinking). As presented in Figure 4.33A, HAc/N-CNDs exhibit stable and prolonged PL emission over a long period of time. Throughout the single-particle measurements no signs of fluorescence intermittency were detected for as-synthesized HAc/N-CNDs.

As a complement, time-correlated single photon counting (TCSPC) measurements were performed for all three major types of CNDs presented in this work (see Fig. 4.33C and Fig. 4.33D).

The obtained fluorescence decay curves differ significantly between the different CND types and

Table 4.3: Excited state lifetimes of CNDs in aqueous PBS buffer solution (pH 7.0) under excitation at 375 nm (OD 0.1 at 340 nm) at room temperature.

CND type	1	2	3	4
C-CND	68 ps (7.2 %)	1.03 ns (30.4 %)	2.45 ns (57.2 %)	9.54 ns (5.3 %)
HAc/N-CND	1.64 ns (5.3 %)	6.35 ns (9.9 %)	20.38 ns (84.8 %)	
CiA/N-CND	11.09 ns (17.3 %)	18.28 ns (82.7 %)		

are best fit by multiexponential fitting functions yielding average lifetimes of 2.22 ns, 18.0 ns and 17.0 ns for C-CNDs, HAc/N-CNDs and CiA-CNDs, respectively (see Table 4.3). These findings can be caused by a number of reasons: (1) several competing deactivation pathways within the same CND particles; (2) a broad dispersion of recombination rates for the same radiative deactivation process; or (3) simultaneous luminescence from different particles.

#### 4.3.9.1 Selective Luminescence of CA/N-CNDs

The selective luminescence behaviour of CA/N-CNDs was quantified by means of: (I) excitation-emission matrix measurements (EEM; see Fig. 4.34) and (II) 3D-excitation spectra matrix measurements (3DEM; see Fig. 4.36), throughout the visible spectrum.<sup>1</sup> The center of PL emission was determined by identifying the center of gravity of the PL emission peak according to the

<sup>1</sup>For clarification: (I) EEM spectra (see Chap. 3.3.1.2, p. 54) are obtained by stacking steady-state photoluminescence emission spectra measured at various excitation wavelength, whereas (II) 3DEM spectra (see Chap. 3.3.1.2, p. 54) are obtained by stacking steady-state photoluminescence excitation spectra measured at various emission wavelength (i.e. observed  $\lambda_{Em}$ ).

4.3. SYNTHESIS AND CHARACTERISATION OF CARBOXYLIC ACID DERIVED,  
NITROGEN-DOPED CARBON NANODOTS

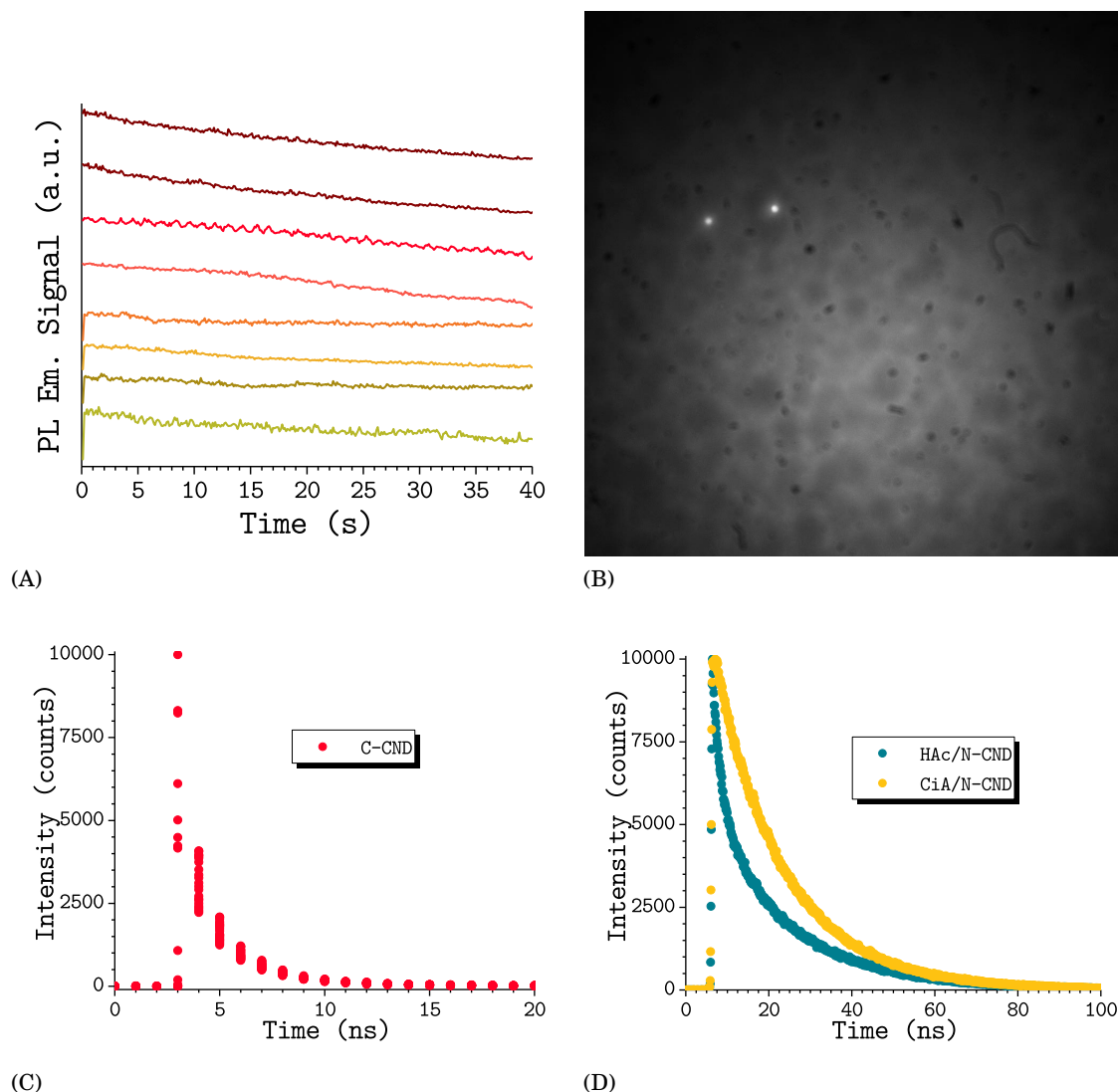


Figure 4.33: Single particle microscopy of HAC/N-CNDs in PVAL ( $\lambda_{Exc} = 488 \text{ nm}$ ,  $\lambda_{Em} = 535 \text{ nm}$ ): (A) Representative, background subtracted, integrated PL emission intensities, as a function of time, of eight single HAC/N-CND particles; and (B) selected confocal fluorescence microscopy image showing two particles. Time-correlated single photon counting (TCSPC) measurements ( $\lambda_{Exc} = 375 \text{ nm}$ ): characteristic fluorescence decay curves for (C) C-CNDs; and (D) HAC/N-CNDs and CiA/N-CNDs.

method presented by Lakowicz [78]. The shift of PL emission wavelength and -FWHM versus the excitation wavelength are then plotted in Figure 4.35 for various HAC/N-CND types and -concentrations.

As presented in Figure 4.34 and Figure 4.38D no selective luminescence was observed for CiA/N-CNDs. However, despite sharing the same synthesis method and similar starting materials as CiA/N-CNDs, selective luminescence was observed for all types of HAC/N-CNDs (see Fig. 4.35

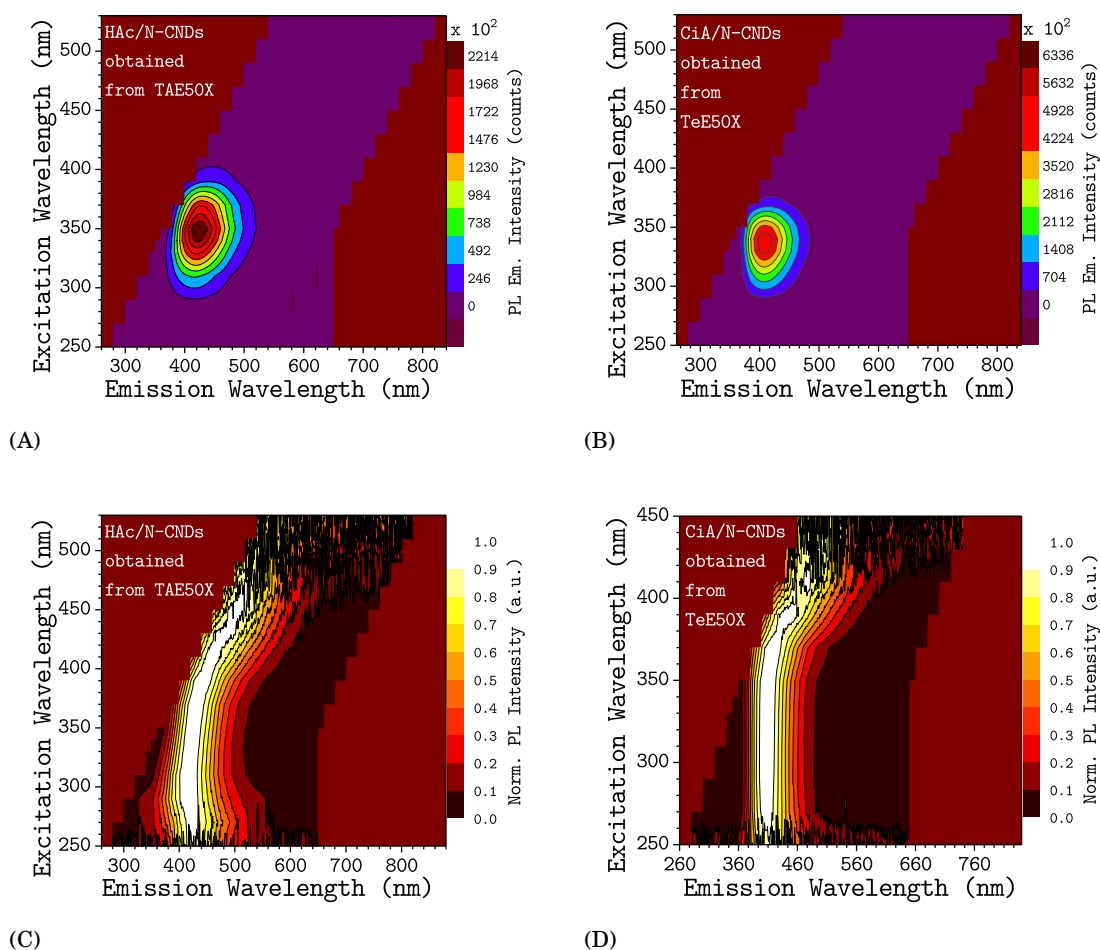


Figure 4.34: Characteristic excitation-emission matrix (EEM) measurements for HAC/N-CNDs and CiA/N-CNDs in aqueous PBS buffer (pH 7.0): (A,B) PL emission EEM; and (C,D) corresponding normalized PL emission EEM for HAC/N-CNDs (OD 0.1 at 350 nm) and CiA/N-CNDs (OD 0.1 at 340 nm), respectively.

and Chap. B.2.1, p. 137). Furthermore, contrary to earlier findings [21, 22], HAC/N-CNDs do not exhibit broad PL emission bandwidth, often linked to selective luminescence behaviour. In HAC/N-CNDs the solvation processes are presumably slowed to the same time scale as that of fluorescence (see Chap. 2.3.3.4, p. 37), hence, emission occurs over a wide excitation range of about 300 nm (see Fig. 4.35). Regarding the PL emission wavelength and -FWHM (see Fig. 4.35), the selective luminescence behaviour is virtually unaffected by HAC/N-CNDs type or -concentration (i.e. optical density). Nevertheless, the excitation wavelength has a significant impact on the PL emission wavelength and -FWHM. The wavelength dependent behaviour of HAC/N-CNDs results in a tunable PL emission range of about 200 nm (from about 413 nm to about 600 nm), caused by an excitation wavelength red-shift of about 320 nm (from 250 nm to 570 nm). Apparently, the strong linearity between PL emission- and excitation wavelength does not apply for the FWHM

### 4.3. SYNTHESIS AND CHARACTERISATION OF CARBOXYLIC ACID DERIVED, NITROGEN-DOPED CARBON NANODOTS

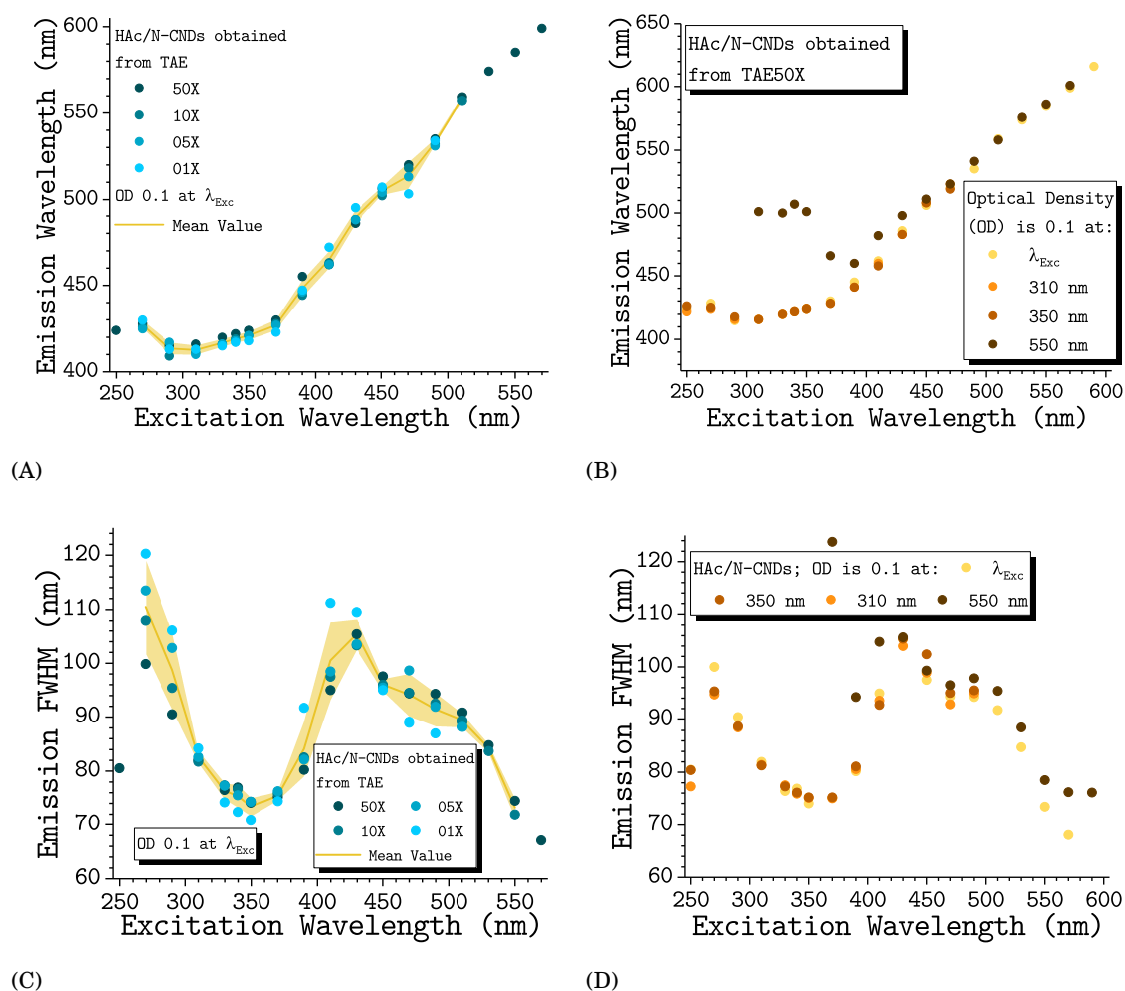


Figure 4.35: Influence of excitation wavelength on PL emission properties: (A,B) PL emission maximum and (C,D) PL emission FWHM as a function of excitation wavelength, for various HAc/N-CND types (blue, left) and -concentrations (yellow, right). Shaded regions around graph represent the standard deviation. For the

(see Fig. 4.35C and Fig. 4.35D). The above shown results support the notion that despite sharing the same synthesis method and similar starting materials, HAc/N-CNDs and CiA/N-CNDs are fundamentally different in their structural composition. CiA/N-CNDs display photophysical properties (e.g. high PLQY and absence of wavelength-dependent behaviour) arising from an ordered structure, i.e. absence of defects, whereas HAc/N-CNDs display photophysical properties (e.g. medium PLQY and presence of wavelength-dependent behaviour) arising from a less ordered structure, i.e. presence of defects. In CDs defects can lead to out-of-plane strain, which was shown to be responsible for selective luminescence behaviour through an excited state process called GREES (see Chap. 2.3.3.4, p. 37) [21].

Excitation spectra can be particularly useful to determine excited state processes in chro-

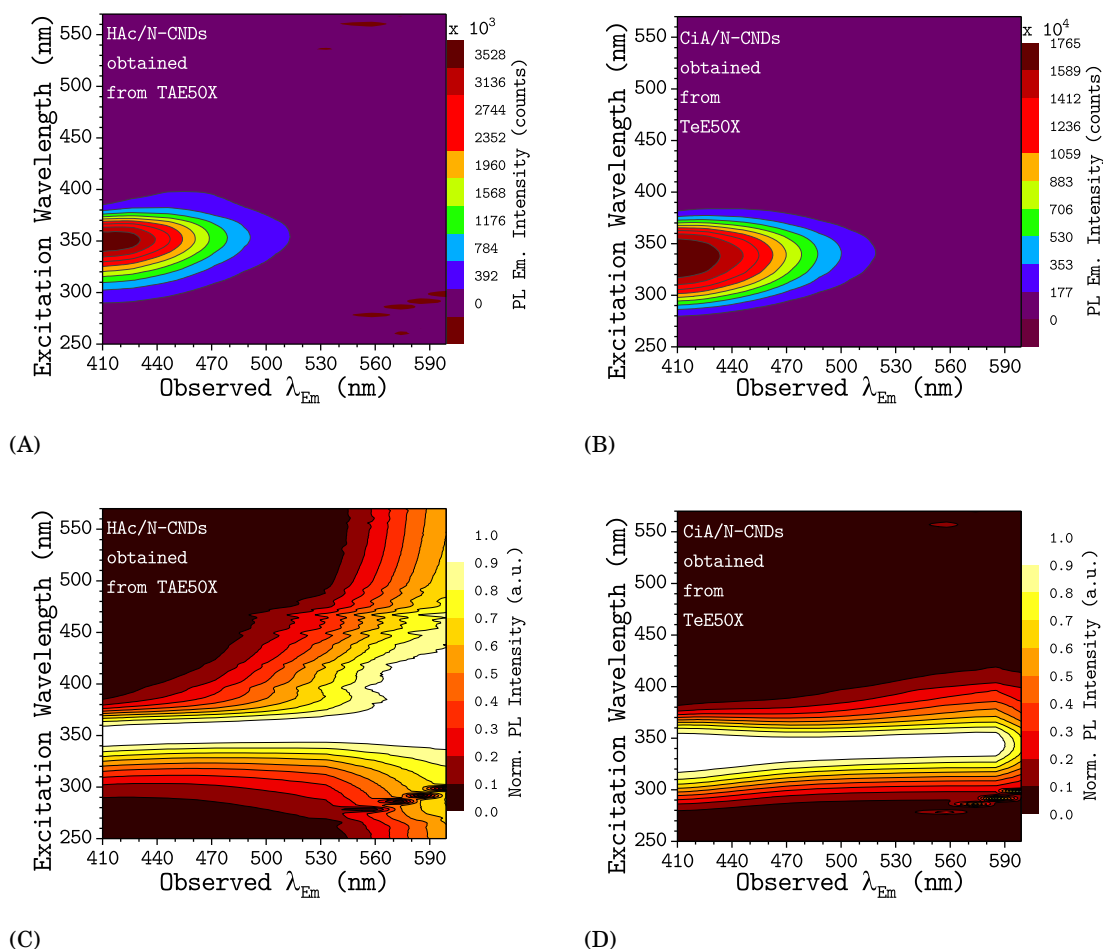


Figure 4.36: Characteristic 3D-excitation spectra matrix (3DEM) measurements for HAc/N-CNDs and CiA/N-CNDs in aqueous PBS buffer (pH 7.0): (A,B) 3DEM; and (C,D) corresponding normalized 3DEM for HAc/N-CNDs (OD 0.1 at 250 nm) and CiA/N-CNDs (OD 0.1 at 340 nm), respectively.

mophores, as they display the excitation wavelength necessary to produce PL emission from the chromophore (at a particular emission wavelength) [78, 164]. As presented in Figure 4.36 and Figure 4.37, the excitation spectra of HAc/N-CNDs and CiA/N-CNDs are virtually unaffected by the excitation wavelength. The results for the excitation spectra can be summarized as follows: (1) the excitation maximum red-shifts only slightly (about 15 nm) over the tunable emission range of about 200 nm (see Fig. 4.37A); and (2) the excitation FWHM increases significantly over the tunable emission range (see Fig. 4.37A). The above shown results further support the notion that the emission in HAc/N-CNDs occurs from the same excited state (e.g.  $S_1$ ), independent of excitation wavelength, and that an excited state process like GREES (see Chap. 2.3.3.4, p. 37) is the origin for the selective luminescence in HAc/N-CNDs.

As presented in Figure 4.37C and Figure 4.37D, the PLQY of as-synthesized HAc/N-CNDs not

### 4.3. SYNTHESIS AND CHARACTERISATION OF CARBOXYLIC ACID DERIVED, NITROGEN-DOPED CARBON NANODOTS

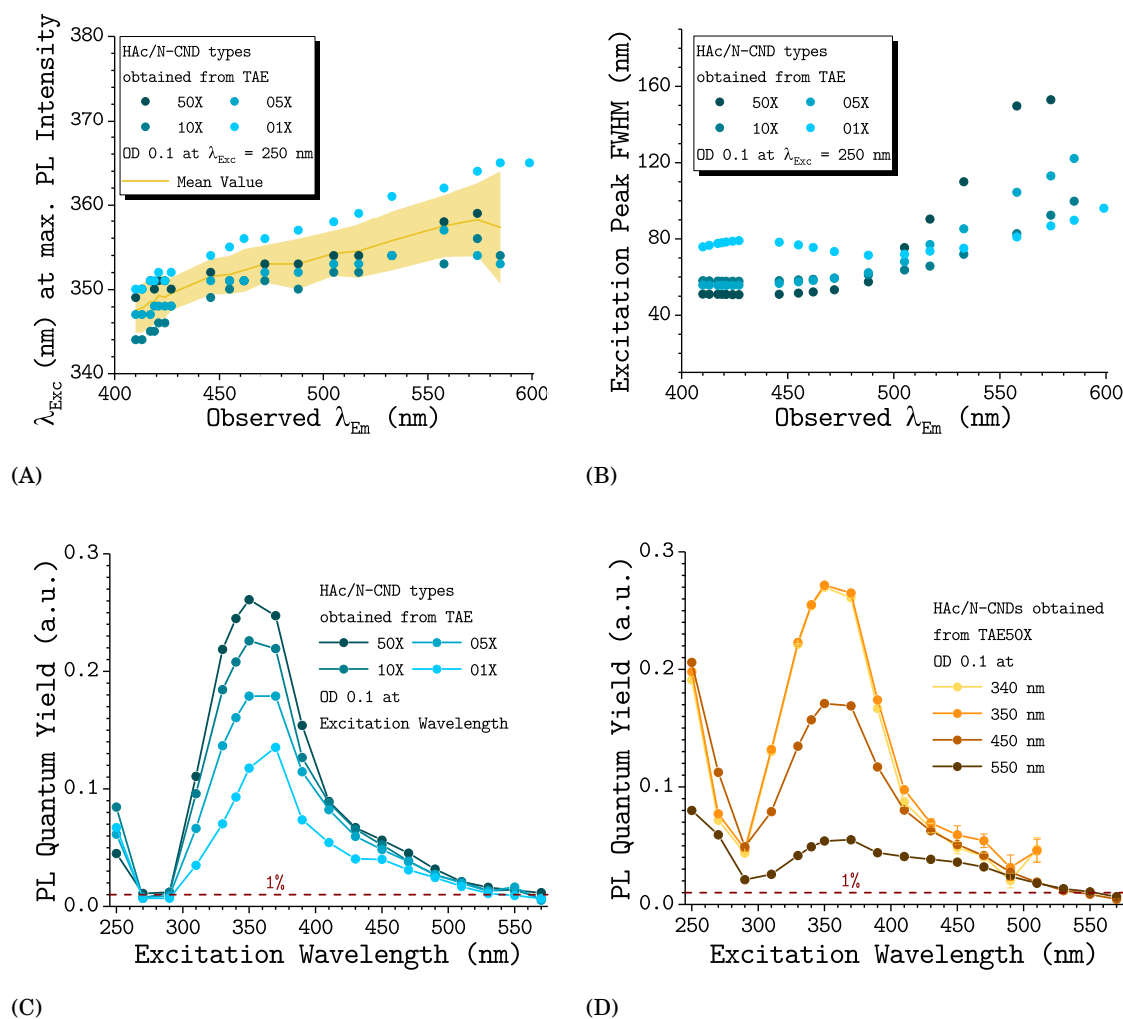


Figure 4.37: Influence of excitation wavelength on PL emission properties: (A) Excitation maximum; and (B) Excitation FWHM as a function of the PL emission wavelength for various HAC/N-CND types (blue); (C,D) PLQY as a function of excitation wavelength, for various HAC/N-CND types (blue) and -concentrations (yellow), respectively. Shaded regions around graph represent the standard deviation.

only depends on the HAC/N-CND type (see Chap. 4.3.3, p. 92), but also on the HAC/N-CND concentration and the excitation wavelength. Regarding the PLQY, the results can be summarized as follows: (1) the maximum PLQY is obtained for excitation at 360 nm, independent of HAC/N-CND type and -concentration; (2) the PLQY decreases with increasing CND concentration, probably due to agglomeration; and (3) the PLQY mirrors the corresponding excitation spectra (see Fig. 4.38A). These results are consistent with all types of HAC/N-CNDs (see Chap. B.2.1, p. 137), and hence support the notion that all types of HAC/N-CNDs share a similar structure and photophysical behaviour. Apparently, HAC/N-CND types differ only in their PLQY, i.e. in the efficiency of their radiative recombination. As presented in Figure 4.38B and Figure 4.38C the



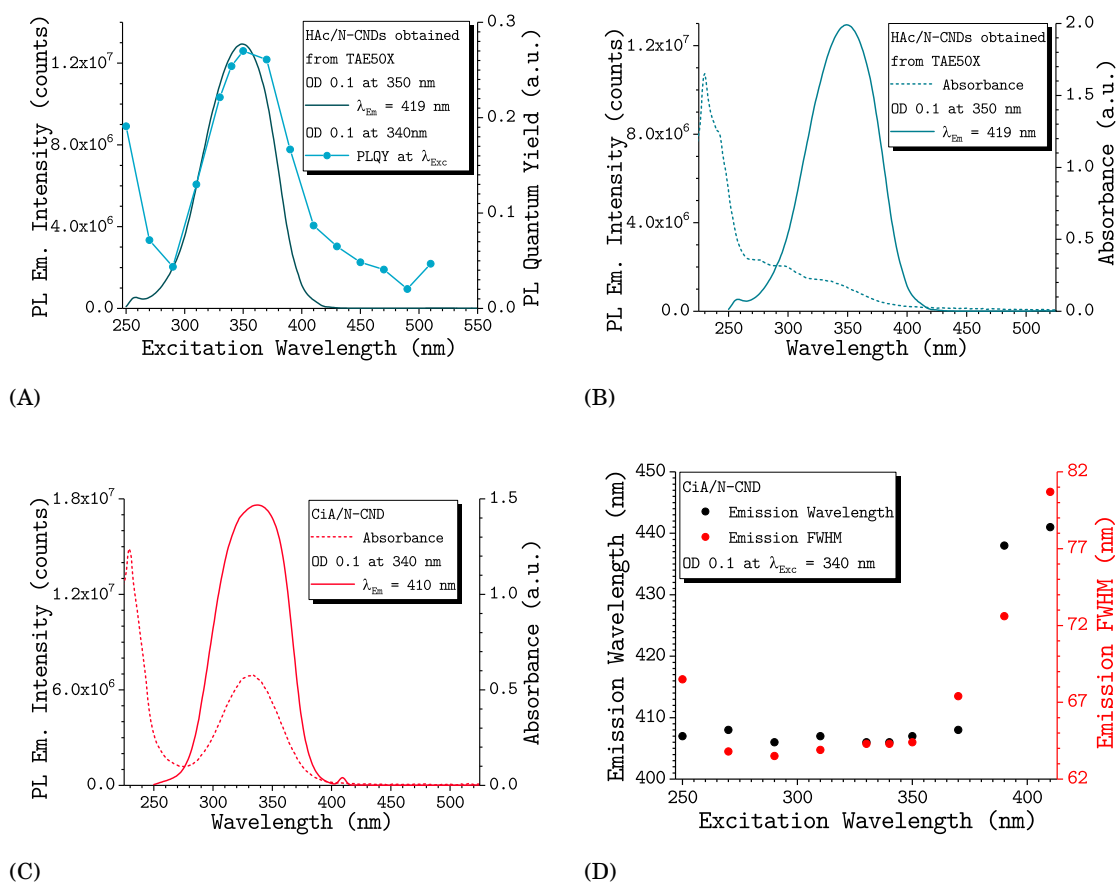


Figure 4.38: Characteristic influence of excitation wavelength on PL emission properties of HAc/N-CNDs and CiA/N-CNDs. (A) Superimposed representation of excitation spectrum ( $\lambda_{Em} = 419$  nm) and PLQY, of HAc/N-CND, as a function of excitation wavelength. (B) Superimposed representation of excitation spectrum ( $\lambda_{Em} = 419$  nm) and UV-Vis absorption spectrum of HAc/N-CND. (C) Superimposed representation of: (C) excitation spectrum ( $\lambda_{Em} = 410$  nm) and UV-Vis absorption spectrum of CiA/N-CND; and (D) PL emission maximum and PL emission FWHM, of CiA/N-CND, as a function of excitation wavelength. CNDs were obtained from TeE50X buffer solutions.

excitation and absorption spectra of both HAc/N-CNDs and CiA/N-CNDs are not superimposable. Hence, either a mixture of several N-CND types is present, or N-CNDs possess different ground states [164]. While the former cannot be completely excluded, the latter appears to be more likely, given the fact that as-prepared CA/N-CNDs proved to be both highly homogeneous in their photoluminescence properties and size distribution. Nevertheless, the position and similarity of excitation spectra for both HAc/N-CNDs and CiA/N-CNDs (see Fig. 4.38B and Fig. 4.38C) lead to the conclusion that excited state processes are similar in HAc/N-CNDs and CiA/N-CNDs and that successful emission occurs upon excitation of the CND carbon core.

In summary, the exact origin of photoluminescence and selective luminescence in carbon nan-



odots is still elusive. Nevertheless, the results presented in this work lead to the conclusion that successful emission occurs upon excitation of the CND carbon core (see Fig. 4.38B and Fig. 4.38C), while emission occurs from the CND surface. Hence, the PL emission properties (e.g. PL emission wavelength, FWHM) are determined by the CNDs surface groups and structure. The CND structure, in particular, plays a crucial role in excitation wavelength dependent behaviour (see

#### 4.3.10 Summary

A new reliable, one-step CA/N-CND synthesis based on hydrothermal treatment of Tris, EDTA and carboxylic acids, with a low environmental footprint, and at reasonable costs is presented. Two major types of CA/N-CNDs, with a high yield of approximately 80 % (w/w), have been prepared using two different sets of starting materials, referred to as HAc/N-CND (acetic acid in TeE) and CiA/N-CND (citric acid in TeE). The as-prepared CA/N-CNDs are highly homogeneous in their photoluminescence properties and size distribution, and are ready to use without need for further purification, modification or surface passivation. The CA/N-CNDs are comparatively small (HAc/N-CNDs:  $2.40 \pm 0.25$  nm) with narrow size distributions; are stable over a long period of time, either in solution or as a solid and maintain their photoluminescence properties when re-dispersed in polar solvents or matrices. Depending on starting material, CA/N-CNDs with photoluminescence quantum yields in the range of 9 % to 90 % were obtained. Furthermore, PL measurements demonstrated that the photophysical properties of as-synthesized CA/N-CNDs are independent of reaction time and -temperature. Nevertheless, the PLQY of as-synthesized CA/N-CNDs was considerably enhanced by means of increased reaction temperatures, -time and optimized precursor concentration and -composition. This chapter also addressed the following issues and their influence on the CA/N-CND formation: influence of (1) reaction time and -temperature, (2) precursor concentration, and (3) type of C-source. Furthermore, the stability of CA/N-CNDs over time, both in solution and as dry solid was investigated. Noticeably, the photophysical properties of CA/N-CNDs stayed unaffected during conversion into a solid and back into solution. Additionally, in comparison to other methods used to prepare nitrogen-doped CNDs, the MiW-hPC presented in this work leads to barely any impurities or by-products, and thus can be considered as superior over other synthesis methods.

The highest PLQYs for CiA/N-CNDs and HAc/N-CNDs of 90 % and 50 %, respectively, were obtained for a reaction temperature of 230 °C, making them one of the highest PLQY values reported for CDs so far (see Table C.1, p. 150). The obtained PLQYs are well in the range of recently reported PLQY for an alginate/tryptophan mixture (47.9 %) [219], and citric acid/ethylendiamin mixtures (73.1 % to 94 %) [84, 133, 212]; but still lower than the highest known value for a citric acid/Tris mixture ( $\leq 99$  %) [197]. Nevertheless, the obtained PLQYs are still significantly higher than the PLQY values reported for most other carbon dots (see Table C.1, p. 150). The strong linearity between PLQY and synthesis temperature (see Chap. 4.3.1, p. 88) suggests that even

higher PLQYs could be achieved with much higher reaction temperatures. Furthermore, there are indications and some initial evidence that post-synthesis oxidation- and reduction treatment (of CND surface groups) can significantly increase the overall PLQY; without significantly altering the absorption- and PL emission properties (see Fig. B.5, p. 133 to Fig. B.7, p. 135). Nevertheless, as-synthesized CA/N-CNDs can be considered equal to or better than commercially available CdSe/ZnS quantum dots (e.g. QDot525); especially with respect to their size distribution and quantum yield. Furthermore, CA/N-CNDs can be synthesized at a fraction of the cost of conventional quantum dots (see Table B.4, p. 129).

CA/N-CNDs share many advantages with their analogues, such as good solubility in water, high colloidal stability, stable emission under a wide range of pH values, and high photostability either in solution or as dried solid. However, nitrogen doping also leads to significant differences in the photophysical- and chemical properties. Compared to C-CNDs, CA/N-CNDs have significantly higher PLQYs, blue-shifted PL emission spectra and a significantly increased hygroscopicity.

Furthermore, the origin of PL emission and selective luminescence behaviour was investigated by means of: (1) excitation versus PL emission wavelength measurements (EEM), (2) 3D-excitation spectra measurements (3DEM), and (3) PLQY measurements. No selective luminescence was observed for CiA/N-CNDs. However, despite sharing the same synthesis method and similar starting materials, selective luminescence was observed for all types of HAc/N-CNDs. The obtained results support the notion that for CNDs the nature of the surface states determines the photoluminescence properties and that selective luminescence behaviour is caused by the "Giant Red-Edge Excitation Shift" (GREES).

Like their analogues, CA/N-CNDs may be interesting for a wide range of applications and further comparative studies are needed, shedding light on the nature of CND emission properties. Especially their high PLQY, ease of functionalization, high photostability and potentially low toxicity make CA/N-CNDs well suited as fluorescence markers for bio-imaging and -sensing [13, 47, 127, 140, 155].

## SUMMARY AND OUTLOOK

Since their discovery in 2004, a multitude of synthesis routes have been developed to obtain CDs of various types and quality. In particular, the ability to prepare CDs from a wide range of accessible organic materials is in drastic contrast to the much more laborious and expensive synthesis routes for other fluorescent nanoparticles, e.g. fluorescent upconversion nanoparticles (UCNPs) and QDs. However, CDs with high PLQYs still remain rare; and current synthesis methods are typically expensive, depend on complex and time-consuming processes or severe synthesis conditions and toxic chemicals. Consequently, new approaches and techniques were needed to obtain homogeneous CDs (with high PLQYs) in a reliable and reproducible way. In order to attain this objective, a fundamental understanding of the CD formation mechanisms, well-defined starting materials and deliberate use of additives is both fundamentally and technically critical. With this in mind, the aim of this work was the development of a new method to overcome aforementioned challenges; thereby paving the way for future large-scale applications of CDs.

An essential part of this work was the utilization of a microwave synthesis reactor, and the hereby-achieved high sample throughput allowed, for the first time, the thorough investigation of a wide range of synthesis parameters, providing valuable insight into the CND formation. In the course of this work, the influence of carbon source, nitrogen additive, precursor concentration and -combination were studied. Additionally, the influence of batch size, reaction time and -temperature, and post-synthesis purification steps were also studied. The achieved high sample throughput required an assessment of obtained CND quality in a quick, but meaningful way. Hence, obtained CND solutions were assessed based on their photophysical properties: UV-Vis absorption spectra (as evidence for molecular structure); position of emission maximum (at a given excitation wavelength); FWHM of the (main) emission band (as means for homogeneity

of obtained CNDs); and PLQY (as means for suitability as fluorescence marker). Selected CND samples were also subject to EDX, FTIR, NMR, photoluminescence lifetime, particle size (TEM), TIRFM, TGA and XRD analysis. Besides structural characterization, the pH- and excitation dependent PL characteristics (i.e. selective luminescence) were examined; giving inside into the origin of the photophysical properties and excitation dependent behaviour of CNDs.

The presented synthesis method is based on the microwave-assisted hydrothermal precursor carbonization of aqueous solutions of starch or various carboxylic acids (as carbon sources) in combination with Tris and EDTA (as nitrogen additives). All materials that can be obtained worldwide at low cost with well-defined properties, in a wide variation of types, and in large quantities without being in competition with food industry. Continuous improvement of the aforementioned synthesis parameters lead to a new, reliable one-step synthesis method, which shortens reaction times to several minutes and eliminates steps involving toxic or dangerous materials, whilst being scalable, and easy to operate. Hence, allowing the large-scale production of homogeneous and water-soluble CNDs, with well-defined and reproducible photoluminescence properties, at reasonable costs (approx. €6.60/g), and low environmental footprint. Depending on starting materials and reaction conditions different types of CNDs, with high yields of approximately 80 % (w/w), have been prepared. Although different in many respects, all three major CND types, namely: (1) starch derived carbon nanodots (C-CNDs), (2) starch derived-nitrogen doped carbon nanodots (C/N-CNDs) and (3) carboxylic acid derived-nitrogen doped carbon nanodots (CA/N-CNDs); share essential properties. They are all amorphous in structure; exhibit reproducible, highly homogeneous and favourable photoluminescence properties with narrow emission bands (approx. 70 nm FWHM); are non-blinking; and are ready to use without need for further purification, modification or surface passivation agents (e.g. PEG). Depending on CND type, the PLQY lies in the range of 1 % to 90 %; one of the highest PLQY values reported (for CDs) so far. Depending on their carboxylic acid type, CA/N-CNDs can vary significantly with respect to their PL emission properties (e.g. emission bandwidth, FWHM and PLQY); and their overall reaction yield (w/w). Nevertheless, all CA/N-CNDs examined in this work abide a basic rule: The highest possible PLQY is achieved when the ratio between the amount of carboxylic acid groups and the amount of Tris based alcohol groups is equal to one (1). Hence, supporting the notion that the CA/N-CND formation, to a large extent, is based on a condensation reaction of Tris and carboxylic acids.

Nevertheless, as-synthesized CNDs are comparatively small (approx. 2 nm to 3 nm), with narrow size distributions; are stable over a long period of time (at least one year), either in solution or as dried solid and maintain their PL properties when re-dispersed in solution. Remarkably, and independent of CND type, the initial brown CND-solutions turn into a non-fluorescent white/slightly yellow to brown solid upon drying, while regaining their full PL properties when re-dispersed in solution. Hence, as-synthesized CNDs can be easily stored and transported as dried solid, giving them a distinct advantage over a wide range of today's nanoparticles, e.g.

---

quantum dots.

Concerning the photoluminescence mechanisms and processes in CNDs, the exact origin of photoluminescence and selective luminescence in CNDs is still elusive. Nevertheless, the results presented in this work lead to the conclusion that successful emission occurs upon excitation of the CND carbon core, while emission occurs from the CND surface. Hence, the PL emission properties (e.g. PL emission wavelength, FWHM) are determined by the CNDs surface groups and structure. Moreover, the measurements indicate that the CND structure (in particular) causes the "Giant Red-Edge Excitation Shift" and is therefore responsible for the selective luminescence behaviour of CNDs.

Although, still being in an early stage, CDs have already demonstrated enormous potential in a wide range of applications, namely: nanoelectronics, energy storage and -conversion, photocatalysis, and optoelectronic devices. Especially the high PLQY, ease of functionalization, high photostability and potentially low toxicity of as-synthesized CNDs make them particularly suitable for bioimaging and -sensing, optical sensing, drug/gene delivery, and theranostics. For example, CNDs (in combination with magnetic nanoparticles) can be used as fluorescent magnetic nanoparticles (FMNs) for magnetic-directed drug delivery or magnetic resonance imaging. Nevertheless, while having proven and anticipated advantages over conventional fluorophores (e.g. QDs), a number of issues remain to be tackled before their full potential can be exploited. Bioimaging and -sensing applications (e.g. deep tissue imaging) in particular desire excitation and PL emission in the long-wavelength regions. Unfortunately, most CDs only possess strong PL emission in the blue, rarely green wavelength region, and only a small fraction possesses optimal PL emission in long-wavelength regions. Therefore, the crucial challenge is to take control over CNDs selective luminescence behaviour by determining and separating the predominant factors responsible for the excitation dependent behaviour. For example, CND surface groups and structure (e.g. defects) are widely claimed to be responsible for the PL emission properties and excitation dependent behaviour, but there is a remaining challenge to correlate specific functional groups to specific emission wavelength. Even if the exact origin of the luminescence and the mechanisms involved are still unknown; the ability to produce CNDs cost-effectively and therefore overcoming the main obstacle of commercial usage; makes them very interesting for a wide range of commercial applications. In this respect they can become superior to semiconductor quantum dots. Future efforts should therefore target towards more advanced spectroscopic technologies such as single particle spectroscopy and -microscopy, ultrafast spectroscopy, and multiplexed fluorescence lifetime measurements. Single particle microscopy, for example, can be applied to determine whether a single particle emits at multiple emission wavelengths or separate particles (types) are responsible for the observed excitation dependent behaviour. Nevertheless, the red-edge effect has great potential impact on biological sensing (e.g. FRET), tunable (full spectrum) light sources, optoelectronics and solar energy harvesting. Meanwhile, research should

also focus on enhancing the sensitivity, selectivity and robustness of current CD based sensing- and imaging platforms.

As the carbon dot family is still rapidly growing, their application scope can be expected to further expand, opening new areas of photoluminescence- and biomedical research. Undoubtedly, carbon (nano)dots have the potential to be the next big small thing.



## ABBREVIATIONS AND SYMBOLS

Table A.1: Overview of abbreviations and symbols, listed in alphabetical order.

---

#COOH	amount of carboxylic acid groups
#OH	amount of Tris based alcohol groups
2SM	two-state model
3DEM	3D-excitation spectra matrix
AFM	atomic-force microscopy
Ag-NP(s)	silver (argentum) nanoparticle(s)
AIE	aggregation-induced emission
At.%	atomic percent
ATR	attenuated total reflection
avg	average
BPEI	branched polyethyleneimine
BtA	1,2,3,4-butanetetracarboxylic acid
BtA/N-CND(s)	1,2,3,4-butanetetracarboxylic acid derived nitrogen-doped carbon nanodot(s)
$\chi$	electronegativity
$c_{CA}$	carboxylic acid concentration
$c_{Tris}$	Tris concentration
C-CND(s)	starch derived carbon nanodot(s)
CA/N-CND(s)	carboxylic acid derived nitrogen-doped carbon nanodot(s)
CD(s)	carbon dot(s)
CEE	crosslink-enhanced emission (effect)
CiA	citric acid
CiA/N-CND(s)	citric acid derived nitrogen-doped carbon nanodot(s)
C/N-CND(s)	starch derived nitrogen doped carbon nanodot(s)
CND(s)	carbon nanodot(s)

---

*Table A: Continued on next page*

*Table A: Continued from previous page*

CNT(s)	carbon nanotube(s)
CQD(s)	carbon quantum dot(s)
CRM	continuous (spectral shift) model
CVD	chemical vapour deposition
DFT	density functional theory
DMF	<i>N,N</i> -Dimethylformamid
EDTA	ethylenediaminetetraacetic acid
EDX	energy-dispersive X-ray spectroscopy
EEM	excitation-emission matrix
ELE	elemental analysis
$\epsilon'$	dielectric constant
$\epsilon''$	dielectric loss
FMN(s)	fluorescent magnetic nanoparticle(s)
FRET	Förster resonance energy transfer
FTIR	fourier transform infrared spectroscopy
FWHM	full width at half maximum
$\Gamma$	rate of radiative decay
GCQD(s)	graphene carbon quantum dot(s)
GNR(s)	graphene nanoribbon(s)
GO	graphene oxide
GU	glucose units
h	hour(s)
HAc	acetic acid
HAc/N-CND(s)	acetic acid derived nitrogen-doped carbon nanodot(s)
HOMO	highest occupied molecular orbital
IC	internal conversion
ICT	internal charge-transfer
IFE	isolated fluorophore effect
ISC	intersystem crossing
$k_1$	rate constant
$k_{nr}$	rate of non-radiative decay
$k_s$	solvent relaxation rate
$\lambda$	wavelength
$\lambda_C$	excitation wavelength at the center of the fluorophores last absorption band
$\lambda_{Em}$	emission wavelength
$\lambda_{Em}^{Max}$	photoluminescence emission maximum
$\lambda_{Exc}$	excitation wavelength
$\lambda_R$	excitation wavelength at the red edge of the fluorophores last absorption band
LUMO	lowest unoccupied molecular orbital
McA	malonic acid
McA/N-CND(s)	malonic acid derived nitrogen-doped carbon nanodot(s)
MTPA	million metric tonnes per annum

*Table A: Continued on next page*



---

*Table A: Continued from previous page*

---

MW	molar mass
MiW(s)	microwave(s)
MiWR(s)	microwave reactor(s)
MiW-hPC	microwave-assisted hydrothermal precursor carbonization
$N_A$	Number of absorbed photons
$N_{\text{COOH}}$	number of active carboxylic acid sides
$N_E$	Number of events
$N_{\text{NH}_2}$	number of active primary amine sides
$N_{\text{OH}}$	number of active alcohol sides
N-CND(s)	nitrogen-doped carbon nanodot(s)
NDA	no data available
NMR	nuclear magnetic resonance
NP(s)	nanoparticle(s)
OD	optical density
OxA	oxalic acid
OxA/N-CND(s)	oxalic acid derived nitrogen-doped carbon nanodot(s)
PD(s)	polymer dot(s)
PEG	polyethylen glycol
PEI	polyethylenimin
$\text{p}K_W$	negative logarithm of the water ion product $K_W$
PLQY	photoluminescence quantum yield ( $\Phi$ )
PPEI-EI	poly(propionyl ethyleneimine-co-ethyleneimine)
PVAL	poly(vinyl alcohol)
QCE	quantum confinement effect
$R$	ratio
RADAR	radio detection and ranging
REES	red edge excitation shifts
RhB	rhodamine B
RIE	reactive-ion etching
RT	room temperature
rGO	reduced graphene oxide
SESE	surface edge state effect
SLS	static light scattering
SPFM	single-particle fluorescence microscopy
SPOS	solid-phase organic synthesis
SPPS	solid phase peptide synthesis
SuA	succinic acid
SuA/N-CND(s)	succinic acid derived nitrogen-doped carbon nanodot(s)
$t$	time
$T$	temperature
TCSPS	time-correlated single photon counting
TBAP	tetrabutylammonium perchlorate
TDDFT	time-dependent density functional theory
TEM	transmission electron microscopy

---

*Table A: Continued on next page*

*Table A: Continued from previous page*

---

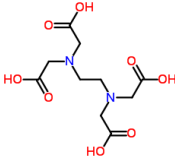
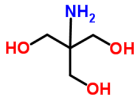
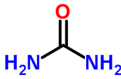
TIRF	total internal reflection fluorescence
TIRFM	total internal reflection fluorescence microscope
TRES	time-resolved emission spectra
Tris	tris(hydroxymethyl)aminomethane
$\tan\sigma$	loss tangent
$\tau$	photoluminescence lifetime
$\tau_F$	photoluminescence lifetime in the <b>F</b> state
$\tau_P$	photoluminescence lifetime in the <b>P</b> state
$\tau_R$	photoluminescence lifetime in the <b>R</b> state
$\tau_n$	natural lifetime
$\tau_s$	solvent relaxation time
UCNP(s)	fluorescent upconversion nanoparticle(s)
WKGP	workgroup
XRD	X-ray diffraction

---

TABLES AND FIGURES

**B.1 Tables**

Table B.1: N-additives used in this work: ethylenediaminetetraacetic acid (EDTA), tris(hydroxymethyl)aminomethane (Tris), and urea.

	Chemical formula	MW (g mol <sup>-1</sup> )	Structure	Number of functional groups
EDTA	C <sub>10</sub> H <sub>16</sub> N <sub>2</sub> O <sub>8</sub>	292.24		$N_{\text{COOH}} = 4$
Tris	C <sub>4</sub> H <sub>11</sub> NO <sub>3</sub>	121.14		$N_{\text{OH}} = 3, N_{\text{NH}_2} = 1$
urea	CH <sub>4</sub> N <sub>2</sub> O	60.06		$N_{\text{NH}_2} = 2$

## APPENDIX B. TABLES AND FIGURES

Table B.2: C-sources used in this work: 1,2,3,4-butanetetracarboxylic acid (BtA), acetic acid (HAc), citric acid (CiA), malonic acid (McA), oxalic acid (OxA), starch, and succinic acid (SuA).

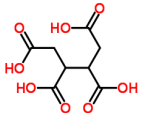
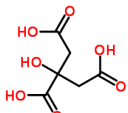
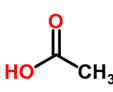
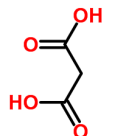
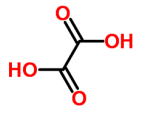
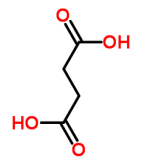
	Chemical formula	MW (g mol <sup>-1</sup> )	Structure	Number of functional groups
BtA	C <sub>8</sub> H <sub>10</sub> O <sub>8</sub>	234.16		$N_{\text{COOH}} = 4$
CiA	C <sub>6</sub> H <sub>8</sub> O <sub>7</sub>	192.12		$N_{\text{COOH}} = 3$
HAc	C <sub>2</sub> H <sub>4</sub> O <sub>2</sub>	60.05		$N_{\text{COOH}} = 1$
McA	C <sub>3</sub> H <sub>4</sub> O <sub>4</sub>	104.06		$N_{\text{COOH}} = 2$
OxA	C <sub>2</sub> H <sub>2</sub> O <sub>4</sub>	90.03		$N_{\text{COOH}} = 2$
SuA	C <sub>4</sub> H <sub>6</sub> O <sub>4</sub>	118.09		$N_{\text{COOH}} = 2$
starch	(C <sub>6</sub> H <sub>10</sub> O <sub>5</sub> ) <sub>n</sub>	n*162.14	see Fig. 3.1, p. 44	$N_{\text{OH}} = 3$

Table B.3: Characteristic absorption bands of CNDs in aqueous PBS buffer solution (pH 7.0); in the order in which they arise in the text.

Peak No.	Absorption	Chromophore <sup>a</sup>	Transition <sup>a</sup>
1	~ 230 nm	a) C-O bonds (e.g. alcohol) b) C-N bonds (e.g. amides)	n- $\sigma^*$ n- $\sigma^*$
2	250 nm - 300 nm	C=O bonds in conjugated carbonyls	n- $\pi^*$
3	300 nm - 500 nm	C=O bonds in carbonyls	n- $\pi^*$
4	~ 250 nm	amines (e.g. R <sub>3</sub> N)	n- $\sigma^*$
5	~ 275 nm	C=O bonds in ketones	n- $\pi^*$
6	~ 300 nm	carboxylic acids [191]	n- $\pi^*$
7	~ 335 nm	C=O bonds of carbonyls	n- $\pi^*$

CND type	Characteristic Absorption Bands
C-CND	Peak 1a; Peak 2; Peak 3
C/N-CND	Peak 1(a,b); Peak 3; Peak 4; Peak 5
HAc/N-CND	Peak 1(a,b); Peak 3; Peak 4; Peak 5; Peak 6; Peak 7
CiA/N-CND	Peak 1(a,b); Peak 4; Peak 7
BtA/N-CND	Peak 1(a,b); Peak 6
McA/N-CND	Peak 3; Peak 4
OxA/N-CND	Peak 3; Peak 5
SuA/N-CND	Peak 3; Peak 4; Peak 6; Peak 7

<sup>a</sup> according to Kellner *et al.* [69] - if not otherwise stated

Table B.4: Comparison between HAc/N-CNDs, CiA/N-CNDs and QDot525 (CdSe/ZnS quantum dot).

	HAc/N-CNDs	CiA/N-CNDs	QDot525 <sup>a</sup>
Average Diameter	(2.40 ± 0.25) nm		(4.0 ± 0.3) nm
Average $\lambda_{\text{Max}}^{\text{Em}}$	(422 ± 2) nm	(407 ± 1) nm	(525 ± 4) nm
Average FWHM	(75 ± 2) nm	(65 ± 1) nm	≤ 32 nm
PLQY	≥ (50 ± 2) %	≥ (90 ± 2) %	≥ 69 %
Estimated Cost	€0.01/nmol <sup>b</sup>		€325/nmol

<sup>a</sup> According to specifications from Thermo Fisher Scientific (Waltham, MA, USA)

<sup>b</sup> Estimated values, based on estimated molar weight and overall cost (approx. €6.60/g).

## B.2 Figures

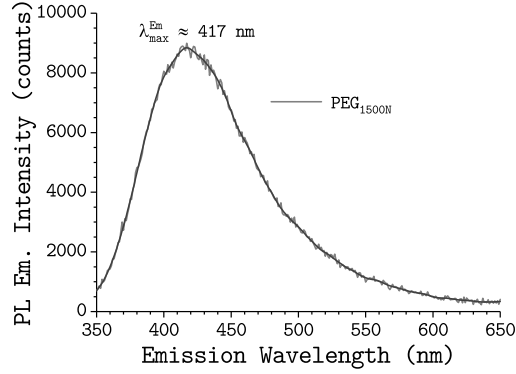


Figure B.1: PL emission spectra under excitation at 340 nm for PEG<sub>1500N</sub> derived N-CNDs. N-CNDs were obtained from aqueous PEG<sub>1500N</sub> solution after MiW-hPC for 45 min at 200 °C.

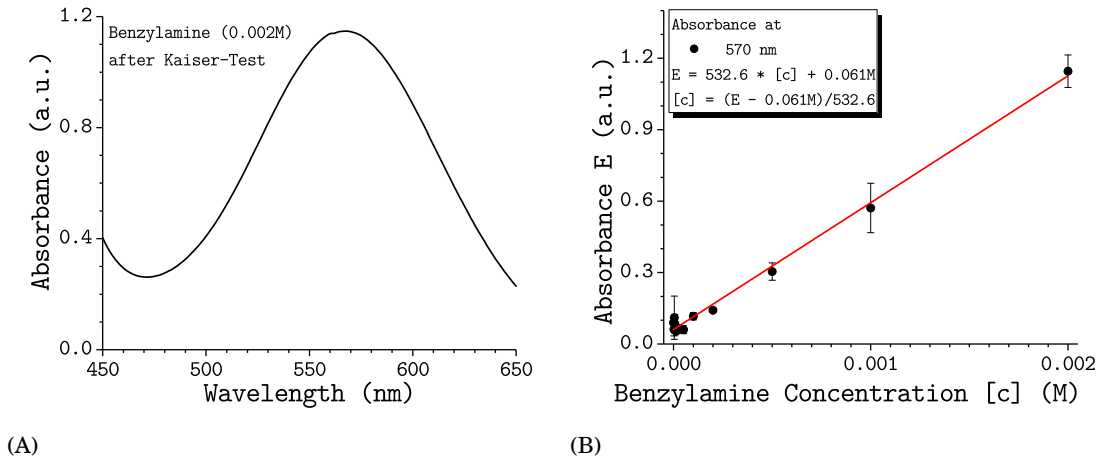


Figure B.2: Details for calibration of the Kaiser test, developed by Jarre *et al.* [62]: (A) UV-Vis absorption spectra of benzylamine (0.002 M) after successful Kaiser test; and (B) calibration curve with benzylamine.

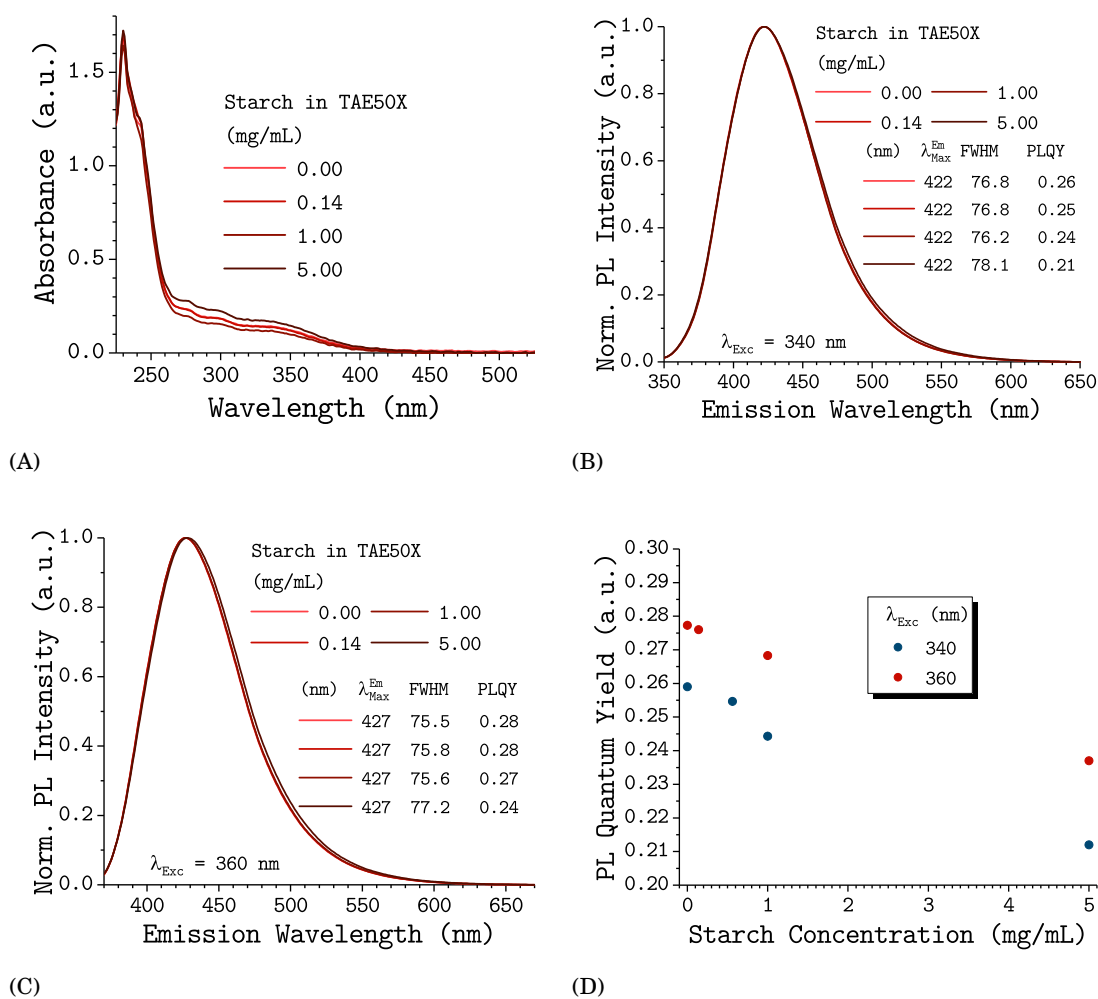


Figure B.3: Effect of various excitation wavelength on the photophysical properties of C/N-CNDs, derived from various aqueous TAE buffer-starch dispersions (see Chap. 4.2.4, p. 80): (A) UV-Vis absorption spectra; (B) normalized PL emission spectra under excitation at 340 nm (OD 0.1); (C) their corresponding normalized PL emission spectra under excitation at 360 nm (OD 0.1); and (D) PLQY as a function of initial starch concentration in TAE50X buffer for excitation at 340 nm and 360 nm, respectively.

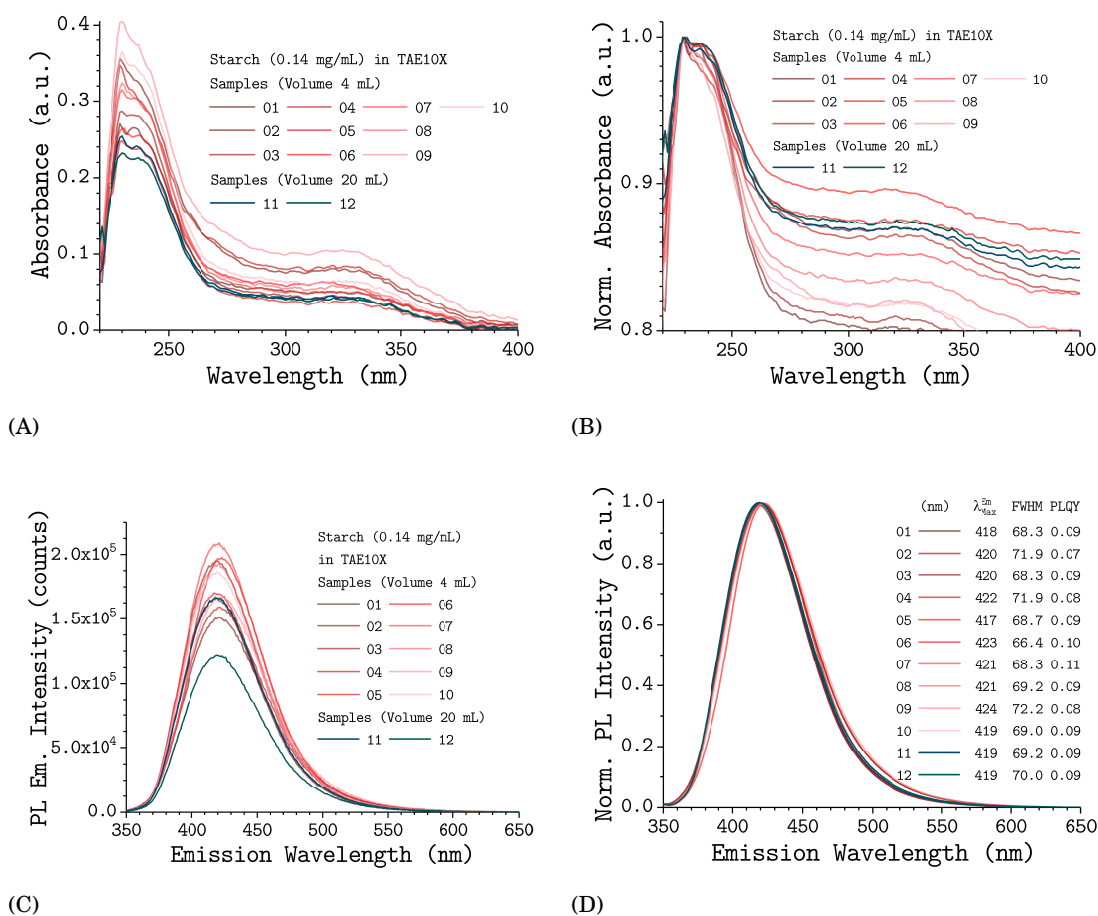


Figure B.4: Reproducibility of C/N-CND Synthesis for 12 independent C/N-CND samples, obtained from 12 synthesis attempts: (A) UV-Vis absorption spectra; (B) the corresponding normalized UV-Vis absorption spectra; (C) PL emission under excitation at 340 nm (OD 0.1); (D) the corresponding normalized PL emission spectra. C/N-CNDs were obtained via MiW-hPC of a C/N-CND precursor solution for 45 min at 230 °C. Precursor solution: starch (0.14 mg/mL) in TAE10X buffer solution.



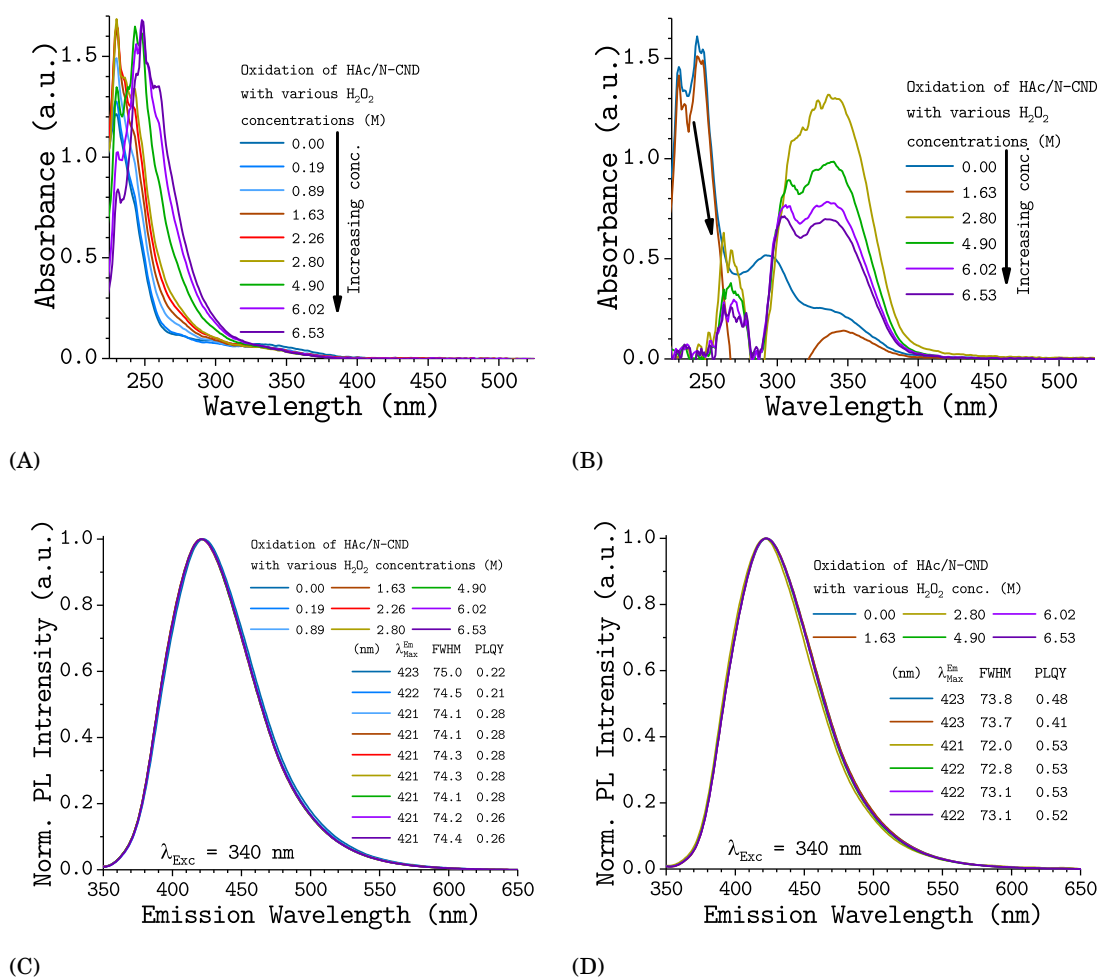


Figure B.5: Effect of oxidation of HAc/N-CNDs with hydrogen peroxide ( $\text{H}_2\text{O}_2$ ): (A,B) UV-Vis absorption spectra; and (C,D) their corresponding normalized PL emission spectra under excitation at 340 nm (OD 0.1) at various  $\text{H}_2\text{O}_2$ -concentrations for TAE50X- and acidified TAE50X buffer derived HAc/N-CNDs, respectively. TAE50X buffer: 0.05 M EDTA, 2.0 M Tris, 1.0 M HAc; and acidified TAE50X buffer: 0.05 M EDTA, 2.0 M Tris, 1.0 M HAc. HAc/N-CNDs were treated with aqueous hydrogen peroxide for 3 days under constant stirring.

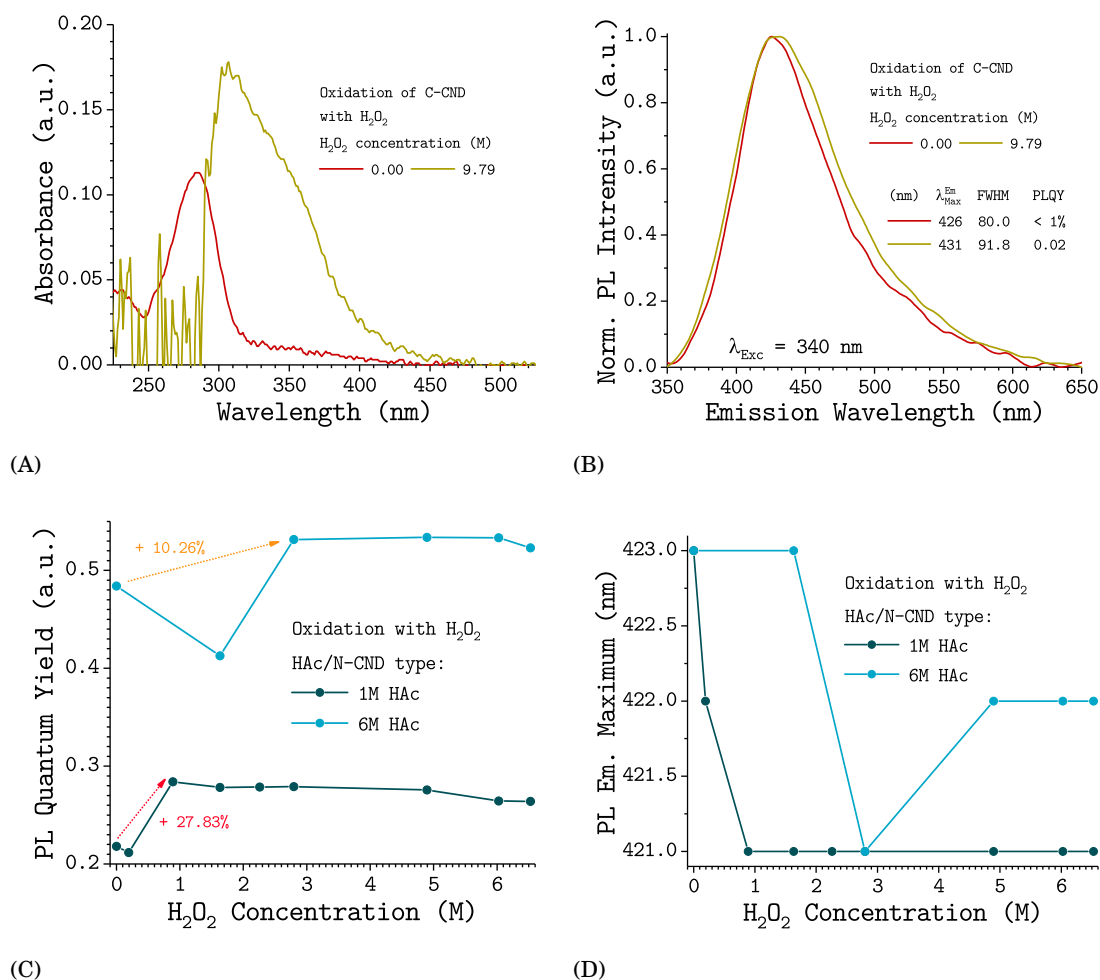


Figure B.6: Effect of oxidation of C-CNDs with hydrogen peroxide ( $\text{H}_2\text{O}_2$ ): (A) UV-Vis absorption spectra; and (B) their corresponding normalized PL emission spectra under excitation at 340 nm (OD 0.1) at two  $\text{H}_2\text{O}_2$ -concentrations. Effect of oxidation of HAC/N-CNDs with hydrogen peroxide ( $\text{H}_2\text{O}_2$ ): (C) PLQY and (D) PL emission FWHM under excitation at 340nm (OD 0.1), as a function of various  $\text{H}_2\text{O}_2$ -concentrations for TAE50X- and acidified TAE50X buffer derived HAC/N-CNDs, respectively. TAE50X buffer: 0.05 M EDTA, 2.0 M Tris, 1.0 M HAC; and TAE50X buffer: 0.05 M EDTA, 2.0 M Tris, 1.0 M HAC. C-CNDs and HAC/N-CNDs were treated with aqueous hydrogen peroxide for 3 days under constant stirring.

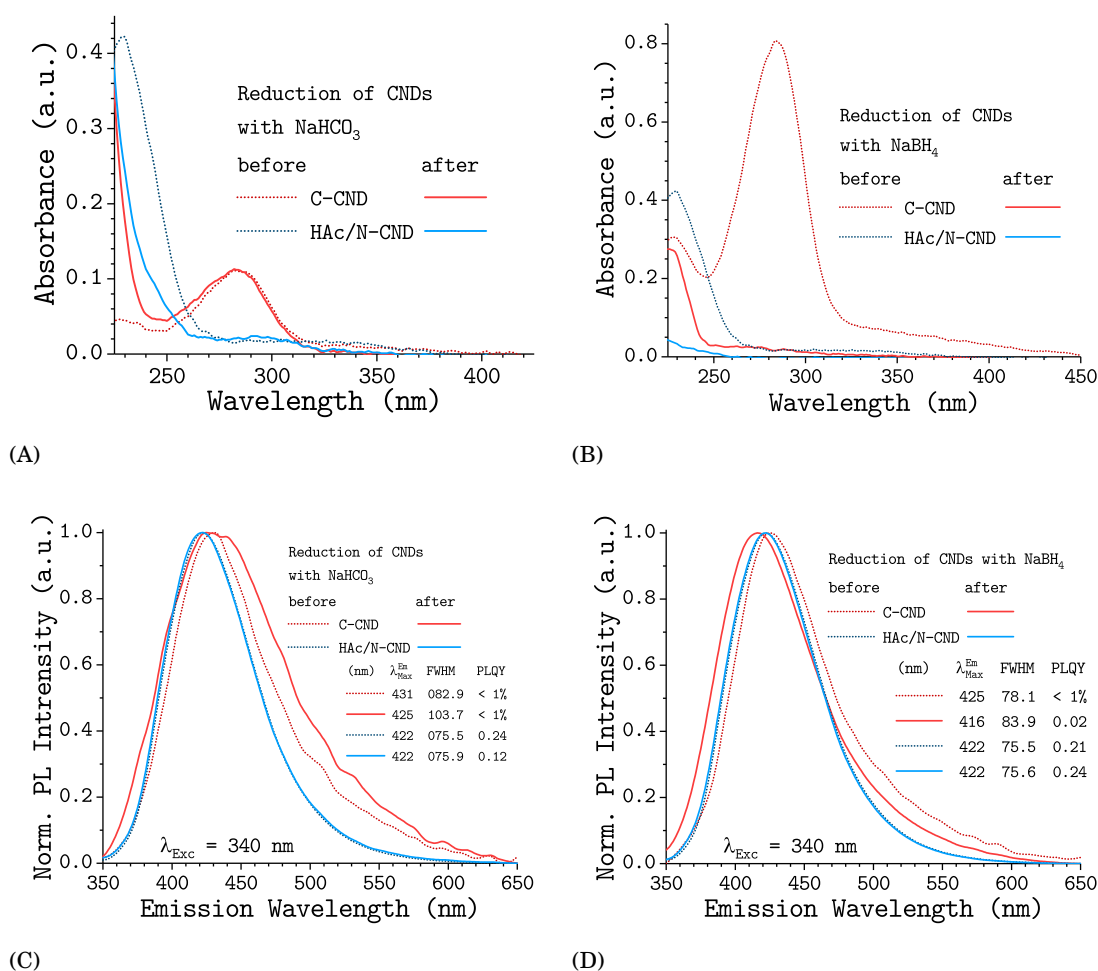


Figure B.7: Effect of reduction of C-CNDs and HAc/N-CNDs with various reduction agents. Method 1: (A) UV-Vis absorption spectra; and (C) their corresponding normalized PL emission spectra under excitation at 340 nm (OD 0.1) for C-CNDs and HAc-CNDs before/after reduction with sodium bicarbonate ( $\text{NaHCO}_3$ ). Method 2: (B) UV-Vis absorption spectra; and (D) their corresponding normalized PL emission spectra under excitation at 340 nm (OD 0.1) for C-CNDs and HAc-CNDs before/after reduction with sodium borohydride ( $\text{NaBH}_4$ ). Method 1: C-CNDs ( $0.25 \text{ mg mL}^{-1}$ ) or HAc/N-CNDs ( $0.5 \text{ mg mL}^{-1}$ ) in 20 mL of aqueous  $\text{NaHCO}_3$  solution ( $200 \text{ mg mL}^{-1}$ ), subsequent heating ( $90^\circ\text{C}$ ) for 4h under reflux and constant stirring. Method 2: 20 mL of aqueous C-CND- ( $1 \text{ mg L}^{-1}$ ) or HAc/N-CND ( $1 \text{ mg L}^{-1}$ ) solution in ice bath, addition of 100 mg  $\text{NaBH}_4$  ( $5.0 \text{ mg mL}^{-1}$ ) under constant stirring for 3h. Excess sodium borohydride was decomposed by neutralising the reaction mixture to pH 7 (slowly and under constant stirring) with PBS buffer.

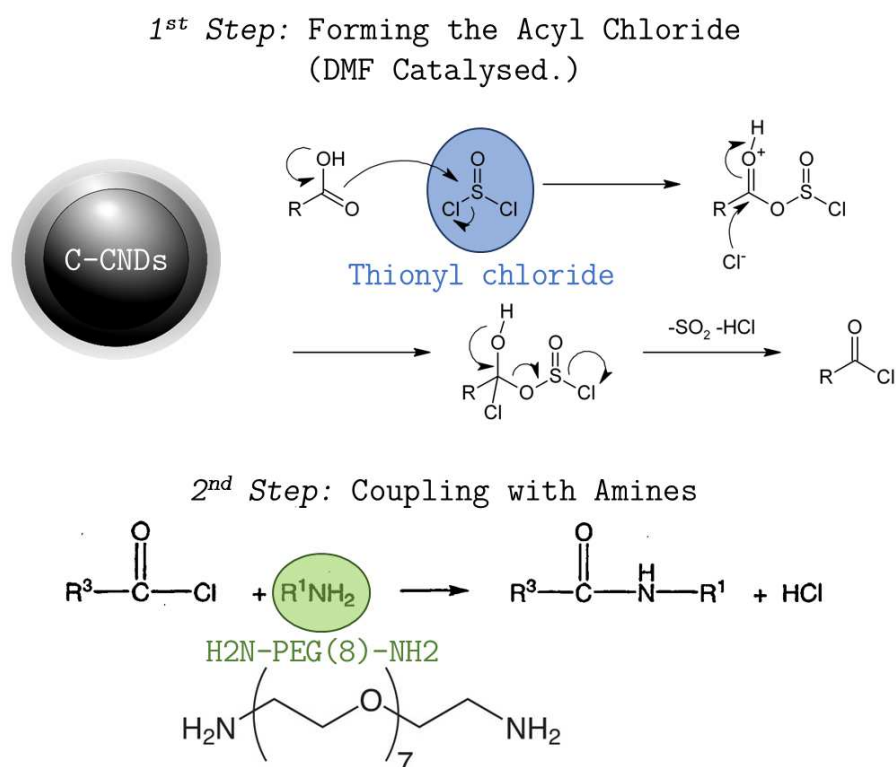


Figure B.8: Schematic representation reaction mechanism for C-CND functionalization via DMF-catalyzed amidation reaction conditions; targeting the carboxylic acid groups on the C-CNDs surface (for details see Chap. 3.2.5.1, p. 53).

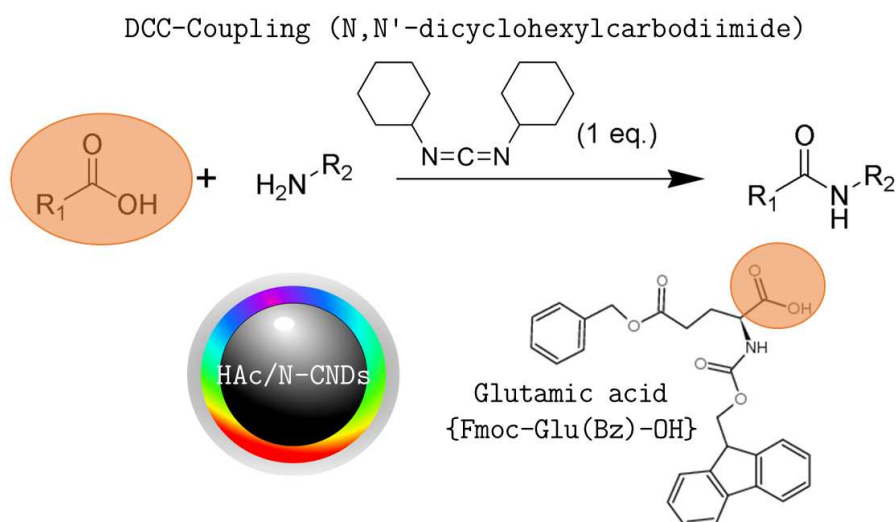


Figure B.9: Schematic representation reaction mechanism for HAC/N-CND functionalization via DDCC-Coupling Route; targeting the primary amines on the HAC/N-CNDs surface (for details see Chap. 3.2.5.1, p. 53).

## B.2.1 EEM- and 3DEM Measurements

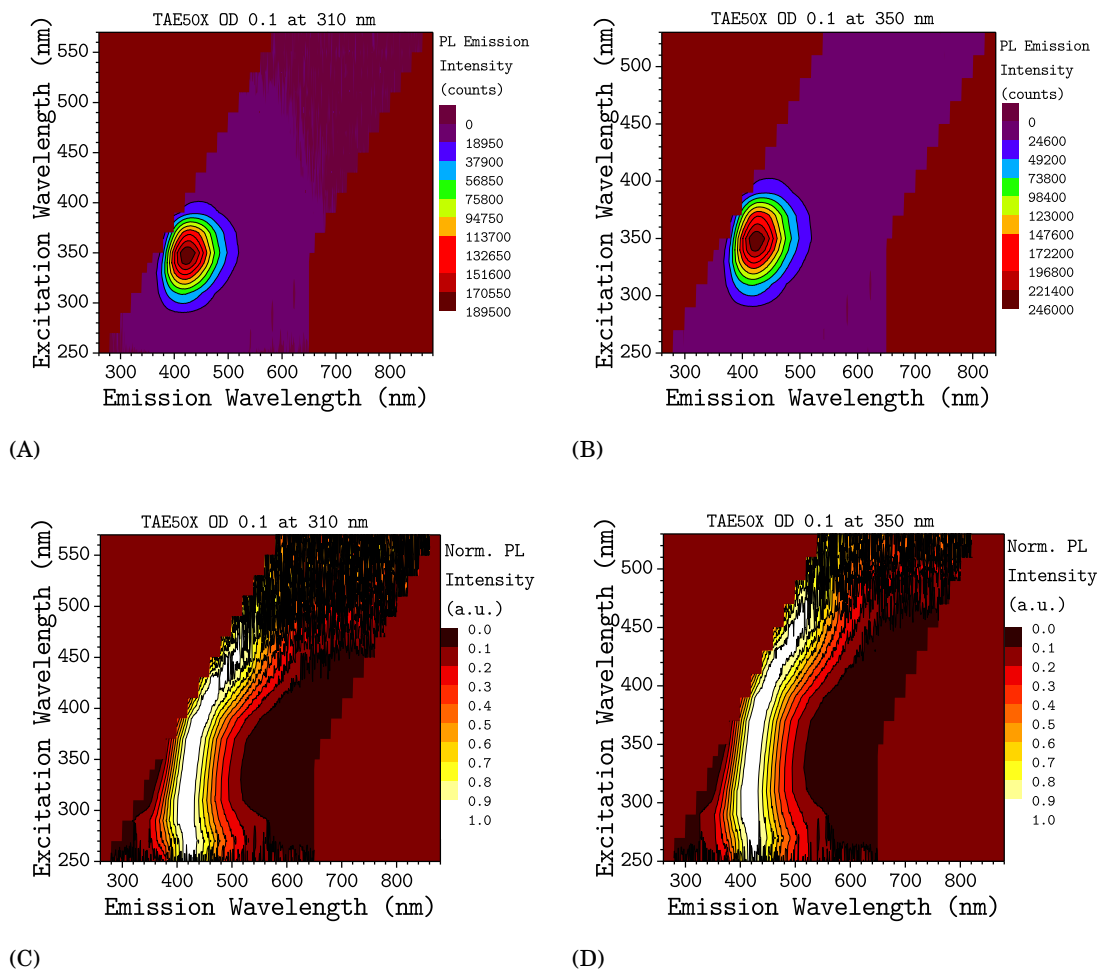


Figure B.10: Characteristic excitation-emission matrix (EEM) measurements for HAc/N-CNDs in aqueous PBS buffer (pH 7.0): (A,B) PL emission EEM; and (C,D) corresponding normalized PL emission EEM for HAc/N-CNDs (OD 0.1 at 310 nm) and HAc/N-CNDs (OD 0.1 at 350 nm), respectively.

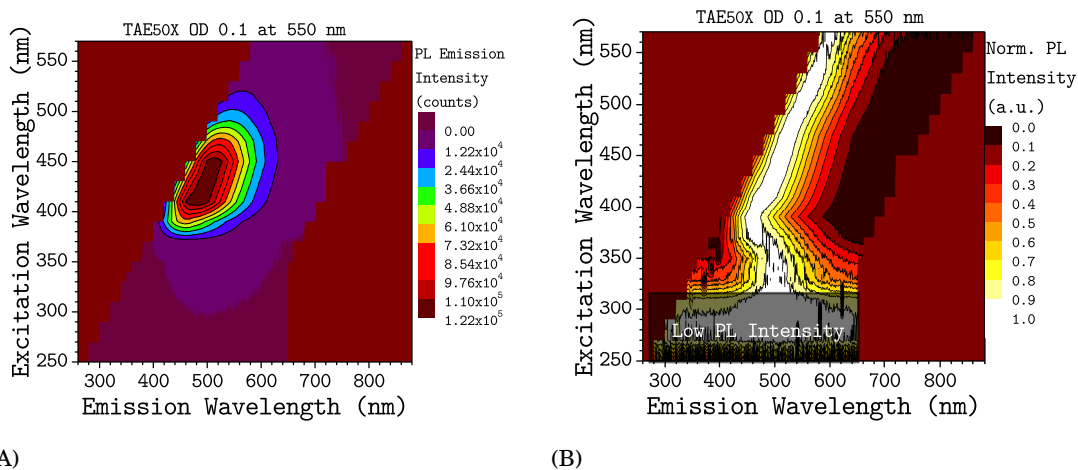


Figure B.11: Characteristic excitation-emission matrix (EEM) measurements for HAC/N-CNDs in aqueous PBS buffer (pH 7.0): (A) PL emission EEM; and (B) corresponding normalized PL emission EEM for HAC/N-CNDs (OD 0.1 at 550 nm).

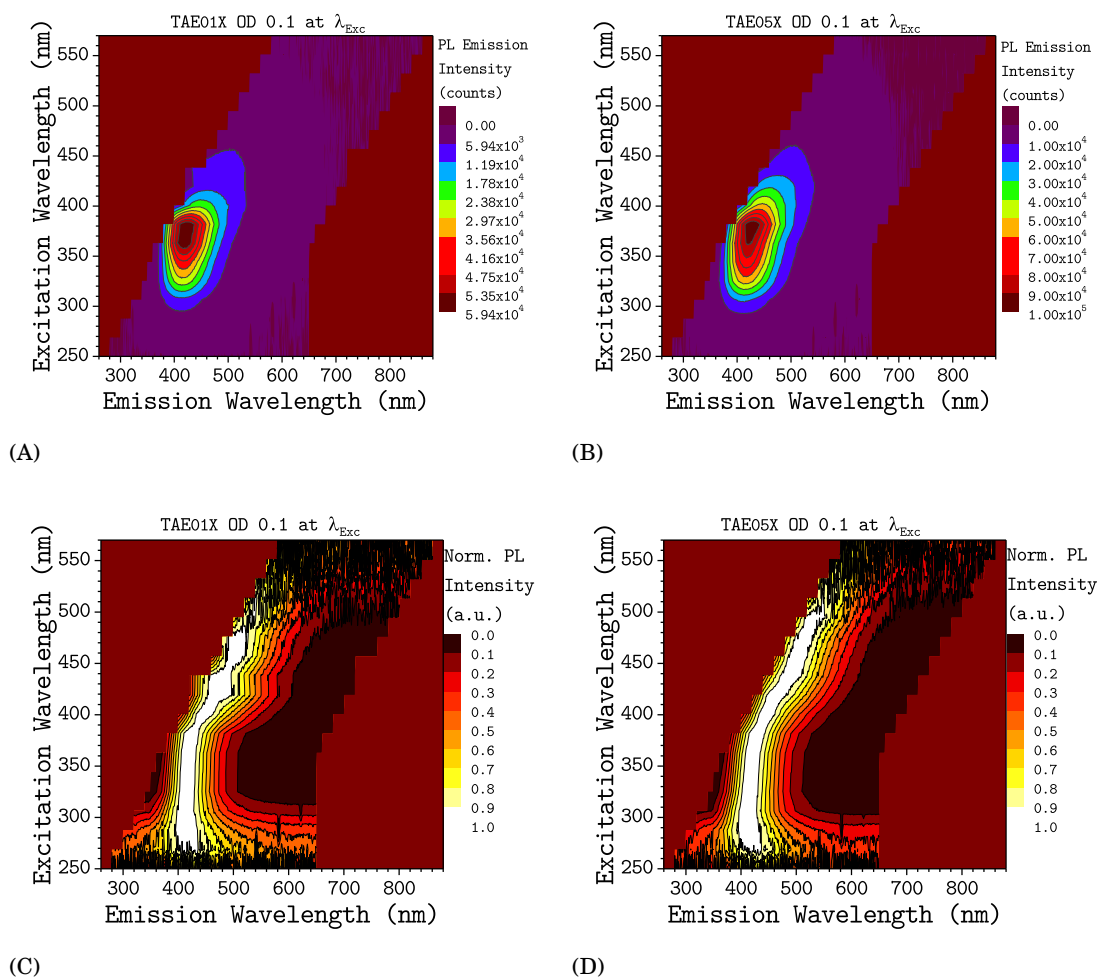


Figure B.12: Characteristic excitation-emission matrix (EEM) measurements for HAC/N-CNDs in aqueous PBS buffer (pH 7.0): (A,B) PL emission EEM (OD 0.1 at  $\lambda_{Exc}$ ); and (C,D) corresponding normalized PL emission EEM (OD 0.1 at  $\lambda_{Exc}$ ) for HAC/N-CNDs obtained from TAE01X and TAE05X, respectively.

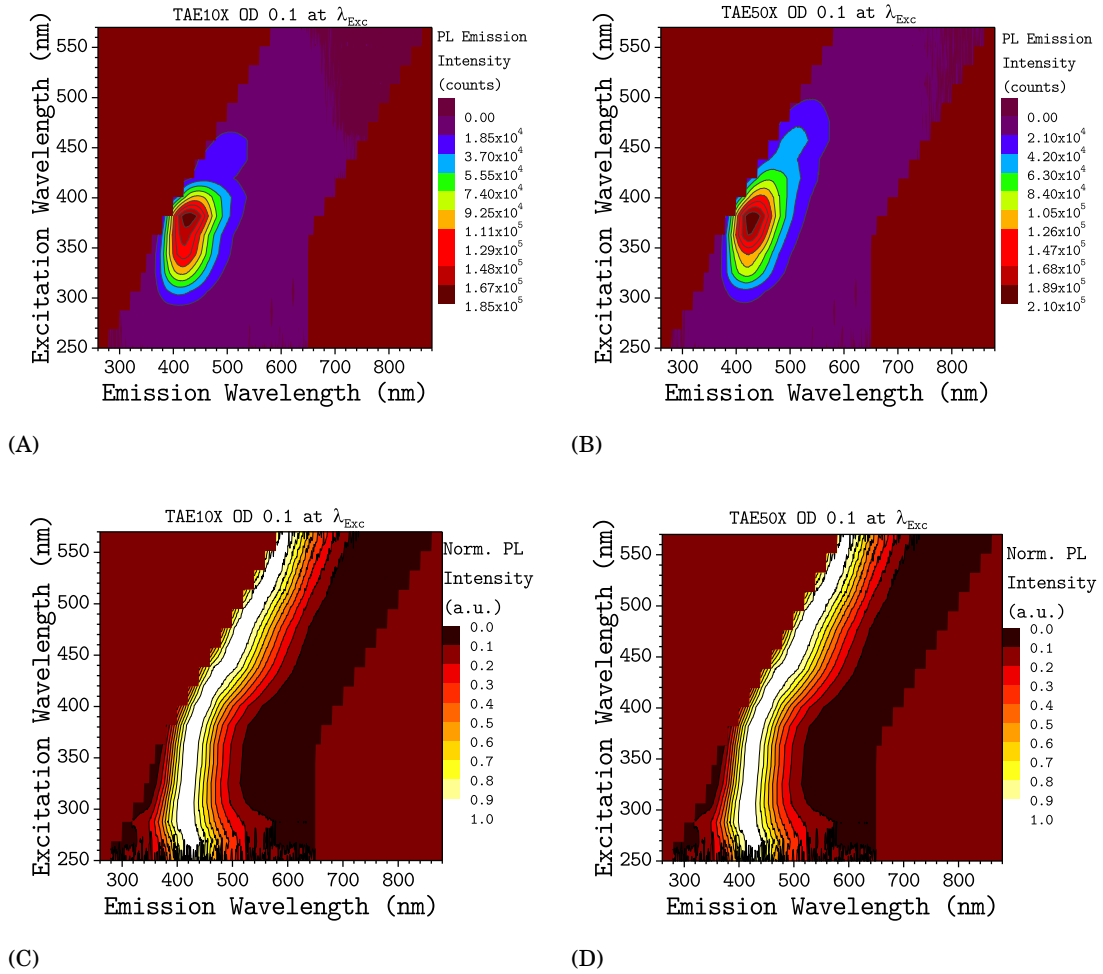


Figure B.13: Characteristic excitation-emission matrix (EEM) measurements for HAC/N-CNDs in aqueous PBS buffer (pH 7.0): (A,B) PL emission EEM (OD 0.1 at  $\lambda_{Exc}$ ); and (C,D) corresponding normalized PL emission EEM (OD 0.1 at  $\lambda_{Exc}$ ) for HAC/N-CNDs obtained from TAE10X and TAE50X, respectively.



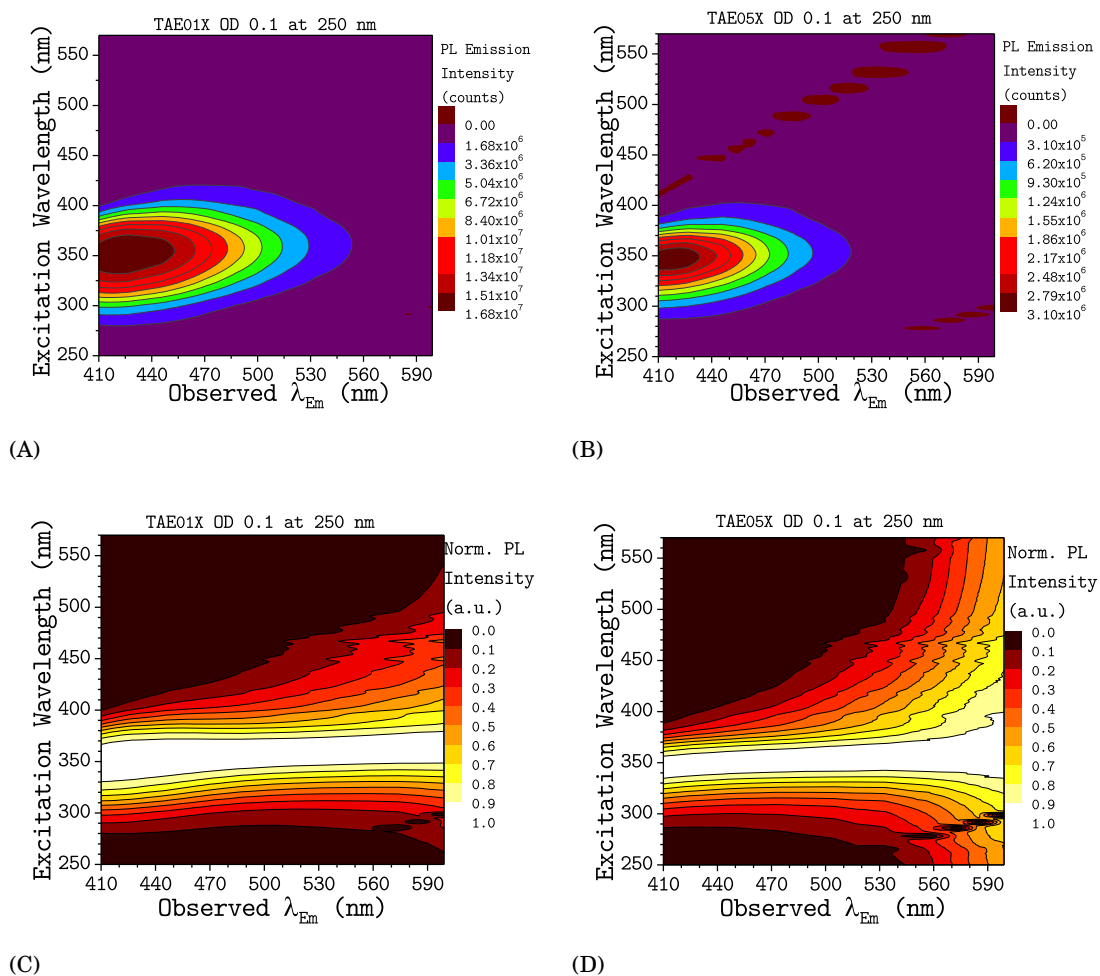


Figure B.14: Characteristic 3D-excitation spectra matrix (3DEM) measurements for HAC/N-CNDs in aqueous PBS buffer (pH 7.0): (A,B) 3DEM (OD 0.1 at 250 nm); and (C,D) corresponding normalized 3DEM (OD 0.1 at 250 nm) for HAC/N-CNDs obtained from TAE01X and TAE05X, respectively.

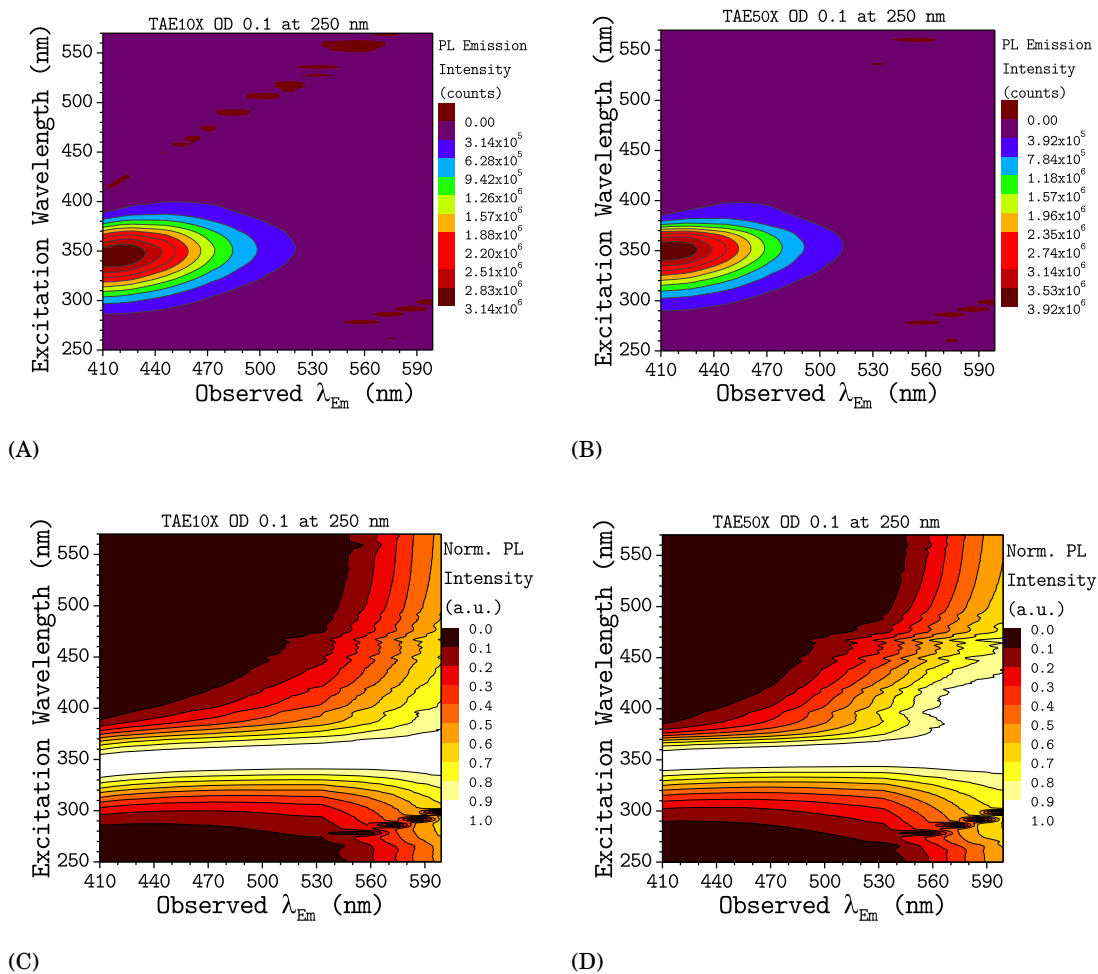


Figure B.15: Characteristic 3D-excitation spectra matrix (3DEM) measurements for HAc/N-CNDs in aqueous PBS buffer (pH 7.0): (A,B) 3DEM (OD 0.1 at 250 nm); and (C,D) corresponding normalized 3DEM (OD 0.1 at 250 nm) for HAc/N-CNDs obtained from TAE10X and TAE50X, respectively.

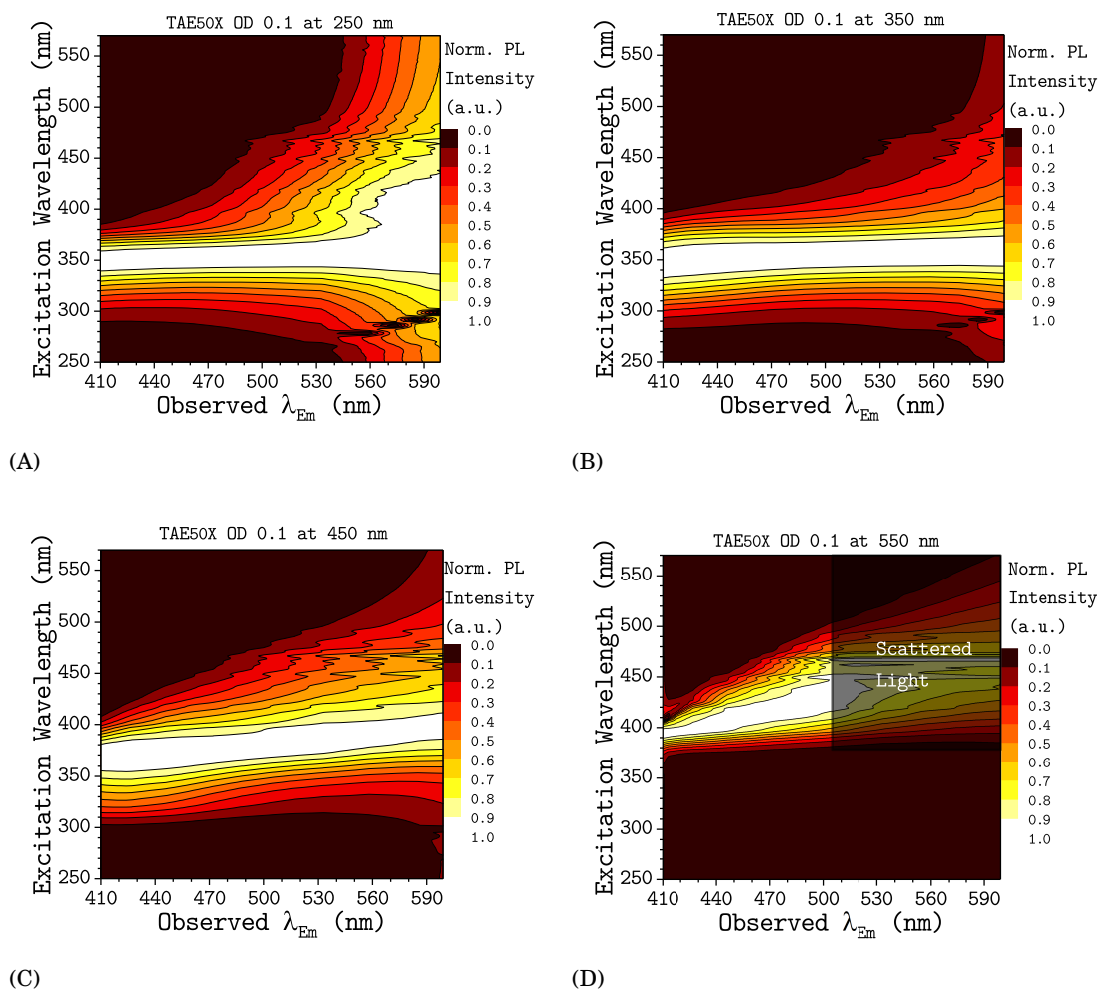


Figure B.16: Characteristic 3D-excitation spectra matrix (3DEM) measurements for HAC/N-CNDs in aqueous PBS buffer (pH 7.0): (A) normalized 3DEM (OD 0.1 at 250 nm); (B) normalized 3DEM (OD 0.1 at 350 nm); (C) normalized 3DEM (OD 0.1 at 450 nm); and (D) normalized 3DEM (OD 0.1 at 550 nm) for HAC/N-CNDs obtained from TAE50X.

### B.3 NMR Spectroscopy

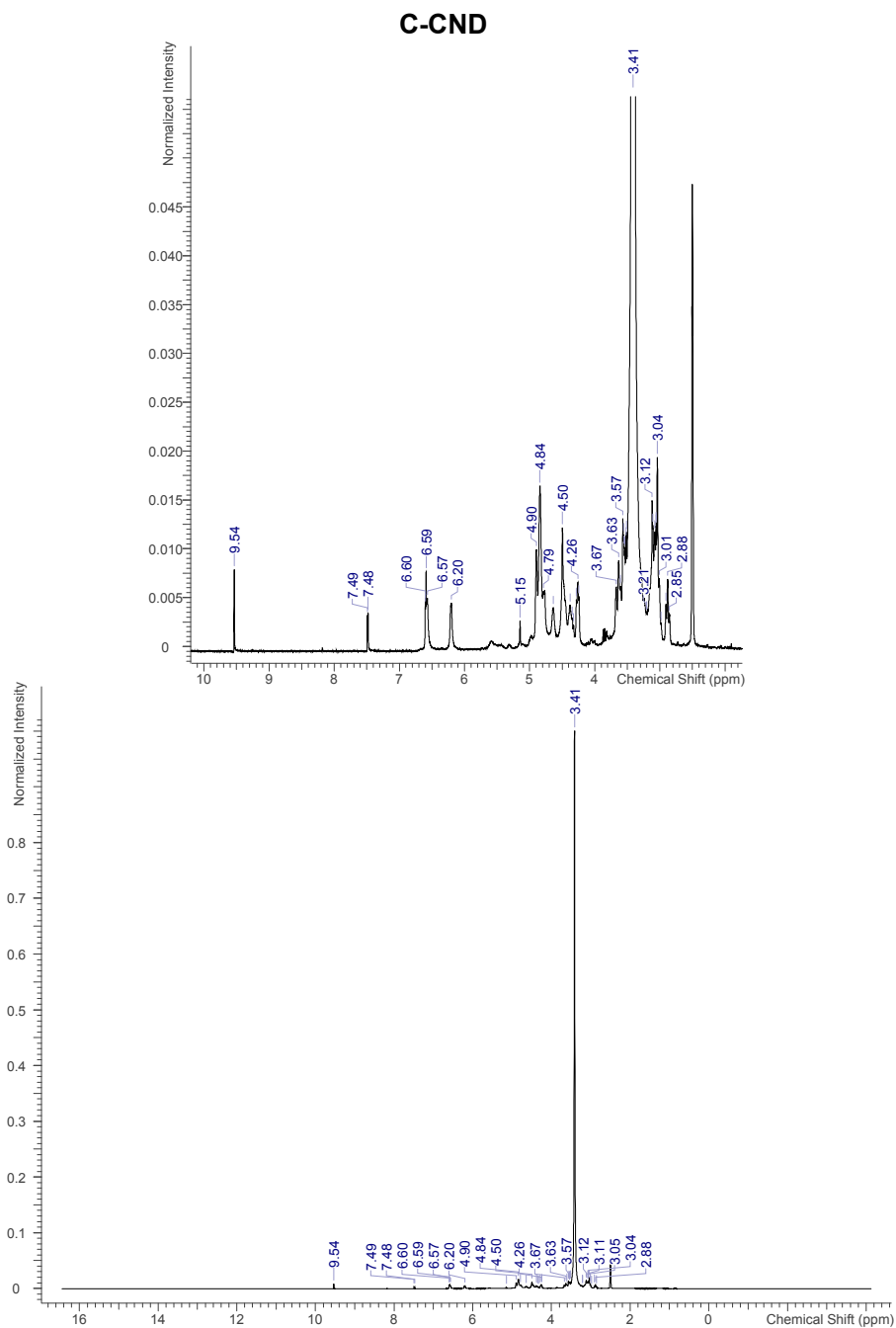
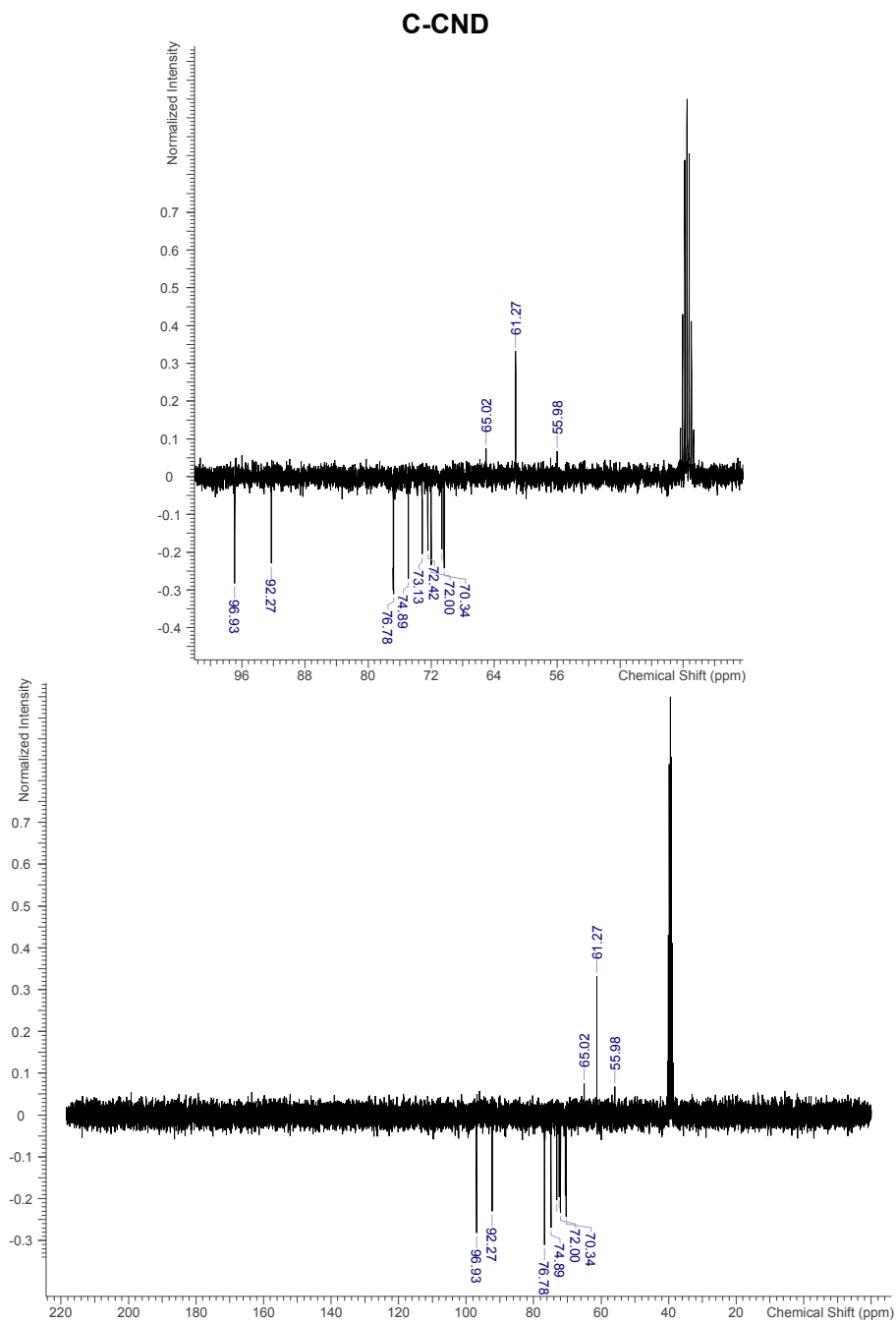


Figure B.17:  $^1\text{H}$ -NMR Spectra of C-CNDs.

Figure B.18:  $^{13}\text{C}$ -NMR Spectra of C-CNDs.

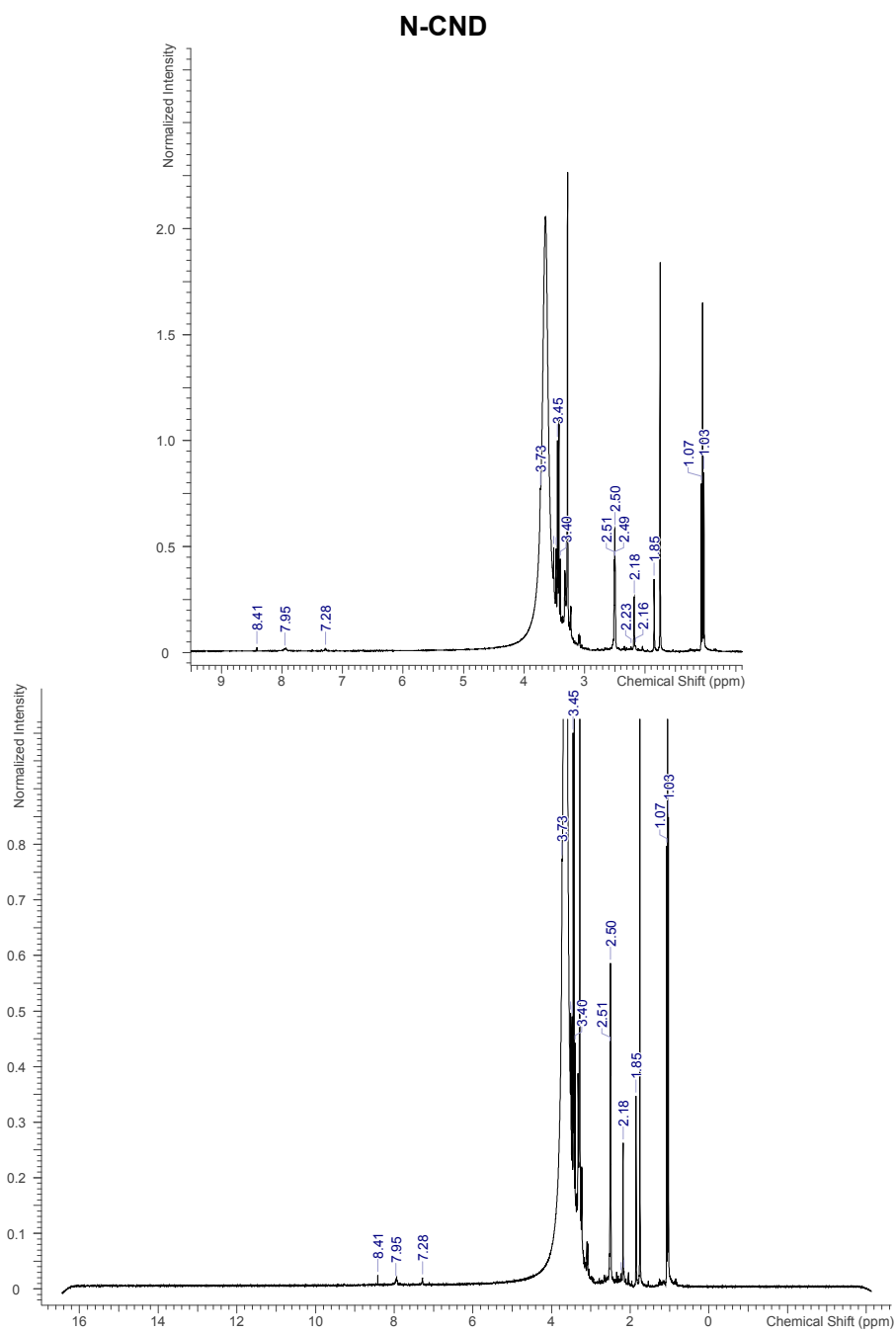
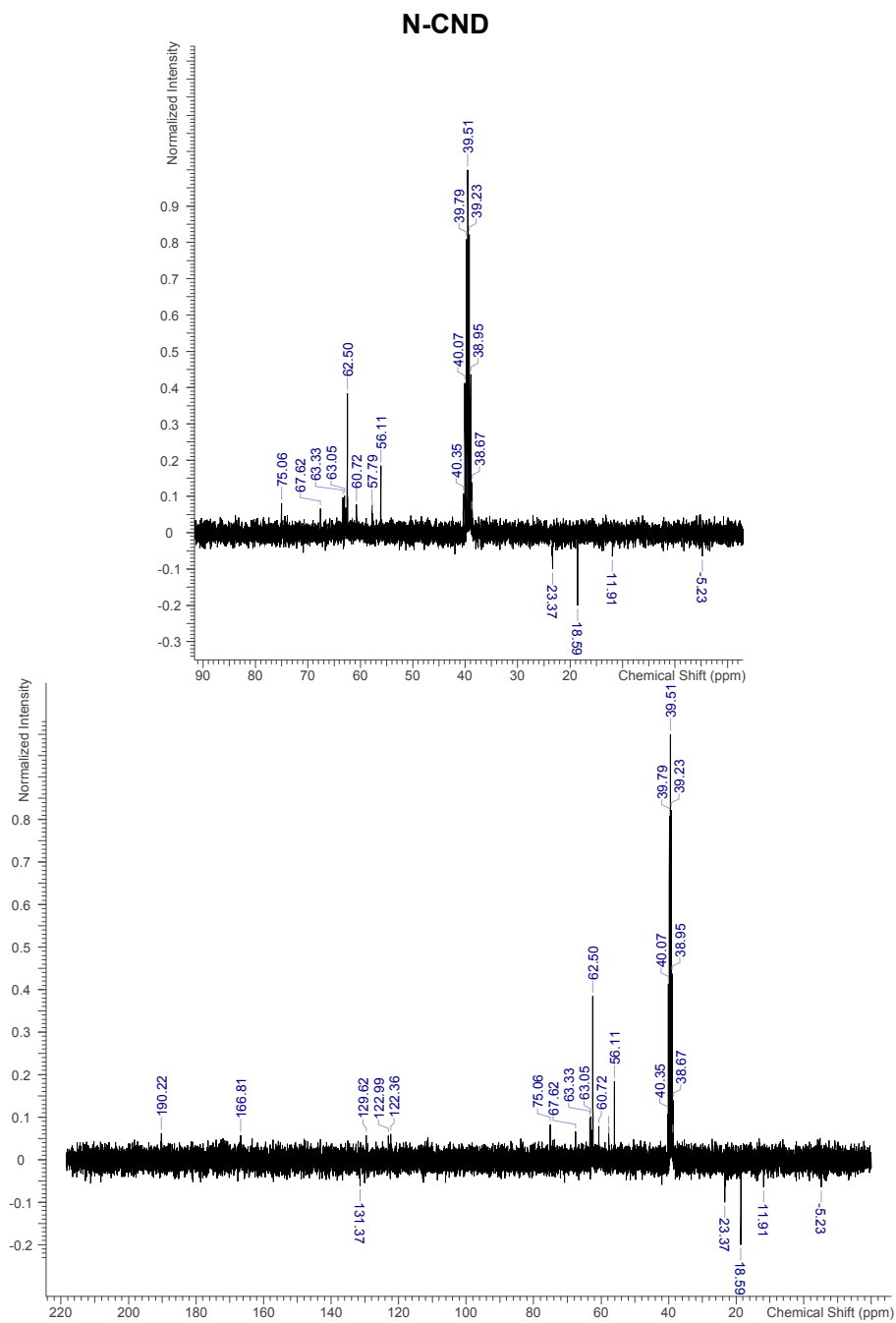


Figure B.19:  $^1\text{H-NMR}$  Spectra of HAc/N-CNDs.

Figure B.20:  $^{13}\text{C}$ -NMR Spectra of HAc/N-CNDs.





APPENDIX



## OVERVIEW OF CARBON DOTS FROM PREVIOUS ARTICLES

Table C.1: Overview of CDs from previous articles; according to CD type; and in the order of decreasing PLQYs. Owing to the vast number of publications about CDs, this overview makes no claim to be complete.

Named	PLQY (%)	$\lambda_{\text{Em}}^{\text{Max}}$ (nm)	SL observed	Size (nm)	Precursor	Method	Time	Ref.
CARBON NANODOTS (CNDS)								
Mg-EDA-CDs	83	437	Yes	NDG	CiA, EDA, Mg(OH) <sub>2</sub>	hPC	3h	[84]
CD	80	443	NDG	2.0-6.0	CiA, EDA	hPC	5h	[212]
N,P-CND	70	NDG	NDG	NDG	CiA, DETA, o-PA	pyrolysis	1h	[6]
OCDs	53	450	Yes	4.0-7.0	CiA, HDA, octadecene	th-PC	3h	[170]
N-CND	46	421	NDG	1.2	L-arginine, EDA	MiW-hPC	3 min	[3]
CDs	35	425	Yes	8.5	CiA, urea	hPC	10h	[168]
EDA-CDs	30.2	460	Yes	2.2-3.0	CiA, EDA	MiW-hPC	2 min-4 min	[192]
WCDs	30	NDG	Yes	12	CiA, PEI	MiW-hPC	5 min	[141]
CDs	23	454	Yes	9.0	folic acid	hPC	2h	[172]
CD-2	22	450	NDG	3.5	CiA, EDA	hPC	15h	[28]
CD	21.6	461	Yes	1.84	sucrose, oil acid	th-PC	5h	[14]
OCDs	16.7	510	Yes	6.2	CPC, NaOH	alkaline	NDG	[201]
Amino-coated CDs	16.3	413	Yes	4.0	acrylic acid, EDA	MiW-hPC	7 min	[36]
EC-Dots	15.9	451	Yes	2.1-4.3	ethanol, NaOH	E/C	3h-4h	[24]
N-dot 2	14	442	Yes	4.62	2-azidoimidazole, methanol	th-PC	24h	[17]
$\beta$ -CDs	13.5	510	Yes	2.5	$\beta$ -cyclodextrin, HCl (cat.)	hPC	4h	[58]

 NDG: no data given; SL: selective luminescence Table 3.1: Continued on next page

Table 3.1: Continued from previous page

Named	PLQY (%)	$\lambda_{\text{Em}}^{\text{Max}}$ (nm)	SL observed	Size (nm)	Precursor	Method	Time	Ref.
CDs	12	440	Yes	3.0-4.0	glycerine, PEG1500N, serine	MiW-PC	5 min - 20 min,	[95]
CDs	11	448	Yes	2.0-6.0	BSA, TTDDA	hPC	NDG	[198]
CD <sub>pey</sub>	8	474	Yes	2.23	egg yolk	plasma PC	NDG	[171]
N-CND 2	7.8	469	Yes	1.0-10	eggshell, urea	th-PC	2h	[68]
CNDs	6.9	455	Yes	6.8	tea leaves	hPC	20 min	[178]
FCN <sub>blue</sub>	6.0-30	440	Yes	2.0-4.0	carbohydrate	hPC	1h	[7]

GRAPHENE CARBON QUANTUMDOTS (GCQDs)								
Named	PLQY (%)	$\lambda_{\text{Em}}^{\text{Max}}$ (nm)	SL observed	Size (nm)	Precursor	Method	Time	Ref.
Tris-CD	99.3	410	Yes	1.34	CiA, Tris	MiW-hPC	> 1h	[197]
GQDs-EDA	94	450	No	2.3	CiA, EDA	hPC	4	[133]
N:GQDs	78	435	No	2.69	CiA, urea	th-PC	4h	[132]
CQDs(3)	76	460	NDG	3.0	resorcinol, H <sub>2</sub> SO <sub>4</sub>	MiW-hPC	> 1 min	[105]
CDs-PEG	75.8	450	Yes	6.0	CiA, PEG-2000, EDA	th-PC	8h	[184]
N-GQDs	74	500	Yes	1.0-3.0	GO, DMF	th-PC	5h	[153]
CD	70	430	Yes	2.0-7.0	CiA, cow urine, glycerol	hPC	4h	[52]
Trp-C-dots	69.1	NDG	NDG	2.88	glucose, tryptophane	MiW-hPC	35 min	[179]
CND1	62	350	Yes	1.5	CiA, oleylamine, octadecene	th-PC	2h	[74]
CDs	61	420	Yes	2.1	egg-white	th-PC	48h	[199]

NDG: no data given; SL: selective luminescence

Table 3.1: Continued on next page

Table 3.1: Continued from previous page

Named	PLQY (%)	$\lambda_{\text{Max}}^{\text{Em}}$ (nm)	SL observed	Size (nm)	Precursor	Method	Time	Ref.
CNP-ZnS	60	NDG	NDG	10	C-nanopowder, HNO <sub>3</sub> , Na <sub>2</sub> S, Zn(CH <sub>2</sub> CO <sub>2</sub> H) <sub>2</sub> , DMF	> 12h	8	[13]
N-GQDs	59.2	425	No	0.5-4.0	CiA, Tris-HMA	th-PC	15 min	[93]
GQDs	54.5	440	Yes	4.66	L-Glutamic acid,	th-PC	> 1h	[180]
CD <sub>200</sub>	47	380	Yes	2.42	PS-co-PGMA	th-PC	2h	[49]
GQD-PVA	43.6	447	NDG	1.0-5.0	CiA, urea, PVA	hPC	11h	[120]
GQDs	41.2	440	Yes	5.0	neem leaf extract	hPC	8h	[139]
glycol-CDs	38	445	Yes	3.4	candle soot, glycol	th-PC	2h	[195]
N-GQDs	31	520	NDG	3.0	GO, DMF	th-PC	4.5h	[99]
EDA-CD	30	NDG	Yes	4.1	C-soot, EDA, HNO <sub>3</sub> , SOCl <sub>2</sub>	th-PC/ox	> 4days	[81]
GQDs	29	NDG	Yes	5.0-7.0	GO, ammonia	th-PC	5h8	[73]
PCQDs	25.1	400	NDG	5.0-15	phosphorous tribromide, hydroquinone, NaOH, acetone	th-PC	3h	[207]
CDs250	24.5	555	Yes	3.9	CiA, RhB	hPC	16h	[46]
NCDs	23,2	450	Yes	4.0	glutamic acid	th-PC	NDG	[117]
GQDs	22	450	NDG	20	graphene, HNO <sub>3</sub> , H <sub>2</sub> SO <sub>4</sub>	U/S; th-PC	10h	[16]
CDs	21.2	NDG	Yes	1.0-4.0	camphor, piranha etch	PC/ox	> 15h	[44]
C-Dots	20.7	526	NDG	2.7	CF, HNO <sub>3</sub>	acid/ox	48h	[4]
p-CDs	20	445	No	1-9	CiA, urea	hPC	5 min	[150]
GCQDs	17.5	457	NDG	3.42	EDTA	hPC	12h	[146]

 NDG: no data given; SL: selective luminescence Table 3.1: Continued on next page

Table 3.1: Continued from previous page

Named	PLQY (%)	$\lambda_{\text{Em}}^{\text{Max}}$ (nm)	SL observed	Size (nm)	Precursor	Method	Time	Ref.
B-C dots	17.1	407	No	1.0-3.0	CHCl <sub>3</sub> , DEA	th-PC	1h	[116]
CD	16-20	510	NDG	1.5-6.0	CDs, PEG1500N, SOCl <sub>2</sub>	hPC	3 days	[175]
CDs	15	405	NDG	NDG	potato	hPC	2h	[181]
CQDs	13	430	NDG	4.65	C-nanopowder, HNO <sub>3</sub>	th-PC/ox	12h	[42]
r-GQDs	12	430	Yes	3.1	GO, NaBH <sub>4</sub>	red	NDG	[217]
E-CMCD <sub>a</sub>	9.7	438	Yes	2.0-5.0	cow milk	hPC	12h	[51]
C-dots	9.0	486	Yes	3.0-7.0	dextrin, H <sub>2</sub> SO <sub>4</sub>	MiW-hPC	2.5 min	[127]
B-GQDs	8.7	425	No	4.0-6.0	graphite, H <sub>2</sub> , He-, B <sub>2</sub> H <sub>6</sub> gas	arc	NDG	[27]
N,S-CDs	7.41	390	Yes	3.7	heparin sodium	hPC	12h	[155]
Fraction 8	7.0	500	No	14	graphite nanofibres, HNO <sub>3</sub> , H <sub>2</sub> SO <sub>4</sub>	th-PC/ox	6h	[165]
FNCPs	6.3	427	Yes	5.2	strawberry juice	hPC	12h	[61]
N-CQDs	1.0	457	Yes	4.5	glucose, urea	MiW-hPC	7 min	[26]
UNDEFINDED CARBON DOTS (CDs)								
CDs	76	442	No	NDG	CiA, EDA	hPC	5h	[174]
N-CNPs	47.9	440	No	NDG	sodium alginate, tryptophan	th-PC	6h	[219]
BPEI-CQDs	40	NDG	NDG	4.0-10	CiA, BPEI	hPC	3h	[35]
CD	26	455	Yes	1.5-4.5	orange juice, ethanol	hPC	2.5h	[140]
Cds	20	NDG	NDG	4.0-5.0	C-soot, HNO <sub>3</sub> , PEG1500N, SOCl <sub>2</sub>	hPC/ox	4 days	[188]

NDG: no data given; SL: selective luminescence

Table 3.1: Continued on next page

Table 3.1: Continued from previous page

Named	PLQY (%)	$\lambda_{\text{Max}}^{\text{Em}}$ (nm)	SL observed	Size (nm)	Precursor	Method	Time	Ref.
V-CDs	20	400	Yes	1.0 - 12	CiA, PEI-EC NaBH <sub>4</sub>	hPC/red	NDG	[60]
CD-Alg	10	NDG	Yes	7.14	alginate, EDA, HCl (cat.)	MiW-hPC	NDG	[20]
CDs	6.9	444	NDG	2.0 - 4.0	pomelo peel	hPC	3h	[104]

**Legend of Above Table** *Synthesis Methods*: acid: acid treatment; arc: arc discharge; (cat.): catalytic amount; E/C: electrochemical; hPC: hydrothermal precursor carbonization; MiW-hPC: microwave-assisted hydrothermal precursor carbonization; ox: oxidation reaction; plasma PC: plasma induces precursor carbonisation; red: reduction reaction; th-PC: thermal precursor carbonisation; U/S: ultrasonic.

*Chemicals*: EDA: 1,2-ethylenediamine; BSA: bovine serum albumin; BPEI: branched poly(ethylenimine); CF: carbon fibres; CPC: cetylpyridinium chloride monohydrate; CHCl<sub>3</sub>: chloroform; DETA: diethylenetriamine; DMF: dimethylformamide; PEI-EC: ethylenediamine endcapped polyethylenimine; GO: graphene oxide; Mg(OH)<sub>2</sub>: magnesium hydroxide; HNO<sub>3</sub>: nitric acid; o-PA: ortho-phosphoric acid; PEI: polyethylenimine; RhB: rhodamin B; NaOH: sodium hydroxide; Na<sub>2</sub>S: sodium sulfide, H<sub>2</sub>SO<sub>4</sub>: sulfuric acid; SOCl<sub>2</sub>: thionyl chloride; TTDDA: 4,7,10-trioxa-1,13-tridecanediamine; Zn(CH<sub>2</sub>CO<sub>2</sub>H)<sub>2</sub>: zinc acetate.

## BIBLIOGRAPHY

- [1] *Corn Starch Market Report 2017 | Industry Analysis, Market Trends, Share Size and Forecast.*
- [2] P. T. ANASTAS AND J. C. WARNER, *Green chemistry: Theory and practice*, Oxford University Press, Oxford, 1. ed., 2000.
- [3] F. ARCUDI, L. DORDEVIC, AND M. PRATO, *Synthesis, Separation, and Characterization of Small and Highly Fluorescent Nitrogen-Doped Carbon NanoDots*, *Angewandte Chemie*, 128 (2016), pp. 2147–2152.
- [4] L. BAO, C. LIU, Z.-L. ZHANG, AND D.-W. PANG, *Photoluminescence-tunable carbon nanodots: surface-state energy-gap tuning*, *Advanced Materials*, 27 (2015), pp. 1663–1667.
- [5] L. BAO, Z.-L. ZHANG, Z.-Q. TIAN, L. ZHANG, C. LIU, Y. LIN, B. QI, AND D.-W. PANG, *Electrochemical tuning of luminescent carbon nanodots: from preparation to luminescence mechanism*, *Advanced Materials*, 23 (2011), pp. 5801–5806.
- [6] M. K. BARMAN, B. JANA, S. BHATTACHARYYA, AND A. PATRA, *Photophysical Properties of Doped Carbon Dots (N, P, and B) and Their Influence on Electron /Hole Transfer in Carbon Dots–Nickel (II) Phthalocyanine Conjugates*, *Journal of Physical Chemistry C*, 118 (2014), pp. 20034–20041.
- [7] S. K. BHUNIA, A. SAHA, A. R. MAITY, S. C. RAY, AND N. R. JANA, *Carbon nanoparticle-based fluorescent bioimaging probes*, *Scientific Reports*, 3 (2013), p. 1473.
- [8] M. BOTTINI, C. BALASUBRAMANIAN, M. I. DAWSON, A. BERGAMASCHI, S. BELLUCCI, AND T. MUSTELIN, *Isolation and characterization of fluorescent nanoparticles from pristine and oxidized electric arc-produced single-walled carbon nanotubes*, *Journal of Physical Chemistry B*, 110 (2006), pp. 831–836.
- [9] A. B. BOURLINOS, A. STASSINOPOULOS, D. ANGLOS, R. ZBORIL, M. KARAKASSIDES, AND E. P. GIANNELIS, *Surface functionalized carbogenic quantum dots*, *Small*, 4 (2008), pp. 455–458.
- [10] G. BRUNNER, *Hydrothermal and supercritical water processes*, vol. 5 of *Supercritical Fluid Science and Technology*, Elsevier, Oxford, 2014.

## BIBLIOGRAPHY

---

- [11] A. BULÉON, P. COLONNA, V. PLANCHOT, AND S. BALL, *Starch granules: Structure and biosynthesis*, International Journal of Biological Macromolecules, 23 (1998), pp. 85–112.
- [12] L. CAO, X. WANG, M. J. MEZIANI, F. LU, H. WANG, P. G. LUO, Y. LIN, B. A. HARRUFF, L. M. VECA, D. MURRAY, S.-Y. XIE, AND Y.-P. SUN, *Carbon dots for multiphoton bioimaging*, Journal of the American Chemical Society, 129 (2007), pp. 11318–11319.
- [13] L. CAO, S.-T. YANG, X. WANG, P. G. LUO, J.-H. LIU, S. SAHU, Y. LIU, AND Y.-P. SUN, *Competitive performance of carbon quantum dots in optical bioimaging*, Theranostics, 2 (2012), pp. 295–301.
- [14] B. CHEN, F. LI, S. LI, W. WENG, H. GUO, T. GUO, X. ZHANG, Y. CHEN, T. HUANG, X. HONG, S. YOU, Y. LIN, K. ZENG, AND S. CHEN, *Large scale synthesis of photoluminescent carbon nanodots and their application for bioimaging*, Nanoscale, 5 (2013), pp. 1967–1971.
- [15] C.-F. CHEN, C.-H. PARK, B. W. BOUDOURIS, J. HORNG, B. GENG, C. GIRIT, A. ZETTL, M. F. CROMMIE, R. A. SEGALMAN, S. G. LOUIE, AND F. WANG, *Controlling inelastic light scattering quantum pathways in graphene*, Nature, 471 (2011), pp. 617–620.
- [16] Q. CHEN, C. SHI, C. ZHANG, S. PU, R. WANG, X. WU, X. WANG, F. XUE, D. PAN, AND M. XIAO, *Magnetic enhancement of photoluminescence from blue-luminescent graphene quantum dots*, Applied Physics Letters, 108 (2016), p. 061904.
- [17] X. CHEN, Q. JIN, L. WU, C. TUNG, AND X. TANG, *Synthesis and unique photoluminescence properties of nitrogen-rich quantum dots and their applications*, Angewandte Chemie International Edition, 53 (2014), pp. 12542–12547.
- [18] C.-T. CHIEN, S.-S. LI, W.-J. LAI, Y.-C. YEH, H.-A. CHEN, I.-S. CHEN, L.-C. CHEN, K.-H. CHEN, T. NEMOTO, S. ISODA, M. CHEN, T. FUJITA, G. EDA, H. YAMAGUCHI, M. CHHOWALLA, AND C.-W. CHEN, *Tunable photoluminescence from graphene oxide*, Angewandte Chemie International Edition, 51 (2012), pp. 6662–6666.
- [19] H. CHOI, S.-J. KO, Y. CHOI, P. JOO, T. KIM, B. R. LEE, J.-W. JUNG, H. J. CHOI, M. CHA, J.-R. JEONG, I.-W. HWANG, M. H. SONG, B.-S. KIM, AND J. Y. KIM, *Versatile surface plasmon resonance of carbon-dot-supported silver nanoparticles in polymer optoelectronic devices*, Nature Photonics, 7 (2013), pp. 732–738.
- [20] Y. CHOI, G. H. RYU, S. H. MIN, B. R. LEE, M. H. SONG, Z. LEE, AND B.-S. KIM, *Interface-controlled synthesis of heterodimeric silver-carbon nanoparticles derived from polysaccharides*, ACS Nano, 8 (2014), pp. 11377–11385.



- [21] S. K. CUSHING, W. DING, G. CHEN, C. WANG, F. YANG, F. HUANG, AND N. WU, *Excitation wavelength dependent fluorescence of graphene oxide controlled by strain*, *Nanoscale*, 9 (2017), pp. 2240–2245.
- [22] S. K. CUSHING, M. LI, F. HUANG, AND N. WU, *Origin of strong excitation wavelength dependent fluorescence of graphene oxide*, *ACS Nano*, 8 (2014), pp. 1002–1013.
- [23] A. DEMMING, *King of the elements?*, *Nanotechnology*, 21 (2010), p. 300201.
- [24] J. DENG, Q. LU, N. MI, H. LI, M. LIU, M. XU, L. TAN, Q. XIE, Y. ZHANG, AND S. YAO, *Electrochemical synthesis of carbon nanodots directly from alcohols*, *Chemistry A European Journal*, 20 (2014), pp. 4993–4999.
- [25] A. M. DERFUS, W. C. W. CHAN, AND S. N. BHATIA, *Probing the Cytotoxicity of Semiconductor Quantum Dots*, *Nano Letters*, 4 (2004), pp. 11–18.
- [26] S. DEY, P. CHITHAIAH, S. BELAWADI, K. BISWAS, AND C. RAO, *New methods of synthesis and varied properties of carbon quantum dots with high nitrogen content*, *Journal of Materials Research*, 29 (2014), pp. 383–391.
- [27] S. DEY, A. GOVINDARAJ, K. BISWAS, AND C. RAO, *Luminescence properties of boron and nitrogen doped graphene quantum dots prepared from arc-discharge-generated doped graphene samples*, *Chemical Physics Letters*, 595-596 (2014), pp. 203–208.
- [28] N. DHENADHAYALAN, K.-C. LIN, R. SURESH, AND P. RAMAMURTHY, *Unravelling the Multiple Emissive States in Citric-Acid-Derived Carbon Dots*, *Journal of Physical Chemistry C*, 120 (2016), pp. 1252–1261.
- [29] T. DIEING, O. HOLLRICHER, AND J. TOPORSKI, eds., *Confocal Raman Microscopy*, vol. 158 of Springer Series in Optical Sciences, Springer-Verlag Berlin Heidelberg, Berlin, Heidelberg, 2011.
- [30] DIVISION OF MICROBIOLOGY, CENTER FOR FOOD SAFETY AND APPLIED NUTRITION, U.S. FOOD AND DRUG ADMINISTRATION, *Bacteriological analytical manual*, AOAC International, Gaithersburg, Md., 8. ed., revision a ed., 1998.
- [31] Y. DONG, C. CHEN, X. ZHENG, L. GAO, Z. CUI, H. YANG, C. GUO, Y. CHI, AND C. M. LI, *One-step and high yield simultaneous preparation of single- and multi-layer graphene quantum dots from CX-72 carbon black*, *Journal of Materials Chemistry*, 22 (2012), p. 8764.
- [32] Y. DONG, Y. CHEN, X. YOU, W. LIN, C.-H. LU, H.-H. YANG, AND Y. CHI, *High photoluminescent carbon based dots with tunable emission color from orange to green*, *Nanoscale*, 9 (2017), pp. 1028–1032.

## BIBLIOGRAPHY

---

- [33] Y. DONG, H. PANG, H. B. YANG, C. GUO, J. SHAO, Y. CHI, C. M. LI, AND T. YU, *Carbon-based dots co-doped with nitrogen and sulfur for high quantum yield and excitation-independent emission*, *Angewandte Chemie International Edition*, 52 (2013), pp. 7800–7804.
- [34] Y. DONG, J. SHAO, C. CHEN, H. LI, R. WANG, Y. CHI, X. LIN, AND G. CHEN, *Blue luminescent graphene quantum dots and graphene oxide prepared by tuning the carbonization degree of citric acid*, *Carbon*, 50 (2012), pp. 4738–4743.
- [35] Y. DONG, R. WANG, G. LI, C. CHEN, Y. CHI, AND G. CHEN, *Polyamine-functionalized carbon quantum dots as fluorescent probes for selective and sensitive detection of copper ions*, *Analytical Chemistry*, 84 (2012), pp. 6220–6224.
- [36] F. DU, Y. MING, F. ZENG, C. YU, AND S. WU, *A low cytotoxic and ratiometric fluorescent nanosensor based on carbon-dots for intracellular pH sensing and mapping*, *Nanotechnology*, 24 (2013), p. 365101.
- [37] G. EBERT, *Biopolymere: Struktur und Eigenschaften*, Teubner Studienbücher Chemie, Teubner, Stuttgart, 1993.
- [38] G. EDA, Y.-Y. LIN, C. MATTEVI, H. YAMAGUCHI, H.-A. CHEN, I.-S. CHEN, C.-W. CHEN, AND M. CHHOWALLA, *Blue photoluminescence from chemically derived graphene oxide*, *Advanced Materials*, 22 (2010), pp. 505–509.
- [39] J. B. ESSNER, C. H. LABER, S. RAVULA, L. POLO-PARADA, AND G. A. BAKER, *Peedots: Biocompatible fluorescent carbon dots derived from the upcycling of urine*, *Green Chemistry*, 18 (2016), pp. 243–250.
- [40] L. FAN, M. ZHU, X. LEE, R. ZHANG, K. WANG, J. WEI, M. ZHONG, D. WU, AND H. ZHU, *Direct Synthesis of Graphene Quantum Dots by Chemical Vapor Deposition*, *Particle & Particle Systems Characterization*, 30 (2013), pp. 764–769.
- [41] Z. FAN, Y. LI, X. LI, L. FAN, S. ZHOU, D. FANG, AND S. YANG, *Surrounding media sensitive photoluminescence of boron-doped graphene quantum dots for highly fluorescent dyed crystals, chemical sensing and bioimaging*, *Carbon*, 70 (2014), pp. 149–156.
- [42] C. FOWLEY, N. NOMIKOU, A. P. MCHALE, B. MCCAUGHAN, AND J. F. CALLAN, *Extending the tissue penetration capability of conventional photosensitisers: a carbon quantum dot-protoporphyrin IX conjugate for use in two-photon excited photodynamic therapy*, *Chemical Communications*, 49 (2013), pp. 8934–8936.
- [43] E. FRIEDEN, *The Chemical Elements of Life*, *Scientific American*, 227 (1972), pp. 52–60.

- [44] R. R. GADDAM, D. VASUDEVAN, R. NARAYAN, AND RAJU, K. V. S. N., *Controllable synthesis of biosourced blue-green fluorescent carbon dots from camphor for the detection of heavy metal ions in water*, RSC Advances, 4 (2014), pp. 57137–57143.
- [45] C. GALANDE, A. D. MOHITE, A. V. NAUMOV, W. GAO, L. CI, A. AJAYAN, H. GAO, A. SRIVASTAVA, R. B. WEISMAN, AND P. M. AJAYAN, *Quasi-molecular fluorescence from graphene oxide*, Scientific Reports, 1 (2011), p. 85.
- [46] Z. GAN, H. XU, AND Y. HAO, *Mechanism for excitation-dependent photoluminescence from graphene quantum dots and other graphene oxide derivatives: consensus, debates and challenges*, Nanoscale, 8 (2016), pp. 7794–7807.
- [47] E. J. GOH, K. S. KIM, Y. R. KIM, H. S. JUNG, S. BEACK, W. H. KONG, G. SCARCELLI, S. H. YUN, AND S. K. HAHN, *Bioimaging of hyaluronic acid derivatives using nanosized carbon dots*, Biomacromolecules, 13 (2012), pp. 2554–2561.
- [48] T. GOKUS, R. R. NAIR, A. BONETTI, M. BÖHMLER, A. LOMBARDO, K. S. NOVOSELOV, A. K. GEIM, A. C. FERRARI, AND A. HARTSCHUH, *Making graphene luminescent by oxygen plasma treatment*, ACS Nano, 3 (2009), pp. 3963–3968.
- [49] X. GUO, C.-F. WANG, Z.-Y. YU, L. CHEN, AND S. CHEN, *Facile access to versatile fluorescent carbon dots toward light-emitting diodes*, Chemical Communications, 48 (2012), pp. 2692–2694.
- [50] D. M. HALL AND J. G. SAYRE, *Internal Architecture of Potato and Canna Starch*, Textile Research Journal, 41 (1971), pp. 404–414.
- [51] S. HAN, H. ZHANG, J. ZHANG, Y. XIE, L. LIU, H. WANG, X. LI, W. LIU, AND Y. TANG, *Fabrication, gradient extraction and surface polarity-dependent photoluminescence of cow milk-derived carbon dots*, RSC Advances, 4 (2014), pp. 58084–58089.
- [52] D. HAZARIKA AND N. KARAK, *Biodegradable tough waterborne hyperbranched polyester/carbon dot nanocomposite: Approach towards an eco-friendly material*, Green Chem, 18 (2016), pp. 5200–5211.
- [53] A. F. HOLLEMAN, E. WIBERG, AND N. WIBERG, *Lehrbuch der anorganischen Chemie*, de Gruyter, Berlin, 101., verb. und stark erw. aufl. ed., 1995.
- [54] S.-H. HONG AND J. WINTER, *Micro-Raman spectroscopy on a-C:H nanoparticles*, Journal of Applied Physics, 98 (2005), p. 124304.
- [55] Y. HONG, J. W. Y. LAM, AND B. Z. TANG, *Aggregation-induced emission: phenomenon, mechanism and applications*, Chemical Communications, (2009), pp. 4332–4353.

## BIBLIOGRAPHY

---

- [56] ———, *Aggregation-induced emission*, *Chemical Society Reviews*, 40 (2011), pp. 5361–5388.
- [57] P.-C. HSU, Z.-Y. SHIH, C.-H. LEE, AND H.-T. CHANG, *Synthesis and analytical applications of photoluminescent carbon nanodots*, *Green Chemistry*, 14 (2012), p. 917.
- [58] M. HU, Y. YANG, X. GU, Y. HU, J. HUANG, AND C. WANG, *One-pot synthesis of photoluminescent carbon nanodots by carbonization of cyclodextrin and their application in Ag + detection*, *RSC Advances*, 4 (2014), pp. 62446–62452.
- [59] S. HU, R. TIAN, L. WU, Q. ZHAO, J. YANG, J. LIU, AND S. CAO, *Chemical regulation of carbon quantum dots from synthesis to photocatalytic activity*, *Chemistry - An Asian Journal*, 8 (2013), pp. 1035–1041.
- [60] S. HU, A. TRINCHI, P. ATKIN, AND I. COLE, *Tunable photoluminescence across the entire visible spectrum from carbon dots excited by white light*, *Angewandte Chemie International Edition*, 54 (2015), pp. 2970–2974.
- [61] H. HUANG, J.-J. LV, D.-L. ZHOU, N. BAO, Y. XU, A.-J. WANG, AND J.-J. FENG, *One-pot green synthesis of nitrogen-doped carbon nanoparticles as fluorescent probes for mercury ions*, *RSC Advances*, 3 (2013), p. 21691.
- [62] G. JARRE, S. HEYER, E. MEMMEL, T. MEINHARDT, AND A. KRUEGER, *Synthesis of nanodiamond derivatives carrying amino functions and quantification by a modified Kaiser test*, *Beilstein Journal of Organic Chemistry*, 10 (2014), pp. 2729–2737.
- [63] X. JIA, J. LI, AND E. WANG, *One-pot green synthesis of optically pH-sensitive carbon dots with upconversion luminescence*, *Nanoscale*, 4 (2012), pp. 5572–5575.
- [64] C. JIANG, H. WU, X. SONG, X. MA, J. WANG, AND M. TAN, *Presence of photoluminescent carbon dots in Nescafe® original instant coffee: applications to bioimaging*, *Talanta*, 127 (2014), pp. 68–74.
- [65] J. JU AND W. CHEN, *Synthesis of highly fluorescent nitrogen-doped graphene quantum dots for sensitive, label-free detection of Fe (III) in aqueous media*, *Biosensors and Bioelectronics*, 58 (2014), pp. 219–225.
- [66] E. KAISER, R. L. COLESCOTT, C. D. BOSSINGER, AND P. I. COOK, *Color test for detection of free terminal amino groups in the solid-phase synthesis of peptides*, *Analytical Biochemistry*, 34 (1970), pp. 595–598.
- [67] C. O. KAPPE, D. DALLINGER, AND S. MURPHREE, *Practical microwave synthesis for organic chemists: Strategies, instruments, and protocols*, Wiley-VCH, Weinheim, 2009.

- [68] Y. KE, B. GARG, AND Y.-C. LING, *Waste chicken eggshell as low-cost precursor for efficient synthesis of nitrogen-doped fluorescent carbon nanodots and their multi-functional applications*, RSC Advances, 4 (2014), pp. 58329–58336.
- [69] R. A. KELLNER, J.-M. MERMET, M. OTTO, M. VALCARCEL, AND H. M. WIDMER, *Analytical chemistry: A modern approach to analytical science*, Wiley-VCH, Weinheim, 2. ed. ed., 2004.
- [70] S. KIM, S. W. HWANG, M.-K. KIM, D. Y. SHIN, D. H. SHIN, C. O. KIM, S. B. YANG, J. H. PARK, E. HWANG, S.-H. CHOI, G. KO, S. SIM, C. SONE, H. J. CHOI, S. BAE, AND B. H. HONG, *Anomalous behaviors of visible luminescence from graphene quantum dots: interplay between size and shape*, ACS Nano, 6 (2012), pp. 8203–8208.
- [71] J. M. KREMSNER AND A. STADLER, *A chemist's guide to microwave synthesis: Basics, equipment & application examples*, Anton Paar GmbH, Graz, 2nd edition ed., 2016.
- [72] H. W. KROTO, J. R. HEATH, S. C. O'BRIEN, R. F. CURL, AND R. E. SMALLEY, *C60: Buckminsterfullerene*, Nature, 318 (1985), pp. 162–163.
- [73] G. S. KUMAR, R. ROY, D. SEN, U. K. GHORAI, R. THAPA, N. MAZUMDER, S. SAHA, AND K. K. CHATTOPADHYAY, *Amino-functionalized graphene quantum dots: origin of tunable heterogeneous photoluminescence*, Nanoscale, 6 (2014), pp. 3384–3391.
- [74] W. KWON, G. LEE, S. DO, T. JOO, AND S.-W. RHEE, *Size-controlled soft-template synthesis of carbon nanodots toward versatile photoactive materials*, Small, 10 (2014), pp. 506–513.
- [75] W. KWON, J. LIM, J. LEE, T. PARK, AND S.-W. RHEE, *Sulfur-incorporated carbon quantum dots with a strong long-wavelength absorption band*, Journal of Materials Chemistry C, 1 (2013), p. 2002.
- [76] W. KWON AND S.-W. RHEE, *Facile synthesis of graphitic carbon quantum dots with size tunability and uniformity using reverse micelles*, Chemical Communications, 48 (2012), pp. 5256–5258.
- [77] C.-W. LAI, Y.-H. HSIAO, Y.-K. PENG, AND P.-T. CHOU, *Facile synthesis of highly emissive carbon dots from pyrolysis of glycerol; gram scale production of carbon dots/mSiO<sub>2</sub> for cell imaging and drug release*, Journal of Materials Chemistry, 22 (2012), p. 14403.
- [78] J. R. LAKOWICZ, *Principles of fluorescence spectroscopy*, Springer, New York, 3rd ed. ed., 2006.
- [79] M. LARHED, ed., *Microwave methods in organic synthesis*, vol. 266 of Topics in Current Chemistry, Springer-Verlag Berlin Heidelberg, Berlin, Heidelberg, 2006.

## BIBLIOGRAPHY

---

- [80] P. LARKIN, *Infrared and Raman spectroscopy: Principles and spectral interpretation*, Elsevier professional, s.l., 1. Aufl. ed., 2011.
- [81] G. E. LECROY, S. K. SONKAR, F. YANG, L. M. VECA, P. WANG, K. N. TACKETT, J.-J. YU, E. VASILE, H. QIAN, Y. LIU, P. G. LUO, AND Y.-P. SUN, *Toward structurally defined carbon dots as ultracompact fluorescent probes*, ACS Nano, 8 (2014), pp. 4522–4529.
- [82] J. LEE, K. KIM, W. I. PARK, B.-H. KIM, J. H. PARK, T.-H. KIM, S. BONG, C.-H. KIM, G. CHAE, M. JUN, Y. HWANG, Y. S. JUNG, AND S. JEON, *Uniform graphene quantum dots patterned from self-assembled silica nanodots*, Nano Letters, 12 (2012), pp. 6078–6083.
- [83] C.-X. LI, C. YU, C.-F. WANG, AND S. CHEN, *Facile plasma-induced fabrication of fluorescent carbon dots toward high-performance white LEDs*, Journal of Materials Science, 48 (2013), pp. 6307–6311.
- [84] F. LI, C. LIU, J. YANG, Z. WANG, W. LIU, AND F. TIAN, *Mg/N double doping strategy to fabricate extremely high luminescent carbon dots for bioimaging*, RSC Advances, 4 (2014), pp. 3201–3205.
- [85] H. LI, X. HE, Z. KANG, H. HUANG, Y. LIU, J. LIU, S. LIAN, C. H. A. TSANG, X. YANG, AND S.-T. LEE, *Water-soluble fluorescent carbon quantum dots and photocatalyst design*, Angewandte Chemie International Edition, 49 (2010), pp. 4430–4434.
- [86] H. LI, Z. KANG, Y. LIU, AND S.-T. LEE, *Carbon nanodots: Synthesis, properties and applications*, Journal of Materials Chemistry, 22 (2012), p. 24230.
- [87] J. H. LI, T. VASANTHAN, R. HOOVER, AND B. G. ROSSNAGEL, *Starch from hull-less barley: IV. Morphological and structural changes in waxy, normal and high-amylose starch granules during heating*, Food Research International, 37 (2004), pp. 417–428.
- [88] L.-S. LI AND X. YAN, *Colloidal Graphene Quantum Dots*, Journal of Physical Chemistry Letters, 1 (2010), pp. 2572–2576.
- [89] Q. LI, T. Y. OHULCHANSKY, R. LIU, K. KOYNOV, D. WU, A. BEST, R. KUMAR, A. BONOIU, AND P. N. PRASAD, *Photoluminescent Carbon Dots as Biocompatible Nanoprobes for Targeting Cancer Cells in Vitro*, Journal of Physical Chemistry C, 114 (2010), pp. 12062–12068.
- [90] X. LI, H. WANG, Y. SHIMIZU, A. PYATENKO, K. KAWAGUCHI, AND N. KOSHIZAKI, *Preparation of carbon quantum dots with tunable photoluminescence by rapid laser passivation in ordinary organic solvents*, Chemical Communications, 47 (2011), pp. 932–934.

- [91] Y. LI, Y. HU, Y. ZHAO, G. SHI, L. DENG, Y. HOU, AND L. QU, *An electrochemical avenue to green-luminescent graphene quantum dots as potential electron-acceptors for photovoltaics*, *Advanced Materials*, 23 (2011), pp. 776–780.
- [92] S. Y. LIM, W. SHEN, AND Z. GAO, *Carbon quantum dots and their applications*, *Chemical Society Reviews*, 44 (2015), pp. 362–381.
- [93] L. LIN, M. RONG, S. LU, X. SONG, Y. ZHONG, J. YAN, Y. WANG, AND X. CHEN, *A facile synthesis of highly luminescent nitrogen-doped graphene quantum dots for the detection of 2,4,6-trinitrophenol in aqueous solution*, *Nanoscale*, 7 (2015), pp. 1872–1878.
- [94] L. LIN AND S. ZHANG, *Creating high yield water soluble luminescent graphene quantum dots via exfoliating and disintegrating carbon nanotubes and graphite flakes*, *Chemical Communications*, 48 (2012), pp. 10177–10179.
- [95] Z. LIN, W. XUE, H. CHEN, AND J.-M. LIN, *Classical oxidant induced chemiluminescence of fluorescent carbon dots*, *Chemical Communications*, 48 (2012), pp. 1051–1053.
- [96] N. LINDEBOOM, P. R. CHANG, AND R. T. TYLER, *Analytical, Biochemical and Physicochemical Aspects of Starch Granule Size, with Emphasis on Small Granule Starches: A Review*, *Starch - Stärke*, 56 (2004), pp. 89–99.
- [97] C. LIU, P. ZHANG, X. ZHAI, F. TIAN, W. LI, J. YANG, Y. LIU, H. WANG, W. WANG, AND W. LIU, *Nano-carrier for gene delivery and bioimaging based on carbon dots with PEI-passivation enhanced fluorescence*, *Biomaterials*, 33 (2012), pp. 3604–3613.
- [98] H. LIU, T. YE, AND C. MAO, *Fluorescent carbon nanoparticles derived from candle soot*, *Angewandte Chemie International Edition*, 46 (2007), pp. 6473–6475.
- [99] Q. LIU, B. GUO, Z. RAO, B. ZHANG, AND J. R. GONG, *Strong two-photon-induced fluorescence from photostable, biocompatible nitrogen-doped graphene quantum dots for cellular and deep-tissue imaging*, *Nano Letters*, 13 (2013), pp. 2436–2441.
- [100] S. LIU, J. TIAN, L. WANG, Y. ZHANG, X. QIN, Y. LUO, A. M. ASIRI, A. O. AL-YOUBI, AND X. SUN, *Hydrothermal treatment of grass: a low-cost, green route to nitrogen-doped, carbon-rich, photoluminescent polymer nanodots as an effective fluorescent sensing platform for label-free detection of Cu(II) ions*, *Advanced Materials*, 24 (2012), pp. 2037–2041.
- [101] S. LIU, L. WANG, J. TIAN, J. ZHAI, Y. LUO, W. LU, AND X. SUN, *Acid-driven, microwave-assisted production of photoluminescent carbon nitride dots from N,N-dimethylformamide*, *RSC Advances*, 1 (2011), p. 951.

- [102] J. LU, J.-X. YANG, J. WANG, A. LIM, S. WANG, AND K. P. LOH, *One-pot synthesis of fluorescent carbon nanoribbons, nanoparticles, and graphene by the exfoliation of graphite in ionic liquids*, ACS Nano, 3 (2009), pp. 2367–2375.
- [103] J. LU, P. S. E. YEO, C. K. GAN, P. WU, AND K. P. LOH, *Transforming C60 molecules into graphene quantum dots*, Nature Nanotechnology, 6 (2011), pp. 247–252.
- [104] W. LU, X. QIN, S. LIU, G. CHANG, Y. ZHANG, Y. LUO, A. M. ASIRI, A. O. AL-YOUBI, AND X. SUN, *Economical, green synthesis of fluorescent carbon nanoparticles and their use as probes for sensitive and selective detection of mercury(II) ions*, Analytical Chemistry, 84 (2012), pp. 5351–5357.
- [105] Y. LU, J. WANG, H. YUAN, AND D. XIAO, *Separation of carbon quantum dots on a C18 column by binary gradient elution via HPLC*, Analytical Methods, 6 (2014), pp. 8124–8128.
- [106] C. H. LUI, K. F. MAK, J. SHAN, AND T. F. HEINZ, *Ultrafast photoluminescence from graphene*, Physical Review Letters, 105 (2010), p. 127404.
- [107] Z. LUO, P. M. VORA, E. J. MELE, A. T. C. JOHNSON, AND J. M. KIKKAWA, *Photoluminescence and band gap modulation in graphene oxide*, Applied Physics Letters, 94 (2009), p. 111909.
- [108] Z. MA, H. MING, H. HUANG, Y. LIU, AND Z. KANG, *One-step ultrasonic synthesis of fluorescent N-doped carbon dots from glucose and their visible-light sensitive photocatalytic ability*, New Journal of Chemistry, 36 (2012), p. 861.
- [109] T. T. MEILING, P. J. CYWINSKI, AND I. BALD, *White carbon: Fluorescent carbon nanoparticles with tunable quantum yield in a reproducible green synthesis*, Scientific Reports, 6 (2016), p. 28557.
- [110] P. MIAO, K. HAN, Y. TANG, B. WANG, T. LIN, AND W. CHENG, *Recent advances in carbon nanodots: synthesis, properties and biomedical applications*, Nanoscale, 7 (2015), pp. 1586–1595.
- [111] V. N. MOCHALIN, O. SHENDEROVA, D. HO, AND Y. GOGOTSI, *The properties and applications of nanodiamonds*, Nature Nanotechnology, 7 (2011), pp. 11–23.
- [112] S. MONDINI, A. M. FERRETTI, A. PUGLISI, AND A. PONTI, *Pebbles and PebbleJuggler: software for accurate, unbiased, and fast measurement and analysis of nanoparticle morphology from transmission electron microscopy (TEM) micrographs*, Nanoscale, 4 (2012), pp. 5356–5372.



- [113] J. MOON, J. AN, U. SIM, S.-P. CHO, J. H. KANG, C. CHUNG, J.-H. SEO, J. LEE, K. T. NAM, AND B. H. HONG, *One-step synthesis of N-doped graphene quantum sheets from monolayer graphene by nitrogen plasma*, *Advanced Materials*, 26 (2014), pp. 3501–3505.
- [114] M. L. MUELLER, X. YAN, B. DRAGNEA, AND L.-S. LI, *Slow hot-carrier relaxation in colloidal graphene quantum dots*, *Nano Letters*, 11 (2011), pp. 56–60.
- [115] A. G. NASIBULIN, P. V. PIKHITSA, H. JIANG, D. P. BROWN, A. V. KRASHENINNIKOV, A. S. ANISIMOV, P. QUEIPO, A. MOISALA, D. GONZALEZ, G. LIENTSCHNIG, A. HASSANIEN, S. D. SHANDAKOV, G. LOLLI, D. E. RESASCO, M. CHOI, D. TOMÁNEK, AND E. I. KAUPPINEN, *A novel hybrid carbon material*, *Nature Nanotechnology*, 2 (2007), pp. 156–161.
- [116] H. NIE, M. LI, Q. LI, S. LIANG, Y. TAN, L. SHENG, W. SHI, AND S. X.-A. ZHANG, *Carbon Dots with Continuously Tunable Full-Color Emission and Their Application in Ratiometric pH Sensing*, *Chemistry of Materials*, 26 (2014), pp. 3104–3112.
- [117] J. NIU, H. GAO, L. WANG, S. XIN, G. ZHANG, Q. WANG, L. GUO, W. LIU, X. GAO, AND Y. WANG, *Facile synthesis and optical properties of nitrogen-doped carbon dots*, *New Journal of Chemistry*, 38 (2014), p. 1522.
- [118] K. S. NOVOSELOV, A. K. GEIM, S. V. MOROZOV, D. JIANG, Y. ZHANG, S. V. DUBONOS, I. V. GRIGORIEVA, AND A. A. FIRSOV, *Electric field effect in atomically thin carbon films*, *Science*, 306 (2004), pp. 666–669.
- [119] A. OBERLIN, M. ENDO, AND T. KOYAMA, *Filamentous growth of carbon through benzene decomposition*, *Journal of Crystal Growth*, 32 (1976), pp. 335–349.
- [120] T. OGI, H. IWASAKI, K. AISHIMA, F. ISKANDAR, W.-N. WANG, K. TAKIMIYA, AND K. OKUYAMA, *Transient nature of graphene quantum dot formation via a hydrothermal reaction*, *RSC Advances*, 4 (2014), pp. 55709–55715.
- [121] D. PAN, L. GUO, J. ZHANG, C. XI, Q. XUE, H. HUANG, J. LI, Z. ZHANG, W. YU, Z. CHEN, Z. LI, AND M. WU, *Cutting  $sp^2$  clusters in graphene sheets into colloidal graphene quantum dots with strong green fluorescence*, *Journal of Materials Chemistry*, 22 (2012), p. 3314.
- [122] D. PAN, J. ZHANG, Z. LI, AND M. WU, *Hydrothermal route for cutting graphene sheets into blue-luminescent graphene quantum dots*, *Advanced Materials*, 22 (2010), pp. 734–738.
- [123] H. PENG AND J. TRAVAS-SEJDIC, *Simple Aqueous Solution Route to Luminescent Carbo-genic Dots from Carbohydrates*, *Chemistry of Materials*, 21 (2009), pp. 5563–5565.

## BIBLIOGRAPHY

---

- [124] J. PENG, W. GAO, B. K. GUPTA, Z. LIU, R. ROMERO-ABURTO, L. GE, L. SONG, L. B. ALEMANY, X. ZHAN, G. GAO, S. A. VITHAYATHIL, B. A. KAIPPARETTU, A. A. MARTI, T. HAYASHI, J.-J. ZHU, AND P. M. AJAYAN, *Graphene quantum dots derived from carbon fibers*, *Nano Letters*, 12 (2012), pp. 844–849.
- [125] K. S. PRASAD, R. PALLELA, D.-M. KIM, AND Y.-B. SHIM, *Microwave-Assisted One-Pot Synthesis of Metal-Free Nitrogen and Phosphorus Dual-Doped Nanocarbon for Electrocatalysis and Cell Imaging*, *Particle & Particle Systems Characterization*, 30 (2013), pp. 557–564.
- [126] D. PRAT, J. HAYLER, AND A. WELLS, *A survey of solvent selection guides*, *Green Chemistry*, 16 (2014), pp. 4546–4551.
- [127] N. PUVVADA, B. N. P. KUMAR, S. KONAR, H. KALITA, M. MANDAL, AND A. PATHAK, *Synthesis of biocompatible multicolor luminescent carbon dots for bioimaging applications*, *Science and Technology of Advanced Materials*, 13 (2012), p. 045008.
- [128] Z. QIAN, J. MA, X. SHAN, L. SHAO, J. ZHOU, J. CHEN, AND H. FENG, *Surface functionalization of graphene quantum dots with small organic molecules from photoluminescence modulation to bioimaging applications: An experimental and theoretical investigation*, *RSC Advances*, 3 (2013), p. 14571.
- [129] Z. QIAN, X. SHAN, L. CHAI, J. MA, J. CHEN, AND H. FENG, *Si-doped carbon quantum dots: a facile and general preparation strategy, bioimaging application, and multifunctional sensor*, *ACS Applied Materials & Interfaces*, 6 (2014), pp. 6797–6805.
- [130] Z.-A. QIAO, Q. HUO, M. CHI, G. M. VEITH, A. J. BINDER, AND S. DAI, *A “Ship-In-A-Bottle” Approach to Synthesis of Polymer Dots@Silica or Polymer Dots@Carbon Core-Shell Nanospheres*, *Advanced Materials*, 24 (2012), pp. 6017–6021.
- [131] Z.-A. QIAO, Y. WANG, Y. GAO, H. LI, T. DAI, Y. LIU, AND Q. HUO, *Commercially activated carbon as the source for producing multicolor photoluminescent carbon dots by chemical oxidation*, *Chemical Communications*, 46 (2010), pp. 8812–8814.
- [132] D. QU, M. ZHENG, P. DU, Y. ZHOU, L. ZHANG, DI LI, H. TAN, Z. ZHAO, Z. XIE, AND Z. SUN, *Highly luminescent S, N co-doped graphene quantum dots with broad visible absorption bands for visible light photocatalysts*, *Nanoscale*, 5 (2013), pp. 12272–12277.
- [133] D. QU, M. ZHENG, L. ZHANG, H. ZHAO, Z. XIE, X. JING, R. E. HADDAD, H. FAN, AND Z. SUN, *Formation mechanism and optimization of highly luminescent N-doped graphene quantum dots*, *Scientific Reports*, 4 (2014), p. 5294.

- [134] S. QU, X. WANG, Q. LU, X. LIU, AND L. WANG, *A Biocompatible Fluorescent Ink Based on Water-Soluble Luminescent Carbon Nanodots*, *Angewandte Chemie International Edition*, 51 (2012), pp. 12215–12218.
- [135] L. R. RADOVIC AND B. BOCKRATH, *On the chemical nature of graphene edges: origin of stability and potential for magnetism in carbon materials*, *Journal of the American Chemical Society*, 127 (2005), pp. 5917–5927.
- [136] K. RAUSCHER AND R. FRIEBE, *Chemische Tabellen und Rechentafeln für die analytische Praxis*, Deutsch, Frankfurt am Main, unveränd. nachdr. der 11. aufl. ed., 2008.
- [137] K. A. RITTER AND J. W. LYDING, *The influence of edge structure on the electronic properties of graphene quantum dots and nanoribbons*, *Nature Materials*, 8 (2009), pp. 235–242.
- [138] A. V. RODE, E. G. GAMALY, AND B. LUTHER-DAVIES, *Formation of cluster-assembled carbon nano-foam by high-repetition-rate laser ablation*, *Applied Physics A: Materials Science & Processing*, 70 (2000), pp. 135–144.
- [139] P. ROY, A. P. PERIASAMY, C.-Y. LIN, G.-M. HER, W.-J. CHIU, C.-L. LI, C.-L. SHU, C.-C. HUANG, C.-T. LIANG, AND H.-T. CHANG, *Photoluminescent graphene quantum dots for in vivo imaging of apoptotic cells*, *Nanoscale*, 7 (2015), pp. 2504–2510.
- [140] S. SAHU, B. BEHERA, T. K. MAITI, AND S. MOHAPATRA, *Simple one-step synthesis of highly luminescent carbon dots from orange juice: application as excellent bio-imaging agents*, *Chemical Communications*, 48 (2012), pp. 8835–8837.
- [141] A. SALINAS-CASTILLO, M. ARIZA-AVIDAD, C. PRITZ, M. CAMPRUBÍ-ROBLES, B. FERNÁNDEZ, M. J. RUEDAS-RAMA, A. MEGIA-FERNÁNDEZ, A. LAPRESTA-FERNÁNDEZ, F. SANTOYO-GONZALEZ, A. SCHROTT-FISCHER, AND L. F. CAPITAN-VALLVEY, *Carbon dots for copper detection with down and upconversion fluorescent properties as excitation sources*, *Chemical Communications*, 49 (2013), pp. 1103–1105.
- [142] P. S. SAUD, B. PANT, A.-M. ALAM, Z. K. GHOURI, M. PARK, AND H.-Y. KIM, *Carbon quantum dots anchored TiO<sub>2</sub> nanofibers: Effective photocatalyst for waste water treatment*, *Ceramics International*, 41 (2015), pp. 11953–11959.
- [143] W. SECK AND G. FISCHER, *Zur Kenntnis der Stärkagallerten*, *Colloid and Polymer Science*, 93 (1940), pp. 207–224.
- [144] J. SHEN, Y. ZHU, C. CHEN, X. YANG, AND C. LI, *Facile preparation and upconversion luminescence of graphene quantum dots*, *Chemical Communications*, 47 (2011), pp. 2580–2582.

## BIBLIOGRAPHY

---

- [145] L. SHEN, M. CHEN, L. HU, X. CHEN, AND J. WANG, *Growth and stabilization of silver nanoparticles on carbon dots and sensing application*, *Langmuir*, 29 (2013), pp. 16135–16140.
- [146] Q.-Q. SHI, Y.-H. LI, Y. XU, Y. WANG, X.-B. YIN, X.-W. HE, AND Y.-K. ZHANG, *High-yield and high-solubility nitrogen-doped carbon dots: Formation, fluorescence mechanism and imaging application*, *RSC Advances*, 4 (2014), pp. 1563–1566.
- [147] D. B. SHINDE AND V. K. PILLAI, *Electrochemical preparation of luminescent graphene quantum dots from multiwalled carbon nanotubes*, *Chemistry A European Journal*, 18 (2012), pp. 12522–12528.
- [148] M. A. SK, A. ANANTHANARAYANAN, L. HUANG, K. H. LIM, AND P. CHEN, *Revealing the tunable photoluminescence properties of graphene quantum dots*, *Journal of Materials Chemistry C*, 2 (2014), pp. 6954–6960.
- [149] G. SOCRATES, *Infrared and Raman characteristic group frequencies: Tables and charts*, Wiley, Chichester, 3. ed., repr. as paperback ed., 2010.
- [150] V. STRAUSS, J. T. MARGRAF, C. DOLLE, B. BUTZ, T. J. NACKEN, J. WALTER, W. BAUER, W. PEUKERT, E. SPIECKER, T. CLARK, AND D. M. GULDI, *Carbon nanodots: toward a comprehensive understanding of their photoluminescence*, *Journal of the American Chemical Society*, 136 (2014), pp. 17308–17316.
- [151] H. SUN, L. WU, N. GAO, J. REN, AND X. QU, *Improvement of photoluminescence of graphene quantum dots with a biocompatible photochemical reduction pathway and its bioimaging application*, *ACS Applied Materials & Interfaces*, 5 (2013), pp. 1174–1179.
- [152] H. SUN, L. WU, W. WEI, AND X. QU, *Recent advances in graphene quantum dots for sensing*, *Materials Today*, 16 (2013), pp. 433–442.
- [153] J. SUN, S. YANG, Z. WANG, H. SHEN, T. XU, L. SUN, H. LI, W. CHEN, X. JIANG, G. DING, Z. KANG, X. XIE, AND M. JIANG, *Ultra-High Quantum Yield of Graphene Quantum Dots: Aromatic-Nitrogen Doping and Photoluminescence Mechanism*, *Particle & Particle Systems Characterization*, 32 (2015), pp. 434–440.
- [154] X. SUN, Z. LIU, K. WELSHER, J. T. ROBINSON, A. GOODWIN, S. ZARIC, AND H. DAI, *Nano-Graphene Oxide for Cellular Imaging and Drug Delivery*, *Nano Research*, 1 (2008), pp. 203–212.
- [155] Y. SUN, C. SHEN, J. WANG, AND Y. LU, *Facile synthesis of biocompatible N, S-doped carbon dots for cell imaging and ion detecting*, *RSC Advances*, 5 (2015), pp. 16368–16375.

- [156] Y.-P. SUN, X. WANG, F. LU, L. CAO, M. J. MEZIANI, P. G. LUO, L. GU, AND L. M. VECA, *Doped Carbon Nanoparticles as a New Platform for Highly Photoluminescent Dots*, *Journal of Physical Chemistry C*, 112 (2008), pp. 18295–18298.
- [157] Y.-P. SUN, B. ZHOU, Y. LIN, W. WANG, K. A. S. FERNANDO, P. PATHAK, M. J. MEZIANI, B. A. HARRUFF, X. WANG, H. WANG, P. G. LUO, H. YANG, M. E. KOSE, B. CHEN, L. M. VECA, AND S.-Y. XIE, *Quantum-sized carbon dots for bright and colorful photoluminescence*, *Journal of the American Chemical Society*, 128 (2006), pp. 7756–7757.
- [158] L. TANG, R. JI, X. CAO, J. LIN, H. JIANG, X. LI, K. S. TENG, C. M. LUK, S. ZENG, J. HAO, AND S. P. LAU, *Deep ultraviolet photoluminescence of water-soluble self-passivated graphene quantum dots*, *ACS Nano*, 6 (2012), pp. 5102–5110.
- [159] H. TAO, K. YANG, Z. MA, J. WAN, Y. ZHANG, Z. KANG, AND Z. LIU, *In vivo NIR fluorescence imaging, biodistribution, and toxicology of photoluminescent carbon dots produced from carbon nanotubes and graphite*, *Small*, 8 (2012), pp. 281–290.
- [160] H. TETSUKA, R. ASAHI, A. NAGOYA, K. OKAMOTO, I. TAJIMA, R. OHTA, AND A. OKAMOTO, *Optically tunable amino-functionalized graphene quantum dots*, *Advanced Materials*, 24 (2012), pp. 5333–5338.
- [161] L. TIAN, D. GHOSH, W. CHEN, S. PRADHAN, X. CHANG, AND S. CHEN, *Nanosized Carbon Particles From Natural Gas Soot*, *Chemistry of Materials*, 21 (2009), pp. 2803–2809.
- [162] M.-M. TITIRICI, R. J. WHITE, N. BRUN, V. L. BUDARIN, D. S. SU, F. DEL MONTE, J. H. CLARK, AND M. J. MACLACHLAN, *Sustainable carbon materials*, *Chemical Society Reviews*, 44 (2015), pp. 250–290.
- [163] S. S. TOOR, L. ROSENDAHL, AND A. RUDOLF, *Hydrothermal liquefaction of biomass: A review of subcritical water technologies*, *Energy*, 36 (2011), pp. 2328–2342.
- [164] B. VALEUR, *Molecular Fluorescence*, Wiley-VCH, Weinheim, 1st ed. ed., 2002.
- [165] J. C. VINCI, I. M. FERRER, S. J. SEEDHOUSE, A. K. BOURDON, J. M. REYNARD, B. A. FOSTER, F. V. BRIGHT, AND L. A. COLÓN, *Hidden Properties of Carbon Dots Revealed After HPLC Fractionation*, *Journal of Physical Chemistry Letters*, 4 (2013), pp. 239–243.
- [166] A. I. VOGEL AND G. H. JEFFERY, *Vogel's textbook of quantitative chemical analysis*, Longman Scientific & Technical, Harlow, 5th ed ed., 1991.
- [167] K. P. C. VOLLHARDT, N. E. SCHORE, H. BUTENSCHÖN, AND B. ELVERS, eds., *Organische Chemie*, Wiley-VCH, Weinheim, 4. aufl., 2. nachdr ed., 2009.

## BIBLIOGRAPHY

---

- [168] B. WANG, Y. WANG, H. WU, X. SONG, X. GUO, D. ZHANG, X. MA, AND M. TAN, *A mitochondria-targeted fluorescent probe based on TPP-conjugated carbon dots for both one- and two-photon fluorescence cell imaging*, RSC Advances, 4 (2014), pp. 49960–49963.
- [169] F. WANG, Y.-H. CHEN, C.-Y. LIU, AND D.-G. MA, *White light-emitting devices based on carbon dots' electroluminescence*, Chemical Communications, 47 (2011), pp. 3502–3504.
- [170] F. WANG, S. PANG, L. WANG, Q. LI, M. KREITER, AND C.-Y. LIU, *One-Step Synthesis of Highly Luminescent Carbon Dots in Noncoordinating Solvents*, Chemistry of Materials, 22 (2010), pp. 4528–4530.
- [171] J. WANG, C.-F. WANG, AND S. CHEN, *Amphiphilic egg-derived carbon dots: rapid plasma fabrication, pyrolysis process, and multicolor printing patterns*, Angewandte Chemie International Edition, 51 (2012), pp. 9297–9301.
- [172] L. WANG, Y. YIN, A. JAIN, AND H. S. ZHOU, *Aqueous phase synthesis of highly luminescent, nitrogen-doped carbon dots and their application as bioimaging agents*, Langmuir, 30 (2014), pp. 14270–14275.
- [173] Q. WANG, H. ZHENG, Y. LONG, L. ZHANG, M. GAO, AND W. BAI, *Microwave-hydrothermal synthesis of fluorescent carbon dots from graphite oxide*, Carbon, 49 (2011), pp. 3134–3140.
- [174] R. WANG, Y. XU, T. ZHANG, AND Y. JIANG, *Rapid and sensitive detection of Salmonella typhimurium using aptamer-conjugated carbon dots as fluorescence probe*, Analytical Methods, 7 (2015), pp. 1701–1706.
- [175] X. WANG, L. CAO, S.-T. YANG, F. LU, M. J. MEZIANI, L. TIAN, K. W. SUN, M. A. BLOODGOOD, AND Y.-P. SUN, *Bandgap-like strong fluorescence in functionalized carbon nanoparticles*, Angewandte Chemie International Edition, 49 (2010), pp. 5310–5314.
- [176] Y. WANG, D. C. ALSMEYER, AND R. L. MCCREERY, *Raman spectroscopy of carbon materials: Structural basis of observed spectra*, Chemistry of Materials, 2 (1990), pp. 557–563.
- [177] Y. WANG, R. HU, G. LIN, I. ROY, AND K.-T. YONG, *Functionalized quantum dots for biosensing and bioimaging and concerns on toxicity*, ACS Applied Materials & Interfaces, 5 (2013), pp. 2786–2799.
- [178] J. WEI, B. LIU, AND P. YIN, *Dual functional carbonaceous nanodots exist in a cup of tea*, RSC Advances, 4 (2014), pp. 63414–63419.
- [179] W. WEI, C. XU, L. WU, J. WANG, J. REN, AND X. QU, *Non-enzymatic-browning-reaction: a versatile route for production of nitrogen-doped carbon dots with tunable multicolor luminescent display*, Scientific Reports, 4 (2014), p. 3564.

- [180] X. WU, F. TIAN, W. WANG, J. CHEN, M. WU, AND J. X. ZHAO, *Fabrication of highly fluorescent graphene quantum dots using L-glutamic acid for in vitro/in vivo imaging and sensing*, *Journal of Materials Chemistry C*, 1 (2013), pp. 4676–4684.
- [181] J. XU, Y. ZHOU, S. LIU, M. DONG, AND C. HUANG, *Low-cost synthesis of carbon nanodots from natural products used as a fluorescent probe for the detection of ferrum(iii) ions in lake water*, *Analytical Methods*, 6 (2014), p. 2086.
- [182] X. XU, R. RAY, Y. GU, H. J. PLOEHN, L. GEARHEART, K. RAKER, AND W. A. SCRIVENS, *Electrophoretic analysis and purification of fluorescent single-walled carbon nanotube fragments*, *Journal of the American Chemical Society*, 126 (2004), pp. 12736–12737.
- [183] Y. XU, M. WU, Y. LIU, X.-Z. FENG, X.-B. YIN, X.-W. HE, AND Y.-K. ZHANG, *Nitrogen-doped carbon dots: a facile and general preparation method, photoluminescence investigation, and imaging applications*, *Chemistry A European Journal*, 19 (2013), pp. 2276–2283.
- [184] L. YANG, W. JIANG, L. QIU, X. JIANG, D. ZUO, D. WANG, AND L. YANG, *One pot synthesis of highly luminescent polyethylene glycol anchored carbon dots functionalized with a nuclear localization signal peptide for cell nucleus imaging*, *Nanoscale*, 7 (2015), pp. 6104–6113.
- [185] S. YANG, J. SUN, P. HE, X. DENG, Z. WANG, C. HU, G. DING, AND X. XIE, *Selenium Doped Graphene Quantum Dots as an Ultrasensitive Redox Fluorescent Switch*, *Chemistry of Materials*, 27 (2015), pp. 2004–2011.
- [186] S. YANG, J. SUN, X. LI, W. ZHOU, Z. WANG, P. HE, G. DING, X. XIE, Z. KANG, AND M. JIANG, *Large-scale fabrication of heavy doped carbon quantum dots with tunable photoluminescence and sensitive fluorescence detection*, *Journal of Materials Chemistry A*, 2 (2014), p. 8660.
- [187] S.-T. YANG, L. CAO, P. G. LUO, F. LU, X. WANG, H. WANG, M. J. MEZIANI, Y. LIU, G. QI, AND Y.-P. SUN, *Carbon dots for optical imaging in vivo*, *Journal of the American Chemical Society*, 131 (2009), pp. 11308–11309.
- [188] S.-T. YANG, X. WANG, H. WANG, F. LU, P. G. LUO, L. CAO, M. J. MEZIANI, J.-H. LIU, Y. LIU, M. CHEN, Y. HUANG, AND Y.-P. SUN, *Carbon Dots as Nontoxic and High-Performance Fluorescence Imaging Agents*, *Journal of Physical Chemistry C*, 113 (2009), pp. 18110–18114.
- [189] Z.-C. YANG, M. WANG, A. M. YONG, S. Y. WONG, X.-H. ZHANG, H. TAN, A. Y. CHANG, X. LI, AND J. WANG, *Intrinsically fluorescent carbon dots with tunable emission derived*

- from hydrothermal treatment of glucose in the presence of monopotassium phosphate*, Chemical Communications, 47 (2011), pp. 11615–11617.
- [190] R. YE, C. XIANG, J. LIN, Z. PENG, K. HUANG, Z. YAN, N. P. COOK, E. L. G. SAMUEL, C.-C. HWANG, G. RUAN, G. CERIOTTI, A.-R. O. RAJI, A. A. MARTÍ, AND J. M. TOUR, *Coal as an abundant source of graphene quantum dots*, Nature Communications, 4 (2013), p. 2943.
- [191] P. YU, X. WEN, Y.-R. TOH, AND J. TANG, *Temperature-Dependent Fluorescence in Carbon Dots*, Journal of Physical Chemistry C, 116 (2012), pp. 25552–25557.
- [192] X. ZHAI, P. ZHANG, C. LIU, T. BAI, W. LI, L. DAI, AND W. LIU, *Highly luminescent carbon nanodots by microwave-assisted pyrolysis*, Chemical Communications, 48 (2012), pp. 7955–7957.
- [193] C. ZHANG, Y. LIU, X.-Q. XIONG, L.-H. PENG, L. GAN, C.-F. CHEN, AND H.-B. XU, *Three-dimensional nanographene based on triptycene: synthesis and its application in fluorescence imaging*, Organic Letters, 14 (2012), pp. 5912–5915.
- [194] M. ZHANG, L. BAI, W. SHANG, W. XIE, H. MA, Y. FU, D. FANG, H. SUN, L. FAN, M. HAN, C. LIU, AND S. YANG, *Facile synthesis of water-soluble, highly fluorescent graphene quantum dots as a robust biological label for stem cells*, Journal of Materials Chemistry, 22 (2012), p. 7461.
- [195] R. ZHANG, Y.-B. LIU, AND S.-Q. SUN, *Preparation of highly luminescent and biocompatible carbon dots using a new extraction method*, Journal of Nanoparticle Research, 15 (2013), p. 6726.
- [196] X. ZHANG, Y. ZHANG, Y. WANG, S. KALYTCHUK, S. V. KERSHAW, Y. WANG, P. WANG, T. ZHANG, Y. ZHAO, H. ZHANG, T. CUI, Y. WANG, J. ZHAO, W. W. YU, AND A. L. ROGACH, *Color-switchable electroluminescence of carbon dot light-emitting diodes*, ACS Nano, 7 (2013), pp. 11234–11241.
- [197] Y. ZHANG, X. LIU, Y. FAN, X. GUO, L. ZHOU, Y. LV, AND J. LIN, *One-step microwave synthesis of N-doped hydroxyl-functionalized carbon dots with ultra-high fluorescence quantum yields*, Nanoscale, 8 (2016), pp. 15281–15287.
- [198] Z. ZHANG, J. HAO, J. ZHANG, B. ZHANG, AND J. TANG, *Protein as the source for synthesizing fluorescent carbon dots by a one-pot hydrothermal route*, RSC Advances, 2 (2012), p. 8599.
- [199] Z. ZHANG, W. SUN, AND P. WU, *Highly Photoluminescent Carbon Dots Derived from Egg White: Facile and Green Synthesis, Photoluminescence Properties, and Multiple Applications*, ACS Sustainable Chemistry & Engineering, 3 (2015), pp. 1412–1418.



- [200] Q.-L. ZHAO, Z.-L. ZHANG, B.-H. HUANG, J. PENG, M. ZHANG, AND D.-W. PANG, *Facile preparation of low cytotoxicity fluorescent carbon nanocrystals by electrooxidation of graphite*, Chemical Communications, (2008), pp. 5116–5118.
- [201] B. ZHENG, T. LIU, M. C. PAAU, M. WANG, Y. LIU, L. LIU, C. WU, J. DU, D. XIAO, AND M. M. F. CHOI, *One pot selective synthesis of water and organic soluble carbon dots with green fluorescence emission*, RSC Advances, 5 (2015), pp. 11667–11675.
- [202] H. ZHENG, Q. WANG, Y. LONG, H. ZHANG, X. HUANG, AND R. ZHU, *Enhancing the luminescence of carbon dots with a reduction pathway*, Chemical Communications, 47 (2011), pp. 10650–10652.
- [203] L. ZHENG, Y. CHI, Y. DONG, J. LIN, AND B. WANG, *Electrochemiluminescence of water-soluble carbon nanocrystals released electrochemically from graphite*, Journal of the American Chemical Society, 131 (2009), pp. 4564–4565.
- [204] X. T. ZHENG, A. ANANTHANARAYANAN, K. Q. LUO, AND P. CHEN, *Glowing graphene quantum dots and carbon dots: properties, syntheses, and biological applications*, Small, 11 (2015), pp. 1620–1636.
- [205] X. T. ZHENG, A. THAN, A. ANANTHANARAYA, D.-H. KIM, AND P. CHEN, *Graphene quantum dots as universal fluorophores and their use in revealing regulated trafficking of insulin receptors in adipocytes*, ACS Nano, 7 (2013), pp. 6278–6286.
- [206] J. ZHOU, C. BOOKER, R. LI, X. ZHOU, T.-K. SHAM, X. SUN, AND Z. DING, *An electrochemical avenue to blue luminescent nanocrystals from multiwalled carbon nanotubes (MWCNTs)*, Journal of the American Chemical Society, 129 (2007), pp. 744–745.
- [207] J. ZHOU, X. SHAN, J. MA, Y. GU, Z. QIAN, J. CHEN, AND H. FENG, *Facile synthesis of P-doped carbon quantum dots with highly efficient photoluminescence*, RSC Advances, 4 (2014), p. 5465.
- [208] J. ZHOU, Z. SHENG, H. HAN, M. ZOU, AND C. LI, *Facile synthesis of fluorescent carbon dots using watermelon peel as a carbon source*, Materials Letters, 66 (2012), pp. 222–224.
- [209] X. ZHOU, Y. ZHANG, C. WANG, X. WU, Y. YANG, B. ZHENG, H. WU, S. GUO, AND J. ZHANG, *Photo-Fenton reaction of graphene oxide: a new strategy to prepare graphene quantum dots for DNA cleavage*, ACS Nano, 6 (2012), pp. 6592–6599.
- [210] C. ZHU, S. YANG, G. WANG, R. MO, P. HE, J. SUN, Z. DI, N. YUAN, J. DING, G. DING, AND X. XIE, *Negative induction effect of graphite N on graphene quantum dots: Tunable band gap photoluminescence*, Journal of Materials Chemistry C, 3 (2015), pp. 8810–8816.

## BIBLIOGRAPHY

---

- [211] H. ZHU, X. WANG, Y. LI, Z. WANG, F. YANG, AND X. YANG, *Microwave synthesis of fluorescent carbon nanoparticles with electrochemiluminescence properties*, Chemical Communications, (2009), pp. 5118–5120.
- [212] S. ZHU, Q. MENG, L. WANG, J. ZHANG, Y. SONG, H. JIN, K. ZHANG, H. SUN, H. WANG, AND B. YANG, *Highly photoluminescent carbon dots for multicolor patterning, sensors, and bioimaging*, Angewandte Chemie International Edition, 52 (2013), pp. 3953–3957.
- [213] S. ZHU, Y. SONG, X. ZHAO, J. SHAO, J. ZHANG, AND B. YANG, *The photoluminescence mechanism in carbon dots (graphene quantum dots, carbon nanodots, and polymer dots): Current state and future perspective*, Nano Research, 8 (2015), pp. 355–381.
- [214] S. ZHU, S. TANG, J. ZHANG, AND B. YANG, *Control the size and surface chemistry of graphene for the rising fluorescent materials*, Chemical Communications, 48 (2012), pp. 4527–4539.
- [215] S. ZHU, L. WANG, N. ZHOU, X. ZHAO, Y. SONG, S. MAHARJAN, J. ZHANG, L. LU, H. WANG, AND B. YANG, *The crosslink enhanced emission (CEE) in non-conjugated polymer dots: from the photoluminescence mechanism to the cellular uptake mechanism and internalization*, Chemical Communications, 50 (2014), pp. 13845–13848.
- [216] S. ZHU, J. ZHANG, C. QIAO, S. TANG, Y. LI, W. YUAN, B. LI, L. TIAN, F. LIU, R. HU, H. GAO, H. WEI, H. ZHANG, H. SUN, AND B. YANG, *Strongly green-photoluminescent graphene quantum dots for bioimaging applications*, Chemical Communications, 47 (2011), pp. 6858–6860.
- [217] S. ZHU, J. ZHANG, S. TANG, C. QIAO, L. WANG, H. WANG, X. LIU, B. LI, Y. LI, W. YU, X. WANG, H. SUN, AND B. YANG, *Surface Chemistry Routes to Modulate the Photoluminescence of Graphene Quantum Dots: From Fluorescence Mechanism to Up-Conversion Bioimaging Applications*, Advanced Functional Materials, 22 (2012), pp. 4732–4740.
- [218] S. ZHU, J. ZHANG, L. WANG, Y. SONG, G. ZHANG, H. WANG, AND B. YANG, *A general route to make non-conjugated linear polymers luminescent*, Chemical Communications, 48 (2012), p. 10889.
- [219] X. ZHU, T. ZHAO, Z. NIE, Z. MIAO, Y. LIU, AND S. YAO, *Nitrogen-doped carbon nanoparticle modulated turn-on fluorescent probes for histidine detection and its imaging in living cells*, Nanoscale, 8 (2016), pp. 2205–2211.
- [220] J. ZONG, Y. ZHU, X. YANG, J. SHEN, AND C. LI, *Synthesis of photoluminescent carbogenic dots using mesoporous silica spheres as nanoreactors*, Chemical Communications, 47 (2011), pp. 764–766.